

Thick Disks in External Galaxies

Peter Yoachim

A dissertation submitted in partial fulfillment
of the requirements for the degree of

Doctor of Philosophy

University of Washington

2007

Program Authorized to Offer Degree: Department of Astronomy

University of Washington
Graduate School

This is to certify that I have examined this copy of a doctoral dissertation by

Peter Yoachim

and have found that it is complete and satisfactory in all respects,
and that any and all revisions required by the final
examining committee have been made.

Chair of the Supervisory Committee:

Julianne J. Dalcanton

Reading Committee:

Julianne J. Dalcanton

Thomas Quinn

Suzanne Hawley

Date: _____

In presenting this dissertation in partial fulfillment of the requirements for the doctoral degree at the University of Washington, I agree that the Library shall make its copies freely available for inspection. I further agree that extensive copying of this dissertation is allowable only for scholarly purposes, consistent with "fair use" as prescribed in the U.S. Copyright Law. Requests for copying or reproduction of this dissertation may be referred to Proquest Information and Learning, 300 North Zeeb Road, Ann Arbor, MI 48106-1346, 1-800-521-0600, to whom the author has granted "the right to reproduce and sell (a) copies of the manuscript in microform and/or (b) printed copies of the manuscript made from microform."

Signature  _____

Date: July 20, 2007 _____

University of Washington

Abstract

Thick Disks in External Galaxies

Peter Yoachim

Chair of the Supervisory Committee:
Professor Julianne J. Dalcanton
Department of Astronomy

This thesis presents results from a series of observations of thick disks in external galaxies. Using photometric decompositions of a sample of edge-on disk galaxies, we characterize the morphological properties of thin and thick disks. The thick disks have larger scale heights and longer scale lengths than the embedded thin disks, by factors of ~ 2 and ~ 1.25 , respectively. The observed structural parameters agree well with the properties of thick and thin disks derived from star counts in the Milky Way and from resolved stellar populations in nearby galaxies. We find that massive galaxies' luminosities are dominated by the thin disk. However, in low mass galaxies ($V_c \lesssim 120$ km s $^{-1}$), thick disk stars contribute nearly half of the luminosity and dominate the stellar mass.

We target thin and thick disk dominated regions with the Dual Imaging Spectrograph (DIS) on the ARC 3.5-meter telescope at Apache Point as well as the GMOS spectrographs on the Gemini 8-meter telescopes. We use the Gemini spectra to analyze the kinematics of stars and ionized gas. Lick indices are extracted from the APO spectra to derive characteristic ages and metallicities for the thin and thick disk stars. For the higher mass galaxies in the sample, we find no major differences between the thin and thick disk kinematics. In the lower mass galaxies, there is a wide range of thick disk behavior including thick disks with substantial lag and one counter-

rotating thick disk. In all our galaxies, the thick disk is markedly older than the thin disk. Our data also suggests that thick disks tend to be metal poor compared to the thin disks. We compare these observations to predictions made by various thick disk formation models. The presence of a counter-rotating thick disk strongly suggests that at least some thick disks are formed via direct accretion of stellar material from satellite galaxies.

TABLE OF CONTENTS

	Page
List of Figures	iv
List of Tables	xiii
Chapter 1: Introduction	1
1.1 The Milky Way Disks	2
1.2 Thick Disks in Other Galaxies	5
1.3 Brief Thesis Outline	7
Chapter 2: Structural Parameters of Thin and Thick Disks in Edge-On Disk Galaxies	8
2.1 Chapter Summary	8
2.2 Introduction	9
2.2.1 Galaxy Sample	12
2.3 2D Fitting	14
2.3.1 Galaxy Models	14
2.3.2 Fitting Method	16
2.3.3 Tests on Artificial Images	19
2.4 Single Disk Fits	20
2.5 Two Disk Fits	24
2.5.1 Need for a Second Component	24
2.5.2 Why Not a Halo?	30
2.5.3 Dust effects	32
2.5.4 Results of Thick + Thin Disk Fits	34
2.6 The Formation of the Thick Disk	56
2.6.1 The Merger Origin of Thick Disks	58
2.6.2 Constraints from the Structures of Thick and Thin Disks	62

2.6.3	Further Implications	69
2.7	Conclusions	73
Chapter 3:	Kinematics of Thin and Thick Disks in External Galaxies . . .	81
3.1	Chapter Summary	81
3.2	Introduction	81
3.3	Observations	84
3.3.1	Target Selection	84
3.3.2	Observing Strategy	85
3.3.3	Data Reduction	87
3.4	Rotation Curves	89
3.4.1	H α Rotation Curves	89
3.4.2	Ca II Rotation Curves	93
3.5	Stellar Kinematics	96
3.5.1	Velocity Dispersions	103
3.6	How Much Counter Rotating Material Could There Be?	109
3.7	Expected Lags	110
3.8	Dust and Projection Effects	114
3.9	Discussion	117
3.10	Conclusions	121
3.11	Stellar Rotation Curves in the Presence of Systematic Errors	122
Chapter 4:	Ages and Metallicities of Thin and Thick Disks Using Lick Indices	126
4.1	Chapter Summary	126
4.2	Introduction	126
4.3	Observations	130
4.4	Data Reduction	132
4.5	Moving Onto the Lick System	136
4.5.1	Emission Line Removal	141
4.5.2	Deriving Ages and Metallicities	146
4.5.3	Radial Gradients	148
4.5.4	Possible Errors	160
4.6	Discussion	166

4.6.1	Are Low Mass Thick Disks Old?	166
4.6.2	Are Low Mass Thick Disks Metal Poor?	166
4.6.3	Are Thick Disks α -enhanced?	167
4.6.4	Are Thick Disks “Normal” Stellar Populations?	168
4.6.5	Radial Color Gradients in the Thin Disks	168
4.7	Conclusions	169
Chapter 5:	Conclusion and Future Work	171
5.1	Observational Properties of Thick Disks	171
5.1.1	Morphological Properties	171
5.1.2	Dynamical Properties	171
5.1.3	Ages and Metallicities	172
5.2	Final Thoughts on Thick Disk Formation	172
5.3	Future Work	175
5.3.1	Radial Gradients of Stellar Populations	175
5.3.2	Behavior of Extra-planer Ionized Gas	175
5.3.3	Stellar Kinematics at Low Surface Brightness Levels	176
	Bibliography	177
	Appendix A: My Personal Objection to Established Grammar Conventions	197

LIST OF FIGURES

Figure Number	Page
<p>1.1 An example edge-on disk galaxy that is analyzed in this thesis. The top panel shows a deep R-band image, while the bottom panel shows a $B - R$ color map. The color map reveals that the faintest regions above and below the midplane are distinctly redder than the midplane. This faint reddish region seems to be analogous to the Milky Way thick disk. By isolating the faint red region, we can observe the properties of the thick disk and compare it to formation models.</p>	6
<p>2.1 Cumulative distributions showing the systematic effects of fitting our galaxies with varying models. All models are compared to a fit using inverse weighting and no masked regions. Fits for all three filters have been combined. The solid curve shows the model which used uniform pixel weighting, while the dotted curve shows the midplane masked model, and the dashed curve shows the $R < 3h_R$ radially masked model.</p>	22
<p>2.2 Single disk scale heights for the R-band fits. Galaxies with prominent dust lanes are plotted with with open circles. For comparison, we show the I-band scale heights from the edge-on sample of Kregel et al. (2002), plotted as red diamonds.</p>	25
<p>2.3 Single disk scale lengths for the R-band (top) and B-band (bottom) fits. Galaxies with prominent dust lanes are plotted with with open circles. For comparison, we show other single disk fits gathered from the literature. The de Jong (1996a) and MacArthur et al. (2003) data are face-on or moderately inclined galaxy samples with the scale lengths measured in the R and B-bands (plotted as blue squares and green triangles respectively). The Swaters & Balcells (2002) sample consists of late-type spiral and irregular galaxies with scale lengths measured in the R and B-band (plotted as red diamonds). The Kregel et al. (2002) data were measured from edge-on galaxies in the I-band (plotted as blue squares).</p>	26

2.4	Comparison of scale lengths and heights for the single disk fits in different bands. Open symbols are used for galaxies with prominent dust lanes.	27
2.5	Single disk fits showing the flatness (h_R/z_0) for each band. Open symbols are used for galaxies with prominent dust lanes. Dotted lines show the average flatness for a sample of 34 galaxies in <i>I</i> -band presented in Kregel et al. (2002). Dashed lines show the average flatness measured from a sample of 153 galaxies from the Revised Flat Galaxy Catalog imaged by 2MASS in the <i>K</i> -band and presented in Bizyaev & Mitronova (2002)	27
2.6	Edge-on peak surface brightnesses for the single disk fits. Open symbols are used for galaxies with prominent dust lanes. Points have not been corrected for internal extinction.	28
2.7	<i>Left</i> : Residuals collapsed along the radial direction and averaged over galaxies binned by mass. The single disk models (dashed lines) are very poor fits, leaving large amounts of excess flux at high latitudes. The two disk models (solid lines) do a much better job fitting the vertical light distribution at <i>all</i> latitudes and show only a small systematic trend to over-subtract at high z	29
2.8	Tully Fisher relation derived from the single disk fits. Open circles show points uncorrected for internal extinction while solid circles have been corrected for internal extinction using the method of Tully et al. (1998). Solid lines on the left and middle panel show TF relations from the Hubble Key Project (Sakai et al., 2000). The solid line in the right panel shows the K' TF-relation of Verheijen (2001). The luminosities for the two disk fits show a comparable offset.	33
2.9	Scale heights of thin and thick disks. Values for the Milky Way from Larsen & Humphreys (2003) are plotted for comparison using $z_0 = 2h_z$ for an exponential vertical profile. Open symbols are used for galaxies with prominent dust lanes. Dashed lines show power-law fits to the data ($z_{0,\text{thin}} = (610 \text{ pc})(\frac{V_c}{100 \text{ km s}^{-1}})^{0.90}$ and $z_{0,\text{thick}} = (1400 \text{ pc})(\frac{V_c}{100 \text{ km s}^{-1}})^{1.0}$). In galaxies that have strong dust lanes, the scale height of the thin disk is likely to be biased towards larger values.	36
2.10	Ratios of the scale heights for the thick and thin disks. Error bars represent the full range of ratios to which different models converged. Galaxies with prominent dust lanes are plotted as open circles. The dotted line shows the median value of $z_{0,\text{thick}}/z_{0,\text{thin}} = 2.35$	37

2.11	Comparison of our scale height ratios to values drawn from the literature. We compare to early-type galaxies (Sb and earlier; red diamonds), late type galaxies (Sc and Sd; blue triangles), the MW (green square), and simulated galaxies (asterisks). The range of values available for the Pohlen et al. (2004) sample of early type galaxies is plotted as a single point with error bars.	39
2.12	Comparison of our results with the scale heights of different stellar populations measured from resolved stars in 6 nearby galaxies (Seth et al., 2005b). The component we have identified as the thin disk appears to be intermediate between the scale height of young Main Sequence stars and medium-age Asymptotic Giant Branch stars while our thick disk component is similar to the old Red Giant Branch populations. . . .	41
2.13	Scale lengths of thick and thin disks from the 2-disk fits. The dashed lines show power law fits. Open symbols are used for galaxies with prominent dust lanes. Dashed lines show power-law fits of $h_{R,\text{thin}} = 3.40(V_c/100 \text{ km s}^{-1})^{1.2}$ kpc and $h_{R,\text{thick}} = 3.9(V_c/100 \text{ km s}^{-1})^{1.0}$ kpc.	42
2.14	Ratios of the scale lengths for the thick and thin disks. The horizontal line indicates where the thin and thick disk components have equal scale lengths. Error bars represent the full range of ratios to which different models converged, and are indicators of our systematic errors. Open symbols are used for galaxies with prominent dust lanes.	43
2.15	Comparison of our scale height ratios to values drawn from the literature. Comparison points are the same as Figure 2.11.	44
2.16	Axial ratio (h_R/z_0) vs circular velocity for the thin (left) and thick (right) disks. Galaxies with prominent dust lanes are plotted as open circles. The axial ratios of Milky Way disk components are plotted for comparison (Table 2.2). The axial ratios of our thin and thick disks agree well with the comparable components for the MW.	46
2.17	Edge-on peak surface brightnesses for the 2-disk fits in the R -band. Galaxies with prominent dust lanes are plotted as open circles.	46
2.18	Ratio of the total R -band luminosity of the thick disk compared to the thin disk for the sample galaxies. The thin disk luminosities have been corrected for internal extinction. The dotted line indicates where the thick and thin disks contribute equally to the total luminosity. Error bars show the full range of values from different models, and are indicative of our systematic errors. Galaxies with prominent dust lanes are plotted as open circles. The solid line is a fitted power-law of the form $L_{\text{thick}}/L_{\text{thin}} = 0.25(V_c/100 \text{ km s}^{-1})^{-2.1}$	48

2.19	Comparison of our luminosity ratios to others in the literature. Comparison points are the same as Figure 2.11. Unlike Figure 2.18, we have made no correction of internal extinction to allow for easier comparison with previous studies.	49
2.20	Extracted colors for the thick and thin disks. The thin disk colors shows the full range of $B - R$ values for the midplane between $h_R < R < 3h_R$. The thin disk has been corrected for internal extinction, but we assume no correction for the thick disk. Open circles show galaxies with dust lanes.	52
2.21	Comparison of thin and thick disk colors. The diagonal line indicates where the two components have equal color. Thin disk colors have been corrected for internal extinction. Open circles show galaxies with dust lanes.	53
2.22	Stellar mass ratios of the thick and thin disks. The thin disks luminosities and corresponding masses have been increased to account for dust extinction. Galaxies with prominent dust lanes are plotted as open circles. The solid line is a power-law fit $(M_{\text{thick}}/M_{\text{thin}})_{\text{stars}} = 0.53(V_c/100 \text{ km s}^{-1})^{-2.3}$	55
2.23	Baryonic mass ratios of the thick and thin disks. The thin disks luminosities, and corresponding masses, have been increased to account for extinction effects and include the estimated thin disk mass stored in gas. Galaxies with prominent dust lanes are plotted as open circles. The solid line is a power-law fit $M_{\text{thick,stars}}/M_{\text{thin,baryons}} = 0.19(V_c/100 \text{ km s}^{-1})^{-1.4}$	56
2.24	Final baryon fractions of the thick and thin components as a function of circular velocity. The thin disk has been corrected for internal dust extinction. The baryonic mass fraction of the thick disk clearly increases towards lower galaxy mass.	57

3.1	Results from different sky subtraction techniques for the midplane of FGC 1415. On the left, we show the results from standard sky subtraction techniques and the right panels show our sky template subtraction. Top panels show the raw galaxy spectrum before the sky has been subtracted. Middle panels show a single subtracted frame and the final combined image. The bottom panel shows the combined spectrum summed along the spatial dimension. An arrow points out a sky line residual present in the standard subtraction that is eliminated in template subtraction. The brightest sky lines leave large residuals in both cases, but the magnitude of residuals is decreased significantly with the nod-and-shuffle-like technique (see the lines near $\sim 8770\text{\AA}$, for example).	90
3.2	Examples of spectra before and after sky subtraction. The top panel shows the results of a single midplane exposure before and after sky template subtraction (top and middle curves respectively). The middle panel shows a single offplane exposure before and after extraction. Dotted lines show the RMS noise level in the spectra. The bottom panel shows the final midplane and offplane spectra after all the frames have been averaged together. The largest systematic residuals from the sky lines have been masked. The three vertical marks show the location of the Ca triplet absorption lines. All of the spectra were extracted over the central $14''$ of the galaxy.	91
3.3	An example of our extracted galaxy spectra. The solid line shows the normalized galaxy spectrum. Red regions mark where the spectra was masked due to sky line contamination. The noise spectrum (multiplied by 5) is plotted as a dotted line. The blue dashed line shows the best fit shifted and broadened stellar spectrum.	95
3.4	Rotation curve measurements for each galaxy. Top panels: R -band images of each galaxy. The color scale goes from dark blue ($\mu_R = 21$) to green ($\mu_R = 23$), to red/white ($\mu_R = 25.5$). Solid black lines have been drawn where the Gemini long-slit jaws were placed. Middle Panels: Rotation curves for midplane (blue) and offplane (red). Points with error bars are from Ca II measurements. Vertical error bars are uncertainties derived from Monte Carlo simulations, horizontal error bars show the spectral extraction regions. Small lines show velocities measured from the $H\alpha$ emission lines. Bottom Panels: Stellar velocity dispersions measured from the Ca II feature. All error bars are from a Monte Carlo simulation. Points with overwhelmingly large error-bars or large systematic uncertainties have been omitted.	97

3.5	Same as Figure 3.4.	98
3.6	Same as Figure 3.4.	98
3.7	Same as Figure 3.4.	99
3.8	Same as Figure 3.4.	99
3.9	Same as Figure 3.4.	100
3.10	Same as Figure 3.4.	100
3.11	Same as Figure 3.4.	101
3.12	Same as Figure 3.4.	101
3.13	The results of fitting various rotation curve models to our data. The top left panels show fits of the simple model where the midplane and offplane observations are fit independently. Upper right panels show shaded regions show the range of fits derived from varying the fraction of thin and thick disk light at each slit position. Solid lines show the fits for when we use the thin and thick disk fractions of the photometric fits in Yoachim & Dalcanton (2006b). Lower panels show the observations as points and solid lines show the models from the above panels once they have been flux weighted and binned in the same manner as the observations. Throughout, red is used for thick disk/offplane and blue is used for thin disk/midplane. Each panel has a dashed line showing the $W_{50/2}$ value from the literature. FGC 1440 is not shown because we failed to measure a stellar rotation curve in the offplane position.	104
3.14	Same as Figure 3.13.	105
3.15	Same as Figure 3.13.	105
3.16	Same as Figure 3.13.	106
3.17	Same as Figure 3.13.	106
3.18	Same as Figure 3.13.	107
3.19	Same as Figure 3.13.	107
3.20	Same as Figure 3.13.	108
3.21	Results from fitting the midplane and offplane rotation curves as a combination of two fixed rotation curves. In the top panel, the rotation curves are a combination of the midplane $H\alpha$ and a flat non-rotating RC. In the bottom panel, the base rotation curves are the midplane $H\alpha$ combined with a rotation curve counter-rotating with one-half the $H\alpha$ velocity. These fits are listed in Table 3.4.	111

3.22	The expected thick disk lags as a function of height above the midplane and thick disk velocity dispersion. The first three panels show model galaxies similar to the ones in our sample. Points show the stellar lags measured from our rotation curve fits. Open points show lags from rotation curves where the offplane and midplane rotation curves are fit independently. Solid points show the average lag for the models which correct for cross-contamination of the thin and thick disk rotation curves, and are generally more reliable estimates of the thick disk lag. The final panel shows the results of our model when we use MW like parameters. Observed galaxies we compare to the models: In the upper left FGC 1642 and FGC 780; upper right FGC 1415, FGC 227, and FGC 2558; and lower left FGCE 1371. All the models and observations are taken at $R = 2.5h_R$. FGC 1948 is excluded from the plot because there is no coherent rotation (so it doesn't make sense to measure a lag. FGC 1440 is excluded because we have no offplane stellar velocity measurements.	115
3.23	Two examples of the effects dust and projection will have on our observed rotation curves. While projection creates considerable changes, the addition of dust extinction is negligible.	117
3.24	Examples of cross-correlating in the presence of different types of noise. In the left hand column, we show a model galaxy spectrum (top) and stellar template (bottom). In the right hand column, we plot the galaxy-star cross-correlation (solid) and stellar auto-correlation (dotted) and note the velocity error resulting from comparing the two. (a) The ideal case of a high signal-to-noise galaxy spectrum. (b) Results from a galaxy spectrum with a $S/N/\text{\AA} \sim 10$. (c) Spectra with a region marked in red of very low S/N affecting a section of one of the Ca absorption features, similar to how bright sky lines leave residuals on our spectra. (d) A traditional cross-correlation where the noisy region has been set to the continuum. (e) Our new cross-correlation technique where we compute the cross-correlation excluding the masked region.	124
4.1	R -band images of our galaxy sample with the APO longslit positions overlaid. All images are stretched to include $20 < \mu_R < 24.2 \text{ mag}/\square''$	132
4.2	Same as Figure 4.1.	133
4.3	Same as Figure 4.1.	133

4.4	Examples of our blue spectra. From top to bottom: Midplane of FGC 1285, Offplane of FGC 1285, Elliptical galaxy NGC 5638, Lick standard star HD114762. All the spectra have been smoothed to a resolution of 8.4 Å and the Lick indices of interest have been labeled.	137
4.5	Comparison of Lick indices measured with DIS compared to the published equivalent widths in Worthey et al. (1994). Dashed horizontal lines show the mean offsets while the dotted lines show the average Worthey et al. $\pm 3\sigma$ uncertainties. Dashed vertical lines show the range of values measured in our galaxy sample. Corresponding means and scatters are given in Table 4.3.	139
4.6	Lick indices measured with APO compared with values published in Trager et al. (2000b). Dashed lines show the median offset between our measurements and those in Trager et al. (2000b). The agreement is good, even with our larger slit and lack of velocity dispersion correction.	140
4.7	Lick index measurements for our observations. Top plots: Model grids from Thomas et al. (2003) along with our observed points. Green, blue and black points are from midplane observations, red and orange points are for offplane measurements. Bottom Plots: The interpolated ages and metallicities for all the above indices. Large filled points are used for spectra from the region $-h_R < R < h_R$ that fall inside the model grids. Large open points are used for observations that fall outside the model grids. Small open blue points show midplane spectra extracted from larger radius. Throughout, blue is used for midplane observations while red is used for offplane observations. Error bars on the points show the statistical uncertainties based on the signal-to-noise of the spectra. The dashed error bars show the typical uncertainties if we assume a 10% error on the emission line correction and a 0.02 Å error on the metal sensitive index.	149
4.8	Same as Figure 4.7.	150
4.9	Same as Figure 4.7.	151
4.10	Same as Figure 4.7.	152
4.11	Same as Figure 4.7.	153
4.12	Same as Figure 4.7.	154
4.13	Same as Figure 4.7.	155
4.14	Same as Figure 4.7.	156
4.15	Same as Figure 4.7.	157

4.16	Average ages and metallicities as measured by Lick indices $H\beta$, Mg b , and Fe 5270. Blue points show midplane (thin disk) observations while red points show offplane (thick disk) observations.	158
4.17	Cumulative distribution plots showing the differences between the thin disk and thick disk ages and metallicities. Positive ages mean the thick disk is older while negative metallicity differences mean the thick disk is metal poor in comparison to the thin disk.	159
4.18	Radial gradients of the Lick equivalent-widths measured in FGC 1440. Top left shows the $H\beta$ index after correcting for emission line fill-in, top right shows Mg b , lower left shows the Fe5270 index, and the lower right shows the uncorrected $H\beta$ EW as well as the $H\alpha$ EW. Dotted lines show the uncertainties calculated from the extracted spectra SNR.	161
4.19	The measured Lick indices from the radial extent of FGC 1440's midplane placed on the model grids of Thomas et al. (2003).	162
4.20	The interpolated age and metallicity measured along the midplane of FGC 1440. There is a very strong age gradient present. The Mg b index shows a fairly flat metallicity gradient, while the Fe 5270 index shows a radially decreasing metallicity.	163
A.1	This data shows no significant trend with time, even if a best-fit line is added to aid the eye (dashed line).	199

LIST OF TABLES

Table Number	Page
2.1 Galaxies rejected from the 2-disk R -band fitting	13
2.2 Thick disks from the literature	38
2.3 Single disk fits for the sample galaxies.	75
2.3 Single disk fits for the sample galaxies.	76
2.4 Vertical light profiles for the two disk models used in fitting R -band structural parameters.	77
2.5 Two disk fits to R -band images. the best values found for each disk having a sech^2 vertical profile. The listed values are medians with uncertainties indicating the full range of convergent fits.	78
2.5 Two disk fits to R -band images. the best values found for each disk having a sech^2 vertical profile. The listed values are medians with uncertainties indicating the full range of convergent fits.	79
2.5 Two disk fits to R -band images. the best values found for each disk having a sech^2 vertical profile. The listed values are medians with uncertainties indicating the full range of convergent fits.	80
3.1 Properties of Targeted Galaxies	86
3.2 Observing Details	86
3.3 Slit Placement	86
3.4 Non-Rotating and Counter Rotating Fractions	111
4.1 Edge-On Galaxy Observations	134
4.2 Elliptical Galaxies Observed	135
4.3 Zero point conversions	138
4.4 Measured Lick Indices in the range $-1 < h_R < 1$	145
4.4 Measured Lick Indices in the range $-1 < h_R < 1$	147

ACKNOWLEDGMENTS

This thesis was a lot of work, but also a lot of fun, and I'd like to thank the folks that made it not just possible but enjoyable.

Caroline: For being the best wife ever.

My Family: My family has given me incredible support throughout my entire academic career. Throughout my life, they have set me up to succeed. It even took them three years before they even started to ask what kind of job I could get with a Ph.D.

The Faculty: Thanks to Suzanne Hawley and Tom Quinn for being on my committee and reading this document. I have to give special thanks to my advisor Julianne Dalcanton for giving me a great project to work on and constant support.

My Fellow Grads: Living and working in the grad student hallway is a blast. I know I can walk down the hall and find great scientific discussions and great friends anytime. I especially have to thank Greg Stinson for being a great officemate as well as the foosers for many quality wasted hours.

The \$: I thank the many fine institutions that have provided funding during this research: NSF, ARCS, Jacobsen Fund, University of Washington, and AAS. I didn't get rich being a grad student, but these groups let me focus on research without having to worry about the bills.

I would like to thank the Flying Spaghetti Monster. This research has been truly touched by His noodly appendage.

Chapter 1

INTRODUCTION

The details of galaxy formation and evolution remain one of the outstanding problems in modern astronomy. Studies focused on illuminating galaxy formation fall into several types: (1) Observing the Milky Way. Living inside the Milky Way, we are able to study individual stars in detail. Stellar abundances can be measured from high resolution spectra element-by-element, and observations can reveal the full three-dimensional motions of nearby stars. While our location provides us the opportunity to observe the MW in unparalleled detail, we are simultaneously denied a global view of the Milky Way. There is also the danger that the Milky Way might not be a typical galaxy and the lessons we learn locally about galaxy formation should not necessarily be applied generally. (2) Observing galaxies at high redshift. Galaxies at high redshift allow one to directly observe the universe during the epoch of galaxy formation. While this is the most direct method of testing galaxy formation theories, it is also one of the most difficult as cosmological dimming makes high- z galaxies incredibly faint. (3) Observing a large sample of galaxies. Large surveys such as the Sloan Digital Sky Survey (SDSS)(York et al., 2000) and the Two Micron All Sky Survey (2MASS)(Skrutskie et al., 2006) have made it possible to build large samples of galaxies where one can try and deduce their formation based on their statistical properties and scaling relations. (4) Simulating galaxy formation. Cosmological N-body simulations offer a chance to observe galaxy formation in a virtual sense. By combining precise cosmological parameters with the gravity and gas physics, it should be possible to re-create galaxy formation through computational brute force. Unfor-

tunately, simulations are only beginning to generate realistic galaxies and are still limited by resolution effects that prevent the creation of pure disk systems.

This thesis seeks a middle ground. We choose to observe a moderate number of nearby galaxies. In this way, we can still make spatially resolved observations of abundances and kinematics and isolate regions of interest while having a sample size large enough that we can make meaningful statements about galaxy formation in general. In particular, we will focus on analyzing the ancient stellar populations observable in edge-on disk galaxies. These oldest stars provide a fossil record of a galaxy's assembly and subsequent evolution.

There is a long and rich history of cataloging galaxy morphologies. Galaxies are traditionally divided into the ellipticals and more complicated disk systems. Disks are further described as having spiral arms, bulges, pseudo-bulges, halos, bars, rings, flares, warps, tails, streams, bridges, and, as their label implies, disks. Even the disks can be broken into thick and thin components. The motivation behind cataloging all these structures is the hope that one can discover the underlying physical cause for each structure.

In this thesis, we shall focus on the simplest possible disk galaxies—those that have only disk components. By only observing pure disk systems, we avoid the complications of subtracting away bulge components, or dealing with the complicated kinematics of merging and interacting systems. In particular, we will inspect the thin and thick disk components of galaxies.

1.1 The Milky Way Disks

The best studied thick disk is the one found in our own Milky Way. Initially detected as an overabundance of stars at high galactic latitudes (Gilmore & Reid, 1983), there were several years of debate about whether these stars actually represented a unique stellar population, or were simply an extension of the thin disk or halo.

The thick disk is now well analyzed in the Milky Way. Studies with sample sizes

of hundreds of stars have isolated it as a chemically and dynamically independent component of the Galaxy (Ramírez et al., 2007). Thick disk stars are found to be metal poor and enriched in α -elements compared to solar composition, an indication that they have been enriched primarily by Type II supernovae, which in turn suggests they were formed over a short cosmic time before Type Ia SNe could increase their iron content (Bensby et al., 2005, 2006). In contrast, thin disk stars have chemical enrichment that is consistent with these stars forming over a much longer timescale.

The formation models for the Milky Way thick disk can be grouped into three broad scenarios. In the first, a thin disk of stars is kinematically heated into a thicker disk. This heating can come from gradual scattering off structures inside the galaxy (spiral arms and giant molecular clouds), or rapidly from merger event. In the second model, the thick disk is created when stars form away from the midplane of a galaxy. Λ CDM cosmology predicts that all galaxies go through an early period of chaotic merging. In such an environment, star formation is not confined to a cold disk, but may also occur off the midplane. Once stars form, they cannot collide and dissipate their energy. This ensures that stars formed off the midplane will be doomed to orbits that rapidly carry them through the midplane and move slowly at high galactic latitudes. The final formation model holds that thick disk stars are the remnants of satellite galaxies which have been disrupted and accreted by the Milky Way.

Because all of these formation mechanisms were proposed to explain the presence of a thick disk in the Milky Way, they are all somewhat consistent with local observations. However, they make different predictions for what we should observe in an ensemble of thick disks.

Predictions of Thick Disk Formation Models:

Thick disks formed by gradual heating: Kinematically, thick disk stars should be similar to the thin disk. Gradually increasing the velocity dispersion of stars with time would slowly build up a a thick disk that slightly lags behind the thin disk.

The age and metallicity distributions of the two disks should flow smoothly together and should be highly correlated, as the thick disk is just an older smooth extension of the thin. The gradual formation should also leave thick disk stars with chemical enrichment patterns similar to the thin disk. A difficulty with this model is that internal heating mechanisms in galaxies tend to rapidly saturate, preventing thin disks from increasing their scale heights by the required amounts.

Formed in a major merger: A major merger should completely disrupt any thin disk. Unlike the gradual heating scenario, we should expect an age gap between the thin and thick disk stars. A break in metallicities is also possible. The sizes of the two disks should be uncorrelated—some mergers could make a large thick disk, while others only a slightly thicker thick disk. We might also expect to find some thin disks that have never been heated as well as thick disks that did not have enough gas to re-form a thin disk. Simulations have consistently shown that major mergers create spheroidal systems, so we should expect any thick disk that forms via major mergers to also have a bulge component.

Formed off the midplane: In this scenario, we would expect thick disks to be old, as star formation out of the midplane would only happen during chaotic merging (Brook et al., 2004). Because the thick disk forms before the gas in a galaxy has settled to form a thin disk, we should expect it to be older and less metal enriched than the subsequently formed thin disk.

Formed via accretion: Unlike the other models, the kinematics of the thick disk can be fairly independent of the thin disk. Because accreted satellites can have a wide variety of initial orbits, they can deposit their stars in a variety of places. They could be co-rotating or counter-rotating. They could have high eccentricity, or dynamical friction could bring them into nearly circular orbits before the satellites are disrupted. Ages and metallicities of thick disk stars should also be fairly independent of the thin disk. Because the thick disk stars form isolated from the thin disk, their metallicities only depend on the local enrichment history.

1.2 *Thick Disks in Other Galaxies*

Originally discovered in S0 galaxies (Burstein, 1979; Tsikoudi, 1979), thick disks have now been observed in galaxies spanning a wide range of Hubble types. Virtually all the thick disk discoveries have been made in galaxies which happen to be aligned edge-on to the line of sight. By observing galaxies which are edge-on, different disk components can be spatially isolated and observed.

While many thick disks have now been discovered in other galaxies, they do not place tight constraints on thick disk formation models. Because thick disks can only be isolated far off the midplane, they are very low surface brightness and observations to date have been limited to only morphologically characterizing thick disks outside the MW. Without detailed information on kinematics, ages, and metallicities, it is difficult to separate the formation models listed above.

In this thesis, we will move beyond mere morphological characterizations and measure more detailed properties of thick disks. Figure 1.1 shows the galaxy FGC 780 as an example of an edge-on galaxy where we can isolate and observe a stellar thick disk. In the R -band image, FGC 780 looks like a flattened disk galaxy, with a very faint region extending away from the midplane. The $B-R$ color-map of FGC 780 shows new details. The color map is dominated by a strong radial gradient, with the center of the galaxy being redder ($B-R \sim 1.0$) than the outer regions ($B-R \sim 0.4$). This is a well known feature of disk galaxies and has typically been interpreted as evidence that disks form from the inside out, with strong star formation occurring in the outer regions of the galaxy. Another striking feature in the color map can be seen at high galactic latitudes. The faint offplane region is much redder than the midplane regions, suggesting that there is a distinct change in the stellar populations one finds in the midplane and the offplane.

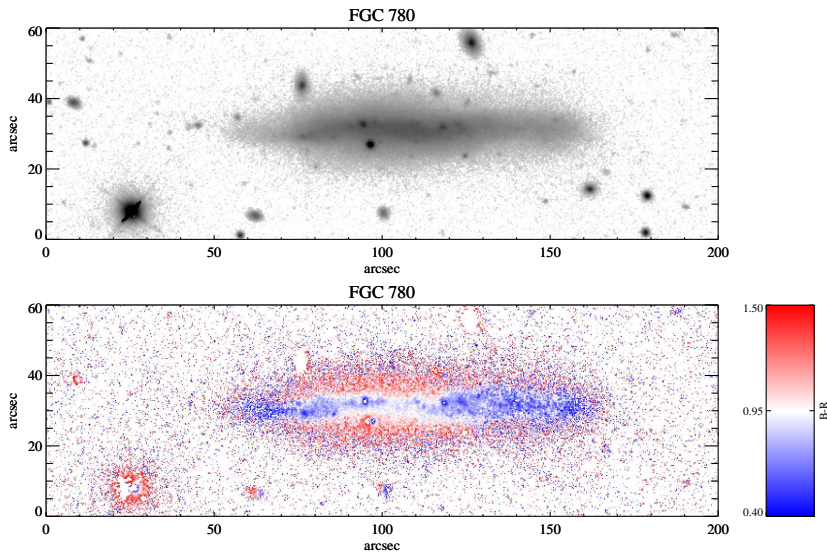


Figure 1.1 An example edge-on disk galaxy that is analyzed in this thesis. The top panel shows a deep R -band image, while the bottom panel shows a $B - R$ color map. The color map reveals that the faintest regions above and below the midplane are distinctly redder than the midplane. This faint reddish region seems to be analogous to the Milky Way thick disk. By isolating the faint red region, we can observe the properties of the thick disk and compare it to formation models.

1.3 *Brief Thesis Outline*

Chapter 2 describes the morphological properties of a sample of edge-on disk galaxies. Chapters 3 and 4 will use the information about thick disk morphology to isolate regions where the thick disk stars dominate and target those regions for more in-depth observations.

In Chapter 3, observations from the Gemini telescopes are used to measure the kinematics of thick disk stars in a variety of galaxies. Targeting regions above the midplanes, we are able to measure the difference between the thick disk and thin disk kinematics. We also develop a new technique for analyzing low signal-to-noise spectra in the presence of bright night sky-line residuals.

Chapter 4 describes observations made with the ARC 3.5 meter telescope at Apache Point Observatory. Once again, we target regions of galaxies that are dominated by the thick disk stars. This time, we analyze spectra to derive age and metallicity measurements of the thin and thick disk components.

Chapter 5 discusses the ramifications of thick disk formation theories in light of the observations from Chapters 2, 3, and 4. We also discuss future work and serendipitous discoveries made during this research.

Chapter 2

STRUCTURAL PARAMETERS OF THIN AND THICK DISKS IN EDGE-ON DISK GALAXIES

2.1 Chapter Summary

We analyze the global structure of 34 late-type, edge-on, undisturbed, disk galaxies spanning a wide range of mass. We measure structural parameters for the galaxies using two-dimensional least-squares fitting to our R -band photometry. The fits require both a thick and a thin disk to adequately fit the data. The thick disks have larger scale heights and longer scale lengths than the embedded thin disks, by factors of ~ 2 and ~ 1.25 , respectively. The observed structural parameters agree well with the properties of thick and thin disks derived from star counts in the Milky Way and from resolved stellar populations in nearby galaxies. We find that massive galaxies' luminosities are dominated by the thin disk. However, in low mass galaxies ($V_c \lesssim 120$ km s $^{-1}$), thick disk stars contribute nearly half of the luminosity and dominate the stellar mass. Thus, although low mass dwarf galaxies appear blue, the majority of their stars are probably quite old.

Our data are most easily explained by a formation scenario where the thick disk is assembled through direct accretion of stellar material from merging satellites while the thin disk is formed from accreted gas. The baryonic fraction in the thin disk therefore constrains the gas-richness of the merging pre-galactic fragments. If we include the mass in HI as part of the thin disk, the thick disk contains $\lesssim 10\%$ of the baryons in high mass galaxies, and $\sim 25 - 30\%$ of the baryons in low-mass galaxies. Our data therefore indicate that the fragments were quite gas rich at the time of merging ($f_{gas} = 75 - 90\%$). However, because low mass galaxies have a smaller

fraction of baryons in their thin disks, the pre-galactic fragments from which they assembled must have been systematically more gas poor. We believe this trend results from increased outflow due to supernova-driven winds in the lower mass pre-galactic fragments. We estimate that $\sim 60\%$ of the total baryonic mass in these systems was lost due to outflows. Pushing the episode of significant winds to early times allows the mass-metallicity relationship for disks to be established early, before the main disk is assembled, and obviates the difficulty in driving winds from diffuse disks with low star formation efficiencies. We discuss other implications of this scenario for solving the G-dwarf problem, for predicting abundance trends in thick disks, and for removing discrepancies between semi-analytic galaxy formation models and the observed colors of low mass galaxies.

Most of this chapter originally appeared in the January, 2006 issue of the *Astronomical Journal* (Yoachim & Dalcanton, 2006b). In that format it is ©2006 by The American Astronomical Society. The *Astronomical Journal* grants authors the right to republish papers, providing the journal is duly noted.

2.2 Introduction

The structure of galactic disks provides strong constraints on their formation and evolution. Spiral galaxies have long been recognized to contain several distinct populations of stars (e.g., disks, bulges and halos), each with distinct chemical and kinematic properties that capture unique epochs in the formation of the galaxy. Observations of the Milky Way and a wide range of other galaxies have revealed the need for yet another component, namely, a thick stellar disk. Originally detected as an excess of light at high galactic latitudes in deep surface photometry of early-type galaxies (Burstein, 1979; Tsikoudi, 1979), a thick disk was later revealed in the Milky Way using star counts (Gilmore & Reid, 1983).

The properties of the Milky Way's thick disk have revealed many differences from the thin disk. Structurally, the Milky Way's thick disk has a significantly larger scale

height than the thin disk, as its name implies (for reviews see Reid & Majewski, 1993; Buser et al., 1999; Norris, 1999, and references therein). It also may have a somewhat longer scale length (Robin et al., 1996; Ojha, 2001; Chen et al., 2001; Larsen & Humphreys, 2003). Thick disk stars are older and more metal-poor than stars in the thin disk (e.g. Reid & Majewski, 1993; Chiba & Beers, 2000). They are also significantly enhanced in α -elements, compared to thin disk stars of comparable iron abundance (Fuhrmann, 1998; Prochaska et al., 2000; Tautvaišienė et al., 2001; Bensby et al., 2003; Feltzing et al., 2003; Mishenina et al., 2004; Brewer & Carney, 2004; Bensby et al., 2005). Kinematically, Milky Way thick disk stars have both larger velocity dispersions and slower net rotation than stars in the thin disk (Nissen, 1995; Chiba & Beers, 2000; Gilmore et al., 2002; Soubiran et al., 2003; Parker et al., 2004).

For many years, however, it remained unclear whether the thick disk was a truly distinct component of the Milky Way, or whether it was only an older, metal-poor extension of the thin disk, as might be created by steady vertical heating over the lifetime of the Galaxy (e.g., Dove & Thronson, 1993). Over the past five years, conclusive evidence that the thick disk is indeed distinct from the thin disk has come from a series of detailed chemical abundance studies. Stars with thick disk kinematics show significant alpha-enhancement compared to thin disk stars with identical iron abundances, thus forming a separate parallel sequence in a plot of $[\alpha/\text{H}]$ vs $[\text{Fe}/\text{H}]$ (see the recent review by Feltzing et al., 2004). Studies of resolved stars in nearby galaxies also find a thick disk of old red giant branch stars whose lack of metallicity gradient cannot be explained by steady vertical heating (Seth et al., 2005b; Mould, 2005).

Three general classes of formation mechanisms have been proposed to explain the properties of the Milky Way thick disk. In the first, a previously thin disk is dynamically heated to form a thick disk, after which a new thin disk forms (Quinn et al., 1993; Velazquez & White, 1999; Robin et al., 1996; Chen et al., 2001). In the second, the thick disk forms directly from gas at a large scale height, possibly during

a largely monolithic proto-galactic collapse (Eggen et al., 1962; Gilmore & Wyse, 1986; Norris & Ryan, 1991; Burkert et al., 1992; Kroupa, 2002; Fuhrmann, 2004; Brook et al., 2004). In the third, the thick disk forms from a series of minor-merger events which directly deposit stars at large scale heights (Statler, 1988; Abadi et al., 2003b). Recent cosmological simulations have suggested a more complicated origin. Disk galaxy simulations by Abadi et al. (2003b) find a thick disk which is composed primarily of tidal debris from disrupted satellites while comparable simulations by Brook et al. (2004) find that thick disk stars form during a period of chaotic mergers of gas-rich building blocks. Recent kinematic measurements favor scenarios where mergers play a significant role in thick disk formation (Gilmore et al., 2002; Yoachim & Dalcanton, 2005, Chapter 3).

While all of the above scenarios are viable explanations for the origin of the Milky Way, the structural parameters of thin and thick disk components in a wide range of galaxies can help distinguish among these formation scenarios. Unfortunately, the measurements required to characterize thick disks are difficult to make outside the Milky Way. The Milky Way thick disk provides less than 10% of the local stellar density (Buser et al., 1999), and this faintness hampers detailed study of comparable extragalactic thick disks. To date, thick disk structural properties have been measured only in a small number of galaxies (Seth et al., 2005b; Pohlen et al., 2004; van Dokkum et al., 1994; Morrison et al., 1997; Neeser et al., 2002; Abe et al., 1999; Wu et al., 2002; de Grijs & van der Kruit, 1996; de Grijs & Peletier, 1997, see Table 2.2 below). These studies analyze galaxies in the edge-on orientation, which allows clear delineation between regions where thin and thick disk stars dominate the flux. The edge-on orientation also allows line of sight integrations of faint stellar populations to reach detectable levels.

In this paper, we analyze a large sample of edge-on galaxies and decompose them into thick and thin disk components. Analysis of B , R , & K_s photometry and color maps has previously revealed that these galaxies are surrounded by a flattened faint

red envelope, with properties very similar to the Milky Way thick disk (Dalcanton & Bernstein, 2002). We now use a full 2-dimensional fitting procedure capable of simultaneously fitting the thick and thin disk light distributions to derive their full structural parameters.

2.2.1 Galaxy Sample

The sample used in this paper was drawn from the optical and infrared imaging found in Dalcanton & Bernstein (2000b, hereafter Paper I). Briefly, our sample of edge-on bulgeless galaxies was initially selected from the Flat Galaxy Catalog (FGC) of Karachentsev et al. (1993), a catalog of 4455 edge-on galaxies with axial ratios greater than 7 and major axis lengths greater than $0.6'$. The color maps and initial detections of the thick disks in 47 galaxies were presented in Dalcanton & Bernstein (2002, hereafter Paper II).

Not all galaxies from Paper I have been included in the analysis presented here. We have excluded several of the more massive galaxies with sizable bulge components that could not be adequately masked or modeled. We likewise eliminated several low mass galaxies with bright central star clusters for similar reasons. We have also removed any galaxies that have either significant warps or visible spiral arms (i.e., that were not viewed perfectly edge-on), as these systems are poorly modeled by our fitting procedure. Finally, we eliminated galaxies whose surface brightness profiles would be severely affected by atmospheric seeing. A full list of the 15 excluded galaxies are listed in Table 2.1, leaving a sample of 34 galaxies suitable for decomposing into thick and thin components. When possible, we have used distances listed in Karachentsev et al. (2000a) derived from a local flow model. Otherwise we use the galaxy's redshift corrected for the motion of the Local Group (Yahil et al., 1977), assuming a Hubble Constant of $H_0 = 70 \text{ km s}^{-1} \text{ Mpc}^{-1}$.

Table 2.1. Galaxies rejected from the 2-disk *R*-band fitting

FGC(E)	Reason for rejection
51	Large central knot
84	Spiral arms visible
143	Bright central star-forming region
442	Spiral arms visible
256	Thin disk below seeing limit, fits did not converge
1863	Large warp, bright foreground stars
1945	Fits did not converge, possibly spiral arms
1971	Polar ring galaxy
2217	Large bulge component
2367	Spiral arms visible
2264	Fits did not converge, scattered light problem
2292	Thin disk below seeing limit, bright foreground stars
E1440	Asymmetric disk
E1447	No velocity data
E1619	Large bulge component

2.3 2D Fitting

2.3.1 Galaxy Models

The distinctive vertical color gradients identified in Paper II suggest that the stellar population above the galaxies' midplanes is different from the one within it. We assume this change is due to the existence of two distinct stellar populations analogous to the MW's thick and thin disks. Our 2-dimensional fitting procedure attempts to decouple these two populations to measure their scale heights, scale lengths, and luminosities.

We model the surface brightness of each disk component as a radially exponential disk. We adopt the luminosity density \mathcal{L} of each disk component to be

$$\mathcal{L}(R, z) = \mathcal{L}_0 e^{-R/h_R} f(z) \quad (2.1)$$

where (R, z) are cylindrical coordinates, \mathcal{L}_0 is the central luminosity density, h_R is the radial scale length, and $f(z)$ is a function describing the vertical distribution of stars.

Throughout, we adopt a generalized vertical distribution

$$f(z) = \text{sech}^{2/N}(Nz/z_0) \quad (2.2)$$

where z_0 is the vertical scale height and N is a parameter controlling the shape of the profile near the midplane. For appropriate choices of N , this equation can reproduce many popular choices for the vertical distribution of star light. With $N = 1$ Equation 2.2 becomes the expected form for a self-gravitating isothermal sheet (Spitzer, 1942; van der Kruit & Searle, 1981a,b, 1982). When $N \rightarrow \infty$, Equation 2.2 reduces to $f(z) \propto e^{-z/h_z}$, where $h_z = z_0/2$. Previous fits to the vertical distribution suggest that an intermediate value of $N = 2$ is a better model of galaxy disks (van der Kruit,

1988), as expected for the superposition of several populations with a range of vertical velocity dispersions (de Grijs & van der Kruit, 1996). However, different values of N only produce differences near the galaxy midplane, and all share exponentially declining profiles at large radii.

When fitting a thick plus thin disk model, we preferentially use $N = 1$ for both components because of its physical motivation. We note that since our main goal is not to model galaxies near their midplane where these functions have their largest differences, our results are not particularly sensitive to the choice of model. To permit comparisons to previous work, we also derive single disk fits to our sample using Equation 2.2 without a fixed N , allowing the shape of the vertical profile to vary to best fit the data.

To translate the adopted luminosity density into the observed surface brightness distribution, we assume that the disks are viewed perfectly edge-on. Other authors have demonstrated that slight deviations from $i = 90^\circ$ have minimal impact on the derived structural parameters (e.g., van der Kruit & Searle, 1981b; de Grijs et al., 1997). We also assume that scale heights are independent of projected radius for late-type galaxies, as found by van der Kruit & Searle (1981b); Bizyaev & Mitronova (2002); de Grijs & Peletier (1997); Shaw & Gilmore (1990). With the above assumptions, the model edge-on disk surface brightness is given by

$$\Sigma(R, z) = \Sigma_{0,0}(R/h_R)K_1(R/h_R)f(z) \quad (2.3)$$

where K_1 is a modified Bessel function of the first order, $\Sigma_{0,0}$ is the edge-on peak surface brightness ($\Sigma_{0,0} = 2h_R\mathcal{L}_0$), and R is now the projected radius along the major axis. The face-on surface brightness of such a disk is $\Sigma(R) = \Sigma_0 e^{-R/h}$ with $\Sigma_0 = 2z_0\mathcal{L}_0$. Throughout, we convert our edge-on peak surface brightnesses to magnitudes using $\mu(0, 0) = m_{zp} - 2.5\log(\Sigma_{0,0})$ where m_{zp} is the photometric zero point from Paper I. The face-on central surface brightness can then be calculated as $\mu_0 = \mu(0, 0) -$

$2.5\log(z_0/h_R)$. The conversion between the edge-on and face-on orientation assumes that disks are optically thin at any orientation, an assumption that is obviously not true for massive galaxies with dust lanes. However, we correct for this effect later in §2.5.3. We do not model any possible disk truncation, as this is a small effect seen only in the region $R > 3h_R$ (van der Kruit & Searle, 1981b; Kregel & van der Kruit, 2004; Pohlen et al., 2000).

Our sample of galaxies was initially selected to be “pure disk” systems, and thus there are very few galaxies which possess a prominent bulge component. We therefore do not attempt to decompose a bulge component from the surface brightness distribution and simply reject galaxies with significant bulges from the sample (Table 2.1).

We have tested if the profiles described by Equation 2.2 could be significantly affected by seeing. We convolved model images with a two-dimensional circular Gaussian kernel to simulate the atmosphere’s effect. We found that this step, in general, was unnecessary. Unconvolved fits differed from convolved fits only for the most distant galaxies. Several of these galaxies have been eliminated from the sample, as listed in Table 2.1.

2.3.2 *Fitting Method*

We use Levenberg-Marquardt least squares fitting of the galaxy images to find the best parameters for the models described in §2.3.1. Before fitting, the images of the galaxies are sky-subtracted and foreground stars and background galaxies are generously masked (see Paper II). The images are cropped at $R \sim 4h_R$ to speed computation time. Our tests have shown that the fits are insensitive to the exact cropping, causing variations in individual parameters of only a few percent. The cropping also reduces the chance that our fits could be biased by warps or flaring of the disks at large radii.

Following the technique of Kregel et al. (2002), we weight each pixel by the inverse of the model surface brightness distribution at that pixel. By using the model rather

than the data to determine the weighting, we eliminate the bias of overweighting positive noise spikes. This weighting scheme places large amounts of weight on the lowest signal-to-noise pixels, ensuring that regions of low surface brightness (i.e., where a faint thick disk could be detected) receive adequate weighting. To prevent the fit from being overwhelmed by regions with low signal-to-noise, we set the weight to zero beyond the $1\text{-}\sigma$ noise contour, defined as where the model falls below the standard deviation of the background. Due to the low signal-to-noise ratio in the K_s band data, these images were clipped at the $1/2\text{-}\sigma$ level to ensure that an adequate number of pixels were included in the fit. Each fit was iterated four times to ensure convergence of the model parameters and weighting scheme. Fits were performed using pixel coordinates and counts, then converted to arcseconds and magnitudes using the calibrations in Paper I.

It is common practice when fitting models to edge-on galaxies to crop out regions near the midplane of the disk (e.e., Kregel et al., 2002; de Jong, 1996a; Bizyaev & Mitronova, 2002). Cropping avoids the hard-to-model effects of dust lanes, bulges, and star forming regions. The color maps of our galaxies imply that galaxies rotating at speeds less than 120 km s^{-1} do not contain concentrated central dust lanes (Dalcanton et al., 2004). For more massive galaxies, our weighting procedure ensures that any midplane structure receives a minimal amount of weighting when calculating the goodness-of-fit χ^2 . We chose to fit models both with and without the midplane cropping to quantify the systematic uncertainties introduced by midplane structure.

We begin by fitting single disk models to all three B , R , and, K_s images, holding the galaxy position and rotation fixed. We then fit 2-component models to the images, allowing the offsets and rotation to vary, but constraining all components to have the same center and orientation. For this second step, we use only the R -band images due to their high signal-to-noise. Ideally, we would perform the 2-disk decomposition in the K_s band which best represents the smooth stellar distribution and is least affected by dust. However, due to the bright infrared sky, the NIR images are lower

signal-to-noise and cannot reach to faint regions where a thick disk would dominate. The R -band therefore represents the best compromise between reaching faint regions of the galaxies while minimizing the effects of dust extinction and bright star forming regions.

When fitting a single disk with only three free parameters, our procedure converges to the same χ^2 minima given any reasonable initial guesses. However, for multiple component models, which have up to 10 free parameters, we find that fits often converge to local minima rather than to the global minimum. To ensure we find the global minimum when fitting multiple components, we fit each galaxy using up to 50 unique initial parameter guesses, following Wu et al. (2002). The initial parameters for each galaxy model were randomly varied up to $\pm 50\%$ to ensure we cast a large net in parameter space.

The formal parameter uncertainties that result from our fits are not meaningful because we used a weighting scheme that is not based on the actual pixel uncertainties. Even if we did minimize χ^2 using formal pixel errors, our returned uncertainties would be much too low. The χ^2 formalism requires residuals to be Gaussian, which is rarely the case when fitting nearby galaxies. The situation is comparable to trying to model Mount Rainier as a cone—you can do it, but the residuals will be dominated by real physical structures and not random Gaussian measurement errors. In the case of spiral galaxies, real substructure exists in the form of spiral arms, dust lanes, regions of active star formation, warps, flares, HII regions, etc. As an alternative assessment of the systematic errors which are likely to dominate our uncertainties, we fit a series of models using a variety of different weighting and masking schemes (Table 2.4) and quote the median result for each parameter. We then adopt the full range of convergent models for each parameter as a measure of the inherent systematic uncertainties. The resulting uncertainties are 2-100 times greater than our formal χ^2 uncertainties, confirming that systematic errors dominate our uncertainties.

2.3.3 Tests on Artificial Images

To assess the reliability of the 2-disk decompositions, we created a set of 100 artificial galaxies. We adopted the surface brightness profile in Equation 2.2 with an $N = 1$ vertical distribution for both a thick and thin component, and varied the structural parameters of the disks within ranges similar to our sample galaxies (for the thin disk: $20.7 \text{ mag}/\square'' < \mu(0, 0) < 22.7 \text{ mag}/\square''$, $2.5'' < h_R < 19.4''$, $0.6'' < z_0 < 3.6''$; and the thick disk had parameters in the range: $21.4 \text{ mag}/\square'' < \mu(0, 0) < 24.2 \text{ mag}/\square''$, $1.5'' < h_R < 51.2''$, $1.4'' < z_0 < 20''$). The model galaxies were convolved with a circular Gaussian with $1''$ FWHM, typical of the seeing for the observations. We then added read noise, sky noise, and Poisson noise to the simulated galaxies, with amplitudes chosen to mimic our R -band data. The galaxy images were rotated up to 2 degrees and offset up to 2 pixels ($0.5''$) from the image center. We then fit the galaxies with the two disk models, with and without seeing corrections. We assume $N = 1$ and use the same spread of initial parameter guesses as described in §2.3.2.

Of the 100 simulated galaxies, only three fits failed to converge. 90% of the scale lengths are recovered to within $\pm 2\%$ of the input value, with all of the results converging within $\pm 10\%$. 90% of the scale heights are recovered within $\pm 3\%$ of the input value with all results within $\pm 12\%$. 90% of the central surface brightnesses converge to within 0.09 mags of the correct result. The orientations were always correct to within 0.1 degrees, with a median error less than 1%. All of the spatial offsets were within 1 pixel of the correct position. There were no systematic trends in the size of the errors versus galaxy properties. The high accuracy of these fits indicates that we are not limited by pixel noise in our fits. However, since our model was a perfect match to the input data, this correspondence is not surprising.

We tested models that did not make a seeing correction convolution and found the fits still returned scale lengths and heights that were accurate to $< 0.2''$, as long as $z_0 > 1''$. The majority of our observed galaxies do have $z_0 > 1''$, and thus we

do not account for seeing in our fits. This result is consistent with the analysis of de Grijs et al. (1997) who find that for an exponential vertical profile, convolution is unnecessary when the seeing FWHM $\leq 0.6h_z$.

In addition to testing our ability to recover the parameters of a known model, we also tested our ability to correctly measure the structural parameters when using an incorrect function for the vertical light distribution. Specifically, we fit an $N = 2$ model instead of the correct $N = 1$ vertical profile to each disk. These fits returned results similar to the fits using the correct model, and the resulting scale heights and lengths fell within $\sim 5\%$ of the correct values. This indicates that the galaxy sizes are constrained primarily by light well away from the midplane. The luminosities were more divergent, however, due to the large differences between these models at their midplanes. The $N = 2$ model was slightly biased towards having over-luminous thick disks (with a few outliers as well), but the majority (70%) of fits were within a factor of 2 of the correct L_{thick}/L_{thin} , despite being fit with the wrong function.

Finally, we also tested our two-disk fitting code on artificial galaxies that had no second thick disk component. In these cases, the fits always converged to extremely faint thick disks ($< 1\%$ of the thin disk flux) and usually converged to either very large or very small thick disk scale lengths, mimicking either a uniform sky background or a small point source. Overall, these results encourage us to believe that if there are no thick disk components in our data our fitted parameters will diverge to unphysical values which are easily diagnosed.

2.4 *Single Disk Fits*

Before discussing the results of decomposing the galaxies into two disk components (§2.5), we discuss the results for fitting single disks to the light distributions. These fits are useful simple descriptions of the galaxies, and the resulting parameters can be directly compared to previous fits of edge-on and face-on galaxies.

As discussed in §2.3.2, we quantify our systematic uncertainties using Equation 2.3

with an $N = 1$ vertical profile and a variety of weighting and masking techniques resulting in five different fits for each galaxy image. The five fits are: (1) the full galaxy with inverse model weighting as described in §2.3.2; (2) the full galaxy with uniform weighting to more heavily weight the high signal-to-noise regions; (3) inverse weighting with the midplane region ($z = \pm z_0$) masked; (4) inverse weighting with the outer region $R > 3h_R$ masked, to eliminate regions where our fit may be affected by unmodeled stellar truncation; and (5) inverse weighting with the high latitude region $z > 2z_0$ masked to minimize the effect of thick disks. The results of the fits are given in Table 2.3 for all 3 band passes. The columns show the median edge-on peak surface brightnesses ($\mu(0, 0)$), radial scale lengths (h_R), and vertical scale parameters (z_0) along with their uncertainties. We emphasize again that these are not the formal statistical uncertainties (which are deceptively small), but instead are the full range of values to which the five different fits converged.

In addition to quantifying our uncertainties, the five different fits provide insight into how variations in fitting methods and weighting schemes affect our results. The systematic effects of the different methods are plotted in Figure 2.1. The most notable features in Figure 2.1 are the large systematic shifts in the values of z_0 for the single disk fits. Models that are weighted to fit the midplane (e.g. the uniform weighting model), return thinner disks while models that mask the midplane return larger values of z_0 . This effect is present in all three filters, and is exactly what one would expect if disk galaxies were dominated by thin disks at their midplanes and by thick disks with larger scale-heights in the fainter regions. The radially cropped and midplane cropped models result in fits that have fainter central regions and slightly larger scale heights. This is a strong indication that most of our galaxies do not have dust lanes which need to be masked. Cropping regions at high z has a minimal ($< 5\%$ change) effect on the fit parameters.

The parameters for the single disk fits listed in Table 2.3 are plotted in Figures 2.2, 2.3, 2.4, 2.5, and 2.6 as a function of the galaxies' circular velocity. In Figure 2.2,

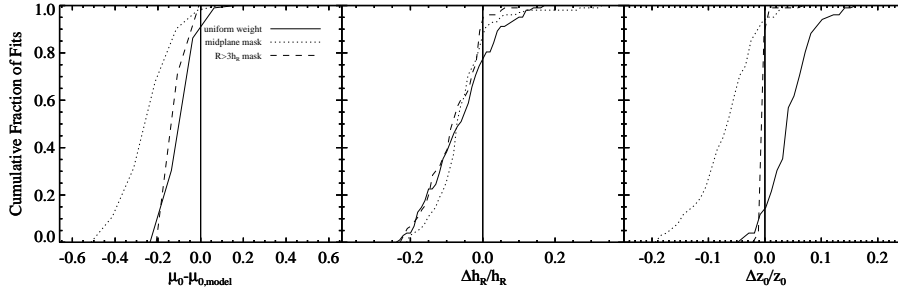


Figure 2.1 Cumulative distributions showing the systematic effects of fitting our galaxies with varying models. All models are compared to a fit using inverse weighting and no masked regions. Fits for all three filters have been combined. The solid curve shows the model which used uniform pixel weighting, while the dotted curve shows the midplane masked model, and the dashed curve shows the $|R| < 3h_R$ radially masked model.

we see the expected trends that more massive galaxies have larger scale heights. We also plot scale heights from the edge-on sample of Kregel et al. (2002) and find that both studies give consistent results for the scale height as a function of galaxy circular velocity. In Figure 2.3 we compare our single disk R - and B -band fitted scale lengths with the edge-on sample of Kregel et al. (2002) and the face-on measurements of MacArthur et al. (2003); de Jong (1996a), and Swaters & Balcells (2002). Overall, we find that lower mass galaxies in the range $50 < V_c < 120$ have scale lengths wholly consistent with measurements made in comparable face-on systems. However, the highest mass galaxies in our sample have scale lengths that are slightly larger than the average found in previous studies, although they are still within the full range of the comparison data. This offset is worse in the B -band than in the R -band, and almost certainly reflects the presence of strong dust lanes in the more massive systems. The higher attenuation towards the central regions of the galaxies will suppress the surface brightness at small radii, leading to apparently larger scale lengths. This offset may also explain why studies of edge-on disks suggest that disks truncate at only $3-4 h_R$, whereas face-on studies see no obvious signature of truncation at these

radii (Barton & Thompson, 1997; Weiner et al., 2001, but see also Pohlen et al. 2002).

In Figure 2.4 we compare the structural parameters derived in different band passes. We confirm that redder filters converge to shorter scale lengths (Figure 2.4), a result of the strong radial color gradients seen in both our sample and in face-on galaxies (e.g., Bell & de Jong, 2001; MacArthur et al., 2004).

We also find that for galaxies without dust lanes the B -band scale heights are predominantly thinner than the R -band. This offset is consistent with the detection of strong vertical color gradients in Paper II, where we found that the midplanes of late-type galaxies were typically bluer than the light above the plane. Somewhat unexpectedly, our K -band scale heights are also significantly thinner than the R -band. We believe that this is due to three effects. First, the K -band data does not reach as deep as the other filters, making it insensitive to the extended thick component. Second, the thinner K -band scale height may indicate the presence of dust which blocks light from the midplane in optical filters. Finally, there is some indication from studies of resolved stars in nearby galaxies that the K -band light is not completely dominated by old red giant stars, but instead has a significant contribution from young stars with small scale heights (Seth et al., 2005b).

In Figure 2.5 we plot the axial ratios of our sample galaxies. Overall, our axial ratios are consistent with the work of Bizyaev & Mitronova (2002) who measure flatness parameters for 153 edge-on galaxies imaged in the 2MASS survey and find values of h_r/z_0 ranging from ~ 2 to ~ 10 . Our results are also consistent with the axial ratios from Kregel et al. (2002). We see a slight trend for more massive galaxies to be flatter than less massive galaxies. Other studies have also suggested that low mass, low surface brightness dwarf galaxies are thicker than regular spirals. Estimates of the intrinsic axial ratios of dwarf irregulars range from $b/a \sim 0.3$ (Hodge & Hitchcock, 1966; Bingeli & Popescu, 1995) to $b/a \sim 0.6$ (Sung et al., 1998; Staveley-Smith et al., 1992), all of which are rounder than typical spirals (e.g. Kudrya et al., 1994). We

have discussed possible explanations for this behavior in Dalcanton et al. (2004).

Figure 2.6 shows the edge-on peak surface brightnesses for the one-disk fits. The peak surface brightness of the B -band data is roughly constant, showing little trend with galaxy mass. However, because the FGC sample was initially selected from the POSS-II survey plates, we would not expect the B -band surface brightnesses to be below $\mu \sim 23 \text{ mag}/\square''$. On the brighter end, the Freeman law (Freeman, 1970) suggests a maximum surface brightness for edge-on disks. Thus, the B -band peak surface brightnesses must be confined to a limited range. In contrast, we do see increasingly strong trends of surface brightness with mass in the redder filters, and particularly in K_s . Because the selection criteria for the FGC limited the range of B surface brightness the observed trends in R and K are due to variations in galaxy color with mass. As we will discuss in §2.5.3, extinction from dust prevents us from being able to reliably convert the edge-on brightnesses to comparable face-on values.

2.5 Two Disk Fits

2.5.1 Need for a Second Component

The traditional signature of thick disks is the presence of excess light at high latitudes after subtracting a single disk component. To demonstrate the expected excess, we subtract the single disk models from the data and sum the residuals (inside the $1\text{-}\sigma$ noise contour) along the major axis. The resulting residuals are plotted in Figure 2.7, and demonstrate that the single disk fits from §2.4 systematically leave excess flux at high latitudes for all masses of galaxies. We also average the vertical profile residuals across different galaxy mass ranges and find the two disk model is superior to the single disk model in all cases. For a single disk model, we can slightly improve the fit at high z by allowing the index N to vary. However, on average, the absolute value of the two-disk model residuals are smaller than the variable N model at *every* height. By collapsing along the radial direction, we are assuming that any disk components

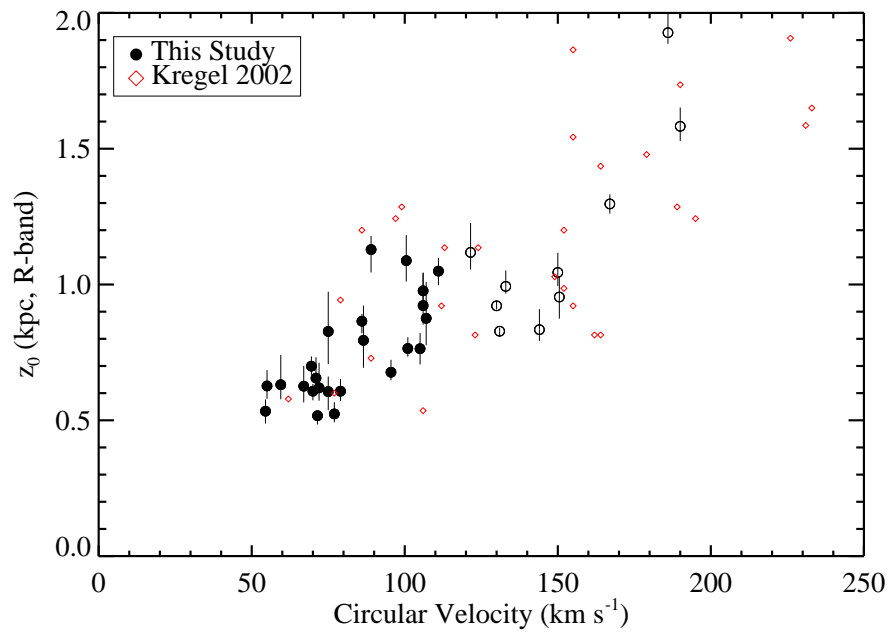


Figure 2.2 Single disk scale heights for the R -band fits. Galaxies with prominent dust lanes are plotted with with open circles. For comparison, we show the I -band scale heights from the edge-on sample of Kregel et al. (2002), plotted as red diamonds.

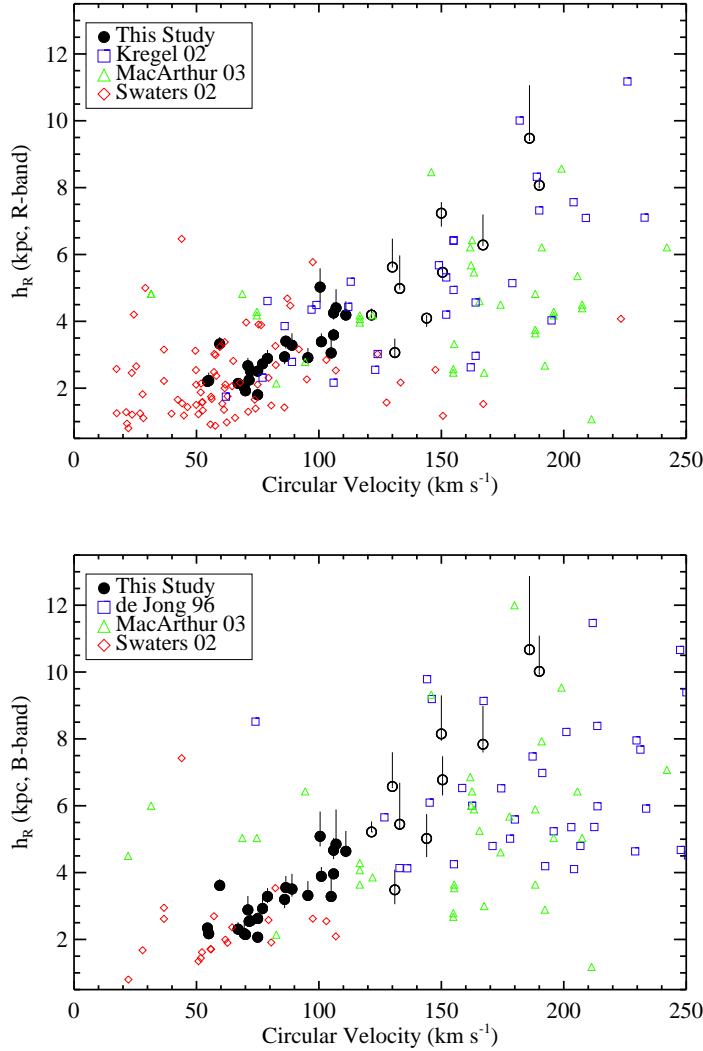


Figure 2.3 Single disk scale lengths for the R -band (top) and B -band (bottom) fits. Galaxies with prominent dust lanes are plotted with with open circles. For comparison, we show other single disk fits gathered from the literature. The de Jong (1996a) and MacArthur et al. (2003) data are face-on or moderately inclined galaxy samples with the scale lengths measured in the R and B -bands (plotted as blue squares and green triangles respectively). The Swaters & Balcells (2002) sample consists of late-type spiral and irregular galaxies with scale lengths measured in the R and B -band (plotted as red diamonds). The Kregel et al. (2002) data were measured from edge-on galaxies in the I -band (plotted as blue squares).

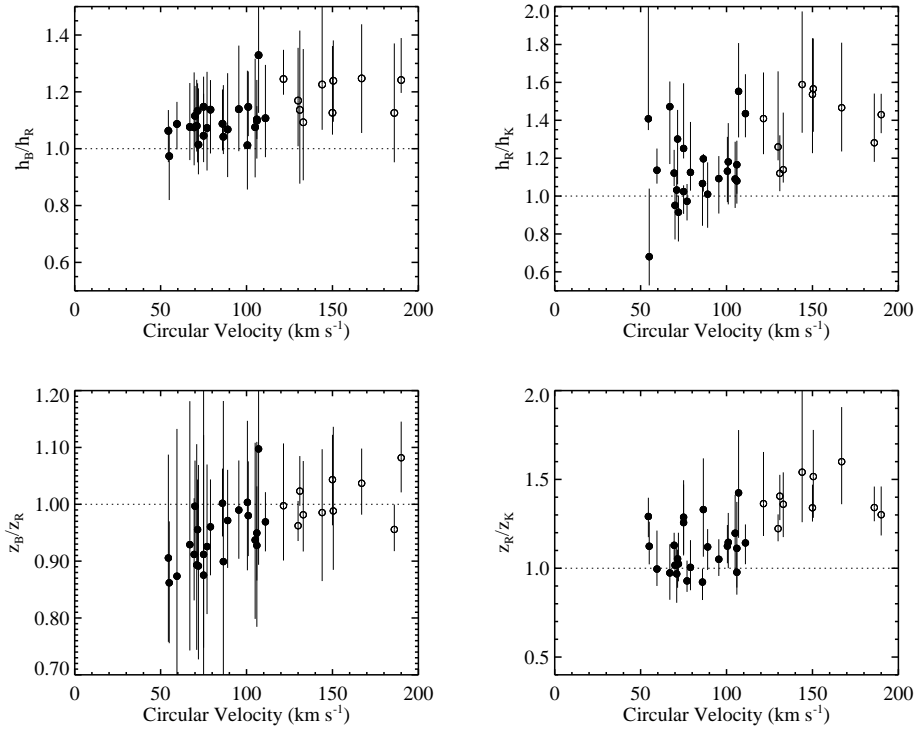


Figure 2.4 Comparison of scale lengths and heights for the single disk fits in different bands. Open symbols are used for galaxies with prominent dust lanes.

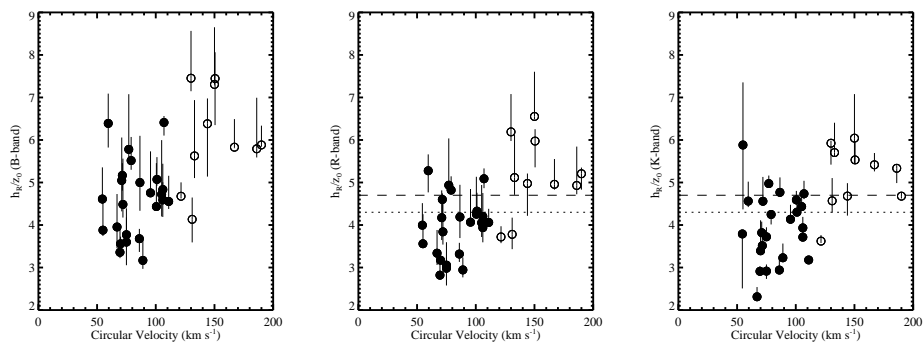


Figure 2.5 Single disk fits showing the flatness (h_R/z_0) for each band. Open symbols are used for galaxies with prominent dust lanes. Dotted lines show the average flatness for a sample of 34 galaxies in I -band presented in Kregel et al. (2002). Dashed lines show the average flatness measured from a sample of 153 galaxies from the Revised Flat Galaxy Catalog imaged by 2MASS in the K -band and presented in Bizyaev & Mitronova (2002)

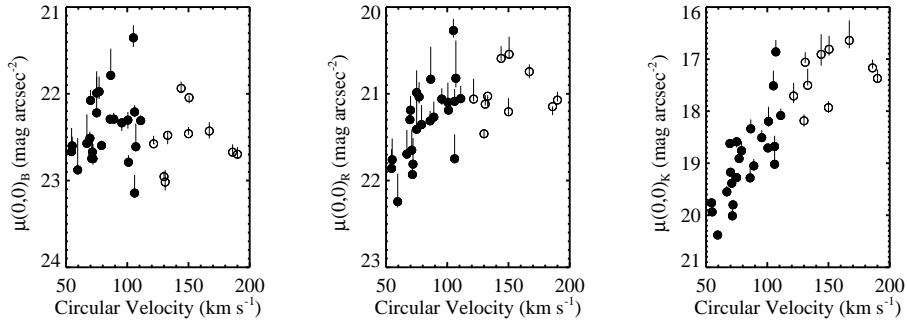


Figure 2.6 Edge-on peak surface brightnesses for the single disk fits. Open symbols are used for galaxies with prominent dust lanes. Points have not been corrected for internal extinction.

have a nearly constant scale height with radius, as has been found for late type disks in many studies (van der Kruit & Searle, 1981b; Bizyaev & Mitronova, 2002; de Grijs & Peletier, 1997).

These tests show that (1) our galaxies are poorly fit at large z by the simple sech^2 model; (2) by leaving the index N free, we can either fit low z or high z regions of the disk well, but not both regions simultaneously; and (3) the two disk model is superior at fitting the vertical profile at all latitudes. We conclude that our galaxies are best modeled by the superposition of two distinct components with unique scale heights.

While we already suspected the galaxies were composed of multiple stellar components based on the observed vertical color gradients and the analogous structures present in the Milky Way, we have now shown that this conclusion can be derived from R -band images alone. This analysis does not preclude the existence of additional components beyond the two disks considered here, although our data do not obviously require them. Our fits also do not demand that the two components trace kinematically and chemically distinct stellar populations that are directly analogous to the thick and thin disks of the Milky Way. On the other hand, when combined with the color gradients observed in Paper II, the data are fairly suggestive of the presence of two genuinely distinct components. We will revisit this issue further in

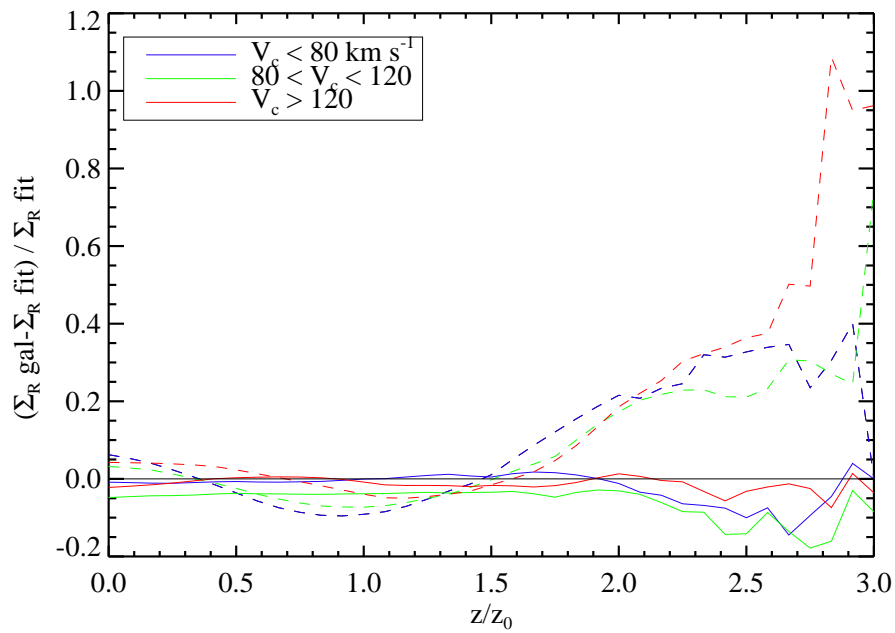


Figure 2.7 *Left*: Residuals collapsed along the radial direction and averaged over galaxies binned by mass. The single disk models (dashed lines) are very poor fits, leaving large amounts of excess flux at high latitudes. The two disk models (solid lines) do a much better job fitting the vertical light distribution at *all* latitudes and show only a small systematic trend to over-subtract at high z .

§2.5.4.

Ideally, we could use a statistical goodness-of-fit test to show that a second disk component is required when modeling edge-on galaxies. To establish the need for a thick disk in UGC 7321, Matthews (2000) used an F -test defined by

$$F = \frac{[\chi^2(1) - \chi^2(2)]/(p - k)}{\chi^2(2)/(n - p)} \quad (2.4)$$

where $\chi^2(1)$ characterizes the single disk model with k free parameters while $\chi^2(2)$ characterizes the more complex model with p free parameters and n total data points. Comparing our two disk models to single disk models with fixed N , the F -test favors two disks at the 95% level or higher confidence for 32 of the 34 galaxies, confirming that the two disk model is a better fit than a single disk, as seen in Figure 2.7. Even if the index N is allowed to vary, the two disk model is still favored in 31 of the 34 galaxies. Although the F -test works well for Matthews (2000) when fitting one-dimensional profiles, there are several caveats we must note for our sample. First, our models do not necessarily minimize the formal χ^2 value because of our inverse weighting system. Second, the F -test relies on the χ^2 formalism and thus assumes all errors are random and Gaussian. As we noted in §2.3.2, our residuals are definitely non-Gaussian, and therefore the results of any F -test should be viewed as suggestive but far from conclusive.

2.5.2 *Why Not a Halo?*

In addition to modeling the galaxies as a superposition of thick and thin disks, we investigated models composed of a single disk and a “stellar halo” component as advocated by Zibetti et al. (2004). For our halo model, we used a generalized Hubble density distribution (Wu et al., 2002) with the luminosity density

$$\mathcal{L}_{\text{halo}}(r, z) = \frac{\mathcal{L}_{0,\text{halo}}}{\{1 + [r^2 + (z/q)^2]/r_0^2\}^{\gamma/2}} \quad (2.5)$$

Viewed edge-on, this density distribution projects to the surface brightness profile

$$\Sigma_{\text{halo}}(R, z) = \mathcal{L}_{0,\text{halo}} \sqrt{\pi} \frac{\Gamma[(\gamma - 1)/2]}{\Gamma(\gamma/2)} \times r_0^\gamma [r_0^2 + R^2 + (z/q)^2]^{(1-\gamma)/2} \quad (2.6)$$

where Γ is the standard gamma function

We find our data strongly prefers a second disk component to a halo. Over half of our halo fits converged on very flattened halos ($q \leq 0.45$), essentially reproducing the properties of a thick disk, although one with a radial gradient in scale height. In addition, 40% of the fits converged to halo luminosities that are less than 1% of the disk luminosity, implying that the fitting procedure cannot actually use the new component to improve upon the single disk fits. When unconstrained, the halo exponential parameter γ ran away to very large or small values (producing a uniform background or a compact point source), again implying that a power-law halo is not the appropriate model for the light distribution at high z .

Using the F -test defined in §2.5.1 to compare the two disk fits with 9 free parameters to the disk plus halo fits with 10 free parameters, we found only 11 of the galaxies were better fit with a halo than the second disk. Even when χ^2 suggested that the halo model was a better fit, the flattening parameter converged to extreme values (less than 0.4, or greater than 1) in 7 of the 11 cases, thus flattening the halo into a more disk-like structure. In those cases, the preference of a halo component may indicate the presence of a radial gradient in disk scale height. In the few cases when a preferred halo fit remained roughly circular, it was because the halo collapsed to fit a small central bulge or star-forming region. Because these regions are bright, they can greatly affect the formal value of χ^2 and the F -test will prefer the halo model despite no real improvement in fitting the flux at large scale heights.

The poor results of our attempted halo fitting do not explicitly rule out the presence of a halo at lower surface brightnesses than we can detect in our images. Indeed, a stellar halo like the MW's would only start to dominate the thick disk component

at $\mu_R \sim 27.5 \text{ mag}/\square''$ (Morrison et al., 1997) around $z \sim 10z_0$ (our fits extend to only $z \sim 3 - 4z_0$). In M31 the stellar halo population dominates at a projected radius of $\sim 30 \text{ kpc}$ and a surface brightness level of $\mu_V \sim 31 \text{ mag}/\square''$ (Guhathakurta et al., 2005), and thus comprises $< 5\%$ of the total stellar luminosity. As before, if a comparable halo component was present in our sample it would be much too faint to be detected in our data.

Zibetti et al. (2004) fit a composite galaxy created by stacking over 1000 edge-on spirals from the Sloan Digital Sky Survey. Using equation 2.6, they found a slightly flattened halo with $q = 0.50$ in g , 0.60 in r and i , and 0.70 in z . There are several reasons we believe the excess light we detect at high latitudes is not equivalent to the halo component discussed by Zibetti et al. (2004): (1) Our R -band is close to r and i , yet when we try to fit a halo component, our values of q are much lower with a median value of 0.4 ; (2) The Zibetti et al. (2004) halos only begin to dominate the surface brightness at very large heights ($z = 16z_0$.) beyond our $1\text{-}\sigma$ cropping limit; (3) Zibetti et al. (2004) find that their stellar halo becomes prominent at a surface brightness of $\mu_r \sim 27 \text{ mag}/\square''$, fainter than what we can detect in our individual images.

2.5.3 Dust effects

We have previously found that galaxies in our sample with rotational velocities greater than 120 km s^{-1} host concentrated dust lanes (Dalcanton et al., 2004). We therefore need to consider the effect that dust extinction will have on our fitted parameters. To quantify the amount of extinction in our edge-on sample, we compare the total luminosities of our best fit models to the Hubble Key Project Tully-Fisher relation (Sakai et al., 2000) in Figure 2.8. We find that all of our galaxies, even those without recognizable dust lanes, lie significantly below the TF-relation for face-on spirals. Tully et al. (1998) fit empirical extinction relations accounting for filter, inclination, and circular velocity for a large sample of galaxies. When we apply the extinction

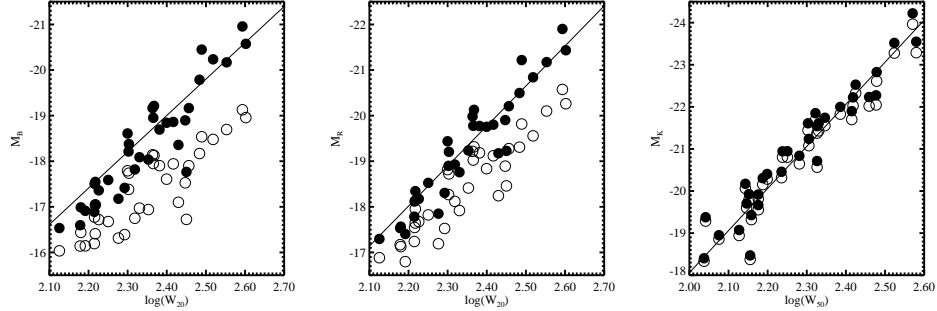


Figure 2.8 Tully Fisher relation derived from the single disk fits. Open circles show points uncorrected for internal extinction while solid circles have been corrected for internal extinction using the method of Tully et al. (1998). Solid lines on the left and middle panel show TF relations from the Hubble Key Project (Sakai et al., 2000). The solid line in the right panel shows the K' TF-relation of Verheijen (2001). The luminosities for the two disk fits show a comparable offset.

correction of Tully et al. (1998), our extinction corrected total luminosities move nicely onto the face-on TF relation.

Their offset from the Tully-Fisher relation implies that our models do not capture all the stellar flux from our galaxies. There are several possible ways dust could influence our fitted parameters to yield lower than expected total luminosities: (1) the peak surface brightnesses could be too low; (2) the scale lengths could be too short; (3) the scale heights could be too small; (4) the vertical profile could appear less peaked than it truly is (e.g., a sech^2 instead of an exponential); or (5) some combination of the above.

We can say with some certainty that the scale lengths do not appear to be shortened by dust extinction. If anything, Figure 2.3 shows that our scale lengths are larger than those measured in face-on systems. In a similar fashion, it is unlikely that our scale heights are shortened greatly due to dust, as their bias is likely to have the same sign as the scale lengths. Moreover, our weighting scheme de-emphasizes the midplane region, and our scale height fit is therefore dominated by flux coming from high galactic latitudes. Therefore, any dust distribution which is concentrated

along the midplane, or uniformly distributed though the galaxy, should have little to no impact on our fitted value for the scale height. Only a truly pathological dust distribution, such as one having large amounts of dust at high z compared to the midplane, would skew our scale height parameter to lower values.

Having eliminated biases in the scale height and scale length, we find that dust extinction is most likely affecting our choice of vertical profile and/or the fitted value of the peak surface brightness. Unfortunately, there is a degeneracy between these two parameters which could only be broken if we knew the intrinsic dust distributions in our galaxies. If the dust affects only the midplane region, then the error could be confined to just the vertical distribution, while a more diffuse and vertically uniform dust distribution would lower the central surface brightness but not affect the vertical profile.

We conclude that while our galaxies display clear signs of internal extinction caused by dust, the lost flux will cause us to either pick the wrong vertical profile (which is not of particular importance since we are not concerned with the midplane behavior), and/or underestimate the overall flux normalization as parameterized by the edge-on central surface brightness. However, since the empirical extinction correction of Tully et al. (1998) does an excellent job of moving our galaxies onto the TF relation (despite the correction originally not being intended for use on galaxies with extreme inclination angles), we chose to apply this correction to the luminosity of our thin disk component. We do not assume any correction for the extended thick component, since a much smaller fraction of its projected area would be obscured by dust.

2.5.4 Results of Thick + Thin Disk Fits

We now discuss the results of fitting two disk components. We fit a total of six 2-disk models, each with different combinations of $N = 1$ and $N = 2$ vertical profiles for the thick and thin components. We also considered models convolved with a

$\sigma = 1''$ circular Gaussian (to model seeing) and models where the midplane ($\pm z_{0,single}$) is masked (to avoid dust lane contamination). The properties of the models are described in Table 2.4. We use the inverse-weighting scheme for all the fits, as we found that one disk component always collapses to fit bright midplane structures if more conventional weighting is adopted. As discussed above, we fit the two-disk models only to the R -band images. Our K_s -band data does not go deep enough to reliably detect the thick disk component, and the B -band suffers from dust extinction, is biased towards young stellar populations, and is a poor tracer of the faint red light expected from an old thick disk.

The resulting parameters for the fits are listed in Table 2.5. For the central value of each parameter we list the median value of convergent $N = 2$ models. The uncertainties are the full range of values to which the different models in Table 2.5 converged, as discussed in §2.3.2. We also list the ratio of total luminosities for the model thick and thin disks. The range of luminosity ratios include models with disks having $N = 1$ or $N = 2$. The luminosity ratios are calculated only for flux which falls inside the $1\text{-}\sigma$ noise region (i.e. only the region that was included in the fit). The true luminosity ratios could therefore be different from our quoted values if the disks extend far beyond our detection limits. We have measured the size of this correction by extrapolating the fits and find it can change the luminosity ratios by only 10% at most. The luminosity ratios in Table 2.5 do not include the extinction corrections derived in §2.5.3.

Scale heights of the thick and thin disks

The scale heights of our thick and thin disks are plotted in physical units in Figure 2.9. The scale heights of both the thin and thick disks increase systematically with circular velocity. Fitting power laws to the relations, we find $z_{0,thin} = (610 \text{ pc}) \left(\frac{V_c}{100 \text{ km s}^{-1}} \right)^{0.90}$ and $z_{0,thick} = (1400 \text{ pc}) \left(\frac{V_c}{100 \text{ km s}^{-1}} \right)^{1.0}$ with RMS scatters of 30% in both cases. In general, the scale heights of the two disks bracket the scale height derived for a single

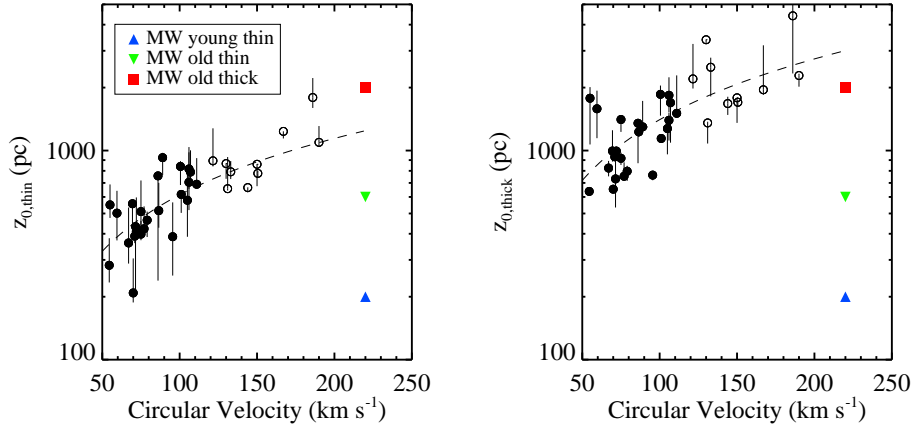


Figure 2.9 Scale heights of thin and thick disks. Values for the Milky Way from Larsen & Humphreys (2003) are plotted for comparison using $z_0 = 2h_z$ for an exponential vertical profile. Open symbols are used for galaxies with prominent dust lanes. Dashed lines show power-law fits to the data ($z_{0,\text{thin}} = (610 \text{ pc}) \left(\frac{V_c}{100 \text{ km s}^{-1}}\right)^{0.90}$ and $z_{0,\text{thick}} = (1400 \text{ pc}) \left(\frac{V_c}{100 \text{ km s}^{-1}}\right)^{1.0}$). In galaxies that have strong dust lanes, the scale height of the thin disk is likely to be biased towards larger values.

disk, as expected.

For massive galaxies with large circular velocities ($V_c \gtrsim 170 \text{ km/s}$), our derived value for the scale height of the thin disk is 2-3 times larger than the MW's thin disk. However, these galaxies have the most prominent dust lanes, which may substantially obscure our view of the thin disk. It is therefore likely that the scale heights of the thin disk may be significantly overestimated in these cases. The plot of $z_{0,R}/z_{0,K}$ for the single disk fits (Figure 2.4, lower right) is also consistent with this interpretation. Unfortunately, this limitation is unavoidable until sufficiently deep K -band data is available.

Figure 2.10 shows the ratio of the thick to the thin disk scale height $z_{0,\text{thick}}/z_{0,\text{thin}}$. We find a mean ratio of 2.5 with a scatter of 30%. In Figure 2.11 we show our data along with other thick and thin disk scale heights derived from the literature. For the Milky Way, these scale heights are derived from star counts. For the other literature

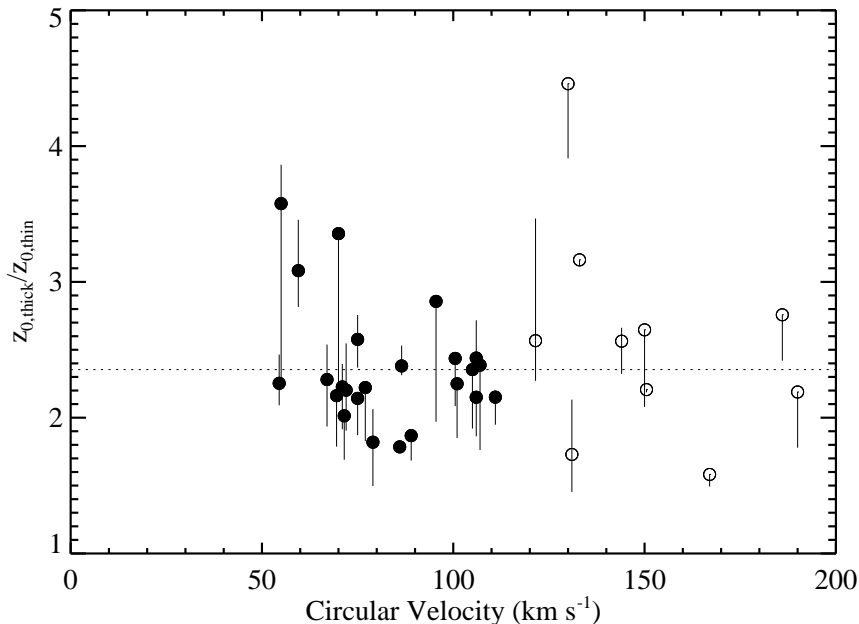


Figure 2.10 Ratios of the scale heights for the thick and thin disks. Error bars represent the full range of ratios to which different models converged. Galaxies with prominent dust lanes are plotted as open circles. The dotted line shows the median value of $z_{0,thick}/z_{0,thin} = 2.35$.

values, the scale heights are derived either from fitting double exponential profiles to 1-d cuts through the galaxies or from 2-d fitting similar to the procedure used in this paper. We summarize these other results in Table 2.2. Figure 2.11 indicates that our scale height ratios are slightly lower than those measured in other systems ($z_{0,thick}/z_{0,thin} \sim 3$), implying that our derived thick disks may be $\sim 25\%$ thinner and/or our thin disks are thicker than those derived in other galaxies with other methods. However, our median $z_{0,thick}/z_{0,thin}$ is very similar to Neeser et al. (2002)'s measurement of the LSB galaxy ESO 342-017, the most comparable galaxy in the literature to galaxies in our sample. These differences may indicate that the thick disks of early type galaxies may be proportionally thicker than those of late type galaxies.

Table 2.2. Thick disks from the literature

galaxy name	Type	Band	Fitted	V_c (km s ⁻¹)	$\frac{z_{0,thick}}{z_{0,thin}}$	$\frac{h_{R,thick}}{h_{R,thin}}$	$\frac{L_{thick}}{L_{thin}}$	Reference
34 galaxies	Sd	R	2-d	55-190	1.6-5.5	0.6-1.6	0.07-7	This study
6 galaxies	Sd	star counts	1-d	67-131	1.7-2.7	-	-	Seth et al. (2005b)
ESO 342-017	Scd	R	1-d	127	2.5	1	0.45	Neeser et al. (2002)
IC 5249	Sd	R	1-d	110	3	0.6	-	Abe et al. (1999)
MW	Sbc	star counts	2-d	220	3	1.3	~ 0.13	Larsen & Humphreys (2003)
NGC 6504	Sb	R	1-d	110 ¹	3.9	-	~ 0.4	van Dokkum et al. (1994)
NGC 891	Sb	R	1-d	224	3.5	-	0.12	Morrison et al. (1997)
NGC 4565	Sb	6660 Å	1-d	244	2.2	1.4	-	Wu et al. (2002)
5 galaxies	S0	R and V	2-d	~ 130 ²	2.6-5.3	1.7-1.9	0.33-1.0	Pohlen et al. (2004)
NGC4710	S0	R	1-d	147	3.2	-	-	de Grijs & van der Kruit (1996)
NGC4762	S0	R	1-d	110	4.6	-	-	de Grijs & van der Kruit (1996)
Simulation	-	-	-	240	4.7	-	0.35	Abadi et al. (2003b)
Simulation	-	-	-	150	2.6	0.63	0.8	Brook et al. (2003)

¹Estimated from Tully-Fisher relation²Dynamical information only available for 2 of the 5 galaxies

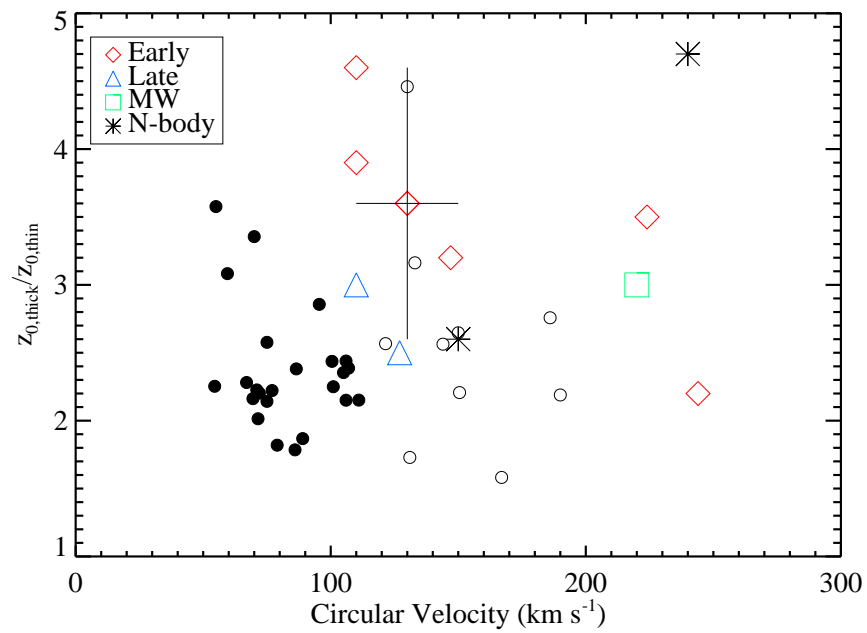


Figure 2.11 Comparison of our scale height ratios to values drawn from the literature. We compare to early-type galaxies (Sb and earlier; red diamonds), late type galaxies (Sc and Sd; blue triangles), the MW (green square), and simulated galaxies (asterisks). The range of values available for the Pohlen et al. (2004) sample of early type galaxies is plotted as a single point with error bars.

We also do not *a priori* know whether our thick and thin components are strict analogs of any particular component in the disk of the Milky Way, which is usually broken into at least three components; (1) the “young star-forming disk” ($z_0 \sim 200$ pc) which is dominated by molecular clouds, dust, and massive OB stars; (2) the “old thin disk” ($z_0 \sim 600$); and (3) the “thick disk” ($z_0 \sim 2$ kpc) (Bahcall & Soneira, 1980; Reid & Majewski, 1993; Buser et al., 1999; Larsen & Humphreys, 2003; Ojha, 2001; Chen et al., 2001), which contains $\sim 15\%$ of the total disk light (Buser et al., 1999; Chen et al., 2001; Larsen & Humphreys, 2003).

One possibility is that our thin and thick disks might be analogous to the MW’s young star forming disk and old thin disk, respectively, with no detectable analog of the MW thick disk. However, we do not believe the second component we have fit is an “old-thin” disk. The scale heights of our thin disks are larger than what has previously been measured for thin star forming layers. Matthews (2000) find UGC 7321 has a “young disk” with $z_0 \approx 185$ pc. Similarly, IC 2531 has a young disk with $z_0 \sim 134$ pc (Wainscoat et al., 1989) and the MW’s young disk has $z_0 \sim 200$ pc (Bahcall & Soneira, 1980; Reid & Majewski, 1993); (using the conversion that at large scale heights $z_0 \approx 2h_z$). All known young star-forming disks thus have $z_0 \sim 200$ pc. The only galaxies in our sample that have thin disk scale heights approaching values this small are far less massive than any of the galaxies in the previous studies.

Having ruled out an old thin disk, we now consider the possibility that our second thicker disk component is analogous to the MW’s thick disk. We find strong support for this possibility from studies of resolved stellar populations in similar systems (e.g., Seth et al., 2005a; Mould, 2005; Tikhonov et al., 2005). In particular, a recent analysis of resolved stellar populations in edge-on galaxies by Seth et al. (2005b) separates stars into young Main Sequence (MS), older Asymptotic Giant Branch (AGB), and still older Red Giant Branch (RGB) stars. Seth et al. (2005b) find that the younger stellar populations have systematically smaller scale heights than the ancient RGB population. In Figure 2.12, we compare our thin and thick disk scale heights with

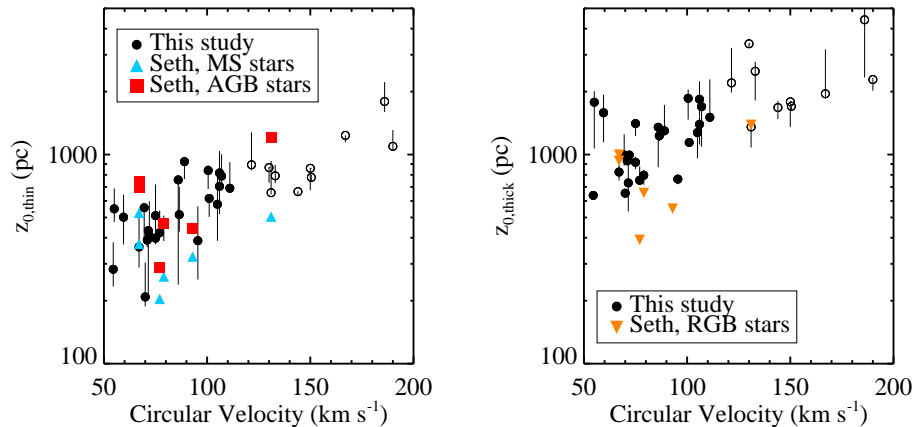


Figure 2.12 Comparison of our results with the scale heights of different stellar populations measured from resolved stars in 6 nearby galaxies (Seth et al., 2005b). The component we have identified as the thin disk appears to be intermediate between the scale height of young Main Sequence stars and medium-age Asymptotic Giant Branch stars while our thick disk component is similar to the old Red Giant Branch populations.

the MS, AGB, and RGB scale heights of Seth et al. (2005b). We find that our thin disk components have scale heights very similar to the young and intermediate age stellar populations of Seth et al. (2005b), while our thick disk components have scale heights similar to, or perhaps slightly larger than, the old RGB populations. Figure 2.12 supports that what we have labeled the thin disk hosts a young and intermediate age stellar population akin to the thin disk of the Milky Way while what we have labeled as the thick disk traces a different older and redder population, not an extension of the thin disk. When coupled with our observation of strong vertical color gradients (Paper II), and kinematic differences above and at the midplane, we believe there is compelling evidence that the second disk component required by our surface photometry does represent a truly distinct stellar population.

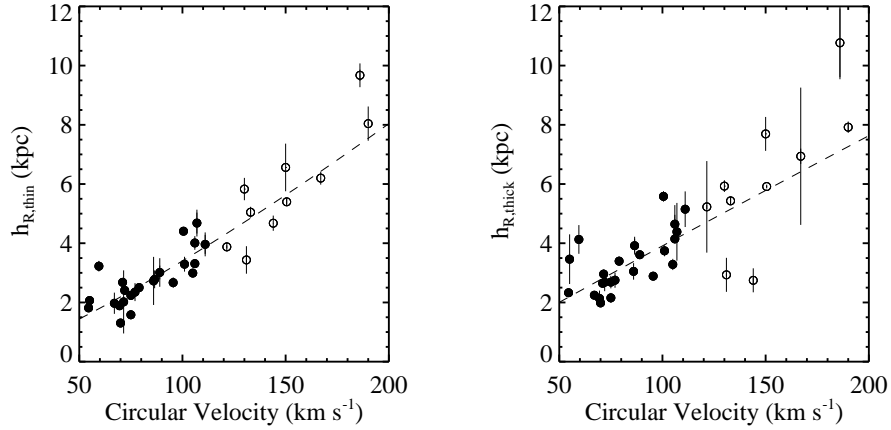


Figure 2.13 Scale lengths of thick and thin disks from the 2-disk fits. The dashed lines show power law fits. Open symbols are used for galaxies with prominent dust lanes. Dashed lines show power-law fits of $h_{R,thin} = 3.40(V_c/100 \text{ km s}^{-1})^{1.2}$ kpc and $h_{R,thick} = 3.9(V_c/100 \text{ km s}^{-1})^{1.0}$ kpc.

Ratio of scale lengths

Physical values of the thick and thin disk scale lengths are plotted in Figure 2.13. We see a systematic increase in the radial scale lengths of both disk components with galaxy mass. The data are well fit by $h_{R,thin} = (3.4 \text{ kpc})(\frac{V_c}{100 \text{ km s}^{-1}})^{1.2}$ and $h_{R,thick} = (3.9 \text{ kpc})(\frac{V_c}{100 \text{ km s}^{-1}})^{1.0}$ with RMS scatters of 22% and 29% respectively.

In Figure 2.14 we plot the ratio of the thick to thin disk scale lengths. We find that the thick disks have systematically larger scale lengths for all but 5 galaxies. Thick disks with long scale lengths are in excellent agreement with previous thick disk measurements, as shown in Figure 2.15 where we include data from the literature (Table 2.2). In all but one measurement of physical (i.e., non-simulated) thick disk scale lengths, the thick disk is found to be slightly longer than the thin disk.

We were initially concerned that this result could be a systematic result of our weighting and masking scheme. For example, if our galactic disks truncate at large radii as found in other edge-on systems (Kregel et al., 2002; Kregel & van der Kruit,

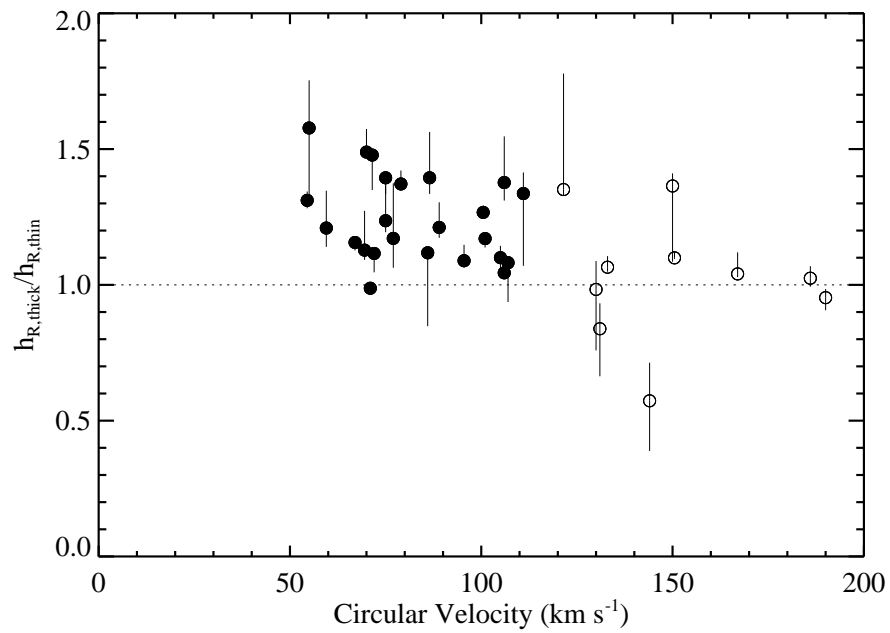


Figure 2.14 Ratios of the scale lengths for the thick and thin disks. The horizontal line indicates where the thin and thick disk components have equal scale lengths. Error bars represent the full range of ratios to which different models converged, and are indicators of our systematic errors. Open symbols are used for galaxies with prominent dust lanes.

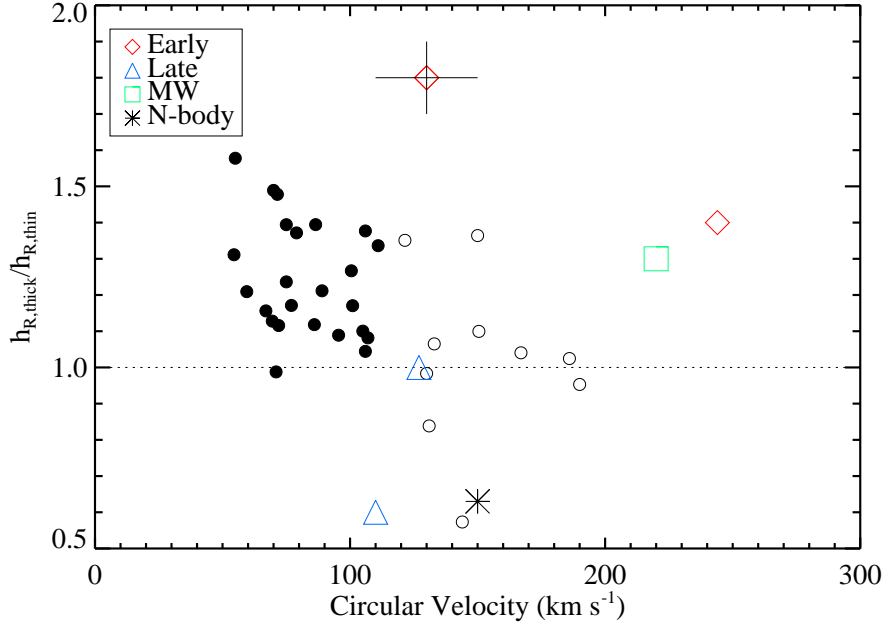


Figure 2.15 Comparison of our scale height ratios to values drawn from the literature. Comparison points are the same as Figure 2.11.

2004), then our model fits would converge to have the fainter thick disk dominate at large R . However, we included a model (Table 2.4) where the midplane is masked (which also effectively removes regions of the galaxy where disk truncation would be detectable) and still found that the thick disks have longer scale lengths.

We note that there are some limitations in interpreting our scale lengths, particularly for the thin disk. First, the derived radial scale lengths do not necessarily reflect the stellar radial scale length. The thin disk in particular shows a strong radial color gradient, implying a mass-to-light ratio that decreases with increasing radius (see color maps in Paper II). This trend suggests that the radial scale length of the stellar mass should be even smaller for the thin disk, further increasing the ratio $h_{R,thick}/h_{R,thin}$. We may also have overestimated the scale length of the thin disk if it is affected by dust in a manner similar to the what is observed in our single disk fits (Figure 2.3 and §2.5.3). Both of these effects suggest that $h_{R,thick}/h_{R,thin}$ may be

even larger than indicated by Figure 2.14. On the other hand, HI is typically more extended than the optical disk (Swaters et al., 2002; Begum et al., 2005), such that the radial scale length of the baryons in the thin disk may be longer than indicated by $h_{R,\text{thin}}$.

Axial ratios of the thick and thin disks

The axial ratios (h_R/z_0) for our thick and thin disks are plotted in Figure 2.16 along with values for the MW thick and thin components for comparison. We find our thick disks have a mean $h_R/z_0 = 3.0$ with an RMS scatter of 0.8 while the thin disk has a mean value of $h_R/z_0 = 5.6$ and RMS scatter of 1.1. Our thin disks therefore tend to be comparable to the MW thin disk, but are slightly rounder at low masses, in agreement with other studies (see §2.4). The axial ratios of the thick disks show a large spread, and are in general comparable to, or slightly thinner than the MW thick disk. However, the radial scale length of the MW is not well constrained since it is determined primarily from star counts near the solar circle. We also note that the thick disk component is drastically rounder than the MW's old thin component, further ruling out the old thin disk as an explanation for our second disk component.

Peak surface brightnesses

The edge-on peak surface brightnesses for our two disk components are plotted in Figure 2.17. There is a trend for more massive thin disks to have brighter peaks, similar to the trend seen in the single disk fits (Figure 2.6). The thick disk components show a large amount of scatter in their peak values.

Performing a naive transformation to convert to the face-on orientation, the central surface brightness becomes $\mu_0 = \mu(0,0) - 2.5\log(z_0/h_R)$. We find that the average central surface brightness of the thick disk is 0.6 mag/□" fainter than the thin disk, implying only $\sim 35\%$ of the stellar flux in the R -band would come from the thick disk if the galaxies were viewed face-on. In the more massive galaxies, the face-on central

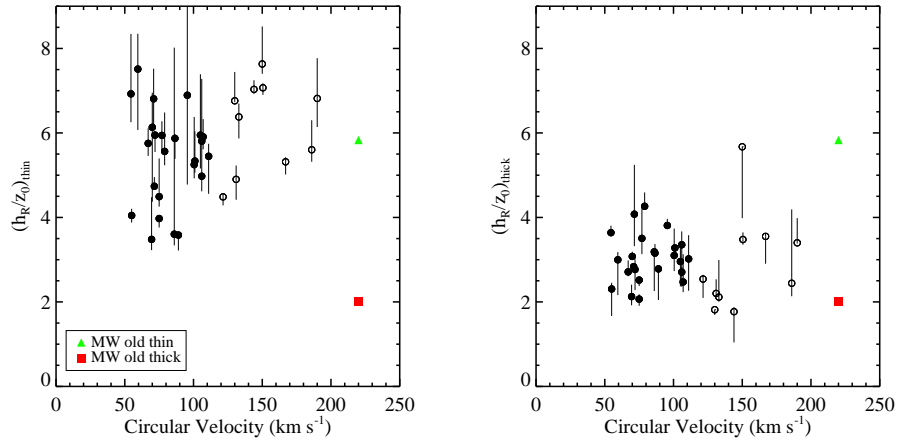


Figure 2.16 Axial ratio (h_R/z_0) vs circular velocity for the thin (left) and thick (right) disks. Galaxies with prominent dust lanes are plotted as open circles. The axial ratios of Milky Way disk components are plotted for comparison (Table 2.2). The axial ratios of our thin and thick disks agree well with the comparable components for the MW.

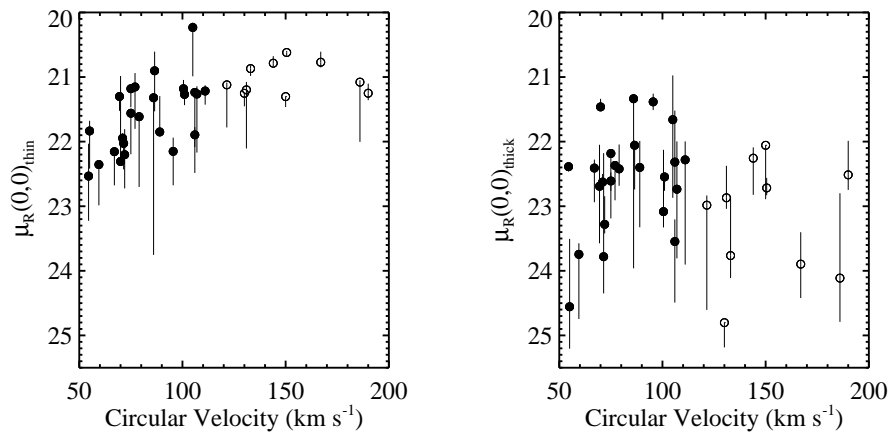


Figure 2.17 Edge-on peak surface brightnesses for the 2-disk fits in the R -band. Galaxies with prominent dust lanes are plotted as open circles.

surface brightness of the thick disk can be up to 2 mag/□" fainter than the thin disk. These values do not include corrections made for extinction. Presumably, the thin disk would suffer less extinction when viewed face on, and would further dominate the observed stellar flux. It is therefore not surprising that the thick disk is largely undetected in face-on galaxies.

The total integrated colors of the galaxies will be biased towards the thin disk population as well. After making the extinction corrections in §2.5.3, we find the total integrated colors of our low mass-galaxies ($V_c \lesssim 100 \text{ km s}^{-1}$) are in the range $0.5 < B - R < 1$, much bluer than the thick disk (see Figure 2.20 below). Using the Bruzual & Charlot (2003) stellar synthesis code, these colors correspond to a stellar population burst with an age of $\sim 1 \text{ Gyr}$, or a galaxy with a uniform star formation history. Thus, in spite of the substantial thick disk population, the mean colors of the galaxy reflect only the youngest disk population.

Ratio of luminosities

We now compare the total luminosities of the thick and thin disks (Figure 2.18). In our raw fits, the luminosity of the thin disk is almost certainly underestimated due to the effects of dust, as shown in §2.5.3. To correct for dust, we assume that all flux lost from extinction (Figure 2.8) should be assigned to the thin disk. This correction will give us the most conservative estimate for the contribution of the thick disk to the total stellar luminosity. Figure 2.18 shows a strong trend with mass (Spearman $\rho = -0.70$, 4.0σ). Thick disks of high mass galaxies ($V_c > 120 \text{ km s}^{-1}$) contribute $\sim 10\%$ of the total luminosity of the galaxy, while in lower mass systems the thick disk contributes up to 40% of the total luminosity. This trend can be well represented by the relation $L_{\text{thick}}/L_{\text{thin}} = 0.25(V_c/100 \text{ km s}^{-1})^{-2.1}$, shown as a solid line in Figure 2.18.

We compare our measurements to previous thick disk measurements in Figure 2.19. Unfortunately, there are few measurements of total disk luminosities in the literature. When possible, we have taken other authors' disk parameters and calculated the

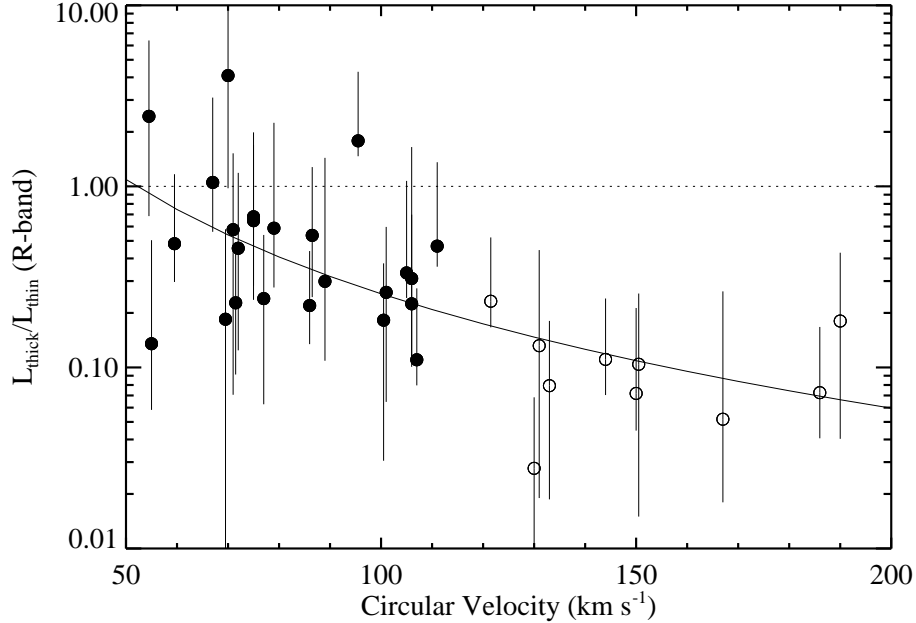


Figure 2.18 Ratio of the total R -band luminosity of the thick disk compared to the thin disk for the sample galaxies. The thin disk luminosities have been corrected for internal extinction. The dotted line indicates where the thick and thin disks contribute equally to the total luminosity. Error bars show the full range of values from different models, and are indicative of our systematic errors. Galaxies with prominent dust lanes are plotted as open circles. The solid line is a fitted power-law of the form $L_{\text{thick}}/L_{\text{thin}} = 0.25(V_c/100 \text{ km s}^{-1})^{-2.1}$.

resulting total luminosities (see Table 2.2). For the Milky Way, the local stellar density of thick disk stars has consistently been measured between 4 and 10% of the local thin disk density (e.g., Buser et al., 1999; Chen et al., 2001), which corresponds to a total luminosity ratio of $\sim 13\%$ for reasonable estimates of scale heights, lengths, and mass-to-light ratios for the two disks. Because the values of $L_{\text{thick}}/L_{\text{thin}}$ from the literature do not include internal extinction corrections, we compare them to our uncorrected luminosity ratios.

Figure 2.19 shows that our luminosities compare well with other thick-thin disk systems in the literature. The higher mass galaxies in our sample ($V_c \sim 140 - 200$

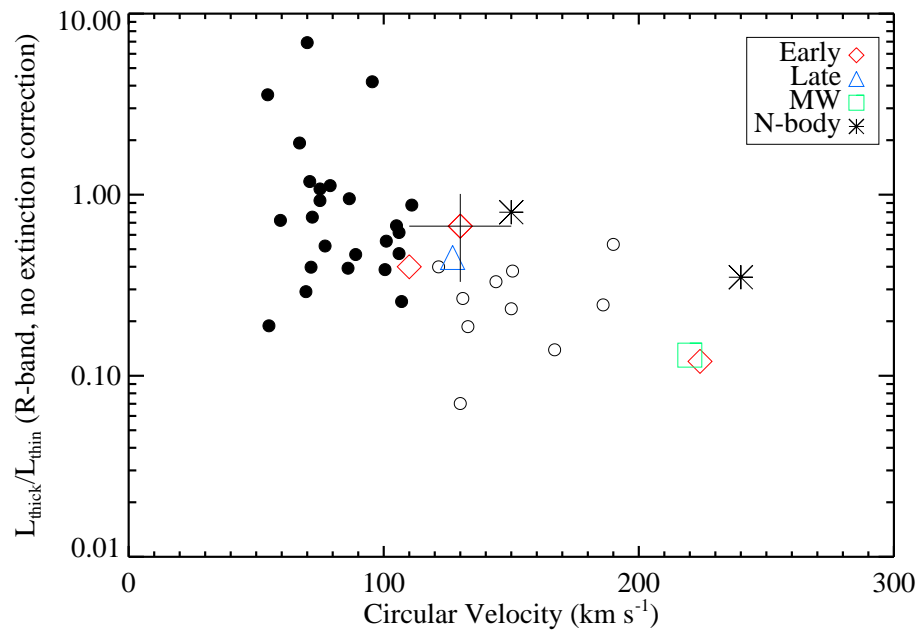


Figure 2.19 Comparison of our luminosity ratios to others in the literature. Comparison points are the same as Figure 2.11. Unlike Figure 2.18, we have made no correction of internal extinction to allow for easier comparison with previous studies.

km s⁻¹) tend to be thin disk dominated with $L_{\text{thick}}/L_{\text{thin}} \sim 0.1 - 0.2$ (corrected for extinction), like the Milky Way and NGC 891. Intermediate mass galaxies ($70 < V_c < 100$ km s⁻¹) have slightly more luminous disks, similar to measurements of ESO 342-017 (Neeser et al., 2002) and S0's (Pohlen et al., 2004). Unfortunately, we cannot find any comparable measurements of thick disks in the low mass systems ($50 < V_c < 70$ km s⁻¹) that are thick disk dominated in our sample.

We believe our measurement of the total luminosities are more robust than the measures of the peak surface brightness. Central surface brightnesses depend strongly on the vertical profile and can vary greatly from author to author. On the other hand, our fits of the total luminosity are good matches the data ($|m_{\text{model}} - m_{\text{observed}}| \sim 0.2$ mags), and fall on the Tully-Fisher relation (Figure 2.8).

Mass ratios

Figure 2.18 indicates that thick disk stars provide a significant fraction of a galaxy's total luminosity. However, as seen in Paper II, the thick disk tends to have a redder color than the thin disk, especially in low mass galaxies, and thus will have larger stellar mass-to-light ratios than the thin disk. Therefore, the thick disk may well dominate the stellar mass in many of our galaxies. We estimated the stellar disks' masses using the luminosities of the two disk components, along with color information from our single disk fits. Specifically we used the spectrophotometric galaxy evolution analysis of Bell & de Jong (2001) to convert our $B - R$ color maps into stellar mass-to-light ratios for each disk, and then convert our luminosity ratios into mass ratios for the thick and thin components.

The initial analysis of vertical color gradients in our sample (Paper II) suggested that the colors of thin disks vary systematically with galaxy mass, but that the colors of thick disks are fairly uniform. We therefore assumed that the thick disks have uniform colors and mass-to-light ratios in each galaxy. To convert disk colors to masses, we first analyzed our R -band 2-disk fits to find regions where the thick disk

contributes more than 75% of the total flux inside the $1\text{-}\sigma$ noise contour. Out of 34 galaxies, 27 have a clearly thick disk dominated region. We created a model $B - R$ color map of each galaxy using our 2-disk R -band model and single-disk B -band fits. Using the model images allowed us to avoid dust lanes, HII regions, and foreground objects that would skew our measure of the stellar population masses. We then used this color map to find the average $B - R$ value in the thick disk dominated regions and took that as the approximate color for all the thick disk stars. We assumed the thick disk has a constant color, thereby guaranteeing that its structural parameters will be the same in both the B and R bands. With the $B - R$ thick disk color from the model color map and the thick disk structural parameters from the 2-disk fit, we then made a model $B - R$ color map for the thin disk by subtracting off the thick disk component from both the B -band and R -band models.

We applied internal extinction and reddening corrections to our models using the results of §2.5.3 and assumed that dust had a uniform effect on the thin disk colors but a negligible effect on the thick disk. Using this approximation, we found $E(B - R) \sim 0.1$ for low mass galaxies and ~ 0.4 for higher mass galaxies. Although it is only a rough approximation, our reddening correction is in good agreement with the radiative transfer model of Matthews & Wood (2001) who find that most disk light in their modeled edge-on galaxies suffer reddening of order $E(B - R) \sim 0.1$, and that the reddening saturates at $E(B - R) = 0.31$.

The resulting colors for thick and thin disks are plotted in Figure 2.20. The thick disks tend to be red with $1.0 \lesssim B - R \lesssim 1.7$, while the thin disks are blue in low mass galaxies and become nearly as red as the thick disks in the higher mass galaxies. This trend is also seen in Figure 2.21, where we directly compare the colors of each component.

Using the colors shown in Figure 2.20, and the color dependent stellar mass-to-light ratios from Bell & de Jong (2001), we converted the thick and thin disk luminosities to stellar masses using $M = (M/L)_R L_R$, where L_R is the extinction corrected R -band

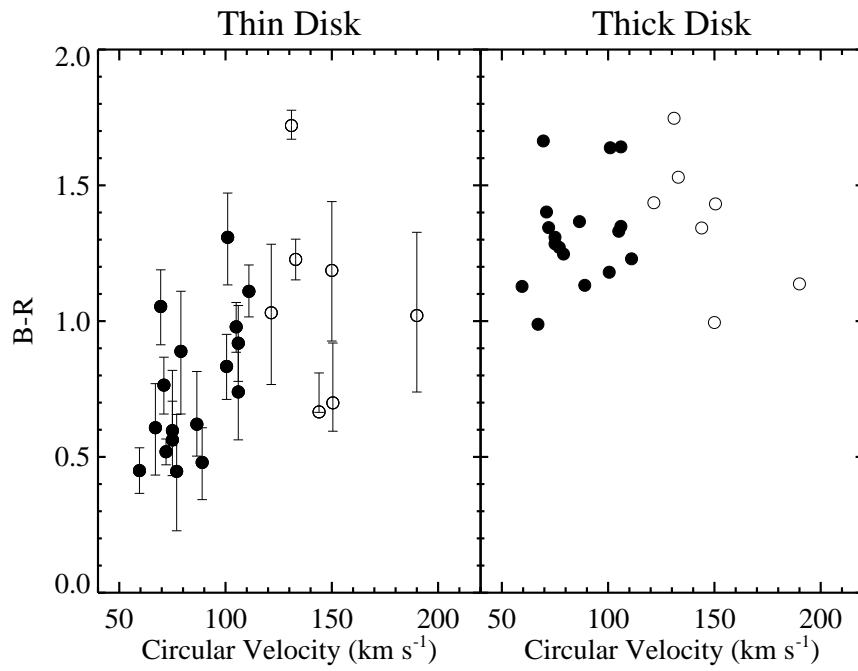


Figure 2.20 Extracted colors for the thick and thin disks. The thin disk colors shows the full range of $B - R$ values for the midplane between $h_R < R < 3h_R$. The thin disk has been corrected for internal extinction, but we assume no correction for the thick disk. Open circles show galaxies with dust lanes.

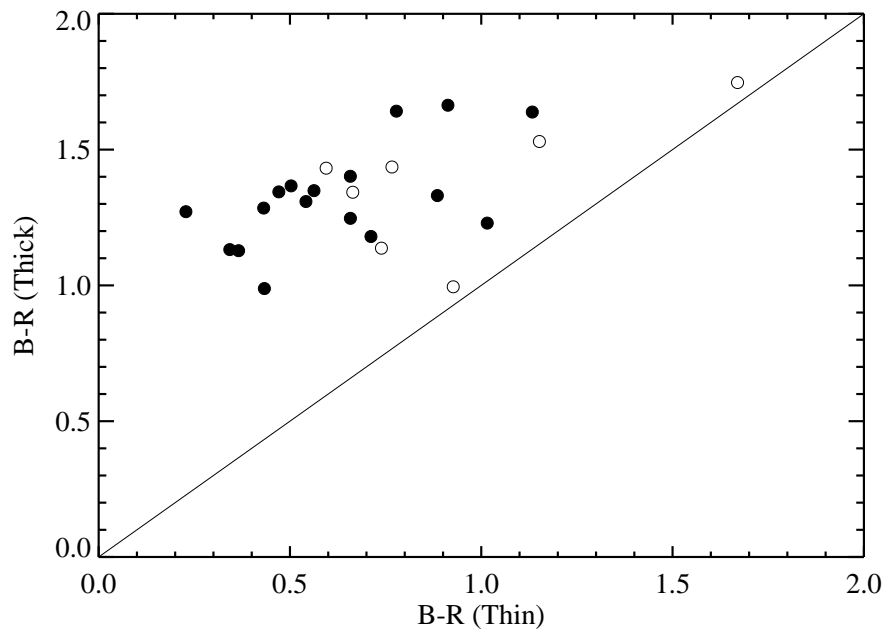


Figure 2.21 Comparison of thin and thick disk colors. The diagonal line indicates where the two components have equal color. Thin disk colors have been corrected for internal extinction. Open circles show galaxies with dust lanes.

luminosity from §2.5.4. For the thin disk, we calculated $(M/L)_R$ using the Bell & de Jong (2001) model which assumes a Salpeter IMF and metallicity of $Z = 0.02$, for the thick disk we use the same model with $Z = 0.008$. Overall, our results were insensitive to the stellar evolution and metallicity differences covered in the Bell & de Jong (2001) models. The different IMF's adopted in Bell & de Jong (2001) return mass-to-light ratios which can vary by a factor of two. Our results could be very skewed if the thin and thick disks have substantially different IMFs.

The resulting mass ratios of the thick and thin disks are plotted in Figure 2.22. As expected, Figure 2.22 confirms the features from our luminosity analysis. First, there is a strong trend for lower mass galaxies to have a larger fraction of their stellar mass in a thick component. The trend has a Spearman correlation of $\rho = -0.86$ (4.1σ) and can be well fit with the relation $M_{\text{thick}}/M_{\text{thin}} = 0.53(V_c/100 \text{ km s}^{-1})^{-2.3}$. Second, in low mass galaxies, $\sim 1/3$ to greater than $1/2$ of the stellar mass is in the thick disk. Thus, the stellar mass of very low mass galaxies are dominated by thick disk stars.

Part of the trend in Figure 2.22 may be due to low star formation efficiency in lower mass disks. These systems have high gas mass fractions, and thus may not yet have built up a significant stellar mass in the thin disk. To investigate this possibility, we calculated the baryonic mass fraction of the thick and thin disks, assuming that all gas in the galaxies is associated with the thin disk and that the thick disk is entirely stellar. We calculate the gas mass as $M_{\text{HI}}/M_{\odot} = 236d^2 \int S dV$ where d is the distance to the source in Mpc, and S is the flux density in mJy over the profile width dV in km s^{-1} (Zwaan et al., 1997). To account for He and metals, we make the standard correction $M_{\text{gas}} = 1.4M_{\text{HI}}$. We do not include a correction for molecular gas.

Figure 2.23 shows the resulting baryonic mass ratio of thick and thin disks with the mass of HI gas added to the thin disk component. When the gas is included in the thin disk component, we find that none of the galaxies remain thick disk dominated although the baryon mass fraction in the thick disk does remain substantial for low mass galaxies. Eleven of our galaxies had no HI data and their gas fraction was

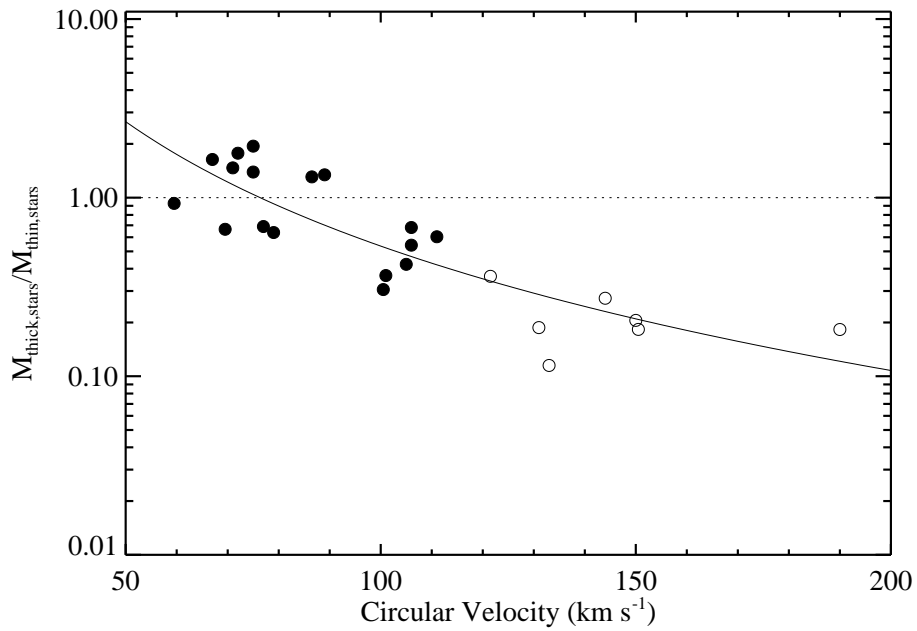


Figure 2.22 Stellar mass ratios of the thick and thin disks. The thin disks luminosities and corresponding masses have been increased to account for dust extinction. Galaxies with prominent dust lanes are plotted as open circles. The solid line is a power-law fit $(M_{\text{thick}}/M_{\text{thin}})_{\text{stars}} = 0.53(V_c/100 \text{ km s}^{-1})^{-2.3}$.

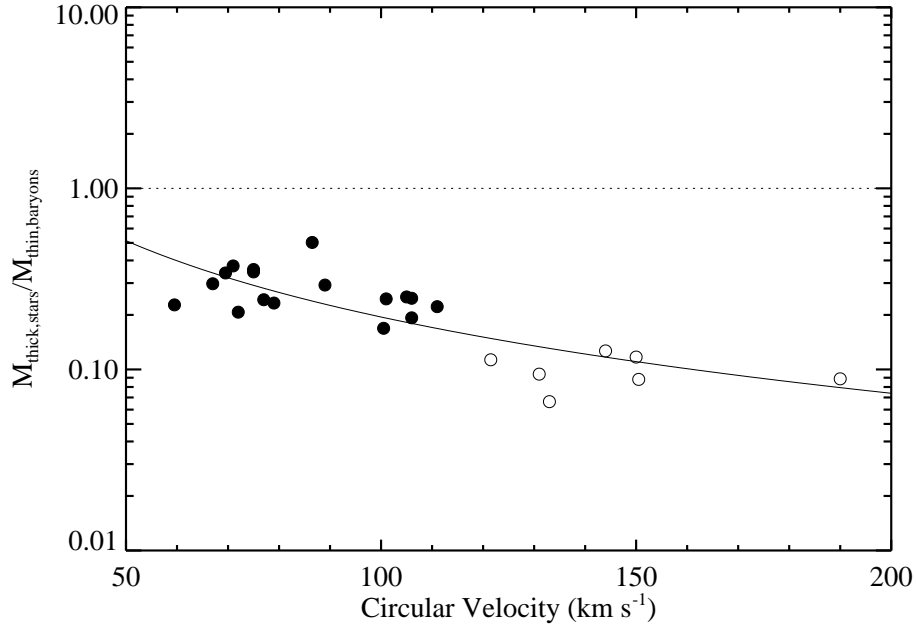


Figure 2.23 Baryonic mass ratios of the thick and thin disks. The thin disks luminosities, and corresponding masses, have been increased to account for extinction effects and include the estimated thin disk mass stored in gas. Galaxies with prominent dust lanes are plotted as open circles. The solid line is a power-law fit $M_{\text{thick,stars}}/M_{\text{thin,baryons}} = 0.19(V_c/100 \text{ km s}^{-1})^{-1.4}$.

estimated by fitting a simple power law to the gas fraction of our galaxies with HI measurements. Figure 2.24 shows the final calculated baryon fractions for all of the stellar and gaseous components, and clearly indicates the increasing importance of the thick disk in lower mass galaxies.

2.6 The Formation of the Thick Disk

Given evidence from the Milky Way and from nearby resolved galaxies, we will assume in the following discussion that thick disks have a formation mechanism distinct from that which forms the thin disk. We will also assume that the properties of “thick” and “thin” components from our 2-D fits will roughly approximate the properties of the

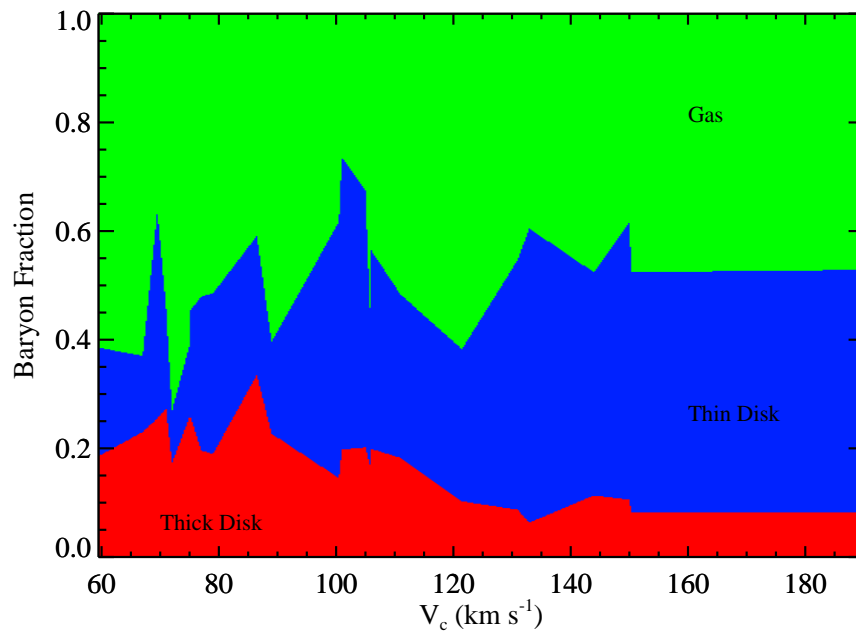


Figure 2.24 Final baryon fractions of the thick and thin components as a function of circular velocity. The thin disk has been corrected for internal dust extinction. The baryonic mass fraction of the thick disk clearly increases towards lower galaxy mass.

chemically and kinematically distinct thick and thin disk analogs of the Milky Way. As we have argued above in §2.5.4, the structural properties of the fits are consistent with those of the corresponding components of the Milky Way and with the results of detailed stellar population studies in nearby galaxies (e.g. Figure 2.12). We therefore will simply assume a perfect correspondence between our fits and distinct thick and thin components for the rest of this discussion. While this assumption is not ideal, it is unavoidable, given that a full kinematic and chemical analysis of the stellar components is presently impossible far outside the Local Group.

2.6.1 *The Merger Origin of Thick Disks*

As discussed above in §2.2, there are three general classes of thick disk formation scenarios – one where the thick disk stars form *in situ*, one where the thick disk stars form in a thin disk but are then impulsively “heated” to large scale heights, and one where thick disk stars form first in other galaxies but are then directly accreted. In the last decade there has been a growing body of evidence in favor of the latter two scenarios. This evidence includes the detection of strong kinematic differences between thick and thin disks in other galaxies (Yoachim & Dalcanton, 2005) and in the Milky Way (Gilmore et al., 2002), as well as evidence from chemical abundance studies for extended star formation histories of Milky Way thick disk stars (e.g., Bensby et al., 2005). These latter two scenarios are also naturally accommodated in current theories of hierarchical structure formation, where mergers and accretion are common.

Of the two merger-driven scenarios, we believe that the data favor an accretion origin for thick disk stars. The strongest evidence comes from our previous measurements of thick and thin disk kinematics in two late-type disks. We found that thick disk stars are rotating with only a small fraction of the rotational velocity of thin disk stars, and are indeed counter-rotating in one of the two cases studied. In contrast to the observed behavior, simulations show that disks heated by satellites would have

nearly the same angular momentum as the initial thin disk. Therefore, barring the unlikely possibility that the thin disk reforms from subsequent accretion of gas with angular momentum opposite to the original disk, creating counter-rotating or slowly-rotating thick disks via vertical heating alone is problematic. Additional supporting evidence comes from recent HST studies of resolved stars in nearby edge-on galaxies (Seth et al., 2005b; Mould, 2005). While Seth et al. (2005b) finds evidence for some *steady* vertical heating, the oldest population of RGB stars shows no evidence of the vertical metallicity gradient expected if they were dominated by stars that had participated in the steady heating. Instead, the thick population of RGB stars must have been established early, when the merger rate was still extremely high. At these early times, the hypothetical picture of a well-defined stable thin disk impulsively heated by a single merging event seems inappropriate. In summary, while the evidence does not yet conclusively rule out a single, thin disk heating merger event as the origin of thick disk stars, we consider it to be sufficiently unlikely that we will focus on interpreting the results in this paper in terms of the accretion scenario.

The idea that stars well above the Galaxy’s midplane may have been directly accreted from satellites was first discussed by Statler (1988)¹, and then codified as a distinct formation mechanism for the thick disk shortly thereafter in the review article by Gilmore et al. (1989) and as “Model 7” in Majewski (1993)’s review. Recent detailed studies of stellar structures in the Milky Way and M31 find evidence that stars are regularly accreted by massive galaxies. For example, Martin et al. (2004) find asymmetries in the distribution of M-giant stars (e.g., the Galactic ‘Ring’ Newberg et al., 2002; Yanny et al., 2003) that are well explained by a single dwarf galaxy accretion event. Martin et al. (2004) also note that their modeled accretion event results in accreted stars having orbits similar to thick disk stars, and that the thick

¹Statler’s work refers to explaining the kinematics of “halo” stars, but given the current understanding of Galactic structure, the specific kinematic data he was trying to explain were measurements of what we would now call thick disk stars.

disk may be continually growing through in-plane accretion of dwarf galaxies. M31 also appears to also be actively disrupting dwarf galaxies with an observable stellar stream (Ibata et al., 2004) and a large extended disk (Ibata et al., 2005).

Direct accretion as the dominant origin of thick disk stars has recently been revived by several numerical studies of disk galaxy formation. Analyzing an N-body simulation of a moderately low mass spiral formed in a cosmological context, Abadi et al. (2003b) found a well-populated thick disk, more than half of which was made up of stars originally formed in accreted satellite galaxies. Although by no means definitive due to the simulated galaxy’s unrealistically large bulge, Abadi et al. (2003b)’s work lead to a revival of the notion that thick disk stars may have formed outside their host galaxies. Subsequent simulations of a collapsing sphere seeded with perturbations by Brook et al. (2004, 2005) generated thick disks associated with an early episode of chaotic merging. Unlike Abadi et al. (2003b), Brook et al. (2004) argued that the thick disk stars formed *in situ* from large velocity dispersion gas deposited by the satellites as they merged together to the final disk structure. Both simulations have significant limitations, making it impossible to decide in favor of either scenario at this time, but both stress the importance of merging and accretion in setting properties of the thick disk.

In the context of hierarchical galaxy assembly, the above simulations point to a straightforward picture of disk formation that necessarily leads to the formation of thick disks. At high redshift, galaxies exist largely as a collection of sub-galactic fragments. These fragments consist of gravitationally bound dark matter “mini-halos”, many of which presumably host some amount of baryonic material. Because these systems are high in the merging hierarchy, they would be expected to be relatively dense, and thus some of the gas hosted by these sub-units is likely to form stars. Early on, the merging rate will be very high, and as these fragments come together, their orbits will tend to circularize, align, and decay due to dynamical friction, as in Statler (1988) and early simulations by Quinn & Goodman (1986) and Walker

et al. (1996). The merged subunits will form a rotating flattened structure provided that the net angular momenta of the satellites is sufficiently high. When the merging rate declines sharply ($z \sim 3$) (Zhao et al., 2003), the disk will be left in place as a long-lived structure relatively unperturbed by significant accretion events. Any dense gas associated with the pre-galactic fragments must then either form stars in a burst during the final merger of the fragments, as in the Brook et al. (2004) simulations, or cool into a thin disk which later converts into stars.

Within this scenario, *any* stars that formed in the sub-units and were not tidally stripped at large radii must necessarily wind up in a thickened disk structure, with a vertical velocity dispersion equal to or greater than the velocity dispersion of the typical pre-galactic fragment. Because they are effectively collisionless, the accreted stars cannot lose energy and cool into a thinner disk, and must retain a large fraction of the initial velocity dispersion and angular momentum of the satellite in which they formed. With this in mind, it seems impossible to imagine *not* forming a thick disk (unless star formation was completely suppressed at early times, for example by reionization, e.g., Bullock et al., 2000; Gnedin, 2000). The only other possible destination for the accreted stars would be the bulge or stellar halo. However, the sample considered here is essentially bulgeless. We also find no evidence for a luminous stellar halo down to our limiting surface brightness. Taking a conservative estimate for the surface brightness of the brightest stellar halo that could be present, but undetected in our data, we find that any stellar halo must be less than 15% of the luminosity of the thick disk. This estimate suggests that the majority of directly accreted stars settle into the thick disk.

In addition to the theoretical arguments for forming thick disks via direct accretion of stars, there is a slowly growing body of observational evidence for this process seen *in situ* at high redshift. First is the analysis of high redshift “clump-cluster” galaxies by Elmegreen & Elmegreen (2005). Morphologically, these galaxies appear to consist of many distinct, high surface brightness clumps merging together. Elmegreen &

Elmegreen (2005) argue persuasively that these systems will wind up in a thickened disk with high velocity dispersion, and are thus likely precursors to thick disks. The colors of the clumps suggest that they already contain some stars, and are not pure gas systems. Elmegreen & Elmegreen (2005) also find field counterparts of the clumps, suggesting that some stars may have formed before the clumps were accreted into the galaxy. The second piece of evidence is the kinematic study of Erb et al. (2004), who find that lumpy disk-like structures at $z \sim 2$ show little net rotation. If their sample consists primarily of the edge-on counterparts of the galaxies in the Elmegreen & Elmegreen (2005) study, then the lack of strong rotation would be consistent with what is expected for material that forms a thick disk. Although this study traces H α kinematics only, and thus leaves the kinematic state of any associated stars unconstrained, it would be peculiar if any stars associated with the accreting gas did not show similarly perturbed kinematics.

2.6.2 Constraints from the Structures of Thick and Thin Disks

In the above accretion scenario, the properties of the thick disk are fixed primarily by the stellar content and orbital properties of the pre-galactic fragments which merge to form the final stable disk. The properties of the thin and thick disks are then set by the kinematics and gas mass fractions of the pre-galactic fragments when they merge.

Within this scenario, we now discuss the implications of three significant properties of thick disks uncovered by our data: first, that thick disks are a ubiquitous and necessary component in modeling late-type edge-on galaxies; second, that the stellar mass of the thick disk is increasingly dominant in lower mass galaxies; and third, that thick disks have systematically larger radial scale lengths than thin disks.

The Ubiquity of Thick Disks

The 2-D fits of our sample confirm the initial suggestion of Dalcanton & Bernstein (2002) that thick disks are a ubiquitous component of disk galaxies. Essentially all

(32 of 34) of the galaxies which were suitable for fitting were statistically significantly better fit by a second disk component (e.g. Figure 2.7). This result adds to the published detections of thick disks in earlier type systems (summarized in Table 2.2). Thick disks are now routinely discovered in every galaxy that has been searched for them².

The evidence therefore supports the idea that thick disks are a generic property of all galaxies with disks, from S0's to Sm's, from high masses ($V_c \sim 250 \text{ km s}^{-1}$) to low ($V_c \sim 50 \text{ km s}^{-1}$). Thick disks must therefore be a natural by-product of disk galaxy formation, independent of the formation of a bulge. The ubiquity of thick disks can be easily explained if most thick disk stars are directly accreted from pre-galactic fragments. As we argue above, if *any* star formation has taken place in the fragments, some fraction of those stars must wind up in a thick disk. The only way to avoid depositing the stars in a thick disk would be if the fragments were completely tidally disrupted at large distances from the central galaxies. However, at large distances the matter density should be much lower than in the dense cores of the low mass galactic fragments, making it unlikely that every merging satellite would experience complete disruption.

The existence of widespread thick disks also suggests that there has been ample star formation in the very low mass halos which merge together to form larger galaxies. Most sub-units must have established stellar populations before merging. If instead the sub-units were entirely gaseous, disk galaxies would have only a thin disk component. Thus, there cannot have been total suppression of star formation by reionization up until the epoch of thick disk formation.

Finally, the pervasiveness of thick disks also presents an additional problem for

²A possible exception is NGC 4244, which Fry et al. (1999) analyzed using fits to 1-D cuts of the vertical R -band light distribution. Based on the lack of a clear break in the vertical surface brightness profile, Fry et al. (1999) claimed there was no thick disk in this galaxy. However, subsequent analyses of the resolved stellar population in NGC 4244 by Seth et al. (2005b) and Tikhonov et al. (2005) revealed the presence of a clear extra-planar population dominated by old red giant branch stars, whose global distribution was characteristic of a thick disk.

merger heating scenarios. It seems unlikely that every galaxy in our sample would have had both a merger that created a thick disk and accretion that reformed a thin disk. If merger heating was the primary driver of thick disk formation we would expect to find some galaxies that were able to avoid a destructive merger, or that failed to subsequently reform a thin disk. Instead, all of our galaxies require both thin and thick disk components.

The Increasing Importance of Thick Disks in Lower Mass Galaxies

In the merging picture we have adopted, sub-galactic fragments contribute both stars and gas to the final galaxy. The stars wind up in the thick disk, and the gas settles into the thin disk, where it gradually converts into stars. From Figure 2.24 we see that low mass disk galaxies have roughly 25% of their baryonic mass locked up into thick disk stars, while massive galaxies have only 10%. Figure 2.24 therefore implies a systematic variation in the gas richness of sub-galactic fragments at the time disks coalesce. In massive late-type galaxies, 90% of the baryonic mass must have remained gaseous during disk assembly, while in low mass galaxies only 75% had not yet converted to stars.

Note that while we are stressing the accretion of stellar material to form the thick disk, our results prove that the vast majority (75-90%) of baryonic accretion must have been gaseous. If some fraction of thick disk stars did form *in situ* as suggested by Brook, then the fraction of gaseous accretion must have been even higher.

There are several ways that lower gas mass fractions in the precursors of low mass galaxies may be achieved. One possibility is that the transformation of gas into stars proceeded further by the time the low mass disk galaxies coalesced. This more complete transformation in low mass disks could be due either to a later epoch of assembly, or to higher gas densities and thus higher star formation rates in the precursor clumps. However, in a closed box model, the resulting thick disk stars would have higher metallicities. In contrast, the estimates of the metallicities of

extra-planar, RGB stars in Seth et al. (2005b) suggest that the metallicities of the thick disk stars are systematically lower in lower mass galaxies, compared to the Milky Way. We therefore rule out the possibility that star formation was more “complete” in the precursors of lower mass galaxies.

Supernova feedback is an alternative pathway to the preponderance of less gas rich sub-units in low mass galaxies. Much of the disk material was initially in several subunits that were necessarily of lower mass than the final galaxy. Thus, the merging fragments must have had lower escape velocities, allowing supernova-driven winds to more effectively drive gas and metals from the galaxy at this early stage. The increased efficiency of SN winds in the sub-units would simultaneously decrease the gas mass fractions and maintain low metallicities in thick disk stars in low mass galaxies³.

We can estimate the amount of gas loss needed to produce the observed trends as follows. First, we assume that the observed baryon fraction in the stellar thin disk and gas component of massive galaxies ($\sim 90\%$, Figure 2.24) is indicative of the gas to stellar mass fraction in subgalactic fragments that are too massive to experience significant SN blowout. We then assume that the precursors of lower mass galaxies lose enough gas to bring their gas to stellar mass fraction down to $\sim 75\%$ at the time of disk assembly. These simple assumptions imply that the sub-units of low mass galaxies must have lost 60% of their initial baryonic mass.

Because we have ignored possible tidal stripping of stars during galaxy assembly, the actual amount of gas lost from the precursors of low mass disks may be different from what we have estimated above. However, assuming that tidally stripped stars wind up in a stellar halo, we expect the total stellar mass lost to stripping to be small.

³Note, however, that the overall gas mass fraction of low mass galaxies can remain high to the present day. The disks of lower mass galaxies have systematically lower baryon surface densities (e.g., Swaters et al., 2002; Hunter & Elmegreen, 2004), and thus are inefficient at converting gas into stars. Their low star formation rate thus allows them to have higher gas mass fractions today, even though they were comparatively gas poor at the time their disks were assembled.

The Milky Way’s thick disk contains a factor of ~ 10 times more stars than its stellar halo, and thus, any correction due to tidal stripping is likely to be negligible.

While our mass-dependent blowout scenario explains our data well, it is not clear that pre-galactic fragments actually suffer $\sim 60\%$ baryon losses due to SN winds. There are a wide range of results on how effective SN winds should be at driving baryon outflow. At the one extreme, several groups argue that large SN driven outflows exist in all galaxies with $V_c < 100 \text{ km s}^{-1}$ (Dekel & Silk, 1986; Dekel & Woo, 2003). At the the other extreme, simulations find that galaxies with $M > 10^6 M_\odot$ experience almost no outflow (Mac Low & Ferrara, 1999). Similarly, observational constraints on the extent of outflow vary. Mayer & Moore (2004) use the baryonic Tully-Fisher relation to claim that dwarf galaxies do not suffer large removal of baryons while Strickland et al. (2004) observe x-ray halos around massive star forming galaxies ($M \sim 10^{10} - 10^{11} M_\odot$) which suggest they must have ejected at least some material. Because we are considering the role of blowout in low mass progenitors of our galaxy sample, we claim that the current knowledge of gas blowout is moderately consistent with our scenario and we await a more definitive cosmological simulation which incorporates star formation and feedback for detailed comparison to our model (Stinson et al., 2006).

There are several limitations with the simplified analysis we have presented above. First, we have ignored the difficult question of how much material is accreted in continuous cold flows rather than bound in halos (Birnboim & Dekel, 2003; Keres et al., 2004). Cold accretion of gas will tend to increase the baryonic fraction of the thin disk. Neglecting steady gas accretion therefore leads us to overestimate the gas richness of the merging pre-galactic fragments. Second, we have not explicitly considered how bulges are formed in the scenario discussed in §2.6.1, but we presume it involves repeated mergers of gas rich sub-units with little net angular momentum, or a higher frequency of major mergers in higher mass galaxies. Within the sample we have studies here, this omission is acceptable. However, more theoretical and

observational work must be done to understand the thick disk population in earlier type galaxies.

Finally, we find it difficult to reconcile the Brook et al. (2004) formation scenario with the increasing fraction of thick disk stars in lower mass galaxies. Brook et al. (2004) suggest that thick disk stars form *in situ* from high velocity dispersion gas during the coalescence of sub-galactic fragments into a final disk. However, we see no obvious mechanism that could lead this scenario to produce a larger fraction of thick disk stars in low mass galaxies. One would need to invoke a mechanism to increase the efficiency of star formation at lower galaxy masses during mergers, while keeping star formation inefficient at later times. An alternative solution would be if steady cold flow gas accretion is more important in massive galaxies. However, massive galaxies are more likely to have established a hot shock-heated halo that would block cold flow (e.g., Dekel & Birnboim, 2004). Thus, the likely behavior of cold flow accretion has the opposite sign as what is needed to explain the high baryonic fraction of thick disks in low mass galaxies. Further simulations will help constrain this and other possible solutions.

The Scale Lengths of Thick & Thin Disks

Our data contribute to a growing number of observations finding that thick disks have larger scale lengths than their embedded thin disks (Ojha, 2001; Larsen & Humphreys, 2003; Wu et al., 2002; Pohlen et al., 2004, see our Figure 2.13, and Table 2.2). The large scale lengths of thick disks argue against their being formed via vertical heating of a thin disk. N-body simulations find that while minor mergers can vertically heat a disk, they do not increase its scale length (Quinn et al., 1993). Such mergers also tend to leave the galaxy looking like an earlier Hubble type (Walker et al., 1996) while all of our galaxies have no prominent bulge components. As an example, simulations by Aguerri et al. (2001) find that minor mergers can extend the scale length of the thin disk somewhat, by 10-60%. However, the same simulations also produce a large

bulge, which is incompatible with our sample.

In contrast, in the accretion scenario one would expect the scale length of the thin disk to be somewhat smaller than that of the thick disk. If the thin disk forms later from gas which has contracted further than the thick disk stars, it should have a smaller scale length. If angular momentum is largely conserved, then the thin disk should also be rotating somewhat faster than the thick disk because of its extra contraction.

The satellite accretion model therefore suggests that there may be correlations between the radial scale lengths and the kinematics of the thick and thin disks. Results in Section 2.5.4 and photometric decompositions by others (Ojha, 2001; Larsen & Humphreys, 2003; Wu et al., 2002; Pohlen et al., 2004) suggest that scale lengths of thick disks are roughly 30% longer than those of their embedded thin disks, on average. Simple angular momentum conservation would then suggest that the thick disk should rotate with approximately $2/3$ the speed of the thin disk, in rough agreement with the Milky Way and FGC 1415 (Yoachim & Dalcanton, 2005). However, the inclusion of any counter-rotating material in the merger could easily break this correlation. For example, the kinematics of FGC 227 indicate that the satellites which contributed the majority of the baryons to the thin disk could not also have deposited the majority of the thick disk stars. This particular formation pathway allows the scale lengths of the thick and thin disks to sometimes decouple, and indeed, the scale lengths of FGC 227's thick disk is comparable to, not larger than, its thin disk.

The structural parameters of the thick disks formed in the Abadi et al. (2003b) and Brook et al. (2004, 2005) simulations are in moderate agreement with our results. However, direct comparisons are difficult because the simulated galaxies tend to be more massive than the galaxies in our sample and also host large bulge components. The simulated thick disks do seem to match the observed trends of scale height ratios (Figure 2.11) and luminosity ratios (Figure 2.19). However, the scale length ratio found in the Brook et al. (2005) simulation is fairly low (Figure 2.15), possibly due to

the fact that their thick disk stars are formed directly from the gas during mergers, increasing the likelihood that the thick and thin disk stars will share similar scale lengths and kinematics. It is also difficult to compare our 2-d decompositions with analysis of simulations that can separate stellar populations based on kinematics.

2.6.3 Further Implications

Given the excellent fit to the body of data on thick disks, we now begin to address other implications of the accretion scenario developed above.

Old Low Mass Galaxies

In hierarchical galaxy formation models, small scale structure collapses first, suggesting that low mass galaxies should be old. This expectation is in direct conflict with observations that low mass galaxies almost always have blue colors consistent with young stellar populations. This difference is one of the most intractable failings of the predictions of semi-analytic models (e.g. Bell et al., 2003a; van den Bosch, 2002). The existence of thick disks that dominate the stellar mass of low mass galaxies (Figure 2.22) solves this conundrum. Our observations show that low mass galaxies are indeed *dominated* by an old stellar population, but one that is sufficiently old, faint, and diffuse that it has no significant impact on the observed colors of the young, high-surface brightness, star-forming thin disk (§2.5.4). We believe that semi-analytic models could be brought into alignment with the data if they were to include both the locking up of material into a diffuse thick disk and the suppression of star formation efficiencies in low mass disks due to their lying entirely below the Kennicutt star formation threshold (e.g., Verde et al., 2002; Dalcanton et al., 2004).

Abundance patterns and the timing of thick and thin disk formation

Studies of α -element abundances of the Milky Way have suggested that star formation in the thick disk took place over several gigayears (e.g., Bensby et al., 2004b). The abundances in thick disk stars show a flat plateau at high $[\alpha/\text{Fe}]$ that extends to $[\text{Fe}/\text{H}] \sim -0.3$, indicating that thick disk stars enriched quickly to relatively high metallicity, before Type Ia supernovae became prevalent. At larger iron abundances ($-0.3 < [\text{Fe}/\text{H}] \lesssim 0$), however, the α abundance declines linearly, suggesting that star formation in the thick disk was sufficiently extended ($\gtrsim 1 - 3$ Gyr) that enrichment from Type Ia's became important. The abundances of thin disk stars show similar, parallel behavior, but the plateau does not extend to equally high metallicities, indicating that early star formation in the thin disk was not nearly as rapid as in the thick disk. The abundance patterns of thick and thin disk stars therefore follow parallel but distinct sequences on the $[\alpha/\text{Fe}]$ vs $[\text{Fe}/\text{H}]$ plane, with significant overlap in $[\text{Fe}/\text{H}]$ (most recently Bensby et al., 2004a; Mishenina et al., 2004; Gratton et al., 2003).

The above sequence of events is typically taken as evidence that the thick disk formed from violent heating of a previous thinner disk. However, it may be possible to accommodate the abundance data in the accretion scenario as well. First, the rapid enrichment of future thick disk stars can easily occur in the pre-galactic fragments. These mini-halos should be dense, leading to high gas densities and star formation rates, which would produce the necessary fast enrichment. While we have hypothesized above that supernova-driven winds will truncate star formation in the lower mass progenitors, some mini-halos will have sufficient mass to retain gas for longer periods of time, allowing stars to form over sufficiently long timescales to produce both the drop in $[\alpha/\text{Fe}]$ and the enrichment of some thick disk stars to near solar metallicities.

The expected timescales for this scenario are compatible with the observational constraints. Theory suggests that the epoch of thick disk assembly should correspond

to the period of rapid mass accretion seen in simulations at $z \gtrsim 3$, or $t_{lookback} \gtrsim 11$ Gyr (e.g., Zhao et al., 2003). Observationally, the relative abundance of [Eu/Ba] indicates that thick disk stars were formed on a timescale of 1-1.5 Gyr (Mashonkina et al., 2003), which makes the theoretical expectation consistent with the age of the universe determined from WMAP.

In addition to the short star formation timescale for thick disk stars, the accretion scenario can produce a long timescale for formation of thin disk stars. After the pre-galactic fragments merge into a disk, the gas that forms the thin disk gradually converts into stars. The timescale of this conversion is controlled primarily by the gas surface density. In general, this timescale should be much longer in the disk than in the pre-galactic fragments, because the gas is spread over much larger areas, leading to lower gas densities and longer star formation timescales. The difference in timescales for thick and thin disk star formation could lead to the appearance of a “delay” between the formation of the two components. However, as accretion of both gas and stars would be on-going from early times until $z \sim 3$, some genuinely old thin disk stars would be allowed to form (see discussion in Abadi et al., 2003b).

The accretion scenario also provides a mechanism for producing thin disk stars with lower α -abundances than thick disks stars at the same metallicity. Because the thin disk assembles from gas that had not been consumed by star formation in pre-galactic fragments, it is possible for the gas to initially have lower mean metallicity than the thick disk stars that were accreted. The gas may come from larger radii within individual mini-halos, and thus be less enriched. It may also come from fragments that have never formed stars, or from cold flow accretion directly. Thus, accretion may allow thin disk stars to be sufficiently metal-poor that they overlap the metallicities of thick disk stars.

The one significant trouble spot is the thinness of the observed $[\alpha/\text{Fe}]$ vs $[\text{Fe}/\text{H}]$ relation for thick disk stars. If the thick disk formed from assembly of many different sub-units of different masses, lifetimes, and gas richnesses, then one might expect

large variations in the degree of α -enhancement in the accreted stars. On the other hand, the potential discrepancy might not be as severe as one might initially believe. If supernova-driven winds truncate star formation in low mass sub-units, then only the most massive mini-halos contribute stars to the high metallicity ($[\text{Fe}/\text{H}] \gtrsim -0.3$) thick disk, since they are the only precursors that could hold gas long enough to allow significant Type Ia enrichment. Massive halos are rarer than low mass halos, and thus a relatively small number of halos may dominate the metal rich end of the thick disk population, much in the way that L_* galaxies dominate the luminosity density of the local universe. These disrupted satellites may also segregate to different radii, as seen in the Abadi et al. (2003b) simulations, such that a sample at the solar circle is dominated by an even smaller number of massive satellites. More detailed simulations are needed to evaluate the size of this possible discrepancy.

Pre-Enrichment of Thin Disks

Chemical abundance data on stars within the Milky Way has led to the conclusion that the thin disk may have been “pre-enriched” (e.g., Caimmi, 2000; Chiappini et al., 1997; Pagel & Tautvaisiene, 1995). Such pre-enrichment naturally explains the lack of truly metal poor stars in the thin disk as well as the under-abundance of more moderately metal-poor stars (i.e. the “G-Dwarf” problem). In the scenario we have explored here, the gas from which thin disk stars form was originally associated with the thick disk, and thus will have been enriched while still in pre-galactic fragments. While this idea has been suggested before (e.g., Brook et al., 2005), the universality of thick disks suggests that it is probably a wide-spread phenomena.

Producing the Mass-Metallicity Relationship in Disks

Another attractive feature of the satellite accretion model is that it facilitates creating the mass-metallicity relationship in disks. Many authors have argued that the lower metallicities and effective yields seen in low mass galaxies is due to the onset of

supernova-driven winds at the mass scale where the metallicity begins to fall ($V_c \sim 120$ km s⁻¹, or $M_{\text{baryon}} < 3 \times 10^{10} M_{\odot}$; e.g. Garnett, 2002; Tremonti et al., 2004; Dekel & Woo, 2003; Kauffmann et al., 2003b). However, simulations of gas outflow find that it is quite difficult to drive coherent winds at these masses (Ferrara & Tolstoy, 2000), particularly given the low star formation rates typical of low mass disks (e.g. Hunter & Elmegreen, 2004).

As an alternative, the satellite accretion model suggests that non-negligible star formation took place in lower mass sub-units. These pre-galactic fragments had much lower escape velocities, and probably had higher gas surface densities due to not yet being organized into a coherent rotating disk. Thus, the sub-units are a more natural environment for driving winds, given their low escape velocities and likely high star formation rates. The origin of the observed mass-metallicity relation may therefore lie not so much in the disks themselves, but in the sub-units from which they assembled.

2.7 Conclusions

We fit thin and thick disk components to a sample of 34 late-type edge-on spiral galaxies. Our thick disk components are very similar to previously detected thick disk systems and the MW thick disk, suggesting they are a remnant stellar population left over from early stages of galaxy formation. In lower mass galaxies ($V_c < 100$ km s⁻¹), the thick disk is the dominant component in both luminosity and stellar mass. For higher mass galaxies, the thick disk is a minor component, and is analogous to the thick disks found in the Milky Way and other higher mass galaxies. In particular, we find:

- Thick disks have a scale height ~ 2 times larger than thin disks
- Thick disks have systematically larger scale lengths than thin disks
- In low mass galaxies, the thick disk can dominate the total R -band luminosity

- The thick disk comprises 5-40% of the total baryonic mass of our galaxies

We combine these results with the findings of other studies of thick disks to analyze possible thick disk formation scenarios. In particular, we include results from thick disk kinematics (Yoachim & Dalcanton, 2005), studies of resolved stellar populations in thick disks (Seth et al., 2005a; Mould, 2005), and simulations which form thick disks (Brook et al., 2004, 2005; Abadi et al., 2003b). Overall, we find that models where the thick disk forms from a kinematically heated thin disk is not supported by the data. Instead, our results favor models where thick disk stars formed in galactic sub-units before merging to create the final galaxy.

We consider a hierarchical galaxy formation scenario where galaxies form through a series of mergers where sub-units deposit both stars and gas. Any stellar component in the sub-units end up in the thick disk, while gas cools and forms a thin disk. We find that the low mass galaxies in our sample must have formed from sub-units that had a higher stellar mass fraction than those that formed higher mass galaxies. We can explain this result if low mass sub-units (which go on to form low mass galaxies) are more susceptible to SN-induced blowout, leaving them with a higher stellar to gas mass fraction. A mass-dependent blowout scenario is consistent with other general observations of disk galaxies, such as the mass-metallicity relation and the chemical pre-enrichment of the MW thin disk.

Table 2.3. Single disk fits for the sample galaxies.

FGC	Adopted Distance ¹ Mpc	<i>B</i>			<i>R</i>			<i>K_s</i>		
		$\mu(0,0)$ (mag/□′′)	h_r ('')	z_0 ('')	$\mu(0,0)$ (mag/□′′)	h_r ('')	z_0 ('')	$\mu(0,0)$ (mag/□′′)	h_r ('')	z_0 ('')
31	51.9	22.67 ^{-0.01} _{0.14}	10.1 ^{0.62} _{-0.61}	1.96 ^{0.05} _{-0.10}	21.93 ^{-0.03} _{0.15}	8.9 ^{1.05} _{-0.20}	2.06 ^{0.05} _{-0.13}	20.01 ^{-0.01} _{0.19}	6.9 ^{1.35} _{-0.00}	1.95 ^{0.21} _{-0.05}
36	80.9	22.33 ^{-0.09} _{0.03}	8.5 ^{1.10} _{-0.37}	1.71 ^{0.07} _{-0.04}	21.06 ^{-0.07} _{0.12}	7.4 ^{0.74} _{-0.41}	1.73 ^{0.12} _{-0.08}	18.51 ^{-0.02} _{0.15}	6.8 ^{0.93} _{-0.06}	1.64 ^{0.08} _{-0.06}
130	233.1	22.67 ^{-0.03} _{0.09}	9.4 ^{1.95} _{-0.12}	1.63 ^{0.04} _{-0.00}	21.15 ^{0.00} _{-0.10}	8.4 ^{1.40} _{-0.07}	1.71 ^{0.07} _{-0.04}	17.17 ^{0.16} _{-0.19}	6.5 ^{0.50} _{-0.19}	1.27 ^{0.05} _{-0.06}
164	69.9	22.88 ^{-0.03} _{0.37}	10.7 ^{0.57} _{-0.28}	1.63 ^{0.30} _{-0.12}	22.24 ^{-0.07} _{0.32}	9.8 ^{0.61} _{-0.17}	1.86 ^{0.32} _{-0.16}	20.38 ^{-0.02} _{0.01}	8.6 ^{0.42} _{-0.31}	1.87 ^{0.02} _{-0.07}
215	131.1	22.46 ^{-0.01} _{0.08}	12.8 ^{1.81} _{-0.33}	1.71 ^{0.04} _{-0.02}	21.21 ^{-0.04} _{0.16}	11.4 ^{0.52} _{-0.63}	1.64 ^{0.11} _{-0.08}	17.93 ^{-0.10} _{0.12}	7.4 ^{1.36} _{-0.91}	1.23 ^{0.01} _{-0.03}
225	74.3	22.29 ^{-0.05} _{0.02}	8.9 ^{0.24} _{-0.72}	2.41 ^{0.02} _{-0.07}	21.31 ^{-0.02} _{0.11}	8.2 ^{0.05} _{-0.61}	2.40 ^{0.07} _{-0.12}	19.28 ^{-0.02} _{0.18}	7.7 ^{1.30} _{-0.03}	2.60 ^{0.17} _{-0.13}
227	89.4	22.52 ^{-0.02} _{0.12}	11.2 ^{2.39} _{-0.21}	2.00 ^{0.02} _{-0.01}	21.21 ^{-0.06} _{0.02}	10.2 ^{1.29} _{-0.10}	2.05 ^{0.05} _{-0.02}	18.48 ^{-0.07} _{0.20}	9.1 ^{1.03} _{-0.42}	2.01 ^{0.16} _{-0.12}
277	84.9	23.14 ^{-0.01} _{0.21}	9.6 ^{0.33} _{-0.14}	2.08 ^{0.22} _{-0.09}	21.75 ^{-0.05} _{0.28}	8.7 ^{0.45} _{-0.06}	2.24 ^{0.30} _{-0.17}	19.02 ^{-0.08} _{0.28}	7.5 ^{1.07} _{-0.38}	2.02 ^{0.31} _{-0.17}
310	80.8	22.79 ^{-0.04} _{0.08}	9.9 ^{0.71} _{-0.23}	1.91 ^{0.10} _{-0.04}	21.19 ^{-0.01} _{0.14}	8.7 ^{0.63} _{-0.29}	1.95 ^{0.11} _{-0.08}	18.20 ^{-0.10} _{0.28}	7.3 ^{1.42} _{-0.62}	1.70 ^{0.17} _{-0.13}
349	117.6	22.21 ^{-0.06} _{0.08}	8.2 ^{0.64} _{-0.46}	1.63 ^{0.07} _{-0.04}	21.09 ^{-0.05} _{0.14}	7.5 ^{0.55} _{-0.34}	1.71 ^{0.11} _{-0.07}	18.68 ^{-0.02} _{0.21}	6.9 ^{0.50} _{-0.06}	1.75 ^{0.18} _{-0.09}
395	109.3	22.95 ^{-0.04} _{0.06}	12.4 ^{1.93} _{-0.09}	1.67 ^{0.05} _{-0.02}	21.46 ^{-0.05} _{0.03}	10.6 ^{1.61} _{-0.02}	1.74 ^{0.03} _{-0.02}	18.18 ^{-0.11} _{0.12}	8.4 ^{0.48} _{-1.06}	1.42 ^{0.07} _{-0.06}
436	109.2	22.58 ^{-0.00} _{0.09}	9.8 ^{0.59} _{-0.00}	2.11 ^{0.10} _{-0.02}	21.06 ^{-0.02} _{0.23}	7.9 ^{0.37} _{-0.16}	2.11 ^{0.20} _{-0.12}	17.71 ^{-0.14} _{0.25}	5.6 ^{0.73} _{-0.60}	1.55 ^{0.14} _{-0.15}
446	88.2	22.43 ^{-0.10} _{0.10}	18.3 ^{2.68} _{-0.57}	3.14 ^{0.09} _{-0.09}	20.74 ^{-0.08} _{0.08}	14.7 ^{-0.13} _{-0.08}	3.03 ^{0.08} _{-0.08}	16.64 ^{-0.15} _{0.39}	10.0 ^{1.81} _{-0.72}	1.89 ^{0.27} _{-0.26}
780	34.4	22.22 ^{-0.03} _{0.41}	15.7 ^{1.08} _{-0.94}	4.34 ^{0.81} _{-0.61}	21.41 ^{-0.05} _{0.40}	15.1 ^{0.48} _{-0.95}	4.96 ^{0.88} _{-0.72}	19.28 ^{-0.00} _{0.02}	14.7 ^{0.86} _{-0.01}	3.95 ^{0.01} _{-0.04}
901	131.2	22.30 ^{-0.10} _{0.09}	8.0 ^{1.16} _{-0.48}	1.72 ^{0.11} _{-0.07}	21.10 ^{-0.04} _{0.22}	7.9 ^{0.88} _{-0.71}	1.71 ^{0.15} _{-0.12}	18.71 ^{-0.03} _{0.05}	7.0 ^{0.44} _{-0.29}	1.52 ^{0.02} _{-0.03}
913	62.5	21.98 ^{-0.08} _{0.17}	9.7 ^{1.02} _{-0.60}	1.60 ^{0.14} _{-0.09}	21.04 ^{-0.08} _{0.17}	9.0 ^{0.81} _{-0.60}	1.73 ^{0.14} _{-0.10}	18.91 ^{-0.05} _{0.03}	9.3 ^{0.39} _{-0.03}	1.86 ^{0.02} _{-0.07}
979	52.0	21.35 ^{-0.10} _{0.15}	13.0 ^{2.57} _{-0.18}	2.84 ^{0.26} _{-0.24}	20.27 ^{-0.08} _{0.13}	12.1 ^{2.18} _{-0.27}	3.03 ^{0.23} _{-0.23}	17.51 ^{-0.06} _{0.29}	11.1 ^{1.52} _{-0.01}	2.53 ^{0.32} _{-0.22}
1043	50.1	21.94 ^{-0.05} _{0.08}	20.7 ^{3.01} _{-2.28}	3.38 ^{0.20} _{-0.14}	20.59 ^{-0.03} _{0.14}	16.9 ^{0.38} _{-1.07}	3.43 ^{0.31} _{-0.17}	16.91 ^{-0.22} _{0.39}	10.6 ^{1.22} _{-1.88}	2.23 ^{0.36} _{-0.36}
1063	56.4	22.08 ^{-0.01} _{0.12}	7.8 ^{0.53} _{-0.23}	2.21 ^{0.05} _{-0.10}	21.19 ^{-0.03} _{0.16}	7.0 ^{0.51} _{-0.17}	2.22 ^{0.10} _{-0.12}	19.17 ^{-0.02} _{0.07}	7.4 ^{1.50} _{-0.02}	2.18 ^{0.01} _{-0.10}
1285	18.8	21.99 ^{-0.06} _{0.25}	22.6 ^{1.20} _{-0.53}	6.05 ^{0.55} _{-0.63}	20.99 ^{-0.11} _{0.26}	19.7 ^{1.74} _{-0.71}	6.63 ^{0.61} _{-0.75}	18.59 ^{-0.11} _{0.09}	15.8 ^{0.10} _{-2.31}	5.15 ^{0.29} _{-0.23}
1303	51.7	22.57 ^{-0.02} _{0.34}	9.2 ^{0.83} _{-0.35}	2.32 ^{0.35} _{-0.24}	21.70 ^{-0.02} _{0.28}	8.5 ^{0.67} _{-0.40}	2.50 ^{0.30} _{-0.24}	19.55 ^{-0.02} _{0.11}	5.8 ^{1.17} _{-0.06}	2.56 ^{0.18} _{-0.10}
1415	38.3	21.79 ^{-0.04} _{0.31}	19.1 ^{1.88} _{-0.73}	3.84 ^{0.56} _{-0.40}	20.83 ^{-0.05} _{0.37}	18.3 ^{0.39} _{-1.18}	4.27 ^{0.69} _{-0.54}	18.34 ^{-0.01} _{0.18}	15.3 ^{1.43} _{-0.00}	3.21 ^{0.29} _{-0.15}

Table 2.3—Continued

FGC	Adopted Distance ¹ Mpc	<i>B</i>			<i>R</i>			<i>K_s</i>		
		$\mu(0,0)$ (mag/□′′)	h_r (′′)	z_0 (′′)	$\mu(0,0)$ (mag/□′′)	h_r (′′)	z_0 (′′)	$\mu(0,0)$ (mag/□′′)	h_r (′′)	z_0 (′′)
1440	70.9	22.04 ^{-0.07} _{0.02}	19.7 ^{2.05} _{-1.36}	2.74 ^{0.15} _{-0.10}	20.54 ^{-0.05} _{0.20}	15.9 ^{0.86} _{-0.15}	2.78 ^{0.22} _{-0.23}	16.81 ^{-0.12} _{0.26}	10.2 ^{1.61} _{-1.00}	1.83 ^{0.15} _{-0.15}
1642	36.6	22.60 ^{-0.04} _{0.10}	12.2 ^{1.16} _{-0.85}	3.04 ^{0.12} _{-0.13}	21.76 ^{-0.01} _{0.24}	12.5 ^{1.32} _{-0.14}	3.53 ^{0.33} _{-0.26}	19.94 ^{-0.07} _{0.04}	18.5 ^{5.02} _{-5.11}	3.14 ^{0.05} _{-0.08}
1948	36.9	22.67 ^{-0.03} _{0.27}	13.1 ^{0.40} _{-0.87}	2.70 ^{0.27} _{-0.26}	21.86 ^{-0.04} _{0.22}	12.3 ^{0.51} _{-0.44}	2.98 ^{0.24} _{-0.25}	19.76 ^{-0.10} _{0.00}	8.7 ^{0.06} _{-2.92}	2.31 ^{0.01} _{-0.00}
2131	41.7	22.51 ^{-0.08} _{0.08}	10.7 ^{1.53} _{-0.33}	3.15 ^{0.18} _{-0.13}	21.30 ^{-0.05} _{0.10}	10.0 ^{1.06} _{-0.32}	3.46 ^{0.18} _{-0.16}	18.62 ^{-0.00} _{0.05}	8.9 ^{0.28} _{-0.03}	3.06 ^{0.10} _{-0.03}
2135	125.3	22.31 ^{-0.04} _{0.06}	7.6 ^{1.00} _{-0.29}	1.67 ^{0.00} _{-0.02}	21.06 ^{-0.06} _{0.15}	6.9 ^{0.67} _{-0.23}	1.73 ^{0.08} _{-0.09}	18.08 ^{-0.05} _{0.14}	4.8 ^{0.28} _{-0.20}	1.51 ^{0.09} _{-0.06}
2369	59.8	22.75 ^{-0.07} _{0.17}	8.8 ^{1.11} _{-0.34}	1.90 ^{0.21} _{-0.12}	21.81 ^{-0.03} _{0.30}	8.7 ^{0.62} _{-0.50}	2.14 ^{0.32} _{-0.16}	19.80 ^{-0.02} _{0.06}	9.5 ^{1.27} _{-0.21}	2.09 ^{0.04} _{-0.04}
2548	55.6	22.75 ^{-0.05} _{0.23}	10.7 ^{1.54} _{-0.03}	2.17 ^{0.30} _{-0.15}	21.65 ^{-0.02} _{0.24}	9.9 ^{0.87} _{-0.05}	2.43 ^{0.29} _{-0.19}	19.39 ^{-0.00} _{0.19}	9.6 ^{0.76} _{-0.01}	2.51 ^{0.27} _{-0.09}
2558	73.8	22.29 ^{-0.03} _{0.07}	9.8 ^{1.27} _{-0.64}	3.06 ^{0.03} _{-0.14}	21.27 ^{-0.02} _{0.18}	9.2 ^{1.00} _{-0.44}	3.15 ^{0.14} _{-0.24}	19.05 ^{-0.05} _{0.13}	9.1 ^{1.41} _{-0.45}	2.82 ^{0.13} _{-0.12}
E1371	82.6	23.02 ^{-0.10} _{0.14}	8.7 ^{1.51} _{-1.07}	2.12 ^{0.08} _{-0.02}	21.12 ^{-0.02} _{0.10}	7.7 ^{1.04} _{-0.44}	2.07 ^{0.03} _{-0.04}	17.06 ^{-0.02} _{0.19}	6.8 ^{0.19} _{-0.25}	1.47 ^{0.12} _{-0.09}
E1404	76.2	22.60 ^{-0.04} _{0.06}	8.9 ^{0.67} _{-0.53}	1.58 ^{0.03} _{-0.03}	21.36 ^{-0.05} _{0.23}	7.8 ^{0.68} _{-0.12}	1.64 ^{0.12} _{-0.10}	18.76 ^{-0.12} _{0.18}	7.0 ^{0.54} _{-0.84}	1.64 ^{0.13} _{-0.11}
E1498	135.5	22.48 ^{-0.10} _{0.04}	8.3 ^{1.89} _{-0.21}	1.48 ^{0.10} _{-0.02}	21.03 ^{-0.12} _{0.01}	7.6 ^{1.51} _{-0.05}	1.51 ^{0.09} _{-0.04}	17.50 ^{-0.01} _{0.32}	6.7 ^{0.38} _{-0.35}	1.11 ^{0.14} _{-0.07}
E1623	261.1	22.70 ^{-0.04} _{0.08}	7.9 ^{0.85} _{-0.08}	1.35 ^{0.03} _{-0.02}	21.07 ^{-0.01} _{0.10}	6.4 ^{0.18} _{-0.07}	1.25 ^{0.05} _{-0.04}	17.37 ^{-0.08} _{0.17}	4.5 ^{0.28} _{-0.20}	0.96 ^{0.06} _{-0.07}

¹ These fits use Equations 2.2 and 2.3 with $N = 1$ (i.e. a sech^2 vertical profile). Peak edge-on surface brightnesses have not been corrected for inclination. When available, distances taken from Karachentsev et al. (2000a). Otherwise, we have used the recessional velocity corrected for Local Group infall to the Virgo cluster (LEDA). Throughout, we assume $H_0 = 70 \text{ km s}^{-1} \text{ Mpc}^{-1}$.

Table 2.4. Vertical light profiles for the two disk models used in fitting R -band structural parameters.

Thin disk model	Thick disk model	Notes
$\text{sech}^2(z/z_0)$	$\text{sech}^2(z/z_0)$	convolved w/1'' FWHM Gaussian midplane masked
$\text{sech}^2(z/z_0)$	$\text{sech}^2(z/z_0)$	
$\text{sech}^2(z/z_0)$	$\text{sech}^2(z/z_0)$	
$\text{sech}(z/z_0)$	$\text{sech}^2(z/z_0)$	
$\text{sech}^2(z/z_0)$	$\text{sech}(z/z_0)$	
$\text{sech}(z/z_0)$	$\text{sech}(z/z_0)$	

Table 2.5. Two disk fits to R -band images. the best values found for each disk having a sech^2 vertical profile. The listed values are medians with uncertainties indicating the full range of convergent fits.

FGC	Thin Disk			Thick Disk			L_{thick}/L_{thin}	n converged
	$\mu(0,0)$ (mag/ \square'')	h_r ($''$)	z_0 ($''$)	$\mu(0,0)$ (mag/ \square'')	h_r ($''$)	z_0 ($''$)		
31	22.0 ^{+0.40} _{-0.03}	8.0 ^{+0.7} _{-4.2}	1.7 ^{+0.0} _{-0.9}	23.8 ^{+0.57} _{-1.60}	11.8 ^{+0.1} _{-0.6}	2.9 ^{+0.6} _{-0.8}	0.40 ^{+0.00} _{-0.16}	3
36	22.2 ^{+0.53} _{-0.21}	6.8 ^{+0.1} _{-0.5}	1.0 ^{+0.5} _{-0.3}	21.4 ^{+0.13} _{-0.13}	7.4 ^{+0.0} _{-0.1}	1.9 ^{+0.0} _{-0.1}	4.20 ^{+1.71} _{-3.46}	4
130	21.1 ^{+0.92} _{-0.03}	8.6 ^{+0.4} _{-0.2}	1.6 ^{+0.4} _{-0.2}	24.1 ^{+0.68} _{-1.31}	9.5 ^{+1.1} _{-1.0}	3.9 ^{+1.1} _{-1.8}	0.25 ^{+0.08} _{-0.14}	5
164	22.4 ^{+0.63} _{-0.04}	9.5 ^{+0.1} _{-0.5}	1.5 ^{+0.4} _{-0.4}	23.7 ^{+1.00} _{-0.17}	12.2 ^{+0.2} _{-1.4}	4.7 ^{+1.0} _{-1.3}	0.72 ^{+0.30} _{-0.44}	5
215	21.3 ^{+0.16} _{0.00}	10.3 ^{+0.0} _{-1.3}	1.4 ^{+0.0} _{-0.3}	22.1 ^{+0.83} _{-0.00}	12.1 ^{+0.0} _{-0.9}	2.8 ^{+0.0} _{-0.7}	0.23 ^{+0.23} _{-0.15}	3
225	21.3 ^{+2.43} _{0.00}	7.6 ^{+0.0} _{-2.3}	2.1 ^{+0.0} _{-1.4}	21.3 ^{+2.63} _{0.00}	8.5 ^{+0.0} _{-0.8}	3.8 ^{+0.0} _{-1.3}	0.39 ^{+0.00} _{-0.24}	3
227	21.3 ^{+0.91} _{-0.12}	10.8 ^{+1.0} _{-0.8}	1.8 ^{+0.5} _{-0.2}	22.7 ^{+1.07} _{-0.74}	10.1 ^{+2.2} _{-0.8}	3.9 ^{+0.1} _{-1.4}	0.26 ^{+0.12} _{-0.19}	5
277	21.9 ^{+0.59} _{-0.12}	8.0 ^{+0.3} _{-0.1}	1.7 ^{+0.7} _{-0.1}	23.5 ^{+0.95} _{-0.34}	11.3 ^{+1.6} _{-0.8}	4.5 ^{+1.0} _{-0.8}	0.47 ^{+0.52} _{-0.24}	5
310	21.3 ^{+0.17} _{-0.00}	8.4 ^{+0.0} _{-0.6}	1.6 ^{+0.0} _{-0.3}	22.5 ^{+0.21} _{0.00}	9.6 ^{+0.0} _{-0.5}	2.9 ^{+0.0} _{-0.0}	0.55 ^{+0.17} _{-0.14}	3
349	21.2 ^{+0.85} _{-0.01}	7.0 ^{+0.2} _{-0.4}	1.4 ^{+0.4} _{-0.5}	22.3 ^{+0.46} _{-0.80}	7.3 ^{+0.0} _{-0.1}	2.4 ^{+0.2} _{-0.5}	0.62 ^{+2.05} _{-0.20}	5
395	21.3 ^{+0.20} _{0.00}	11.0 ^{+0.0} _{-0.7}	1.6 ^{+0.0} _{-0.3}	24.8 ^{+0.38} _{0.00}	11.2 ^{+0.0} _{-0.4}	6.4 ^{+0.0} _{-0.2}	0.07 ^{+0.03} _{-0.02}	3
436	21.1 ^{+0.66} _{-0.04}	7.3 ^{+0.3} _{-0.1}	1.7 ^{+0.7} _{-0.1}	23.0 ^{+1.62} _{-0.15}	9.9 ^{+2.9} _{-0.1}	4.2 ^{+1.9} _{-0.4}	0.40 ^{+0.10} _{-0.29}	5
446	20.8 ^{+0.08} _{-0.16}	14.5 ^{+0.5} _{-0.0}	2.9 ^{+0.0} _{-0.2}	23.9 ^{+0.52} _{-0.49}	16.2 ^{+5.4} _{-0.6}	4.6 ^{+2.9} _{-0.2}	0.14 ^{+0.43} _{-0.05}	4
780	21.6 ^{+0.63} _{-0.07}	13.4 ^{+0.7} _{-0.4}	3.1 ^{+1.3} _{-0.4}	22.6 ^{+0.58} _{-0.13}	16.1 ^{+1.3} _{-0.3}	8.4 ^{+0.4} _{-1.1}	0.93 ^{+0.57} _{-0.34}	5

Table 2.5—Continued

FGC	Thin Disk			Thick Disk			L_{thick}/L_{thin}	n converged
	$\mu(0,0)$ (mag/□ $''$)	h_r ($''$)	z_0 ($''$)	$\mu(0,0)$ (mag/□ $''$)	h_r ($''$)	z_0 ($''$)		
901	21.2 ^{+0.07} _{-0.14}	6.9 ^{+0.1} _{-0.1}	1.3 ^{+0.1} _{-0.2}	23.1 ^{+0.24} _{-0.96}	8.8 ^{+0.3} _{-0.1}	2.9 ^{+0.3} _{-0.6}	0.39 ^{+0.02} _{-0.06}	4
913	21.2 ^{+0.65} _{-0.22}	7.8 ^{+1.0} _{-0.5}	1.4 ^{+0.4} _{-0.1}	22.4 ^{+0.54} _{-0.01}	9.1 ^{+0.8} _{-0.5}	2.5 ^{+0.4} _{-0.1}	0.52 ^{+0.13} _{-0.14}	5
979	20.2 ^{+0.76} _{-0.08}	11.9 ^{+0.2} _{-0.5}	2.3 ^{+1.0} _{-0.8}	21.7 ^{+1.21} _{-0.69}	13.0 ^{+0.7} _{-0.6}	5.1 ^{+0.2} _{-1.2}	0.67 ^{+0.82} _{-0.49}	5
1043	20.8 ^{+0.05} _{-0.11}	19.3 ^{+0.0} _{-1.1}	2.7 ^{+0.0} _{-0.1}	22.3 ^{+0.57} _{-0.17}	11.3 ^{+1.7} _{-0.5}	6.9 ^{+0.5} _{-0.8}	0.33 ^{+0.06} _{-0.21}	5
1063	22.3 ^{+0.04} _{-1.32}	4.8 ^{+0.1} _{-0.1}	0.8 ^{+0.4} _{-0.1}	21.5 ^{+0.01} _{-0.12}	7.3 ^{+0.4} _{-0.2}	2.4 ^{+0.0} _{-0.1}	6.91 ^{+4.69} _{-1.65}	4
1285	21.2 ^{+0.29} _{-0.05}	17.3 ^{+1.6} _{-1.2}	4.4 ^{+0.7} _{-0.3}	22.2 ^{+0.58} _{-0.02}	23.6 ^{+1.8} _{-1.0}	10.1 ^{+0.6} _{-0.7}	1.08 ^{+1.00} _{-0.45}	5
1303	22.2 ^{+0.52} _{-0.06}	7.9 ^{+0.0} _{-1.4}	1.4 ^{+0.7} _{-0.3}	22.4 ^{+0.53} _{-0.13}	9.0 ^{+0.3} _{-0.3}	3.3 ^{+0.3} _{-0.3}	1.93 ^{+1.82} _{-1.03}	5
1415	20.9 ^{+0.63} _{-0.30}	15.0 ^{+0.6} _{-1.6}	2.8 ^{+1.0} _{-0.5}	22.1 ^{+0.68} _{-0.07}	21.1 ^{+1.6} _{-1.3}	6.6 ^{+0.8} _{-0.4}	0.95 ^{+0.36} _{-0.43}	5
1440	20.6 ^{+0.05} _{-0.02}	15.7 ^{+0.4} _{-0.3}	2.3 ^{+0.1} _{-0.1}	22.7 ^{+0.11} _{-0.16}	17.2 ^{+0.1} _{-0.2}	5.0 ^{+0.1} _{-0.2}	0.38 ^{+0.17} _{-0.05}	4
1642	21.8 ^{+0.58} _{-0.16}	11.6 ^{+0.4} _{-0.4}	3.1 ^{+0.8} _{-0.4}	24.6 ^{+0.65} _{-1.05}	19.5 ^{+0.9} _{-4.7}	10.0 ^{+1.3} _{-4.0}	0.19 ^{+0.33} _{-0.08}	5
1948	22.5 ^{+0.69} _{-0.50}	10.1 ^{+0.8} _{-0.4}	1.6 ^{+0.5} _{-0.3}	22.4 ^{+0.07} _{-0.06}	13.0 ^{+0.5} _{-0.3}	3.6 ^{+0.0} _{-0.1}	3.56 ^{+2.22} _{-1.00}	4
2131	21.3 ^{+0.22} _{-0.00}	9.3 ^{+0.2} _{-0.7}	2.8 ^{+0.1} _{-0.8}	22.7 ^{+0.88} _{-0.64}	10.5 ^{+1.3} _{-0.1}	4.9 ^{+1.3} _{-0.5}	0.29 ^{+0.33} _{-0.00}	4
2135	21.2 ^{+0.21} _{-0.09}	6.5 ^{+0.7} _{-0.5}	1.1 ^{+0.4} _{-0.0}	22.3 ^{+1.62} _{-0.29}	8.5 ^{+0.1} _{-1.0}	2.5 ^{+1.3} _{-0.1}	0.88 ^{+0.79} _{-0.67}	4
2369	22.2 ^{+0.52} _{-0.40}	8.3 ^{+0.1} _{-0.5}	1.4 ^{+0.6} _{-0.0}	23.3 ^{+0.14} _{-0.44}	9.3 ^{+0.2} _{-1.0}	3.4 ^{+0.2} _{-0.4}	0.75 ^{+0.46} _{-0.21}	3

Table 2.5—Continued

FGC	Thin Disk			Thick Disk			L_{thick}/L_{thin}	n converged
	$\mu(0,0)$ (mag/ \square'')	h_r ($''$)	z_0 ($''$)	$\mu(0,0)$ (mag/ \square'')	h_r ($''$)	z_0 ($''$)		
2548	$21.9^{+0.05}_{-0.08}$	$9.9^{+0.1}_{-0.1}$	$1.4^{+0.2}_{-0.1}$	$22.6^{+0.09}_{-0.12}$	$9.8^{+0.0}_{-0.0}$	$3.5^{+0.1}_{-0.1}$	$1.18^{+0.76}_{-0.14}$	4
2558	$21.8^{+0.06}_{-0.56}$	$8.4^{+1.3}_{-0.7}$	$2.6^{+0.1}_{-0.4}$	$22.4^{+0.93}_{-0.41}$	$10.1^{+0.0}_{-0.2}$	$3.6^{+1.2}_{-0.0}$	$0.47^{+1.31}_{-0.17}$	4
E1371	$21.2^{+0.91}_{-0.12}$	$8.6^{+0.3}_{-1.2}$	$1.6^{+0.7}_{-0.0}$	$22.9^{+0.17}_{-0.49}$	$7.3^{+0.1}_{-1.4}$	$3.4^{+0.0}_{-0.7}$	$0.27^{+0.37}_{-0.04}$	5
E1404	$21.6^{+1.09}_{-0.06}$	$6.8^{+0.2}_{-0.3}$	$1.3^{+0.1}_{-0.2}$	$22.4^{+0.26}_{-0.38}$	$9.2^{+0.4}_{-0.3}$	$2.2^{+0.1}_{-0.2}$	$1.12^{+2.04}_{-0.53}$	4
E1498	$20.9^{+0.11}_{-0.05}$	$7.7^{+0.3}_{-0.2}$	$1.2^{+0.2}_{-0.1}$	$23.8^{+0.35}_{-0.91}$	$8.3^{+0.2}_{-0.2}$	$3.8^{+0.4}_{-1.0}$	$0.19^{+0.05}_{-0.04}$	4
E1623	$21.3^{+0.11}_{-0.15}$	$6.4^{+0.1}_{-0.5}$	$0.9^{+0.2}_{-0.0}$	$22.5^{+0.23}_{-0.53}$	$6.3^{+0.1}_{-0.2}$	$1.8^{+0.0}_{-0.2}$	$0.53^{+0.20}_{-0.12}$	4

Chapter 3

KINEMATICS OF THIN AND THICK DISKS IN EXTERNAL GALAXIES

3.1 Chapter Summary

We present kinematic measurements of thin and thick disk components in a sample of nine edge-on galaxies. We extract stellar and ionized gas rotation curves at and above the galaxies' midplanes using the Ca II triplet absorption features and H α emission lines measured with the GMOS spectrographs on Gemini North and South. For the higher mass galaxies in the sample, we find no major differences between the thin and thick disk kinematics. In the lower mass galaxies, there is a wide range of thick disk behavior including thick disks with substantial lag and one counter-rotating thick disk. We compare our rotation curves with expectations from thick disk formation models and conclude that the wide variety of thick disk kinematics favors a formation scenario where thick disk stars are accreted during merger events as opposed to models that form thick disks through gradual thin disk heating.

3.2 Introduction

The detailed distribution of stars in galaxies gives vital information regarding their formation and subsequent evolution. Of particular interest are the oldest stellar populations, which in the Milky Way are the thick disk and halo. These old components provide the best record of early galaxy assembly. Originally detected in edge-on S0 galaxies (Burstein, 1979; Tsikoudi, 1979), thick stellar disks have now been found in a wide variety of galaxies—S0's (de Grijs & van der Kruit, 1996; de Grijs & Peletier, 1997; Pohlen et al., 2004), Sb's (van der Kruit, 1984a; Shaw & Gilmore, 1989; van

Dokkum et al., 1994; Morrison et al., 1997; Wu et al., 2002), and later type galaxies (Dalcanton & Bernstein, 2002; Abe et al., 1999; Neeser et al., 2002; Yoachim & Dalcanton, 2006b). Observations with HST have allowed thick disks in other galaxies to be studied as resolved population (Seth et al., 2005b, 2007; Tikhonov et al., 2005; Tikhonov & Galazutdinova, 2005; Mould, 2005), while observations at high redshift show potential thick disks in the process of forming (Elmegreen & Elmegreen, 2006).

The most detailed studies of thick disks come from observations within the Milky Way. Since its discovery (Gilmore & Reid, 1983), the MW thick disk has been found to be structurally, chemically, and kinematically distinct from the thin disk. Structurally, star counts with large surveys such as SDSS and 2MASS reveal the galaxy is best fit with two disk components (e.g., Ojha, 2001; Juric et al., 2005). Chemically, thick disk stars are more metal-poor and older than stars in the thin disk (e.g., Reid & Majewski, 1993; Chiba & Beers, 2000). They are also significantly enhanced in α -elements, compared to thin disk stars of comparable iron abundance (Prochaska et al., 2000; Tautvaišienė et al., 2001; Bensby et al., 2003; Feltzing et al., 2003; Mishenina et al., 2004; Brewer & Carney, 2004; Bensby et al., 2005; Brewer & Carney, 2006; Ramírez et al., 2007). Kinematically, thick disk stars have both a larger velocity dispersion and slower net rotation than stars in the thin disk (Nissen, 1995; Chiba & Beers, 2000; Gilmore et al., 2002; Soubiran et al., 2003; Parker et al., 2004; Girard et al., 2006). All of these facts lead to the conclusion that the thick disk is a relic of the young Galaxy. As such, it provides an excellent probe of models of disk galaxy formation (see reviews by Nissen et al. (2003); Freeman & Bland-Hawthorn (2002)).

Given these systematic differences between their properties, thick and thin disks are likely to have distinct formation mechanisms. The structure, dynamics, and chemical abundance of the thin disk strongly suggest that the majority of its stars formed gradually from a thin rotating disk of high angular momentum gas (Fall & Efstathiou, 1980; Chiappini et al., 1997; Cescutti et al., 2007). In contrast, the formation of the thick disk is still poorly constrained and is likely to be more complex.

Thick disk formation models can be grouped into three broad categories. In the first, a previously thin disk is kinematically heated. In this scenario, stars form in a thin disk and gradually increase their velocity dispersion with time. This vertical heating can be rapid, due to interactions and mergers (Quinn et al., 1993; Walker et al., 1996; Velazquez & White, 1999; Chen et al., 2001; Robin et al., 1996) or gradual due to scattering off giant molecular clouds, spiral arms, and/or dark matter substructure (Villumsen, 1985; Carlberg, 1987; Hänninen & Flynn, 2002; Benson et al., 2004; Hayashi & Chiba, 2006). In the second formation scenario, stars “form thick” with star formation occurring above the midplane of the galaxy (Brook et al., 2004) or form with large initial velocity dispersions in large stellar clusters (Kroupa, 2002). In the final class of models, thick disk stars are directly accreted from satellite galaxies. Numerical simulations have shown that stars in disrupted satellite galaxies can be deposited onto thick disk like orbits (Abadi et al., 2003b; Martin et al., 2004; Bekki & Chiba, 2001; Gilmore et al., 2002; Navarro et al., 2004; Statler, 1988), producing extended stellar debris such as seen around M31 (Ibata et al., 2005; Kalirai et al., 2006; Ferguson et al., 2002). While these models were originally developed to explain the origin of the MW thick disk, they should work equally well for thick disks in other galaxies.

Measuring the kinematics of thick disk stars is one of the best discriminators between the formation models. If the thick disk forms from a heated thin disk, we expect the kinematics of the two components to be closely related. On the other hand, if the thick disk stars form outside the galaxy and are later accreted, we could find systems where the thick disk kinematics are completely decoupled from the thin disk.

In this paper, we present observations of stellar and gas kinematics in nine edge-on systems as part of our continuing analysis of thick disks in a large sample of edge-on galaxies (Dalcanton & Bernstein, 2000b). Compared to Yoachim & Dalcanton (2005), which presented the first two galaxies in this study, we have improved the analysis

techniques and significantly expanded our sample size.

3.3 Observations

3.3.1 Target Selection

We have carried out long-slit spectroscopic observations using the Gemini North and South telescopes of nine galaxies drawn from the Dalcanton & Bernstein (2000b) sample of edge-on late-type galaxies. The original sample of 49 galaxies was selected from the Flat Galaxy Catalog (Karachentsev et al., 1993) and imaged in B , R , and K_s (Dalcanton & Bernstein, 2000b). This sample was selected to contain undisturbed pure disk systems spanning a large range of mass. Dalcanton & Bernstein (2002) used this imaging to demonstrate the ubiquity of thick disks around late-type galaxies, while Yoachim & Dalcanton (2006b) used two-dimensional photometric decompositions to measure the structural parameters for the thick and thin disks.

Our spectroscopic program targeted galaxies spanning a wide range of masses ($50 < V_c < 150 \text{ km s}^{-1}$). The sample targets were limited to those that had thick disks that we believed we could isolate adequately—i.e., those that had very different scale heights from the thin disk and that were bright enough that we could acquire spectra in reasonable observing times. This constraint caused several of the higher mass galaxies to be rejected from the kinematic sample, as the regions where the thick disk could be expected to dominate was simply too faint. This bias is consistent with the conclusion of Yoachim & Dalcanton (2006b) that the thick disk is more prevalent in lower mass galaxies. Our selection criterion limited the sample to ~ 20 galaxies of the original 49. We also selected galaxies to be at redshifts such that the Ca features did not land on night sky emission lines. In our initial observations, we submitted more galaxies than we could observe and let the Gemini observing specialists select which galaxies would best fit with the queue scheduling. For the final observing runs we explicitly selected galaxies to ensure that a reasonable mass range was observed

in the final sample. The properties of the final sample are listed in Table 3.1.

3.3.2 Observing Strategy

Based on the thin and thick disk decompositions in Yoachim & Dalcanton (2006b), we targeted regions of the galaxies where the flux is dominated by either the thin or thick disk stars. The two highest mass galaxies in our sample have notable dustlanes (Dalcanton et al., 2004), and for these we offset the spectra slit to observe regions of the galaxy which should be optically transparent. We discuss possible residual dust effects in detail in §3.8. When selecting slit placement for the offplane, the direction of offset was based primarily on avoiding foreground objects and the ability to use a single guide star for all dither positions.

For our instrumental setup, we used GMOS on Gemini North in longslit mode with a $0.5''$ slit and the R400_G5305 grating set to a central wavelength of $\sim 8440 \text{ \AA}$ along with the OG515_G0306 filter. Similarly for observations from Gemini South, we used a $0.5''$ slit the R400+_G5325 and OG515_G0330 filter. For both GMOS setups, we binned the CCDs by 2 in the spatial direction during readout giving a pixel scale of $0.145''/\text{pix}$ in the spatial direction and $0.69 \text{ \AA}/\text{pixel}$ in the spectral direction. The resulting spectra cover the wavelength range of $\sim 6330 - 10570 \text{ \AA}$, although there is heavy residual fringing redward of 9300 \AA . Exposure times for individual frames were 900, 1200, or 1800 seconds. The midplanes were observed 3-5 times while offplane positions were observed 18-51 times depending on the galaxy. Exposures were spatially dithered $\sim 30''$ along the slit. These configurations allow us to simultaneously observe the $\text{H}\alpha$ emission and Ca II triplet absorption features out to large radii.

All of the observations were executed in queue mode over five semesters. The observation details for each galaxy are listed in Table 3.2, with details of the slit positions listed in Table 3.3

Table 3.1. Properties of Targeted Galaxies

Galaxy FGC	Dist ¹ Mpc	V_c km s ⁻¹	h_R "	$z_{0,thin}$ "	$z_{0,thick}$ "	L_{thick}/L_{thin}
227	89.4	106.0	10.2	1.8	3.9	0.47
780	34.4	75.0	15.1	3.1	8.4	0.93
1415	38.3	86.5	18.3	2.8	6.6	0.95
1440	70.9	150.5	15.9	2.3	5.0	0.38
1642	36.6	55.0	12.5	3.1	10.0	0.19
1948	36.9	54.5	12.3	1.6	3.6	3.56
2558	73.8	89.0	9.2	2.6	3.6	0.47
E1371	82.6	131.0	7.7	1.6	3.4	0.27
E1498	135.5	133.0	7.6	1.2	3.8	0.19

¹Karachentsev et al. (2000a)

Table 3.2. Observing Details

Galaxy FGC	Gemini ID	Observation Dates	Midplane Exposure # x time (s)	Offplane Exposure # x time (s)
1415	GN-2003A-Q-6	3-28-2003 to 06-06-2003	3x900	41x1200
227	GN-2003B-Q-51	9-21-2003 to 11-22-2003	3x1200	27x1200
1642	GN-2004A-Q-54	02-16-2004 to 06-24-2004	3x1200	51x1200
780	GN-2004A-Q-54	02-20-2004 to 04-27-2004	5x1200	31x1200
2558	GN-2004B-Q-29	07-15-2004 to 11-20-2004	3x1200	36x1200
E1498	GS-2004B-Q-44	03-11-2005 to 06-10-2005	3x1200	50x1200
1948	GN-2005A-Q-21	08-12-2004 to 08-24-2004	5x1800	18x1800
E1371	GS-2005A-Q-17	04-05-2005 to 04-14-2005	3x1200	21x1800
1440	GS-2005A-Q-17	02-11-2005 to 04-05-2005	3x1200	30x1800

Table 3.3. Slit Placement

Galaxy FGC	Midplane Offset ¹		Offplane Offset			
	arcsec	kpc	arcsec	kpc	$z/z_{0,thin}$	$z/z_{0,thick}$
227	0.0	0.0	3.0	1.3	1.7	0.8
780	0.0	0.0	6.5	1.1	2.1	0.8
1415	0.0	0.0	5.4	1.0	1.9	0.8
1440	0.5	0.2	4.5	1.5	2.0	0.9
1642	0.0	0.0	4.2	0.7	1.4	0.4
1948	0.0	0.0	3.1	0.6	1.9	0.9
2558	0.0	0.0	3.9	1.4	1.5	1.1
E1371	0.5	0.2	2.8	1.1	1.8	0.8
E1498	0.0	0.0	2.0	1.3	1.7	0.5

¹Midplane offset to avoid obvious dust lanes.

3.3.3 Data Reduction

A combination of Gemini IRAF packages, standard IRAF packages, and custom IDL code were used to reduce our data. These procedures have been improved since initial results for FGC 227 and FGC 1415 were published in Yoachim & Dalcanton (2005) and have been applied to the entire data set. We bias corrected the images using a fit determined from the overscan region followed by subtracting residual structure measured from a bias frame. Because both GMOS North and South are extremely stable, we were able to create bias frames by combining ~ 60 bias frames per observing semester. We stitched together the three GMOS chips using the Gemini IRAF tasks, after which the standard IRAF reduction tools were used. For Gemini-South observations, we also needed to subtract a dark current correction of ~ 6 -12 counts from the science frames. Gemini-North images showed no detectable dark current. Images were flat-fielded using GCAL lamp flats that were taken every hour interspersed with the science observations, minimizing the amount of fringing present in the final frames. We applied a slit illumination correction using twilight sky observations.

For wavelength calibration, we used the night-sky atlases of Osterbrock et al. (1996) and Osterbrock et al. (1997) to create a sky line list containing only lines (or stable unresolved doublets) that could be centroided with our instrumental set-up. For each science exposure, we identified 100-110 sky lines to use for rectification. We then used these lines for a 5th order Legendre polynomial fit for wavelength calibration, and rebinned our spectra to a common dispersion. Typical dispersions were $0.69 \text{ \AA pixel}^{-1}$ with calibration arc lamps showing a FWHM of 3.8 \AA . The wavelength solutions were stable over each observing night.

Sky subtraction proved difficult because of the large number of strong sky emission lines. If we use standard sky subtraction techniques, we find that there are large systematic residuals left on our frames due to variation in the width of the slit along its length. The RMS deviation in the position of a single sky line is $\sim 0.07 \text{ \AA}$ while the

RMS of its Gaussian FWHM is 0.11 \AA . This is a surprisingly high variation for the width of the slit. We have tried the sky-subtraction techniques described in Kelson et al. (2000) and find that the systematic residuals remain, although the Kelson et al. (2000) sky-subtraction technique does eliminate problems associated with wavelength rectification and interpolation. Having eliminated our data-reduction procedure as the cause, we conclude the high dispersion in sky line FWHM is indicative of a systematically varying slit width. In many cases, such residuals can be removed using the nod-and-shuffle technique (Glazebrook & Bland-Hawthorn, 2001). Unfortunately, our galaxies are too large (~ 1 arc minute, or $1/3$ of the total slit width) to make effective use of traditional nod-and-shuffle.

To remove the systematic residuals present in the bright sky lines, we employ a nod-and-shuffle like template subtraction. Because we placed different galaxies on different spatial sections of the chips, all of the slit was illuminated by sky for at least some observations. We therefore could construct high S/N sky frames by masking objects in our 2-d spectra and combining the wavelength rectified frames. By doing this, we create a deep sky frame for each observing quarter. We then remove the sky background by selecting a sky-dominated region in a science frame and scaling the sky image column-by-column to match the science frame sky region, then subtract the rescaled sky frame from the science image. In most cases, we were forced to apply sky frames generated from different observing semesters to the science frames. Luckily, our instrument setup quarter-to-quarter was identical, and the GMOS instruments are stable enough that this technique works well at removing systematics caused by the variable slit width. This sky subtraction technique appears to give results comparable to nod-and-shuffle technique for individual frames. Our sky subtraction procedure incurs a small signal-to-noise penalty, but is effective at removing the systematic residuals from moderate sky lines (Figure 3.1).

This excessive agonizing over sky subtraction is demanded by the very low surface brightness levels of our targets. For an individual midplane image, the brightest part

of the galaxy is $\sim 20\%$ brighter than the sky level, and for individual offplane images the signal is only $\sim 11\%$ the sky background. Examples of the spectra extracted over the central $14''$ spatial extent of the galaxy before and after sky subtraction are shown in Figure 3.2.

When we combine several hours of observations we are more sensitive to low surface brightness features, and find some wavelengths are still dominated by systematic noise. Even with our sky template correction, some sky lines are so bright that we cannot completely remove them. When we use conventional sky-subtraction techniques, residual errors have maximum deviations of $\pm 55\%$ while the template subtraction gives deviations of $\pm 38\%$. While deviations of 38% swamp out the signal from any stellar absorption lines near bright sky lines, the residual deviations for smaller sky lines are decreased to a level where the stellar absorption lines can be accurately measured. In Figure 3.1, we compare the two sky subtraction routines. The extracted spectra look similar, with both being dominated by the sky line residuals redward of 8750 \AA . The template subtraction is able to eliminate the residuals left from the sky line at 8555 \AA , just to the right of the weakest triplet line, and reduces the large residuals at the reddest wavelengths plotted.

After the sky had been removed, the images were Doppler-corrected for motion relative to the Local Standard of Rest and combined. Before cross-correlation was performed, the spectra were rebinned into logarithmic wavelength bins.

3.4 Rotation Curves

3.4.1 H α Rotation Curves

Both our midplane and offplane observations show clear H α emission. For each galaxy, we extracted a series of 1-D spectra by summing 28 pixels ($\sim 4''$) along the spatial dimension. The ionized gas rotation curve was fit with a Gaussian peak to the H α line. In principle, an envelope-tracing method would produce a more robust

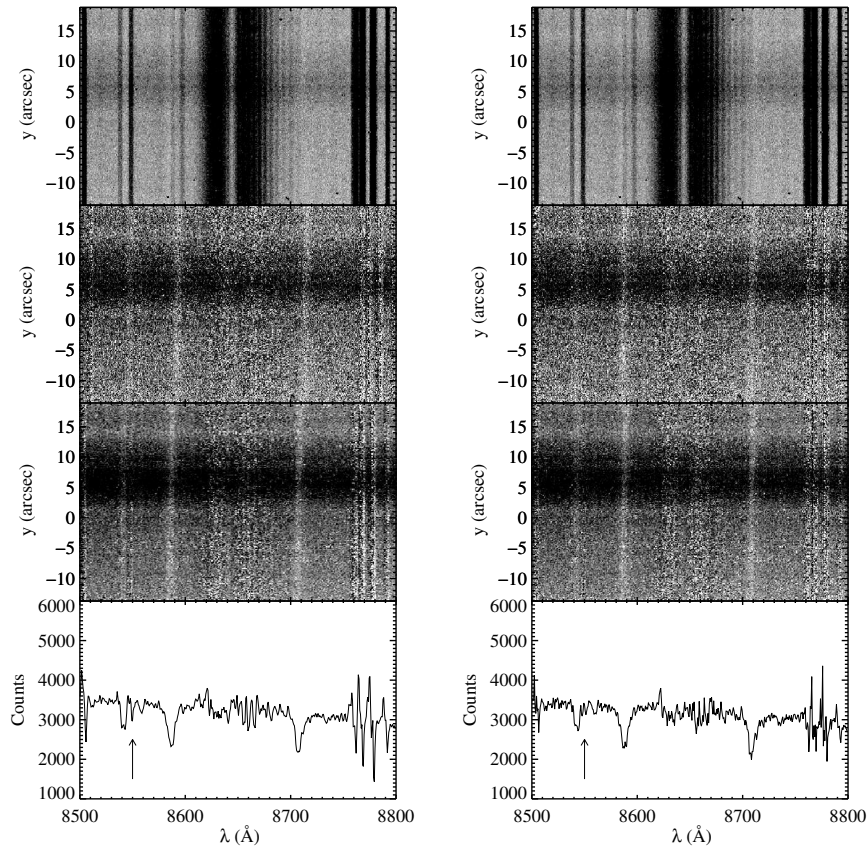


Figure 3.1 Results from different sky subtraction techniques for the midplane of FGC 1415. On the left, we show the results from standard sky subtraction techniques and the right panels show our sky template subtraction. Top panels show the raw galaxy spectrum before the sky has been subtracted. Middle panels show a single subtracted frame and the final combined image. The bottom panel shows the combined spectrum summed along the spatial dimension. An arrow points out a sky line residual present in the standard subtraction that is eliminated in template subtraction. The brightest sky lines leave large residuals in both cases, but the magnitude of residuals is decreased significantly with the nod-and-shuffle-like technique (see the lines near $\sim 8770\text{\AA}$, for example).

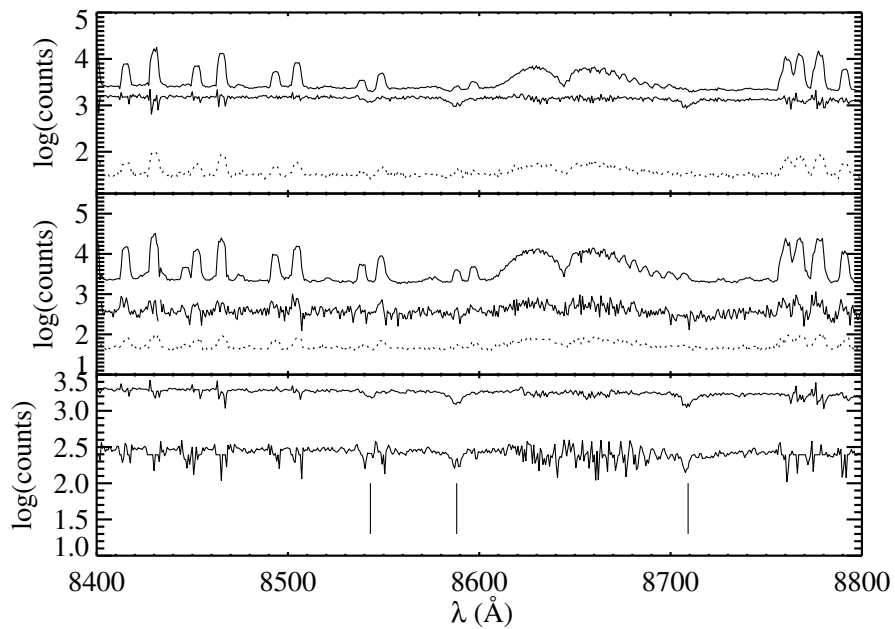


Figure 3.2 Examples of spectra before and after sky subtraction. The top panel shows the results of a single midplane exposure before and after sky template subtraction (top and middle curves respectively). The middle panel shows a single offplane exposure before and after extraction. Dotted lines show the RMS noise level in the spectra. The bottom panel shows the final midplane and offplane spectra after all the frames have been averaged together. The largest systematic residuals from the sky lines have been masked. The three vertical marks show the location of the Ca triplet absorption lines. All of the spectra were extracted over the central $14''$ of the galaxy.

measure of the rotation curve. However, we find that the width of the $H\alpha$ lines (FWHM $\sim 3.8\text{\AA}$) are identical to the instrumental dispersion as measured from the arc lamps (FWHM $\sim 3.8\text{\AA}$), and we would thus not gain much accuracy from a more detailed rotation curve extraction.

The [NII] and [SII] lines are all present as well, but the $H\alpha$ line is so strong that we found no additional advantage in fitting all the emission lines simultaneously. We find typical uncertainties in the central wavelength of the $H\alpha$ Gaussian peak of 1-2 km s^{-1} for midplane observations and 4-7 km s^{-1} for offplane observations.

To double check the accuracy of our extracted rotation curve, we fit rotation curves to night sky lines before the background is subtracted off. Perfect calibration would result in sky line rotation curves with zero rotation. The central wavelengths of the sky lines vary with an RMS error of 2.4-3.5 km s^{-1} , with the higher value resulting from larger spatial extraction windows. Most of this scatter can be attributed to uncertainties in the wavelength rectification solution. With fewer sky lines around $H\alpha$ compared to the redder regions of our spectra, the rectification is not as well constrained. Overall, these tests suggest that we are able to extract the ionized gas rotation curve with an error of a few km s^{-1} .

The resulting $H\alpha$ rotation curves are plotted as solid lines in Figure 3.4. Our data show a tight agreement between the midplane and offplane $H\alpha$ curves, which is a good sign that dust is not obscuring the midplane rotation curves. If we were observing along major dustlanes, we could expect to see the offplane observations rotating faster than the midplane, especially at small galactic radii (see §3.8).

We leave a detailed analysis of the gas kinematics for a later paper. At this time, we simply note that the midplane and offplane $H\alpha$ rotation curves are surprisingly well matched. This is slightly unexpected, as several recent studies have found extended gaseous halos of edge-on galaxies to be lagging in rotational speed when compared to the midplane gas (Heald et al., 2006a, 2007; Fraternali & Binney, 2006). These offplane lags have been detected in both the diffuse ionized gas (DIG) and HI. There

is some difficulty in comparing our measurements of longslit rotation curves to other detailed measurements of offplane gas which typically utilize 2-d information from radio (Barbieri et al., 2005; Fraternali & Binney, 2006), Integral Field Units (Heald et al., 2006a, 2007), and Fabry-Perot spectra (Heald et al., 2006b) all of which detect gas at larger scale-heights than those probed with our offplane measurements. The other major difference between these previous studies and our offplane rotation curves is that we have targeted lower mass galaxies. The studies cited above target galaxies with $220 > V_{max} > 110 \text{ km s}^{-1}$ while the sample studied here extends to galaxies with rotation speeds of less than 60 km s^{-1} .

The gaseous lags observed in other systems are usually modeled with either a galactic fountain that ejects gas to large scale-heights or with a gas infall model where galaxies slowly accrete rotating gas. The lack of significant lags in our $\text{H}\alpha$ rotation curves could simply be a sign that these galaxies are not as active in forming galactic fountains or accreting gas as the more massive galaxies.

3.4.2 *Ca II Rotation Curves*

To derive absorption line rotation curves, we require higher signal-to-noise than for the $\text{H}\alpha$ rotation curve. We therefore sum the 2D spectra in the spatial direction until the 1D spectra reaches an adequate S/N (~ 15 per spectral pixel). The resulting bins have variable widths across the face of the galaxy, but roughly comparable S/N per bin. For the central regions of the galaxies the bin size is around $10''$ while the outer regions and offplane components have bin sizes $\sim 20''$. These bins correspond to $\sim 3\text{-}6$ kpc at the typical distances of the galaxies. For reference, the typical exponential disk radial scale lengths are $h_R \sim 12''$.

Extracting kinematic information from this data required developing a new procedure. In Yoachim & Dalcanton (2005), we tried both direct χ^2 -fitting of a template spectrum as well as cross-correlation of the galaxy with a stellar template to measure the stellar rotation and line-of-sight velocity dispersion (LOSVD). We have since con-

cluded that these traditional methods are not optimal for our data. Direct fitting of a template star results in the template being over-broadened (i.e., the fitted LOSVD diverges to large values). This can be understood as the template star fitting the continuum region of the galaxy spectrum at the expense of a small portion of the absorption line. Because the normalized continuum is very low S/N, it is best fit by a straight line, which is equivalent to a stellar spectrum which has been smoothed by a very broad filter. In Yoachim & Dalcanton (2005) we were forced to hold the velocity dispersion fixed during the χ^2 minimization to prevent this problem. Cross-correlation is also problematic, as the bright sky lines leave regions of very low S/N and systematic residuals caused by variations in the slit-width (Figure 3.1). Without a constant S/N throughout the spectra, the cross-correlation peak can become skewed by noisy regions.

To extract both velocity and velocity dispersion information from our spectra we developed a modified cross-correlation technique that allows regions of very low signal-to-noise to be masked. This modification prevents us from using the usual mathematical techniques involving Fourier transforms and instead utilizes a brute-force methodology. What it lacks in mathematical elegance, our procedure makes up for in functionality by being the only procedure we know of that works on spectra that are both low S/N and contaminated with systematic residuals. We describe our modified cross-correlation in detail in Appendix 3.11 and compare its results to more traditional analysis methods in Figure 3.24. It may also be possible to use a penalized pixel-fitting technique to measure the kinematics from our spectra, but simulations show that the fitted parameters can become biased when the S/N is low (60), or the LOSVD is poorly sampled (Cappellari & Emsellem, 2004).

For the stellar template, we used a KIII spectrum of star HD4388 downloaded from the Gemini archive along with accompanying calibration frames of program GN-2002B-Q-61. The stellar spectrum was reduced and extracted using the Gemini IRAF routines. Once extracted, the 1D stellar spectrum was broadened with a Gaus-

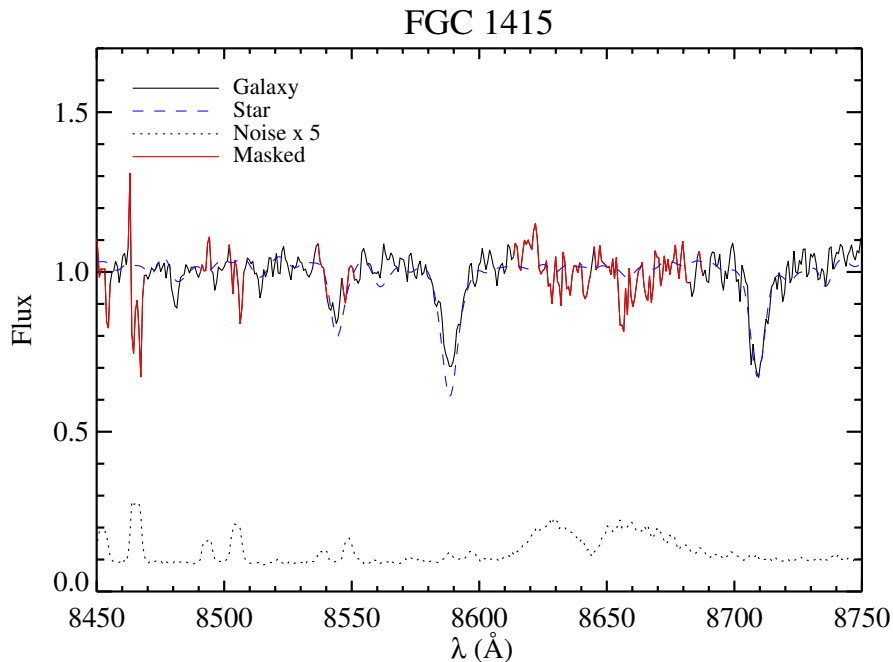


Figure 3.3 An example of our extracted galaxy spectra. The solid line shows the normalized galaxy spectrum. Red regions mark where the spectra was masked due to sky line contamination. The noise spectrum (multiplied by 5) is plotted as a dotted line. The blue dashed line shows the best fit shifted and broadened stellar spectrum.

sian kernel to match the instrumental resolution of our observations. We found no significant changes when trying different template stars and find our uncertainties are never dominated by template mismatch.

Because we have modified the traditional cross-correlation technique, we have no formal means of calculating uncertainties in our fitted velocity and LOSVD. We therefore run a series of Monte Carlo realizations to quantify the errors in our fitting procedure. For each galaxy, we create 100 artificial 2D spectra. A template stellar spectrum is shifted to match a realistic rotation curve, and broadened to simulate both stellar velocity dispersion and instrumental resolution. We vary the detailed shape of the rotation curve and velocity dispersion for each realization by $\sim 20\%$. The fake spectra have radial exponential flux profiles similar to the real galaxies. We add

Poisson noise to the artificial spectra, as well as systematic residuals by adding regions of sky from our science frames that do not have any detectable objects. Thus, our artificial spectra have both the same Gaussian sky background and similar systematic residuals as the real data.

Once the artificial spectra are made, we extract and analyze 1D spectra identically to the real data (i.e., we use the same extraction windows and the cross-correlation with masking procedure). In many instances, we found that our measured LOSVD poorly matched the input. The loss of reasonable LOSVD measurements is dominated by how many of the CaII lines are masked due to sky line contamination. We therefore clip points where the Monte Carlo error analysis suggests we cannot reliably recover the input parameters (i.e. the RMS error between input and output is $> 50 \text{ km s}^{-1}$ or the output has a systematic error of $> 20 \text{ km s}^{-1}$). These clipped regions typically correspond to regions of the rotation curve where the Ca triplet line passes through a large sky residual.

Our final extracted rotation curves, LOSVDs, and Monte Carlo derived uncertainties are plotted in Figure 3.4 along with *R*-band images of the galaxies showing the Gemini longslit placements.

3.5 Stellar Kinematics

Although we attempted to place our slits in regions of the galaxies where the thin and thick disk light makes up the majority of the flux, it is nearly impossible to target regions where one stellar component completely dominates the flux. In the lower-mass galaxies, we found that the thick disk is a major stellar component and we should expect spectra taken along the midplane to include a large amount of thick disk light. In the higher mass galaxies, the thin disk is the dominant component, and we are forced to observe off-plane regions that still contain a large fraction of thin disk light. Using the photometric fits of Yoachim & Dalcanton (2006b), we can estimate the fractional flux levels of the thin and thick disk at each slit position. Because each slit

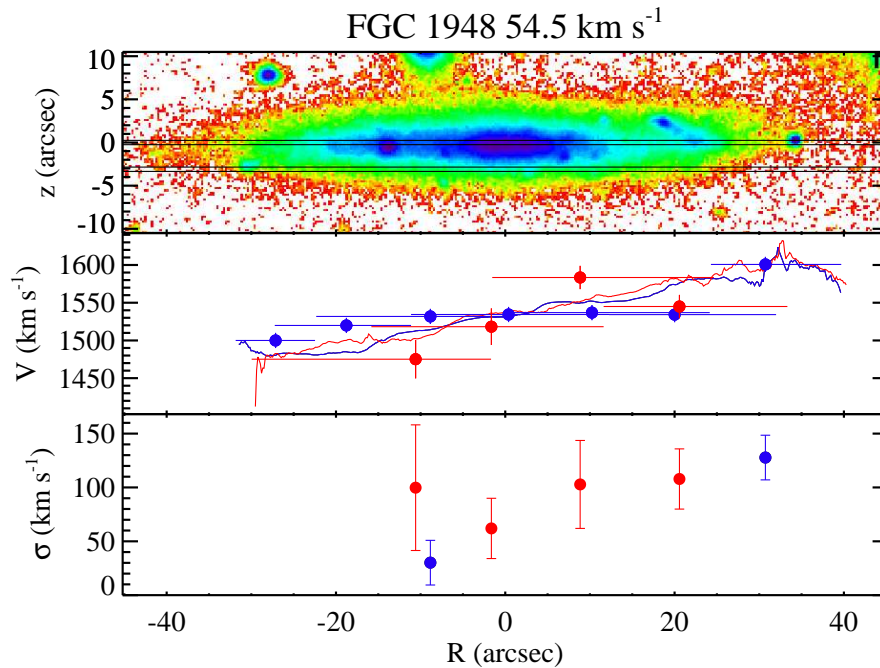


Figure 3.4 Rotation curve measurements for each galaxy. Top panels: R -band images of each galaxy. The color scale goes from dark blue ($\mu_R = 21$) to green ($\mu_R = 23$), to red/white ($\mu_R = 25.5$). Solid black lines have been drawn where the Gemini long-slit jaws were placed. Middle Panels: Rotation curves for midplane (blue) and offplane (red). Points with error bars are from Ca II measurements. Vertical error bars are uncertainties derived from Monte Carlo simulations, horizontal error bars show the spectral extraction regions. Small lines show velocities measured from the $H\alpha$ emission lines. Bottom Panels: Stellar velocity dispersions measured from the Ca II feature. All error bars are from a Monte Carlo simulation. Points with overwhelmingly large error-bars or large systematic uncertainties have been omitted.

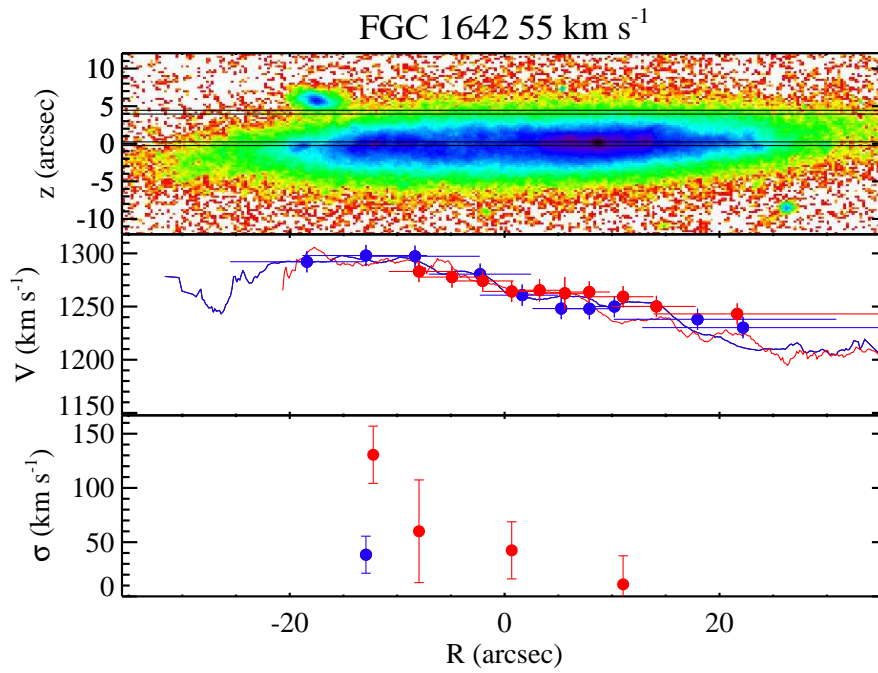


Figure 3.5 Same as Figure 3.4.

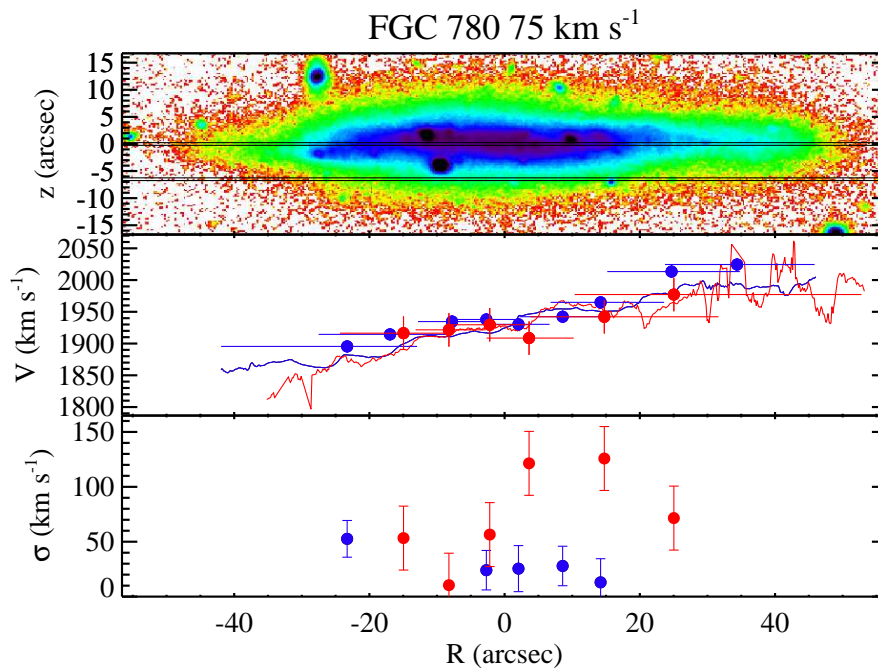


Figure 3.6 Same as Figure 3.4.

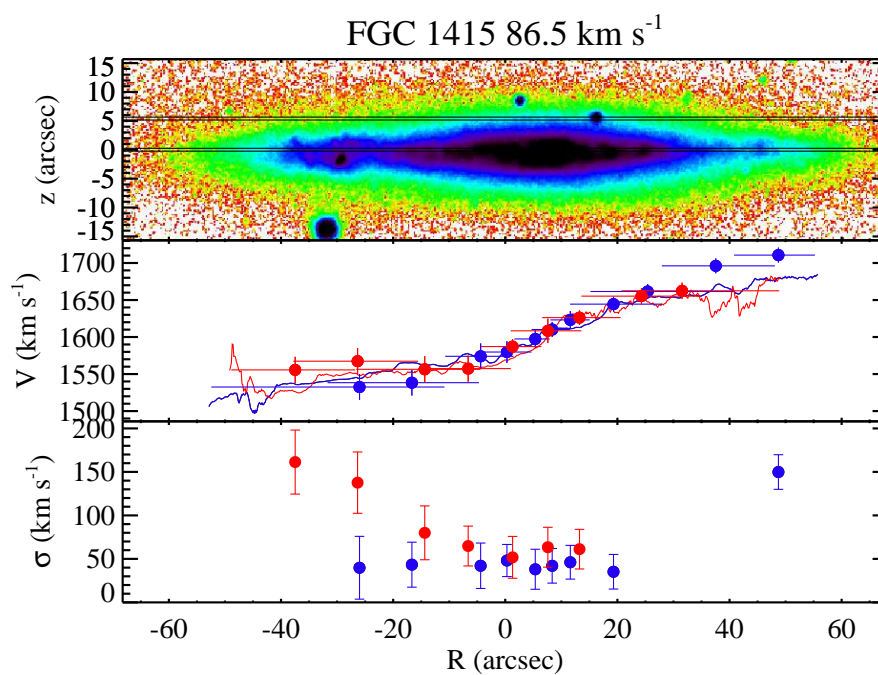


Figure 3.7 Same as Figure 3.4.

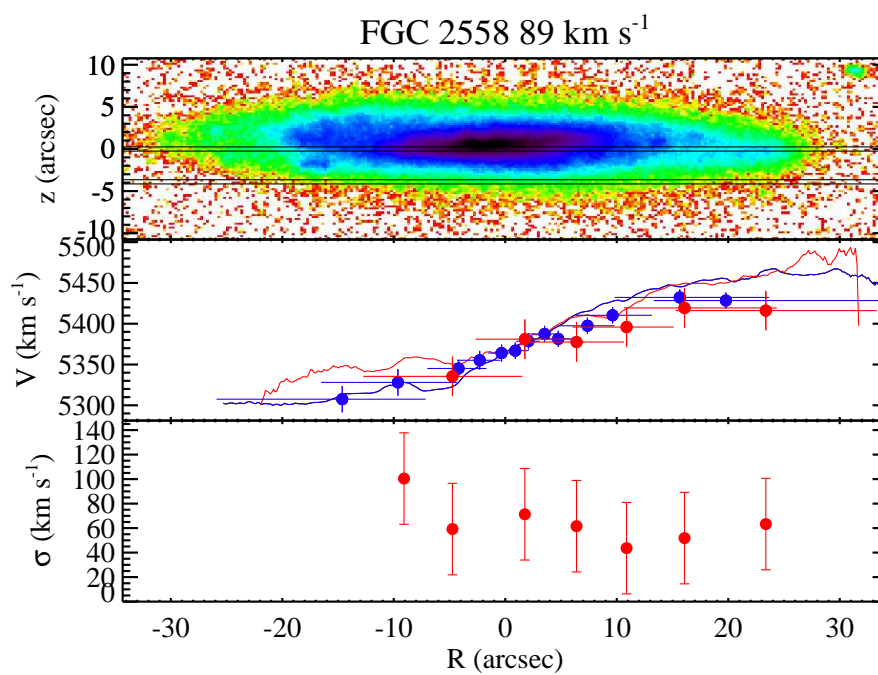


Figure 3.8 Same as Figure 3.4.

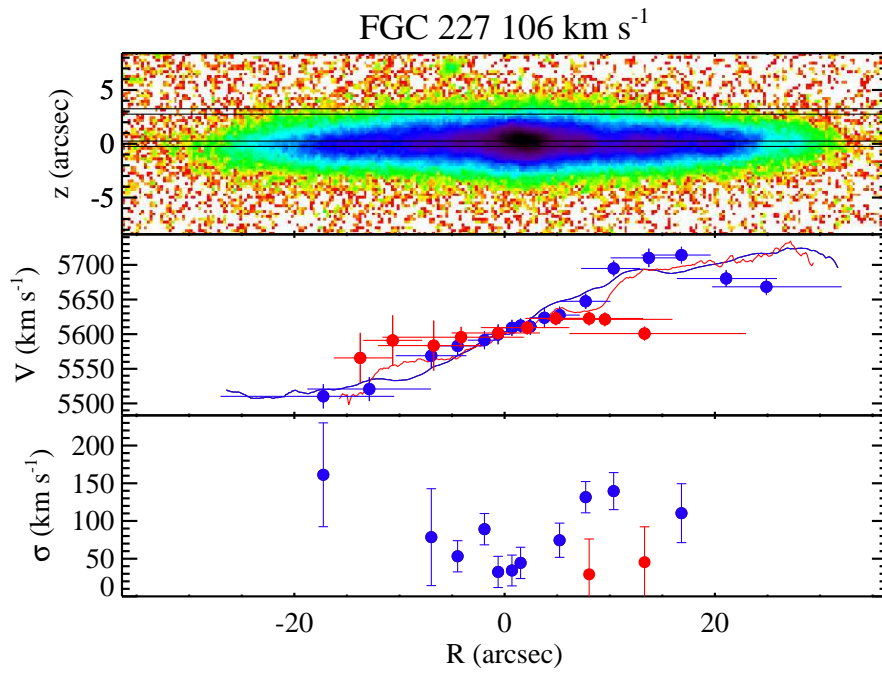


Figure 3.9 Same as Figure 3.4.

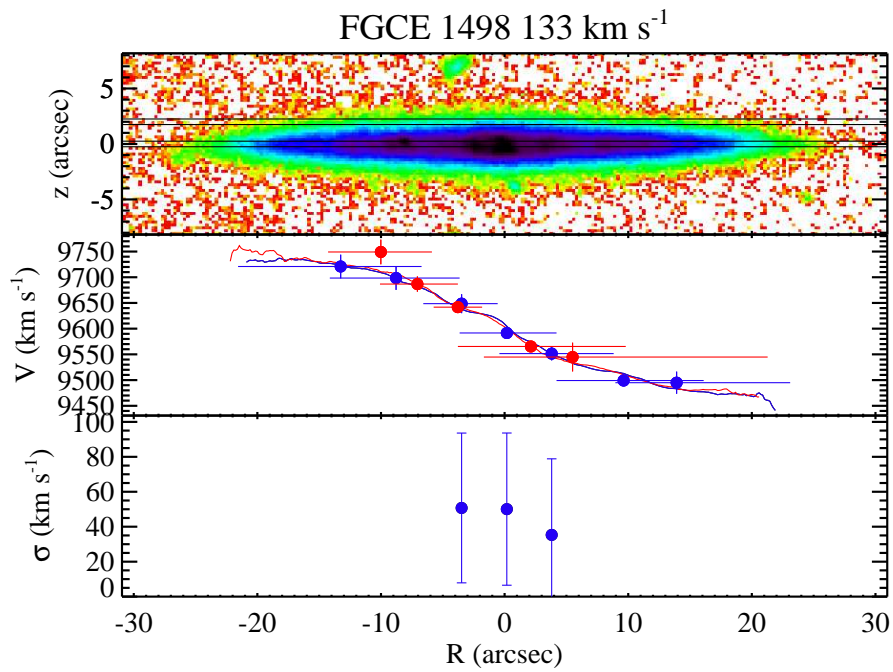


Figure 3.10 Same as Figure 3.4.

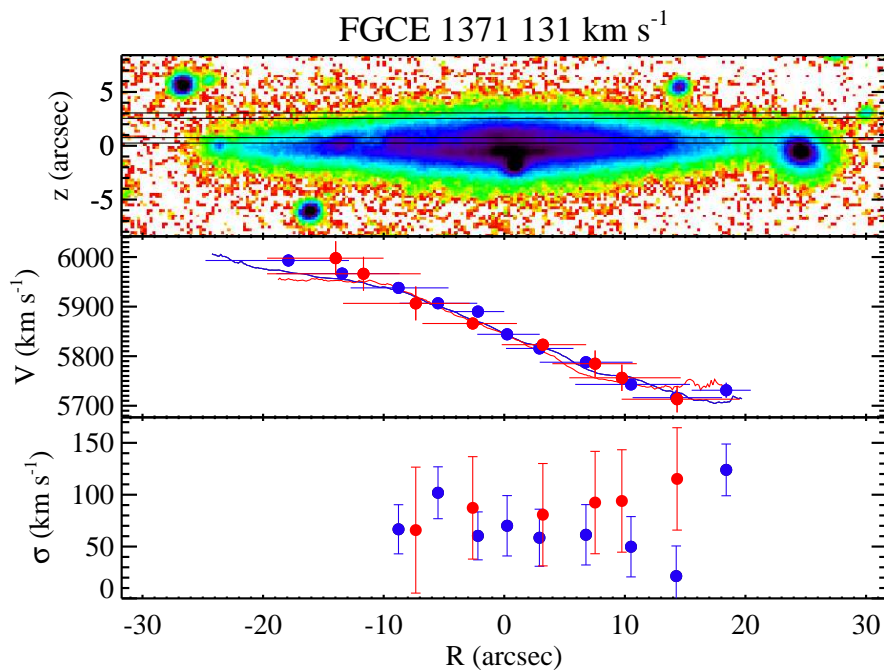


Figure 3.11 Same as Figure 3.4.

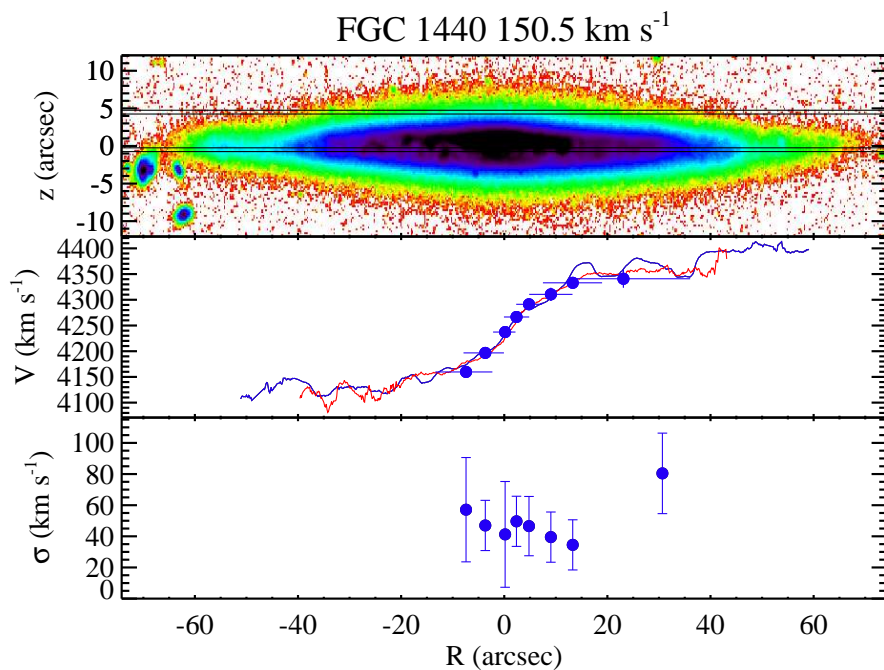


Figure 3.12 Same as Figure 3.4.

position should include both thin and thick disk stars, we make an attempt to model the true underlying rotation curves for each population. For simplicity, we assume that the thin and thick disk stars are each rotating cylindrically and therefore have the same rotation curve for both the on and off-plane observations. We discuss this choice in more detail in §3.7.

The details of the vertical profiles of the stellar disks (exponential vs sech^2) can dramatically influence what fraction of the midplane light belongs to thin disk stars versus thick disk stars. As in Yoachim & Dalcanton (2005), we adopt a series of photometric decomposition models that should cover the full range of possible thin and thick disk fractions. At one extreme, we use a simple model where we assume the midplane is composed of only thin disk light and the offplane observations purely thick disk stars. As a more accurate model, we use the thin/thick fractions from the best fitting models of Yoachim & Dalcanton (2005) as well as models where we vary the parameters by their $1\text{-}\sigma$ values to create a “bright-thick and faint-thin” model along with a “faint-thick and bright-thin” model. The differences between the thin and thick disk scale lengths are small enough that we do not expect much radial variation in the fraction of thin and thick disk light.

In Yoachim & Dalcanton (2005), we fit analytic functions to the stellar rotation curves to decompose the thin and thick disk components. This worked well for the initial two galaxies we observed, but our expanded sample now includes galaxies with slightly irregular kinematics that are not well described by common parameterization of rotation curves. Instead of using an analytic function, we use the midplane $\text{H}\alpha$ rotation curve as a basis function for the overall shape of the rotation curve. Because we are most interested in finding the velocity of the thin and thick disk stars relative to each other, we compare them both to the well resolved and high signal-to-noise midplane $\text{H}\alpha$ rotation curve. This reduces the number of parameters that need to be fit to characterize the stellar rotation curves.

We model the stellar rotation curves as $V_{stars}(R) = xV_{\text{H}\alpha} + c$. We constrain c to

be in the range ± 5 (to account for any small error in wavelength calibration between frames or regions on the chip) and x is limited to $-1 < x < 1.4$, allowing for stars to be rotating faster than the gas by up to 40% ($x=1.4$), not rotating ($x=0$), or counter rotating with the opposite velocity of the $H\alpha$ ($x=-1$).

The decomposed rotation curves are plotted in Figure 3.13. The left hand panels show the best fit stellar rotation curve scaled from the $H\alpha$ at each slit position. If there were no cross-contamination of thin and thick disk stars, then the offplane and midplane rotation curves would show the true thick and thin disk kinematics. The right hand panels show the more realistic case where we have adopted likely amounts of thin and thick disk contamination at each slit position before inferring the underlying kinematics of each population.

For the higher mass galaxies, we find no substantial difference between the thin and thick disk rotation curves, even when we correct for the expected cross contamination. There is a slight tendency for the thick component to be lagging, but never by more than 5 km s^{-1} . In the higher mass galaxies, we have therefore either failed to observe an offplane region with a high enough thick disk flux fraction, or the thick disks are not lagging significantly compared to the thin disk in these systems.

For the low-mass galaxies, we find a wide range of behavior. The fits for FGC 1948 diverge, as the stellar rotation curves do not show coherent rotation at either slit position. For the rest of the galaxies, the best fits find thick disks that are slightly lagging compared to the thin (FGC 2558, FGC 1415), that are lagging to the extent of near non-rotation (FGC 1642, FGC 780), and that are fully counter-rotating (FGC 227). We note that there is strong qualitative agreement with initial results in Yoachim & Dalcanton (2005) for FGC 1415 and FGC 227.

3.5.1 *Velocity Dispersions*

The low signal-to-noise of our spectra prevents us from reliably measuring velocity dispersions for many of our galaxies. Most of the galaxies with high quality spectra

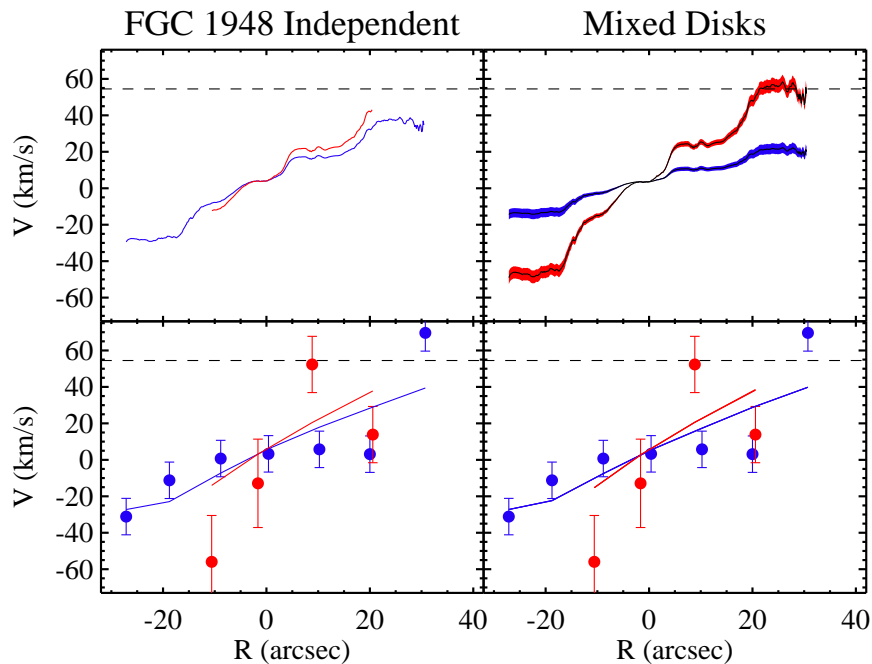


Figure 3.13 The results of fitting various rotation curve models to our data. The top left panels show fits of the simple model where the midplane and offplane observations are fit independently. Upper right panels show shaded regions show the range of fits derived from varying the fraction of thin and thick disk light at each slit position. Solid lines show the fits for when we use the thin and thick disk fractions of the photometric fits in Yoachim & Dalcanton (2006b). Lower panels show the observations as points and solid lines show the models from the above panels once they have been flux weighted and binned in the same manner as the observations. Throughout, red is used for thick disk/offplane and blue is used for thin disk/midplane. Each panel has a dashed line showing the $W_{50/2}$ value from the literature. FGC 1440 is not shown because we failed to measure a stellar rotation curve in the offplane position.

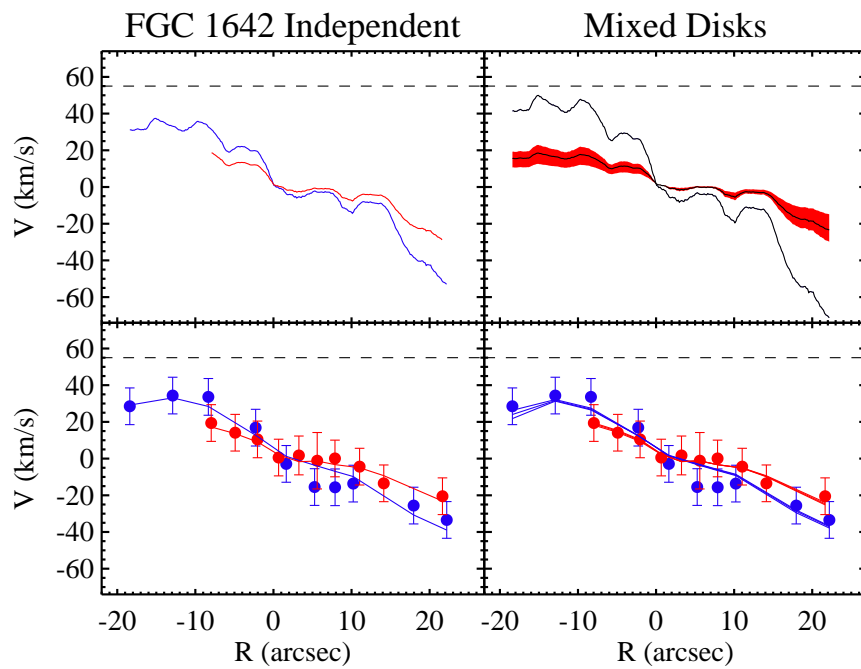


Figure 3.14 Same as Figure 3.13.

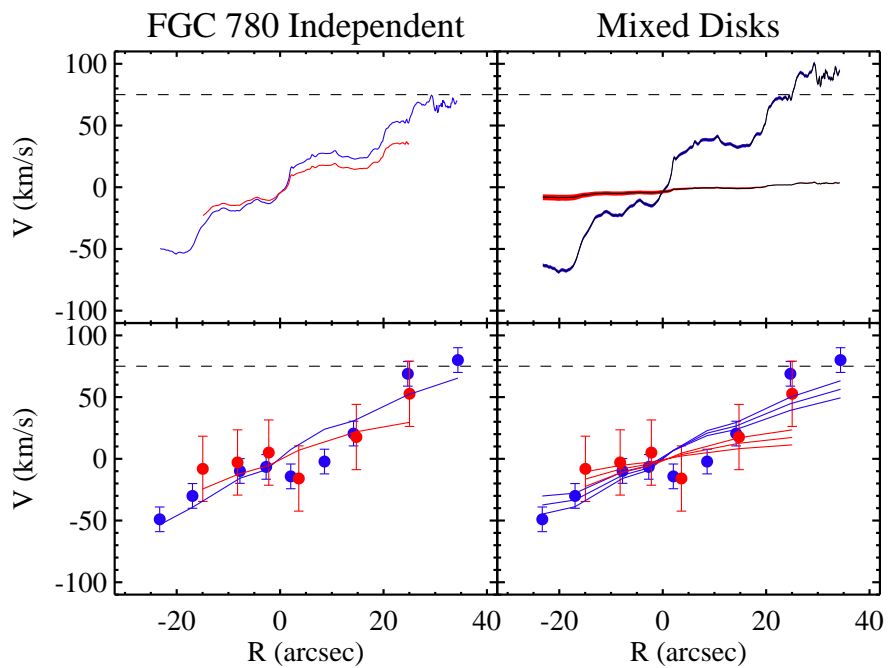


Figure 3.15 Same as Figure 3.13.

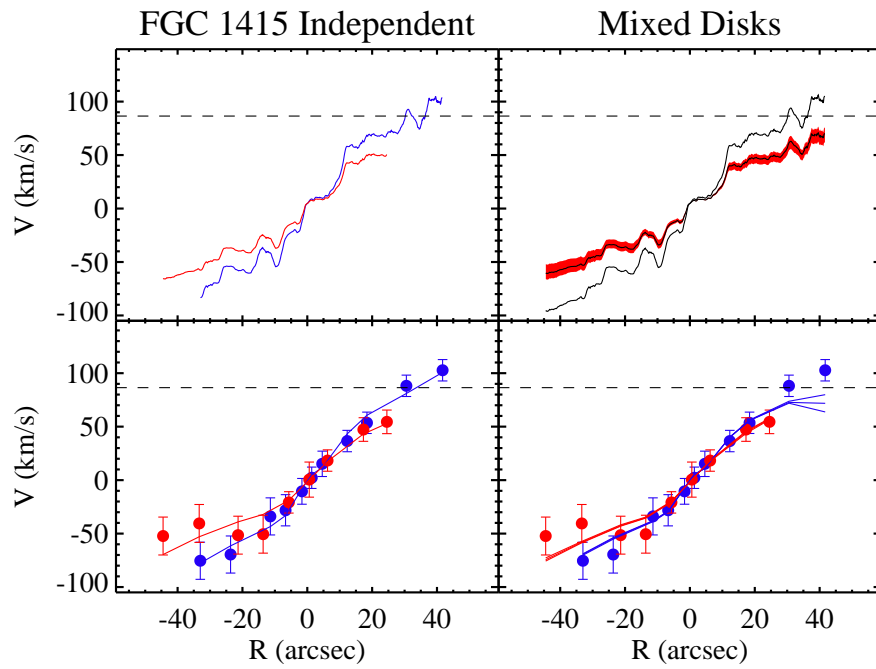


Figure 3.16 Same as Figure 3.13.

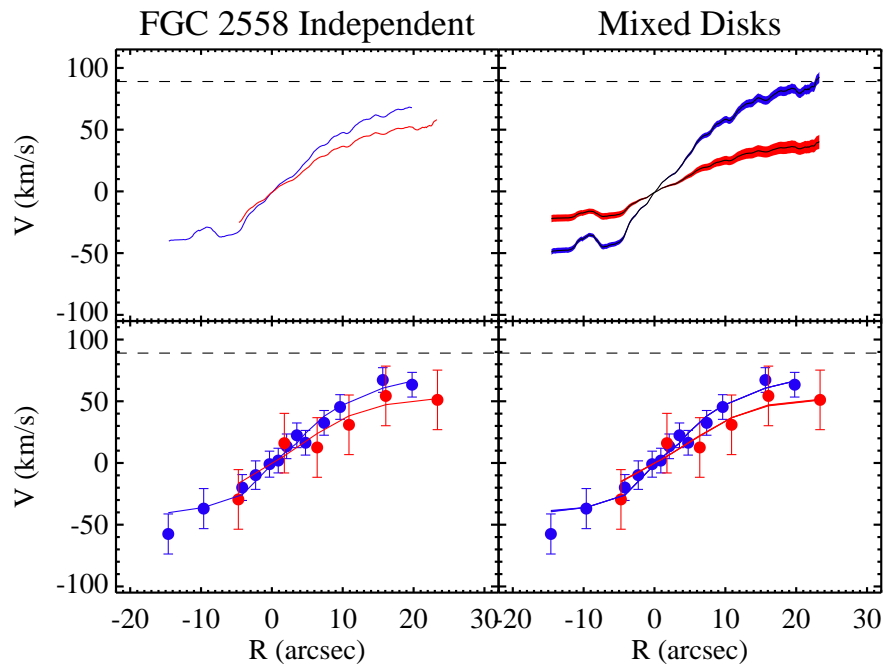


Figure 3.17 Same as Figure 3.13.

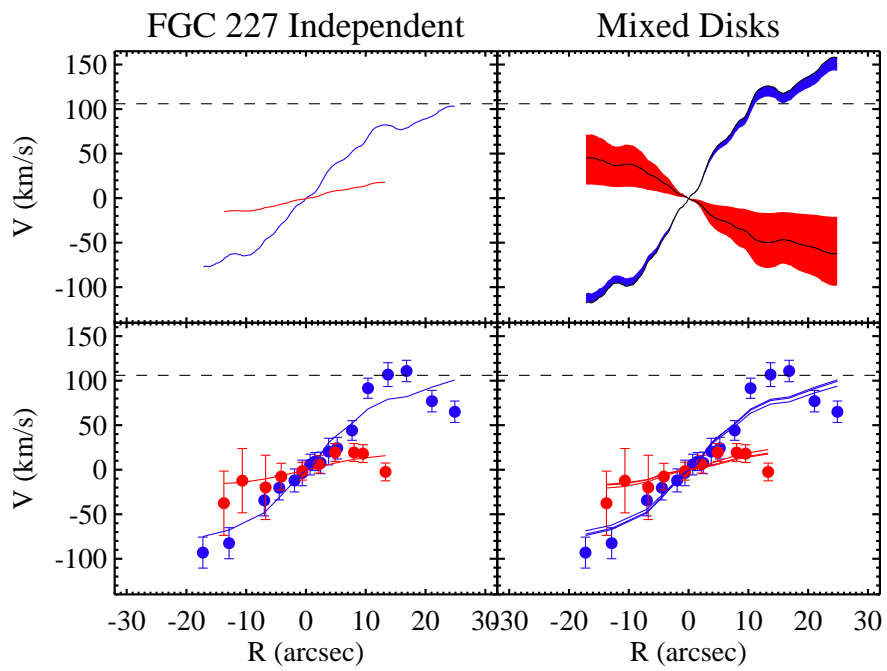


Figure 3.18 Same as Figure 3.13.

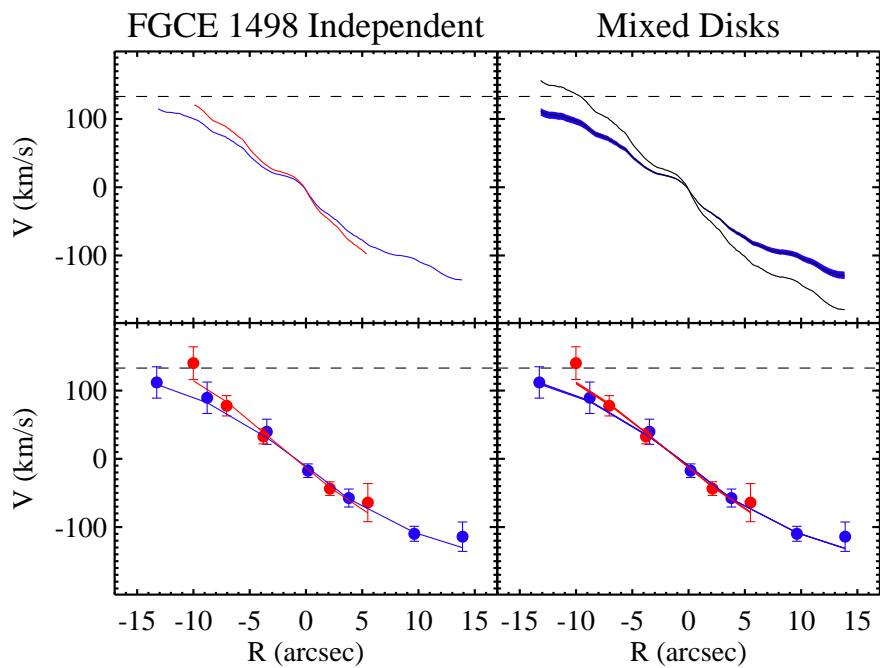


Figure 3.19 Same as Figure 3.13.

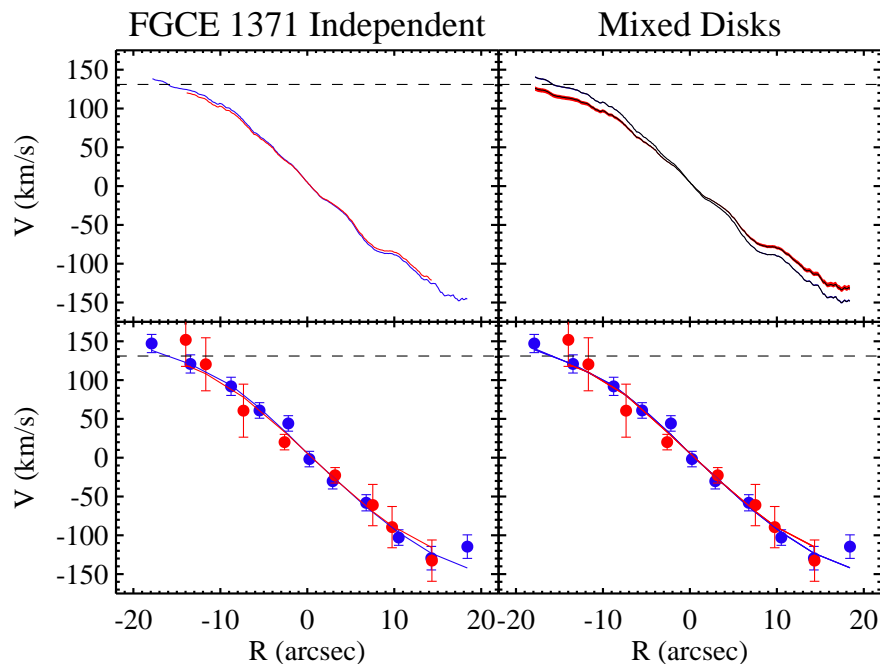


Figure 3.20 Same as Figure 3.13.

have very low velocity dispersions, as we would expect from systems predominantly supported by rotation. Given that our instrumental resolution is 60 km s^{-1} , we are unlikely to resolve the line widths in galaxies where $\sigma/V_c < 0.6$, for the $V_c < 100 \text{ km s}^{-1}$ galaxies that dominate our sample. The major exceptions are FGC 1948, which has an irregular rotation curve, and FGC 227, which has a counter-rotating thick disk.

FGC 1948 has surprisingly large LOSVD, with many regions of the disk having $\sigma > 100 \text{ km s}^{-1}$. For comparison, most of the other galaxies in our sample have LOSVDs across the disk of $\sim 50 \text{ km s}^{-1}$, essentially the same as our instrumental resolution at the Ca II triplet. The stellar rotation curve for FGC 1948 also shows large deviation from the H α RC, suggesting that the stars in this galaxy might not be fully rotationally supported and/or fully dynamically relaxed.

FGC 227's LOSVD also deviates from the simple interpretation of a dynamically

cold rotating disk. In the midplane observations, the central regions of FGC 227 appear cold ($\sigma \sim 40 \text{ km s}^{-1}$), but the outer disk reaches LOSVD values of 100-150 km s^{-1} . This makes little sense for a galaxy with a well defined rotation curve as the intrinsic stellar velocity dispersions should be decreasing with radius. In contrast, the LOSVD can be well explained by a rotationally supported galaxy if there are two stellar populations moving in opposite rotational directions. As our rotation curve decomposition showed, FGC 227 is best fit by a model where the thick disk is counter rotating relative to the thin disk. As we showed in Yoachim & Dalcanton (2005), this would cause an increase in the observed velocity dispersion of order 50 km s^{-1} . Similar projection effects are found in elliptical galaxies with counter-rotating cores as they also show radially increasing LOSVDs (Geha et al., 2005).

3.6 How Much Counter Rotating Material Could There Be?

Inspired by the best-fit rotation curve for FGC 227, we investigate the possibility that all thick disks contain some fraction of counter-rotating stars. Our data is able to place tight constraints on the amount of counter rotating material since both the offplane rotation curves and the midplane LOSVD will be strongly affected by any counter-rotating stars.

In Section 3.5, we imposed thin and thick disk flux fractions based on previous photometric decompositions. We now leave the flux fractions as free parameters and instead hold the rotation curve shapes fixed. We fit two simple models, each with two kinematically independent stellar components. In the first model, we assume there are two stellar components, one rotating identically as the gas and one with zero net rotation, as one might expect for a stellar halo. The final observed rotation curve is a flux weighted average of these two curves and we fit for the best fitting flux ratio. We restricted the explored parameter such that the rotation curves had to be some positive linear combination of the midplane $\text{H}\alpha$ and a non-rotating or counter-rotating rotation curve. In the second model, we assume the second component is

counter-rotating with a velocity one-half the magnitude of the $H\alpha$ rotation curve. For both models, we calculate uncertainties from the covariance matrix and scale them upwards such that the reduced- χ^2 equals unity (i.e., we assume our model should be a good fit). We do not calculate uncertainties when the fit converges to a boundary condition. We also do not construct detailed models for cases like FGC 1415 where the stars could be better fit with a faster rotation curve than the gas; these galaxies naturally converge on the boundary condition of having no second component.

The resulting fractions of non-rotating or counter rotating stars are plotted in Figure 3.21 and are listed in Table 3.4. The midplane stellar rotation curves are typically consistent with the $H\alpha$ rotation curve, with 6 of the 9 midplanes being best fit without a non-rotating or counter-rotating component. The remaining three galaxies do have midplane rotation curves that are consistent with the presence of an additional lagging component. FGC 1948 is low mass with a surprisingly large LOSVD. FGC 227 is the counter rotator with a LOSVD that dramatically increases with radius. FGC 2558 is the only galaxy to show a large discrepancy between midplane and offplane $H\alpha$ rotation curves, has a stellar lag that appears to be only on the receding side of the galaxy.

The offplane spectra show larger evidence for non- or counter-rotating motion, with only 3 of the 9 galaxies requiring no slow rotating component. This effect can be seen in Figure 3.21, where all of the offplane spectra show a preference for equal or larger value of the counter-rotating fraction than seen in the midplane.

3.7 Expected Lags

Having found a wide range of thick disk behaviors, we now investigate the expected stellar lags we should see in our sample of thick disks using a dynamical model originally designed for the Milky Way. The large scale height of thick disk stars implies they have larger velocity dispersions than thin disk stars. If the larger vertical velocity dispersion also reflects a larger radial velocity dispersion, then the larger random

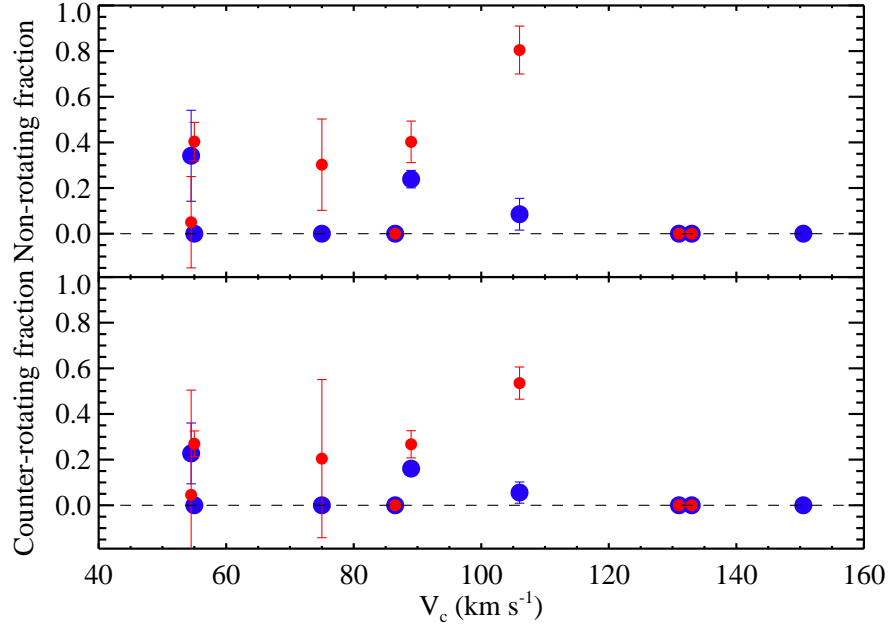


Figure 3.21 Results from fitting the midplane and offplane rotation curves as a combination of two fixed rotation curves. In the top panel, the rotation curves are a combination of the midplane H α and a flat non-rotating RC. In the bottom panel, the base rotation curves are the midplane H α combined with a rotation curve counter-rotating with one-half the H α velocity. These fits are listed in Table 3.4.

Table 3.4. Non-Rotating and Counter Rotating Fractions

FGC	Non-Rotating Fraction		Counter-Rotating Fraction	
	Thin Disk	Thick Disk	Thin Disk	Thick Disk
227	0.1 \pm 0.1	0.8 \pm 0.1	0.1 \pm 0.0	0.5 \pm 0.1
780	0.0	0.3 \pm 0.2	0.0	0.2 \pm 0.3
1415	0.0	0.0	0.0	0.0
1440	0.0	...	0.0	...
1642	0.0	0.4 \pm 0.1	0.0	0.3 \pm 0.1
1948	0.3 \pm 0.2	0.1 \pm 0.2	0.2 \pm 0.1	0.0 \pm 0.5
2558	0.2 \pm 0.0	0.4 \pm 0.1	0.2 \pm 0.0	0.3 \pm 0.1
E1371	0.0	0.0	0.0	0.0
E1498	0.0	0.0	0.0	0.0

motions of thick disk stars should lead to their requiring less rotational support. The thick disk stars should therefore lag in velocity compared to the kinematically colder thin disk stars and ionized gas.

Girard et al. (2006) use the Jeans equation and a series of reasonable assumptions to model the expected thick disk lag in the MW as a function of height above the midplane. While this model was built to explain the observed lag of thick disk stars in the Milky Way, the formalism is easily generalizable to the galaxies in our sample.

Using the Jean’s equation, Girard et al. (2006) find that the rotational velocity of a thick disk rotating in a Plummer dark matter potential with an embedded thin disk is given by:

$$\begin{aligned} \overline{v_\Theta}^2(z, R) = \sigma_R^2(z) \left[-\Upsilon_{a,b}R + 0.5\lambda \left(1 - \frac{z}{h_{zthick}} \right) + 1 - \frac{\sigma_\Theta^2}{\sigma_R^2} \right] \\ + \frac{(v_c^2 - v_{disk}^2(R, 0))(R^2 + a^2)^{3/2}}{(R^2 + z^2 + a^2)^{3/2}} + v_{disk}^2(R, z), \end{aligned} \quad (3.1)$$

where R , z , and Θ are galactocentric cylindrical coordinates. The term $\overline{v_\Theta}$ is the average thick disk velocity in the direction of galactic rotation, σ_R and σ_Θ are the radial and tangential components of velocity dispersion for the thick disk stars, v_c is the local standard of rest velocity at the radius of interest, v_{disk} is the portion of the thick disk rotational velocity due to the gravitational potential of the thin disk, h_{zthick} is the exponential thick disk scale height and a is the halo core radius. The term $\Upsilon_{a,b}$ lets one approximate the thick disk as entirely self gravitating, or gravitationally dominated by the embedded thin disk. Because the thick disk mass is small compared to the total gas and thin disk mass in all of our galaxies, we choose to use $\Upsilon_b \sim 2/h_R$. The λ term takes values of 1 or 0 in order to include or exclude the velocity dispersion cross-term.

We calculate dynamical models for three fiducial galaxy masses and three thick disk velocity dispersions. We use realistic galactic parameters taken from Yoachim &

Dalcanton (2006b) to generate $h_{z_{thick}}$ and $v_{disk}^2(R, 0)$. For terms for which we do not have explicit measurements, we use the approximation $a[\text{kpc}] \approx 13(h_{r_{thin}}[\text{kpc}]/5)^{1.05}$ given by Donato et al. (2004), assume $\sigma_{\Theta} \sim \sigma_R$, and set $\lambda = 0$. We compute models for different values of σ_R , as this is the dominant term in producing stellar lags. For simplicity, we assume the thick disk velocity dispersion does not vary with height above the midplane. This last approximation is not particularly valid given that Girard et al. (2006) find that the velocity dispersion in the MW increases with a slope of $9 \text{ km s}^{-1}\text{kpc}^{-1}$. However the difference between a variable and constant velocity dispersion will be most pronounced at large scale heights, beyond the range probed by our observations ($z \sim 1.5 - 2 \text{ kpc}$). The resulting models are plotted in Figure 3.22 along with the lags we have measured in our galaxies. For reference, we also include a model using the same assumptions but with morphology and velocities similar to the Milky Way in Figure 3.22.

For most of the galaxies where we measure a thick disk lag, Figure 3.22 shows the thick disk kinematics could be well explained by a population with radial velocity dispersion of between 15 and 30 km s^{-1} and $v_c/\sigma < 4$. As before, the major exception is FGC 227. The stellar lag for FGC 227 is so severe that it would imply the thick disk is completely supported by random motions. However, we only detect flattened stellar populations in FGC 227, again consistent with our interpretation that the thick disk is counter-rotating in this system.

To verify that our model galaxies are reasonable, we use an identical procedure to build a MW-like model. Our MW-like model is a fair fit to actual observations of the MW. The measured thick disk velocity dispersion in the solar neighborhood is 50 km s^{-1} , for which our model correctly predicts the midplane thick disk lag of 30 km s^{-1} . On the other hand, the increase of the thick disk lag with scale height is poorly fit by our model; the observed lag increases with a slope of $30 \text{ km s}^{-1}\text{kpc}^{-1}$, and our model has a slope around half that. This is purely due to our choice to hold the velocity dispersion fixed—a thick disk velocity dispersion that increased with height

would generate a more accurate slope.

Modeling the disks as cylindrically rotating is only a crude approximation to account for the stellar cross-contamination. In reality, we expect the thin disk stars which reach large z heights to be the thin disk stars with larger velocity dispersions. This would mean that the thin disk stars at high z should also be lagging compared to the midplane thin disk stars. Ideally, we would construct a fully self-consistent dynamical model of each galaxy, but our large uncertainties and limited LOSVD information would result in model degeneracies. Constructing a robust self consistent dynamical model of a galaxy also benefits from larger numbers of data points (Girard et al., 2006). With only a handful of stellar rotation curve points per galaxy, we do not have enough data to constrain a more complex model. We simply point out that when we correct for the cross-contamination of the rotation curves we may be overcorrecting the data. We estimate the magnitude of the overcorrection using dynamical models in § 3.7.

3.8 Dust and Projection Effects

As a final check that our observed kinematics indeed reflect the true stellar motions, we now explore the expected impact of projection effects and dust extinction, both of which can create differences between the observed and underlying rotation curves. In Figure 3.23, we show how two input rotation curves are modified by being viewed edge-on, with and without dust. For these models, we assumed an exponential disk of stars and dust, and for simplicity only considered absorption (i.e. ignoring scattering). The amount of dust adopted in the model would generate an extinction of 2.2 magnitudes in the total apparent magnitude of the galaxy. This is a rather large extinction for the near-IR, given that the observed galaxies in our sample are only offset by 0.2 mag from the face-on NIR Tully-Fisher relation (Yoachim & Dalcanton, 2006b). We adopted an underlying rotation curve shape from Courteau (1997).

As can be seen from Figure 3.23, the inner regions of the rotation curve are

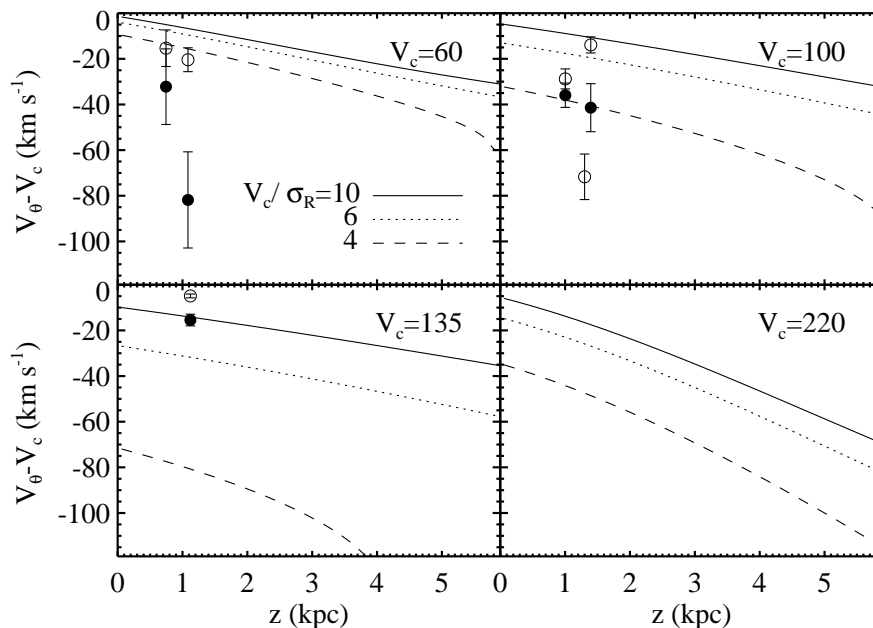


Figure 3.22 The expected thick disk lags as a function of height above the midplane and thick disk velocity dispersion. The first three panels show model galaxies similar to the ones in our sample. Points show the stellar lags measured from our rotation curve fits. Open points show lags from rotation curves where the offplane and midplane rotation curves are fit independently. Solid points show the average lag for the models which correct for cross-contamination of the thin and thick disk rotation curves, and are generally more reliable estimates of the thick disk lag. The final panel shows the results of our model when we use MW like parameters. Observed galaxies we compare to the models: In the upper left FGC 1642 and FGC 780; upper right FGC 1415, FGC 227, and FGC 2558; and lower left FGCE 1371. All the models and observations are taken at $R = 2.5h_R$. FGC 1948 is excluded from the plot because there is no coherent rotation (so it doesn't make sense to measure a lag. FGC 1440 is excluded because we have no offplane stellar velocity measurements.

generally unchanged due to projection, and the only significant changes happen in the outer parts, where the true rotation curve is flat. These projection effects create a lag of 7.2 km s^{-1} .

We have not corrected our rotation curves for these projection effects, as we are primarily interested in the differences between the thin and thick disk rotation curves. This could lead us to make systematic errors in interpreting the rotation curves if the morphologies of the thin and thick disk are radically different, but we have no reason to assume this is the case.

When dust is added to the model, it creates an additional 2.6 km s^{-1} lag, in spite of the very high extinction adopted here. This model is completely consistent with the results of Matthews & Wood (2001), who found that projection effects are dominant compared to extinction in edge-on systems. We do not expect our sample galaxies to have larger extinctions than assumed in the model in Figure 3.23.

Full radiative transfer models (Kregel & van der Kruit, 2005; Bianchi, 2007; Xilouris et al., 1999), as well as comparisons of gaseous and optical rotation curves (Bosma et al., 1992) have consistently found massive disk galaxies have a central face-on optical depth near unity in the V -band, with lower extinction levels in less massive systems like those that dominate our sample (Calzetti, 2001). Dust levels this low should not be expected to alter the observed rotation curve significantly, even if a galaxy is viewed edge-on. Moreover, most of our offplane rotation curves exhibit a lag compared to the midplane. In contrast, If there were strong dustlanes affecting our midplane observations (and not the offplane), the midplane would be the lagging component.

The combination of working at near-IR wavelengths, offsetting our slit from any prominent dustlanes, and observing intrinsically linearly rising rotation curves means our rotation curves should be fairly unaffected by extinction or projection. However, the same cannot be said for our measured line-of-sight velocity dispersion (LOSVD). Unlike the rotational velocity measurement, which is mostly unaffected by flux con-

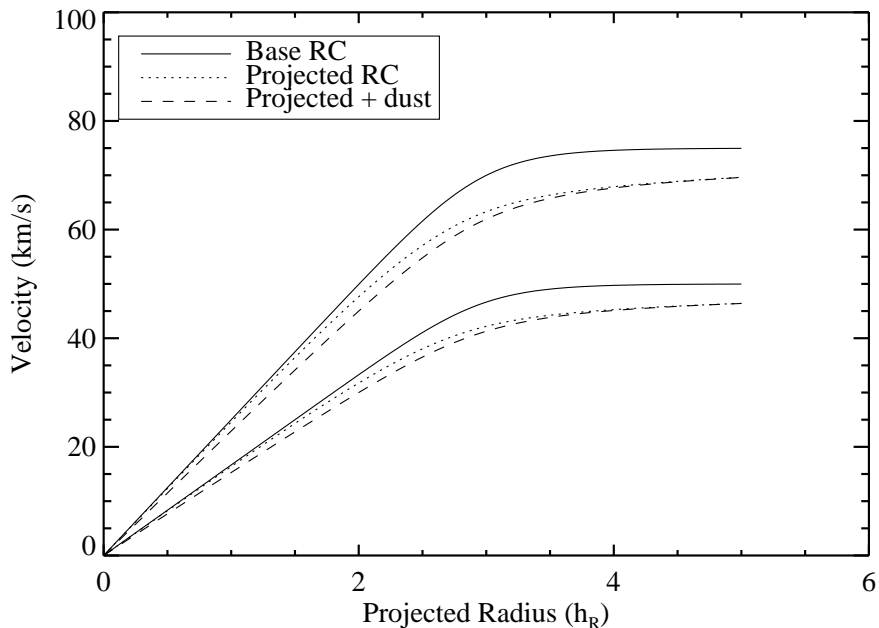


Figure 3.23 Two examples of the effects dust and projection will have on our observed rotation curves. While projection creates considerable changes, the addition of dust extinction is negligible.

tributions from different radii, we expect the LOSVD to be significantly broadened by projection effects. We also find that in most of our galaxies the LOSVD is very close to the instrumental resolution, making any interpretation of the velocity dispersion suspect. Because of these challenges, we limit our analysis of the LOSVD to only those cases where we believe our measurements are of high quality and not dominated by the instrumental dispersion.

3.9 Discussion

The results of Sections 3.4.2 and 3.5 show that thick disk kinematics display a wide range of behaviors. In higher mass systems (FGCE 1371, FGCE 1498, FGC 1440), our midplane and offplane spectra show no clear signature of a hot thick disk component. The stellar rotation curves for these galaxies are well matched by the midplane ionized

gas $H\alpha$ RCs. All three of these galaxies converged to models where the rotation curves contain no lagging component (Table 3.4). The lack of any observed lag in these higher mass galaxies is probably best interpreted as insufficient flux from the thick disk component in our offplane slit. Yoachim & Dalcanton (2006b) found that the stellar flux in higher mass galaxies are dominated by the thin disk component. Therefore, the lack of a significant lag in these systems is just a result of the kinematically cold thin disk dominating the stellar flux to scale heights of 1 kpc. This result is not completely unexpected, as the MW thin and thick disks should have similar luminosities 1 kpc off the midplane. We note that there is still ample photometric evidence that these higher mass galaxies contain thick disks, but they are simply too faint relative to the thin disk to be observed spectroscopically.

The low mass galaxies in our sample do show measurable differences between the midplane and offplane observations. At large radii, we find several galaxies where the offplane component is lagging compared to the midplane (Figure 3.22). In three of the low mass systems (FGC 1415, FGC 1642, and FGC 780), the lags in the offplane observations become more pronounced when we correct for the expected thin disk contamination. These lags are consistent with those that are expected from dynamics alone (Equation 3.1), provided that the thick disk has a radial velocity dispersion between 15 and 30 km s^{-1} (i.e., 10-25% of v_c). Thus, the lags in these systems do not necessarily require the presence of counter-rotating material, although a small amount of such material could be present. FGC 2558 may also fall into this category; however the offplane RC is very similar to the midplane, implying this could be another galaxy where we have not successfully isolated the thick disk. The observed lags were easier to detect in these lower mass systems, due to their more prominent thick disks.

The final two low mass galaxies in our sample, FGC 227 and FGC 1948, have remarkably different rotation curves between the midplane and offplane. FGC 1948 does not display coherent stellar rotation in either the midplane or the offplane, and therefore our subsequent fits converge to extreme, and probably incorrect, models.

FGC 227 does show rotation on the midplane, and a very low level of net rotation on the offplane. Our best fitting model for this galaxy has the thick disk counter-rotating relative to the thin disk, consistent with the radially increasing LOSVD which is a signature of unresolved counter rotating stellar components.

Our measurements of the LOSVD are less than enlightening. With the exception of the radial increase in the LOSVD in FGC 227 and the high LOSVD in FGC 1948, the rest of our LOSVD measurements show no significant trends with radius and are close to the instrumental resolution limit, suggesting that the radial velocity dispersions of both the thin and thick disks are cold enough that we cannot reliably measure their velocity dispersions at our spectral resolution.

Given the above results, our galaxies can be described as falling into three categories: The high mass systems which have little to no thick disk lag (or, more likely, thick disks which are so faint that we have failed to measure their kinematics); the moderately lagging systems; and the counter rotating system. We can now compare these results to the predictions of popular formation models for the thick disk.

If thick disks are the result of gradual stochastic heating, we would expect to always find thick disks co-rotating with the embedded thin disks. Moreover, with stronger spiral arms, larger molecular clouds, and more massive dark matter substructure, the high mass systems should be able to more efficiently heat their thin disk stars into a thicker disk. Instead, we have found the opposite, with more prominent thick disks with larger lags in the lower mass systems, and evidence for counter-rotating stars. This seems to rule out gradual heating as the dominant method of thick disk formation, particularly for low mass galaxies.

Forming thick disks in major mergers also does a poor job explaining our observations. If thick disks were predominantly formed in major mergers that disrupt and heat previously thin disks, we should expect to find galaxies that never had a thick disk creation event, or galaxies which have failed to accrete and cool enough gas to rebuild their thin disk components. Major mergers also typically result in the forma-

tion of large spheroidal components, making them a poor mechanism for forming a thick disk in the bulge-less disks observed here.

Unlike the two heating models, the variety of thick disk kinematics is compatible with minor mergers and/or accretion. Presumably, the thick disk kinematics we observe are simply the kinematics left over from the accretion event which deposited the majority of thick disk stars or which triggered the formation of stars from gas accreted at large scale heights. The wide variety of possible accretion events (co-rotating vs counter rotating, early disruption vs late disruption, high eccentricity vs circular initial orbit) can evolve into virialized thick disks with kinematics that are sometimes decoupled from the thin disks and that show large variation from galaxy to galaxy. The ubiquity of thick disks is also well explained by the merger/accretion scenario, given that galaxy formation in a Λ CDM cosmology is dominated by hierarchical merging, and predicts that every galaxy has a rich merger history.

Although the available data all points to a merger/accretion origin for the thick disk, it is difficult to disentangle models where thick disk stars are directly accreted from those where the stars form *in situ* further off the midplane during gas rich mergers (Brook et al., 2004).

This ambiguity results from two sources. First there is no clear dividing line between what one calls a star-forming region off the midplane and a merging star-forming satellite galaxy. Second, we know from Yoachim & Dalcanton (2006b) that at least 75-90% of accretion onto galaxies was gaseous, and some fraction of this was certainly accreted in bound subhalos. The kinematics of stars that formed in the subhalos and accreted are likely to be similar to those that formed from gas in the subhalos during accretion, making the two scenarios difficult to distinguish. Presumably, one could use detailed stellar age and abundance information to help, but unfortunately this is only possible for the closest galaxies.

In this study, we have measured thick disk kinematics in only very late-type disk systems. However, thick disks have been photometrically detected in a wide variety

of Hubble types (e.g., Seth et al., 2005b; Pohlen et al., 2004; Morrison et al., 1997; van Dokkum et al., 1994). The kinematics in our sample are most consistent with merger/accretion forming for the thick disks, but, except for the Milky Way, there have been no measurements of thick disk kinematics in earlier type galaxies.

By focusing on disk systems, we may not be sensitive to how thick disks form across all Hubble types. Almost by definition, late-type galaxies have not suffered a major-merger since the formation of their stellar disks, otherwise they would possess large spheroidal components and be classified as an earlier type system. The only way pure disk galaxies could form thick disks is either through accretion or stochastic heating.

3.10 Conclusions

We have expanded the kinematic observations of Yoachim & Dalcanton (2005) to include a total of nine galaxies with thick disks. Analyzing our low signal to noise spectra with the presence of systematic sky line residuals prompted us to develop a brute-force method of cross-correlation in order to extract stellar rotation curves. In Galaxies with $V_c > 120 \text{ km s}^{-1}$, we do not detect any measurable difference between the thin and thick disk stellar kinematics. This is most likely due to a combination of thin disks being brighter in more massive galaxies, and the expected change in rotation curve as a function of scale height is smaller.

In lower mass galaxies ($V_c < 120 \text{ km s}^{-1}$), we find a variety of thick disk behaviors. Thick disks are found which both small and large magnitude lags, as well as a counter-rotating thick disk.

The observed kinematics are best explained by thick disk formation models where the thick disks are composed of stars that have been accreted from satellite galaxies. Models where the thick disks form during major mergers or through stochastic heating would be unable to explain the wide range of thick disk kinematics we observe. While we strongly favor a formation model of thick disks via stellar accretion, we stress that

this result can not necessarily be generalized other Hubble types.

3.11 Stellar Rotation Curves in the Presence of Systematic Errors

Working in the near-IR, we find our spectra have regions which are dominated by both Gaussian and systematic errors caused by bright atmospheric emission lines. To properly measure stellar kinematics based on spectral absorption features we must employ a method that is not affected by our sky line residuals.

There are two common techniques of deriving the kinematic information from galaxy spectra—direct χ^2 -fitting and cross-correlation. In direct χ^2 -fitting (Rix & White, 1992; Kelson et al., 2000; Barth et al., 2002), a template star is redshifted and broadened to fit a galaxy spectrum, while in cross-correlation techniques (Simkin, 1974; Tonry & Davis, 1979; Statler, 1995) a template star is cross-correlated with the galaxy spectrum and the kinematic properties are deduced from the position and shape of the cross-correlation peak.

Cross-correlation techniques have the advantage of being computationally efficient, often making use of fast Fourier transform algorithms. The cross-correlation technique benefits greatly from the fact that the Fourier transform of Gaussian noise is also Gaussian noise. In this way, noise in the galaxy spectrum transforms into random noise in the cross-correlation while the kinematic information becomes concentrated in the peak. However, this is only true if the noise is uniform throughout the spectrum. Using a direct chi-squared fit is more computationally expensive, but has the added benefit of being able to weight individual wavelengths according to their specific signal-to-noise, or completely mask wavelengths that are affected by systematic errors.

Although direct chi-squared fitting works well in some situations, at low S/N (<20), any direct chi-squared fitting routine will over-smooth the data because the low S/N continuum is best fit by a straight line (i.e., an over-broadened template star). In previous studies that have used direct fitting, Kelson et al. (2000) has a median S/N of $35/\text{\AA}$, while Barth et al. (2002) report a S/N/pixel of 100-200. In contrast, our

data has $\text{SNR} < 20/\text{\AA}$, due to the very low surface brightness of our targets.

Because we have both low S/N and regions which require masking, we have created a fitting procedure which utilizes cross-correlation without making use of the computational time saving FFT techniques of previous authors.

Traditional cross-correlation of discrete functions is defined as

$$(f \star g)_i \equiv \sum_j f_j g_{i+j}. \quad (3.2)$$

We adopt a normalized version, where the means of the spectra have been subtracted before the cross-correlation is computed

$$(f \star g)_L = \frac{\sum_{k=1}^{N-L} f_L g_{k+L}}{\sqrt{\sum_{k=1}^N (f_k)^2 \sum_{k=1}^N (g_k)^2}}, \quad (3.3)$$

where N is the number of points in the given spectra. For lags less than zero, the numerator becomes $\sum_{k=1}^{N-|L|} f_{k+|L|} g_k$. This ensures spectra with perfectly matching shapes will have a maximum cross-correlation amplitude of unity.

Finally, we define masks δ for each spectrum which have values of 1 in regions of good data and 0 for masked wavelengths. Given a stellar spectrum S and Galaxy spectrum G that are binned in logarithmic wavelength intervals and have both been normalized by division of a low order polynomial and had their means subtracted, we compute our modified cross-correlation as

$$(S \star G)_L = \frac{\sum_{k=1}^{N-L} S_L G_{k+L} \delta_S \delta_G}{\sqrt{\sum_{k=1}^N (S_k \delta_S \delta_G)^2 \sum_{k=1}^N (G_k \delta_S \delta_G)^2}}. \quad (3.4)$$

We then generate a model galaxy spectrum M by redshifting and broadening the stellar template, $M(x) = S(x+v) \otimes B(x)$ where $B(x)$ is a Gaussian broadening function, v is a velocity shift, and \otimes represents convolution. We then calculate the

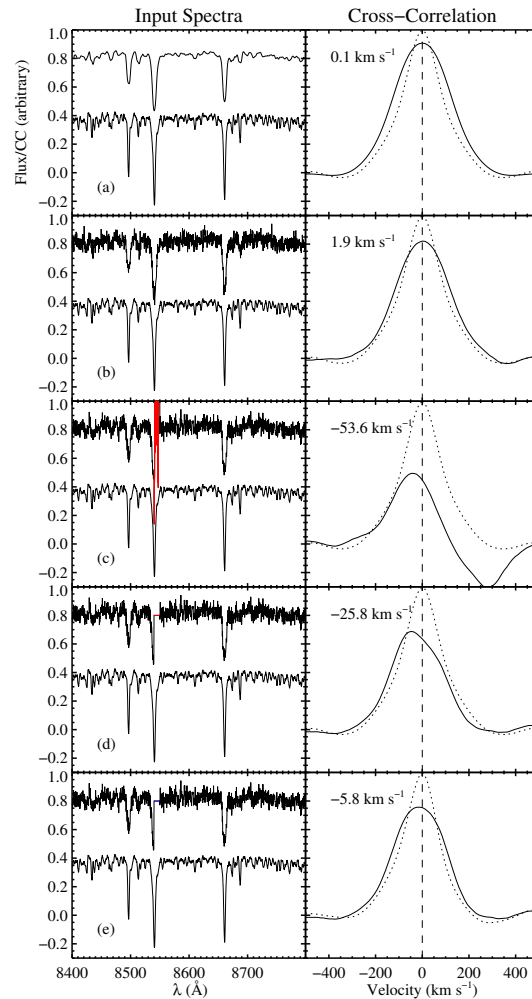


Figure 3.24 Examples of cross-correlating in the presence of different types of noise. In the left hand column, we show a model galaxy spectrum (top) and stellar template (bottom). In the right hand column, we plot the galaxy-star cross-correlation (solid) and stellar auto-correlation (dotted) and note the velocity error resulting from comparing the two. (a) The ideal case of a high signal-to-noise galaxy spectrum. (b) Results from a galaxy spectrum with a $S/N/\text{\AA} \sim 10$. (c) Spectra with a region marked in red of very low S/N affecting a section of one of the Ca absorption features, similar to how bright sky lines leave residuals on our spectra. (d) A traditional cross-correlation where the noisy region has been set to the continuum. (e) Our new cross-correlation technique where we compute the cross-correlation excluding the masked region.

model's modified cross-correlation using the masks from the actual galaxy spectrum

$$(S \star M)_L = \frac{\sum_{k=1}^{N-L} S_L M_{k+L} \delta_S \delta_G}{\sqrt{\sum_{k=1}^N (S_k \delta_S \delta_G)^2 \sum_{k=1}^N (M_k \delta_S \delta_G)^2}}. \quad (3.5)$$

We vary the velocity shift and broadening to minimize the χ^2 between $(S \star G)$ and $(S \star M)$. We focus on the region of the primary peak, and clip regions beyond the bracketing local minima. Examples of traditional cross-correlation and our modified cross-correlation are shown in Figure 3.24. In general, our masked cross-correlation technique cannot reproduce the excellent fits that are possible with data that is unaffected by systematics, but we can reduce the errors to be of order 5 km s^{-1} in our typical spectra.

Chapter 4

AGES AND METALLICITIES OF THIN AND THICK DISKS USING LICK INDICES

4.1 Chapter Summary

We have measured Lick index equivalent widths to derive luminosity weighted stellar ages and metallicities for thin and thick disk dominated regions of 9 edge-on disk galaxies with the ARC 3.5 meter telescope at Apache Point Observatory. In all cases, the thick disks are confirmed to be old stellar populations, with typical ages between 5 and 12 Gyr. The thin disks are uniformly younger than the thick disks, and show strong radial age gradients, with the outer regions of the disk being younger than 1 Gyr. We do not detect any significant metallicity differences or α -element enhancement in the thick disk stars compared to the thin disk, due to the insensitivity of the Lick indices to these differences at low metallicity. We compare these results to thick disks measured in other systems and to predictions from thick disk formation models.

4.2 Introduction

Old stellar populations present a fossil record of a galaxy's early formation and evolution. In the Milky Way, the stellar thick disk and halo have been recognized as the oldest stellar components and studied extensively. Stars in the MW thick disk are old (~ 8 -12 Gyr), and are metal poor when compared to local thin disk stars (Reid & Majewski, 1993; Chiba & Beers, 2000). Their chemical composition shows that they are enhanced in α -elements compared to thin disk stars, suggesting a rapid formation timescale (< 1 Gyr) (Bensby et al., 2003, 2005; Prochaska et al., 2000).

Because stellar thick disks and halos are intrinsically low surface brightness features, they have been observed in detail in only a handful of galaxies. Thick disks have been photometrically detected as an excess flux at large galactic latitudes across a range of Hubble types (Dalcanton & Bernstein, 2002; Burstein, 1979; Tsikoudi, 1979; de Grijs & van der Kruit, 1996; de Grijs & Peletier, 1997; Pohlen et al., 2004; van der Kruit, 1984a; Shaw & Gilmore, 1989; van Dokkum et al., 1994; Morrison et al., 1997; Wu et al., 2002; Abe et al., 1999; Neeser et al., 2002), as well as detected in star counts using resolved stellar populations from HST (Seth et al., 2005b; Mould, 2005; Tikhonov et al., 2005; Tikhonov & Galazutdinova, 2005).

Three general classes of formation mechanisms have been put forward to explain the formation of thick disks. In the first, a previously thin disk is kinematically heated. In this scenario, stars form in a thin disk and gradually increase their velocity dispersion with time. This vertical heating can be rapid, due to interactions and mergers (Quinn et al., 1993; Walker et al., 1996; Velazquez & White, 1999; Chen et al., 2001; Robin et al., 1996) or gradual due to scattering off giant molecular clouds, spiral arms, and/or dark matter substructure (Villumsen, 1985; Hänninen & Flynn, 2002; Benson et al., 2004; Hayashi & Chiba, 2006). In the second formation scenario, stars “form thick” with star formation occurring above the midplane of the galaxy (Brook et al., 2004) or form with large initial velocity dispersions in massive stellar clusters (Kroupa, 2002). In the final class of models, thick disk stars are directly accreted from satellite galaxies. Numerical simulations have shown that stars in disrupted satellite galaxies can be deposited onto thick disk like orbits (Abadi et al., 2003b; Martin et al., 2004; Bekki & Chiba, 2001; Gilmore et al., 2002; Navarro et al., 2004; Statler, 1988). While these models were originally developed to explain the origin of the MW thick disk, they should work equally well for thick disks in other massive galaxies.

On the other hand, some of these mechanisms are likely to be less effective in lower mass galaxies which have lower density disks, little or no spiral structure, and fewer satellites hosting stars. Lower mass galaxies also have different formation times,

environments, and gravitational potentials which may also lead to variation in the mass, age, and metallicity of thick disks of low mass galaxies.

To test these formation models, detailed comparisons of thin and thick disk properties are required across a range of galaxy masses. In particular, the relative ages and chemical enrichment patterns of the thin and thick disks should differ among these formation models. If the thick disk is just a gradually kinematically heated thin disk, there should be a smooth age and enrichment gradient between the two. In contrast, if the thick disk is formed from accreted stars we should expect the ages and metallicities of the thin and thick disks to be only weakly correlated. We may also expect to see variations with the mass of the galaxies, with less massive galaxies being more susceptible to external heating and more massive galaxies being better able to tidally disrupt satellites.

Measuring the ages and metallicities of thick disks outside the MW has proved to be challenging. Ages and metallicities can be derived from isochrone fits to thin and thick disk stars resolved with HST, provided that the host galaxies are sufficiently close and oriented edge-on to the line of sight. The systems studied this way show older populations at large scale heights but little vertical metallicity gradient, at least for the low mass ($V_c, 100 \text{ km s}^{-1}$) which dominate these samples (Seth et al., 2005b; Tikhonov et al., 2005; Mould, 2005).

For the systems that are farther away, only broadband colors have been used to estimate the ages and metallicities of the thick disks. When thick disks are photometrically detected, they typically have very red colors ($B - R \sim 1.3 - 1.5$) (Yoachim & Dalcanton, 2006b; Dalcanton & Bernstein, 2002; van Dokkum et al., 1994) suggestive of an old population. However, stellar parameters are notoriously difficult to derive from broadband colors due to the age-metallicity degeneracy in the optical colors, and a lack of IR-colors at the low surface brightnesses of the thick disk region. In disk systems some progress has been made in measuring the metallicity of the disk using high signal-to-noise emission lines (e.g. Tremonti et al., 2004; Zaritsky et al., 1994;

van Zee et al., 1998), and in measuring metallicity gradients (e.g., Zaritsky et al., 1994). While the emission lines studies can constrain the total chemical enrichment a galaxy has experienced, they tell us nothing about the underlying stellar populations in the galaxies. Emission lines are also unable to provide constraints on the properties of extra-planar stellar populations, which are likely to be dominated by old, dormant stellar populations.

To better measure the ages and metallicities of thick disks in a larger sample of galaxies, we turn to the integrated spectrum of these galaxies and use the Lick/IDS absorption line system to derive luminosity-weighted stellar population properties. The Lick indices were originally developed for studying older stellar populations (Burstein et al., 1984; Faber et al., 1985), and have been used extensively in analyzing elliptical galaxies and globular clusters (e.g., Trager et al., 1998, 2000a; Sánchez-Blázquez et al., 2007). Worthey et al. (1994) showed that using a combination of age sensitive (i.e. Balmer lines) and metallicity sensitive (Mg *b*, and Fe) indices, one can lift the age-metallicity degeneracy for a stellar population. Stellar spectral libraries have now been used to create SSP models over a large range of metallicity and age combinations (Worthey, 1994; Vazdekis & Arimoto, 1999), including models with variable α -element enhancement (Thomas et al., 2003). The tools also now exist to calculate expected Lick indices for composite stellar populations (Bruzual & Charlot, 2003).

Despite the development of stellar synthesis codes that can be extended to younger stellar populations, relatively few studies have attempted to observe Lick indices in disk galaxies. Studies using tunable filters have been able to detect Mg and Fe index gradients in disks (Beauchamp & Hardy, 1997; Ryder et al., 2005), but have not been combined with measurements of age-sensitive indices. Studies of disk systems have tended to focus on the high surface brightness bulge components (Moorthy & Holtzman, 2006; Peletier et al., 2007; Prugniel et al., 2001; Proctor et al., 2000), and fail to reach very far into the disks. In the most extensive study observing Lick indices in disk galaxies, MacArthur (2006) observed Lick indices in 8 galaxy disks, including

several late-type galaxies. These observations probed to ~ 1 scale length. However, all of these galaxies were fairly face-on, preventing thick and thin disk components from being separated.

In this paper, we target regions of edge-on galaxies that are dominated by both the stellar thick disk and thin components. We then compare ages and metallicities derived from Lick indices both between the two components and from galaxy-to-galaxy.

4.3 Observations

The original sample of 49 galaxies was selected from the Flat Galaxy Catalog (Karachentsev et al., 1993) and imaged in B , R , and K_s (Dalcanton & Bernstein, 2000b). Dalcanton & Bernstein (2002) used this imaging to demonstrate the ubiquity of thick disks around late-type galaxies. We have since used two-dimensional decompositions of the galaxy images to measure structural parameters for the thick and thin disks (Yoachim & Dalcanton, 2006b). We have also measured kinematic properties of the thick and thin disks using GMOS on the Gemini telescopes (Yoachim & Dalcanton, 2005, 2007).

For this study, we selected a subset of galaxies where the photometric decompositions suggested we would be able to isolate thin and thick disk regions and obtain adequate signal-to-noise spectra. This limits us to observing predominantly lower-mass galaxies, as Yoachim & Dalcanton (2006b) found these are the galaxies with proportionally larger thick disks.

Observations were made using the Dual Imaging Spectrograph (DIS) on the ARC 3.5 meter telescope at Apache Point Observatory (APO) between June 2003 and February 2006 during a total of 34 half-nights of observing. Although the telescope aperture is much smaller than used for previous studies (3.5m compared to 8m), we were able to reach the needed signal-to-noise using a novel slit design. Spectroscopy of extended low surface brightness objects has traditionally been limited by the need

to collect a large number of photons while maintaining adequate spectral resolution. However, since the Lick indices are defined at low spectral resolution ($\sim 8\text{\AA}$) and cover a limited wavelength range, it is possible to capture more photons by using a much wider slit to feed a spectrograph with a higher resolution grating. We therefore built a custom $5'' \times 4'$ slit for all our observations to allow the largest possible amount of light to reach the detector. On the blue side, we used a grating with 1200 lines/mm and on the red side, 830 lines/mm. The resulting spectral resolution was $4.9(7.1)\text{\AA}$ FWHM as measured from calibration lamps for the blue(red) chip. The blue chip gave wavelength coverage from $4390\text{-}5430\text{\AA}$ sufficient to measure the age sensitive $H\beta$ and metallicity sensitive Mg and two Fe Lick indices. The red side covered $6140\text{-}7860\text{\AA}$, which allowed us to measure the strength of the $H\alpha$ line. The CCDs were binned by 2 during readout in the spectral direction to reduce read noise. Combining a large aperture slit with a high resolution grating is an unconventional setup, but the increased throughput of the wide slit allows us to observe the low surface brightness regions where the thick disk dominates.

The slit camera on DIS allowed us to accurately place the slit by centroiding nearby bright stars. The slit camera has a plate-scale of $0.298''/\text{pixel}$, and we were typically able to place the slit within 1 pixel of our target region. Slit camera images were taken throughout long exposures to ensure accurate tracking. For each galaxy, we gathered spectra at the midplane as well as at several vertical scale heights above the midplane where photometric decompositions imply the majority of flux should be supplied by the thick disk component. Images of the slit placement are shown in Figure 4.1 and the observation log is listed in Table 4.1.

We found that there were several prominent skylines near the relevant indices that would slowly fade for several hours after sunset. Most problematic was a skyline of OH at 5200\AA , which often contaminated the Mg b index. To avoid the skylines, we took advantage of the APO 3.5m scheduling system which allocates observations in half-night intervals and scheduled most of our observations for the second half of the

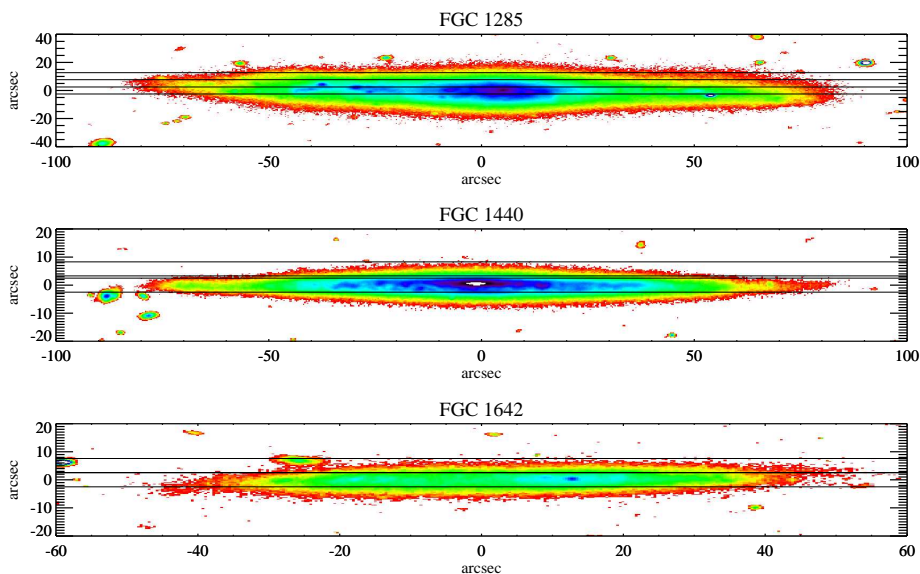


Figure 4.1 R -band images of our galaxy sample with the APO longslit positions overlaid. All images are stretched to include $20 < \mu_R < 24.2 \text{ mag}/\square''$

night.

4.4 Data Reduction

Data were processed with standard IRAF/PyRAF routines along with several custom scripts written in IDL. Reduction steps for the red and blue side were identical unless otherwise noted. All the frames were bias corrected by subtracting the mean from the overscan region. Any residual bias structure was removed by subtracting a bias frame constructed from 5-10 bias exposures taken every night. For one half night (Feb 11, 2004 observations of FGC 913), the blue chip suffered from 60 Hz noise which resulted in diagonal streaks across the images. This pattern was removed by shifting and subtracting a single bias frame that had similar variation in the readout pattern. The images were flat-fielded using spectra of a quartz lamp. Spectra of the twilight sky showed no need for an illumination correction. The spectra were wavelength calibrated using He, Ne, and Ar arc lamps along with night-sky emission

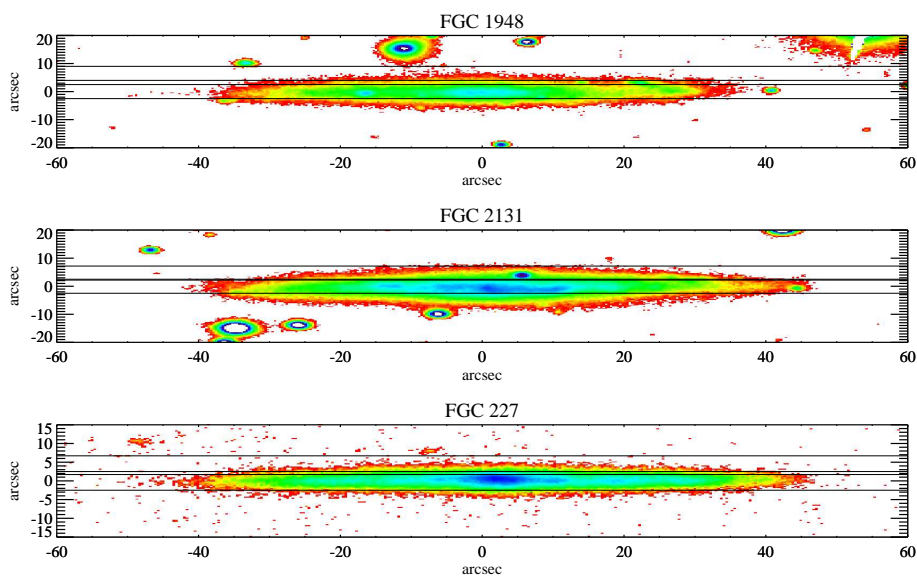


Figure 4.2 Same as Figure 4.1.

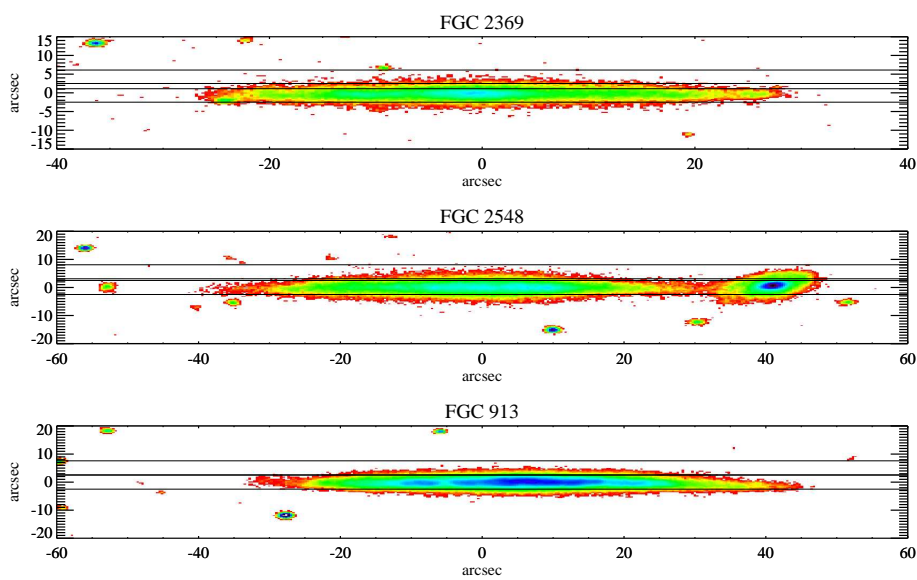


Figure 4.3 Same as Figure 4.1.

Table 4.1. Edge-On Galaxy Observations

Galaxy FGC	Date Range Observed	Midplane		Offplane		Offsets		Scale Length arcsec
		exposures	total time (min)	exposures	total time (min)	arcsec	kpc ¹	
227	10/2004 to 10/2005	7	150	20	480	4.2	1.7	10.2
913	02/2004 to 03/2004	7	80	32	698	5.1	1.5	9.0
1285	02/2004 to 04/2004	8	105	18	510	10.2	0.9	19.7
1440	03/2004 to 02/2006	4	80	10	270	5.8	2.0	15.9
1642	06/2003 to 05/2005	5	100	5	150	5.1	0.9	12.5
1948	06/2003 to 05/2005	5	95	15	405	6.5	1.2	12.3
2131	06/2005 to 06/2005	3	45	17	338	4.7	1.0	10.0
2369	10/2004 to 08/2005	5	105	25	521	3.6	1.0	8.7
2548	10/2003 to 10/2003	5	75	27	536	5.6	1.5	9.9

¹Distances from Karachentsev et al. (2000a)

Table 4.2. Elliptical Galaxies Observed

Galaxy	exposures	total time (min)
NGC1453	2	25.
NGC1600	2	20.
NGC2778	3	9.
NGC3379	1	5.
NGC5638	2	10.
NGC6127	2	20.
NGC6702	2	10.
NGC6703	2	20.
NGC7052	1	5.

lines (Osterbrock et al., 1996). Arc spectra were taken interspersed with the science exposures throughout the night, approximately every hour. Stellar spectra were used to correct the spatial distortions (tilt) in the observations. Observations of standard stars and standard atmospheric extinction curves were used to flux calibrate the spectra. Few of the observations were made in photometric conditions, thus our flux calibration is primarily used as a first order removal of the instrumental sensitivity profile. Because we are primarily interested in measuring equivalent widths, the exact flux normalization is not crucial. The sky was subtracted using a second order polynomial fit to regions dominated by the sky. The spectra were finally corrected for motion relative to the Local Standard of Rest, scaled to a common flux level, spatially aligned, and combined rejecting cosmic ray hits.

Our final spectra have a spatial scale of 0.42 arcsec/pixel on both the red and blue chips, and a wavelength solution of 1.24 Å/pixel in the blue and 1.68 Å/pixel in the red. Measurement of arc lamp lines showed a FWHM resolution of 4.9 Å on the blue chip and 7.1 Å on the red chip. Worthey & Ottaviani (1997) report that the resolution (FWHM) of the original Lick indices of interest as 8.4 Å. We therefore

broaden our spectra with a Gaussian kernel with $\sigma = 2.9 \text{ \AA}$ to match the Lick system resolution.

Systematic and rotational velocities were removed by cross-correlating a (logarithmically-binned) stellar template plus Gaussian emission lines. The shifts were accurate to within 1 pixel ($\sim 1.2 \text{ \AA}$). The midplane rotation curve was used for both the midplane and offplane spectra, as any difference between the two should be small at our resolution (Yoachim & Dalcanton, 2007).

After the 2D spectra were broadened to match the Lick resolution, any foreground stars were masked and 1D spectra were extracted by summing in the spatial direction. For both the midplane and offplane, we extracted spectra from the region of ± 1 scale length (h_R), as measured in Yoachim & Dalcanton (2005). In the higher S/N midplane spectra, we also extracted 1D spectra from the regions of $0.5h_R$ to $2.5h_R$ and $-0.5h_R$ to $-2.5h_R$. These outer regions tend to be dominated by younger stellar populations.

We tested how the SNR of our spectra affects the accuracy of the measured Lick indices. Adding artificial noise to template stellar spectra, we find the RMS error in a measured Lick index scales with S/N as $\sigma_{index} \sim 9(SNR)^{-1} \text{ \AA}$. Therefore, to achieve an Lick EW uncertainty of $\pm 0.2 \text{ \AA}$ requires a SNR of ~ 45 per \AA , which agrees with the previous determinations by Trager et al. (2000b).

Throughout our analysis, we will calculate the uncertainties in our derived ages and metallicities using the SNR of the extracted spectra. As an additional check, we have extracted 1D spectra from $0 < R < 1h_R$ and $-1 < R < 0h_R$ to find the variance in the Lick indices from one side of the galaxy to the other and note cases where there are large discrepancies. This procedure allows us to flag systems where systematic errors are likely to dominate over our random uncertainties.

4.5 Moving Onto the Lick System

While we have matched the Lick resolution reported in Worthey & Ottaviani (1997), this is not enough to ensure that we are on the Lick system. Because the Lick indices

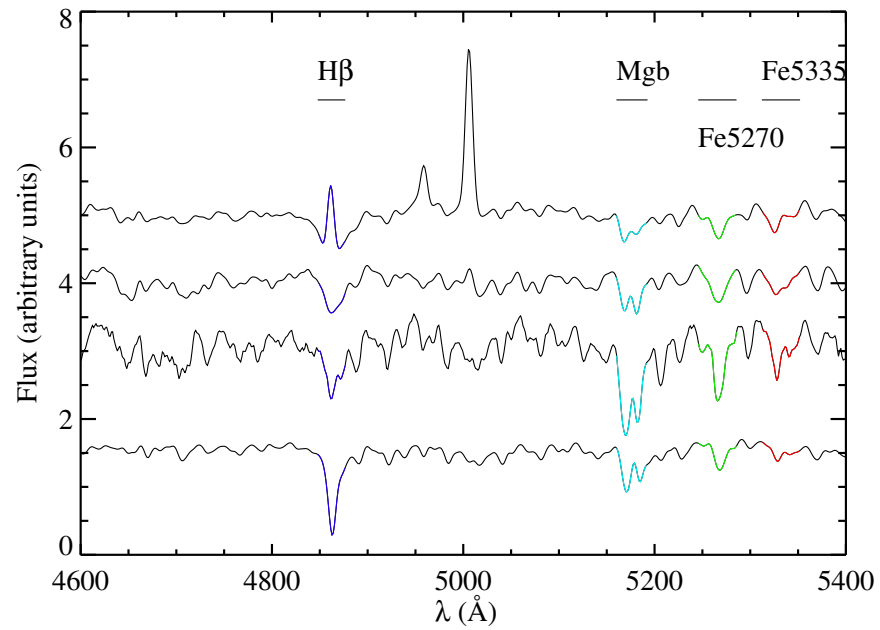


Figure 4.4 Examples of our blue spectra. From top to bottom: Midplane of FGC 1285, Offplane of FGC 1285, Elliptical galaxy NGC 5638, Lick standard star HD114762. All the spectra have been smoothed to a resolution of 8.4 \AA and the Lick indices of interest have been labeled.

Table 4.3. Zero point conversions

index	H β	Mg <i>b</i>	Fe 5270	Fe 5335
zero point ¹ (Å)	0.13	0.00	-0.01	-0.05
RMS (Å)	0.23	0.26	0.35	0.29

¹Value subtracted from our measured indices to move onto the Lick system

were originally defined from spectra that had not been flux-calibrated, additional corrections are needed. To do so, we made 144 observations of 37 unique Lick standard stars. Stars for which we have repeat observations have a mean RMS error of 0.09 Å for each index. Our standard star EWs are compared to values listed in Worthey et al. (1994), and are shown in Figure 4.5. The derived zero point corrections are listed in Table 4.3. In general, the agreement is quite good, with a typical Gaussian scatter of 0.26 Å and little systematic offset. The notable exception is for Mg *b*, for which the APO system measures low EW for metal rich systems with Mg *b* > 3 Å. We do not explicitly correct for this offset as we are observing metal poor galaxies which have Mg *b* indices < 2 Å. We also compare our standard star EWs with stars we have in common with Schiavon (2006) and find a spread of 0.2-0.4 Å. Schiavon (2006) points out that measurements of EWs of bright stars are disturbingly inconsistent, and that there can be surprisingly large variations between observations. Schiavon (2006) argue that these offsets are caused by errors in the flat-fielding, which dominate the errors of the bright stars, unlike fainter galaxy spectra which are background limited.

We also observed a sample of elliptical galaxies which have reported Lick measurements in the literature. The ellipticals were observed when light cloud cover made observing faint regions of disks impossible, or during brief periods when the primary targets were not visible. We observed 9 galaxies in common with Trager et al. (2000b) listed in Table 4.2. Our indices are not directly comparable to the ones

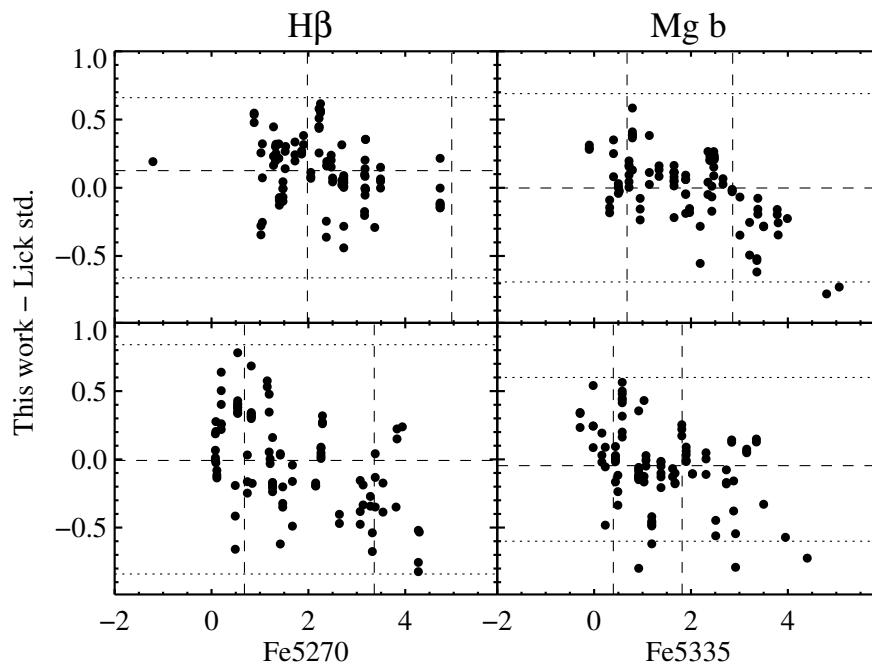


Figure 4.5 Comparison of Lick indices measured with DIS compared to the published equivalent widths in Worthey et al. (1994). Dashed horizontal lines show the mean offsets while the dotted lines show the average Worthey et al. $\pm 3\sigma$ uncertainties. Dashed vertical lines show the range of values measured in our galaxy sample. Corresponding means and scatters are given in Table 4.3.

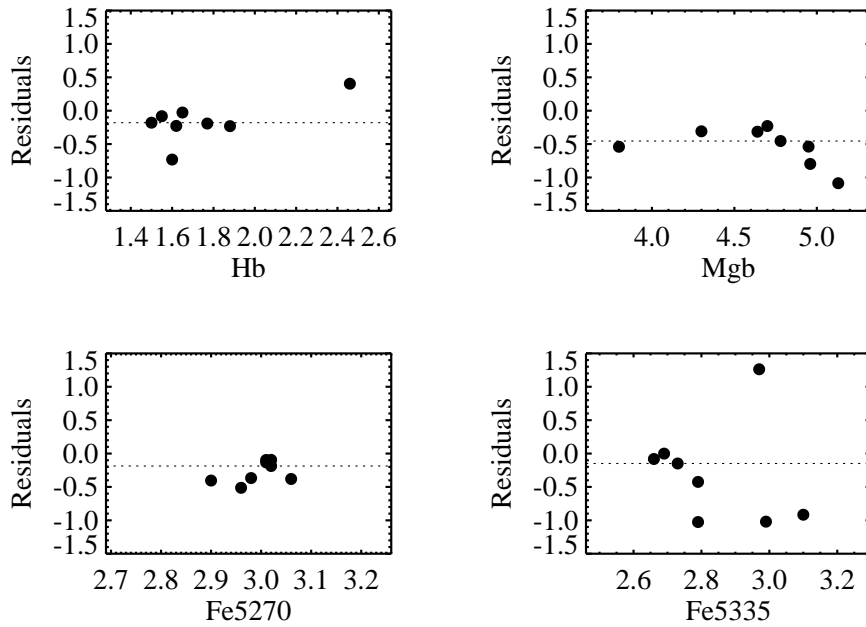


Figure 4.6 Lick indices measured with APO compared with values published in Trager et al. (2000b). Dashed lines show the median offset between our measurements and those in Trager et al. (2000b). The agreement is good, even with our larger slit and lack of velocity dispersion correction.

listed in Trager et al. (2000b), as we used our large 5'' slit which samples more flux from the outer regions of the galaxies, and we have not replicated the corrections for velocity dispersion and emission line fill-in as done in Trager et al. (2000b). Thus, some amount of scatter is expected. For the H β , Mg *b*, and Fe 5270 indices, we measure RMS scatters of 0.16-0.31 Å around the Trager et al. (2000b) values. There is a much larger scatter for Fe 5335 because the feature approaches the DIS dichroic cut-off for galaxies with a redshift greater than 4000 km s⁻¹ and becomes very low signal-to-noise. The residuals between our measurements and those in Trager et al. (2000b) are plotted in Figure 4.6.

4.5.1 Emission Line Removal

Unlike most observations of ellipticals and globular clusters, we must remove any emission lines that contaminate the index passbands before we can derive ages and metallicities from the absorption features. The removal of emission lines is not trivial. We would like to remove the H β emission, but to do so we would need to know the underlying shape of the stellar continuum. This shape in turn depends strongly on the stellar population's age and metallicity, which is what we set out to measure. We therefore must turn to other parts of the spectrum to estimate the amount of H β emission.

Lick indices, particularly H β , are often contaminated with emission lines. González (1993) popularized using the correction $H\beta_{emission} = 0.7[O III]5007$. This correction was derived by fitting a stellar template to the underlying spectrum of their elliptical galaxies to isolate the emission feature. Unfortunately, the shape of the template can determine the magnitude of the emission correction and the ratio of $F_{H\beta}/F_{[OIII]}$ is highly metallicity sensitive (Kewley & Dopita, 2002), making this correction inappropriate for low metallicity systems with varying stellar ages. Moorthy & Holtzman (2006) make a correction by fitting a Gaussian to the emission peak inside the H β Lick index. This correction probably underestimates the H β correction since the Gaussian

fit will not be sensitive to the fraction of $H\beta$ emission that has filled the absorption feature. This correction is also very sensitive to the resolution of the measured spectrum. When we try to fit a Gaussian to the emission feature after broadening, we find that the correction is 0.4 \AA smaller than when we make the correction before broadening. MacArthur (2006) takes the most extreme measure of masking regions where the spectrum is contaminated by emission lines.

Using the Oxygen emission line to estimate $H\beta$ is a fine approximation when the $H\beta$ emission correction is small, as in elliptical galaxy spectra. However, our midplane spectra are clearly dominated by the $H\beta$ emission (Figure 4.4), and we must use a more accurate technique to remove the emission. To do so, we measure the EW of the $H\alpha$ emission line from the spectra taken simultaneously with the red DIS spectrograph and use this to estimate the EW of the $H\beta$ emission line.

Our procedure for removing the $H\beta$ emission is as follows. We first assume case B recombination with $F_{H\alpha} = 2.86F_{H\beta}$ (Osterbrock, 1989). This correction is used in Rampazzo et al. (2005) and Denicoló et al. (2005) when measuring Lick indices in elliptical galaxies. However, because the $H\alpha$ and $H\beta$ emission lines were measured on different CCDs, we are hesitant to use the measured flux ratios. While both CCDs are calibrated using the same flux standard stars, the subsequent scaling and co-adding of frames was done independently and could skew the absolute flux calibration between the two. Instead, we make corrections based on equivalent widths as follows.

The definition of the EW is

$$\text{EW} = \int_{\lambda_1}^{\lambda_2} \left(1 - \frac{F_{I\lambda}}{F_{C\lambda}} \right) d\lambda \quad (4.1)$$

where $F_{I\lambda}$ is the spectrum in the index passband and $F_{C\lambda}$ is the continuum spectrum calculated from the flanking pseudo-continuum regions. Our goal is to remove the contaminating emission feature to recover the equivalent-width of the underlying Lick

absorption feature.

$$EW_{\text{observed}} = EW_{\text{Lick}} + EW_{\text{emission}} \quad (4.2)$$

In the case where the continuum is constant, the EW from the emission alone is given by

$$EW_{\text{emission}} = \Delta\lambda - \frac{F_{em} + F_{C\lambda} \Delta\lambda}{F_{C\lambda}} = -\frac{F_{em}}{F_{C\lambda}} \quad (4.3)$$

where F_{em} is the integrated flux in the emission line and $F_{C\lambda}$ is the continuum level. We can then write the expected EW ratio for the Balmer emission lines as

$$\frac{EW(\text{H}\alpha)_{\text{em}}}{EW(\text{H}\beta)_{\text{em}}} = \frac{F_{\text{H}\alpha} F_{C\lambda, \text{H}\beta}}{F_{\text{H}\beta} F_{C\lambda, \text{H}\alpha}}. \quad (4.4)$$

This in turn can be modified to account for differential extinction between the stars and HII regions.

$$\frac{EW(\text{H}\alpha)_{\text{em}}}{EW(\text{H}\beta)_{\text{em}}} = \frac{F_{\alpha} F_{C\lambda, \beta}}{F_{\beta} F_{C\lambda, \alpha}} \frac{10^{0.4E(B-V)_{gas}k(\text{H}\beta)-k(\text{H}\alpha)}}{10^{0.4E(B-V)_{stars}k(\text{H}\beta)-k(\text{H}\alpha)}} \quad (4.5)$$

Calzetti (2001) lists $k(\text{H}\beta) - k(\text{H}\alpha) = 1.163$ and finds that $E(B - V)_{stars} = 0.44E(B - V)_{gas}$. The difference in reddening is due to the geometrically clumpy distribution of HII regions compared to the smoother distribution of stars. Finally, we get the relation

$$\frac{EW(\text{H}\alpha)_{\text{em}}}{EW(\text{H}\beta)_{\text{em}}} = \frac{F_{\text{H}\alpha} F_{C\lambda, \text{H}\beta}}{F_{\text{H}\beta} F_{C\lambda, \text{H}\alpha}} 10^{0.26E(B-V)_{gas}}. \quad (4.6)$$

For the offplane spectra, we assume there is negligible dust extinction, a fairly flat continuum level ($F_{C\lambda, \text{H}\beta} \approx F_{C\lambda, \text{H}\alpha}$), and case B recombination, resulting in the standard correction of $EW(\text{H}\beta)_{\text{em}} = yEW(\text{H}\alpha)_{\text{em}}$ with $y = 2.86$. In the case of the midplane spectra, there is a younger bluer stellar population and the possibility of dust extinction. In the case of our midplane spectra, we adopt case B recombination, a continuum ratio of 1.1, and $E(B - V) \sim 0.1$ resulting in $y = 3.3$. For elliptical galaxies identified as dusty, Denicoló et al. (2005) adopt a correction of $y = 3.0$.

These adopted corrections give results consistent with what we expect from the broadband colors and SSP models. Most of the corrected $H\beta$ Lick EWs fall within the range expected from the model grids, and we find younger ages where the stellar populations are blue and older ages where they are red. In Figure 4.7, we show how a 10% change in our adopted value of y would propagate to the derived ages and metallicities, which corresponds to extinction values $0.08 < E(B - V) < 0.42$ or continuum ratios $1.05 < F_{C\lambda, H\alpha}/F_{C\lambda, H\beta} < 1.3$.

While we consider how dust affects the emission line EW ratios, the Lick absorption features themselves are fairly insensitive to dust (MacArthur, 2005) and require no extra corrections even if the galaxies are dusty.

Table 4.4. Measured Lick Indices in the range $-1 < h_R < 1$

Galaxy	SNR/Pixel	$H\beta_{\text{raw}}$	$H\alpha$	$H\beta_{\text{corr}}$	Mg <i>b</i>	Fe 5270	Fe 5335
FGC1285 midplane	272.18	-0.02 ± 0.0	-9.82 ± 0.1	2.92 ± 0.0	1.16 ± 0.0	1.45 ± 0.0	1.54 ± 0.0
offplane	91.21	1.68 ± 0.1	-1.43 ± 0.1	2.18 ± 0.1	1.89 ± 0.1	1.21 ± 0.1	1.27 ± 0.1
FGC1440 midplane	200.25	-0.92 ± 0.0	-11.83 ± 0.1	2.62 ± 0.0	2.29 ± 0.0	1.83 ± 0.1	1.23 ± 0.1
offplane	36.24	0.59 ± 0.2	-4.28 ± 0.1	2.09 ± 0.2	2.63 ± 0.2	3.36 ± 0.3	6.75 ± 0.5
FGC1642 midplane	76.15	0.35 ± 0.1	-11.28 ± 0.1	3.73 ± 0.1	0.78 ± 0.1	0.68 ± 0.1	0.40 ± 0.2
offplane	60.95	-0.24 ± 0.1	-8.29 ± 0.1	2.66 ± 0.1	1.45 ± 0.1	1.45 ± 0.2	0.84 ± 0.3
FGC1948 midplane	77.36	-2.30 ± 0.1	-22.40 ± 0.1	4.41 ± 0.1	0.53 ± 0.1	-0.16 ± 0.1	0.87 ± 0.2
offplane	15.83	0.05 ± 0.5	-8.99 ± 0.1	3.19 ± 0.5	-0.20 ± 0.6	-0.31 ± 0.6	-1.35 ± 0.6
FGC2131 midplane	98.92	-3.82 ± 0.1	-29.31 ± 0.1	4.96 ± 0.1	0.68 ± 0.1	0.94 ± 0.1	1.82 ± 0.1
offplane	14.71	0.16 ± 0.5	-8.13 ± 0.1	3.01 ± 0.5	1.47 ± 0.6	1.51 ± 0.7	0.88 ± 0.7
FGC227 midplane	104.72	-0.58 ± 0.1	-16.33 ± 0.1	4.30 ± 0.1	0.77 ± 0.1	1.24 ± 0.1	0.87 ± 0.1
offplane	21.54	-1.60 ± 0.3	-10.25 ± 0.1	1.98 ± 0.3	2.03 ± 0.4	2.45 ± 0.4	8.97 ± 0.6
FGC2369 midplane	51.41	-0.70 ± 0.1	-14.38 ± 0.1	3.60 ± 0.1	1.05 ± 0.1	0.99 ± 0.2	-0.31 ± 0.3
offplane	9.37	1.64 ± 0.9	-4.84 ± 0.1	3.33 ± 0.9	3.43 ± 0.9	0.19 ± 0.9	0.33 ± 1.1
FGC2548 midplane	81.29	0.64 ± 0.1	-11.25 ± 0.1	4.00 ± 0.1	-0.12 ± 0.1	0.99 ± 0.1	-0.04 ± 0.2
offplane	28.38	0.67 ± 0.2	-3.66 ± 0.1	1.95 ± 0.2	0.12 ± 0.3	-0.32 ± 0.4	-1.74 ± 0.6

4.5.2 *Deriving Ages and Metallicities*

Ideally, we would fit full star formation and chemical evolution histories for our galaxies. However, we have chosen to focus on only 4 of the most prominent Lick indices, limiting the total number of parameters we can hope to fit. We therefore choose to interpret the spectra using SSP models. While our galaxies are clearly more complicated than single-burst stellar populations (given that we see old stellar populations along with signs of current star formation), the SSP models will still give a reasonable approximation of the luminosity weighted mean ages, metallicities, and α -element enhancements.

To convert our measured indices to ages we start with the model grids of Thomas et al. (2003) and interpolate them to a finer grid with age steps of $\delta t = 0.1$ Gyr and metallicity steps of $\delta[Z/H]=0.01$. We exclude the very young age grid points (age < 0.1 Gyr) as the Lick indices expected for such young ages are degenerate with older populations. To calculate the uncertainties, we interpolate ages and metallicities for 100 Lick index pairs distributed according to the equivalent width uncertainties. We also test for possible systematic errors caused by incorrect emission line corrections and calculate how a 10% error in the emission line correction propagates to errors in age and metallicity.

Figure 4.7 shows the Lick indices measured for each of our galaxies, placed on the model grids of Thomas et al. (2003), assuming no α -enhancement. For each galaxy, we calculate the age and metallicity by interpolating onto grids of $H\beta+Mg\ b$, $H\beta+Fe\ 5270$, and $H\beta+Fe\ 5335$. These age-metallicity pairs are calculated for the central midplane, central offplane, and two outer midplane spectra.

Three of the galaxies (FGC 1948, 2369, and 2548) have Lick indices that consistently fall far outside the model grids. This is not surprising, as the offplane SNR for FGC 1948 and 2369 were so low we should not have expected to measure Lick indices (Table 4.4), and FGC 2548 is only on the cusp of having adequate SNR. For the

Table 4.4—Continued

Galaxy	SNR/Pixel	H β_{raw}	H α	H β_{corr}	Mg <i>b</i>	Fe 5270	Fe 5335
FGC913 midplane	71.87	-2.43 \pm 0.1	-22.14 \pm 0.1	4.20 \pm 0.1	1.37 \pm 0.1	1.30 \pm 0.2	-0.79 \pm 0.3
offplane	35.48	-0.57 \pm 0.2	-9.45 \pm 0.1	2.73 \pm 0.2	2.86 \pm 0.2	1.19 \pm 0.3	-1.94 \pm 0.4

remaining six galaxies, we plot the average interpolated ages and metallicities for the midplane and offplane in Figure 4.16 and plot cumulative distributions of the age and metallicity differences between the thin and thick disk components in Figure 4.17.

For the 6 galaxies where our observations fall on the model grids, we find the thick disks have a median age of 6.4 Gyr and metallicity of $[Z/H]=-0.6$. The thin disks have a similar median metallicity as expected for their low mass, but are uniformly much younger, with a median age of 3.6 Gyr. This age determination for the thin disk is derived after making very large emission line corrections and represents a flux-weighted average of all the stars within a radius of one scale length. It is certainly possible that the oldest central regions of the thin disk contain stars whose ages are similar to those of the thick disks. We return to these results in §4.5.3 below.

4.5.3 Radial Gradients

The observations of the midplane of FGC 1440 were deep enough that we can extract radial gradients of the Lick indices. We extracted spectra by binning $6.3''$ spatially in a sliding region across the galaxy, and moving the observations onto the Lick system as before. This gives us a SNR of 200 in the central regions of the galaxy and 50 at $1.3 h_R$. The radial variation of the Lick indices along with the interpolated ages and metallicities are plotted in Figures 4.18-4.20. The $H\beta$, Mg b , and Fe 5270 indices have radial gradients of 2.8, -1.5, and $-1.3 \text{ \AA}/h_R$ respectively. These gradients are fairly large for pure disk systems. MacArthur (2006) finds similar gradients with similar magnitudes in a sample of four face-on systems. Moorthy & Holtzman (2006) also find strong radial gradients, but attribute them to the transition between bulge and disk dominated regions of their galaxies.

The gradients in the Lick indices correspond to a large age gradient, with the central region of FGC 1440 having an SSP age of ~ 12 Gyr dropping to 2 Gyr after one scale length. The metallicity gradients, however, are slightly ambiguous. The metallicity measured from the Mg b index shows a mostly flat radial gradient, with

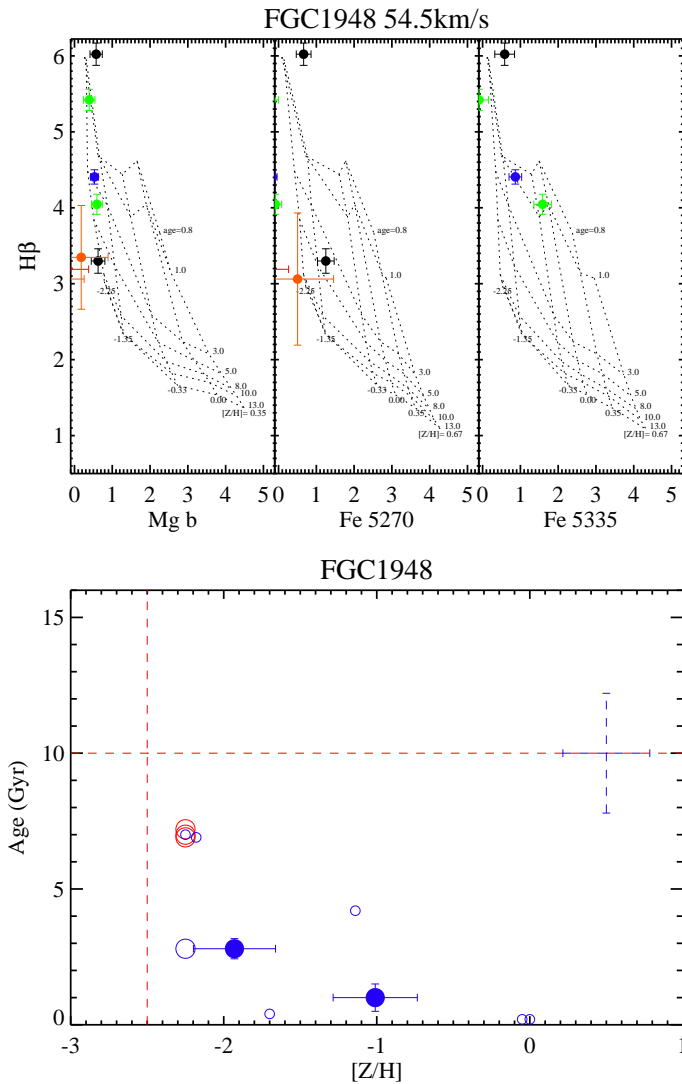


Figure 4.7 Lick index measurements for our observations. Top plots: Model grids from Thomas et al. (2003) along with our observed points. Green, blue and black points are from midplane observations, red and orange points are for offplane measurements. Bottom Plots: The interpolated ages and metallicities for all the above indices. Large filled points are used for spectra from the region $-h_R < R < h_R$ that fall inside the model grids. Large open points are used for observations that fall outside the model grids. Small open blue points show midplane spectra extracted from larger radius. Throughout, blue is used for midplane observations while red is used for offplane observations. Error bars on the points show the statistical uncertainties based on the signal-to-noise of the spectra. The dashed error bars show the typical uncertainties if we assume a 10% error on the emission line correction and a 0.02 Å error on the metal sensitive index.

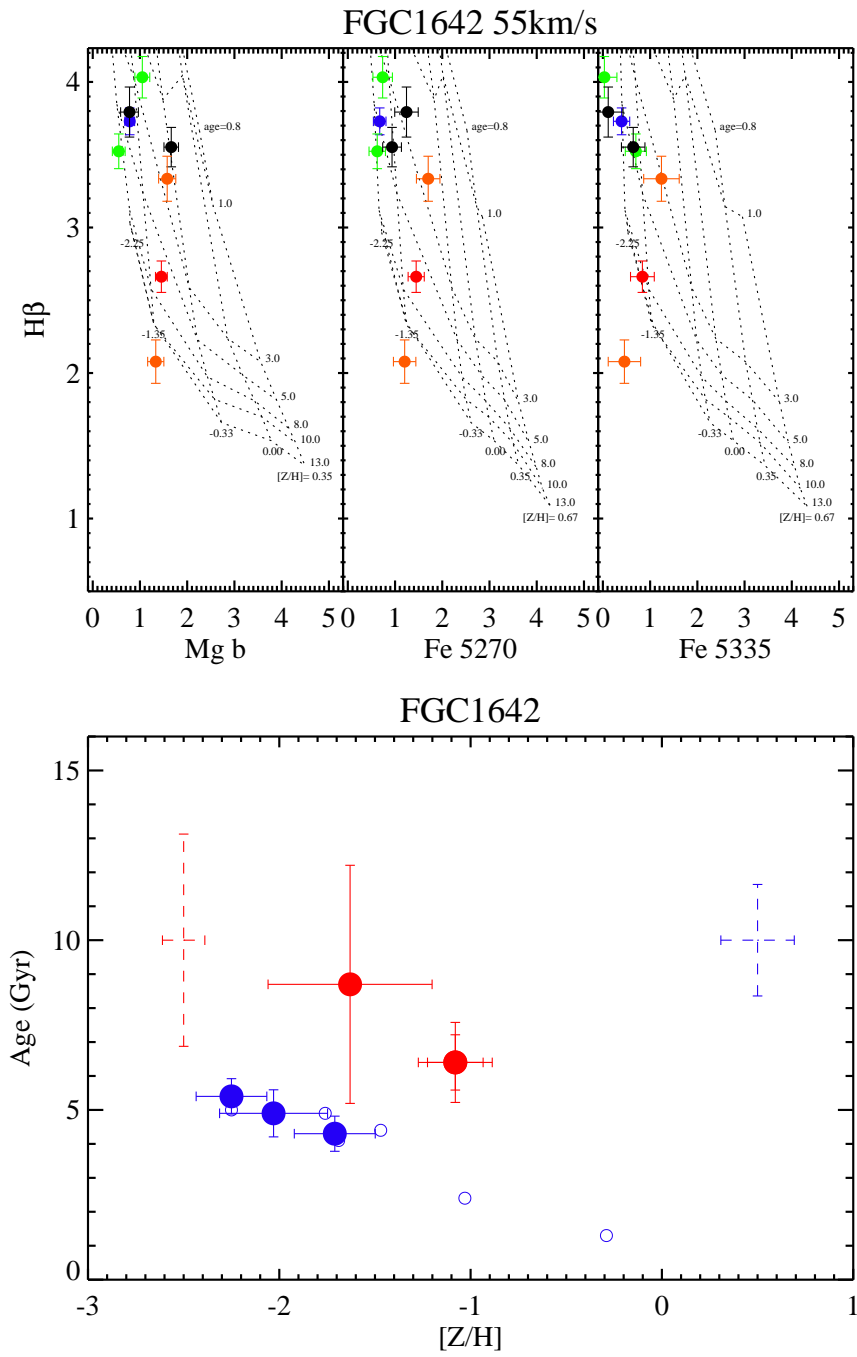


Figure 4.8 Same as Figure 4.7.

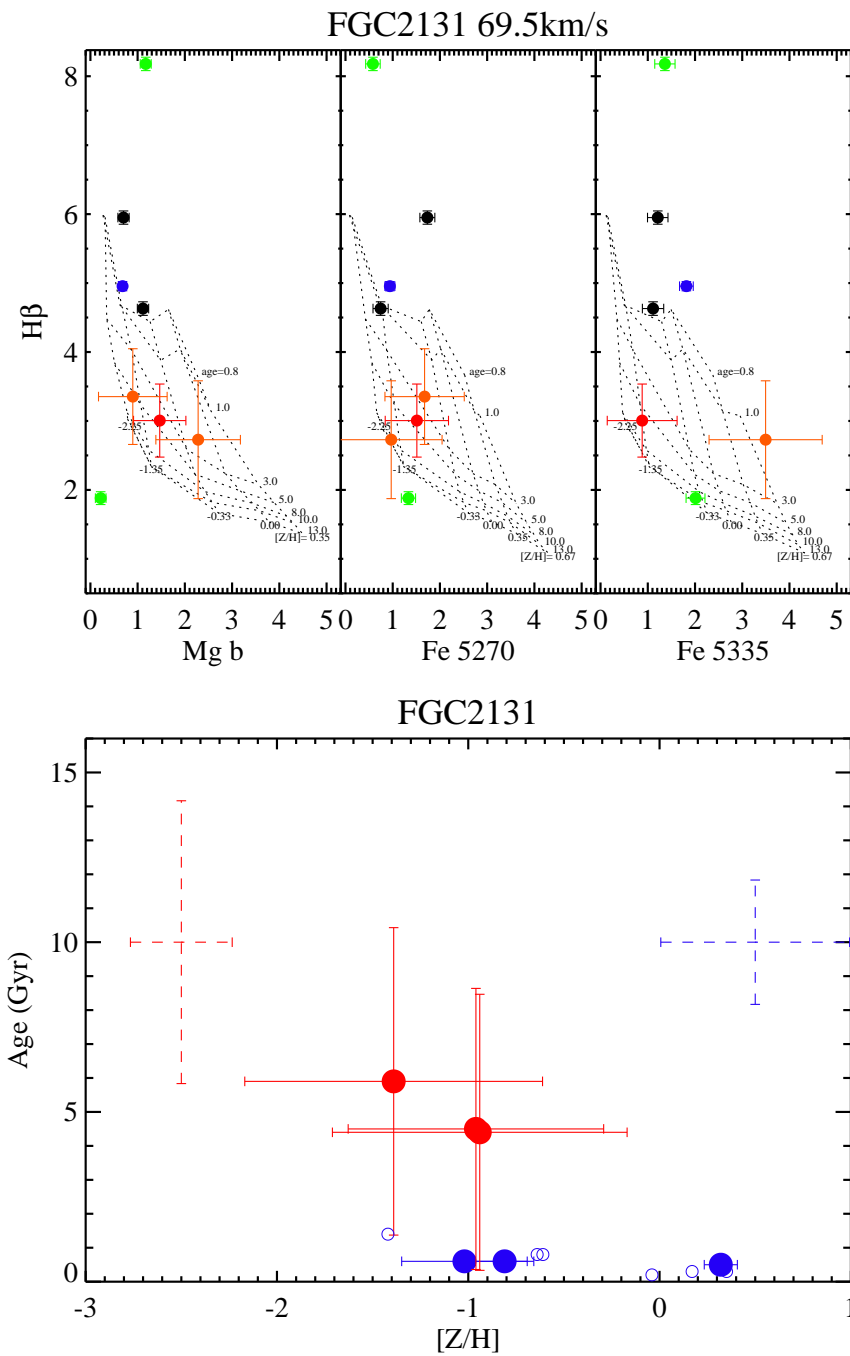


Figure 4.9 Same as Figure 4.7.

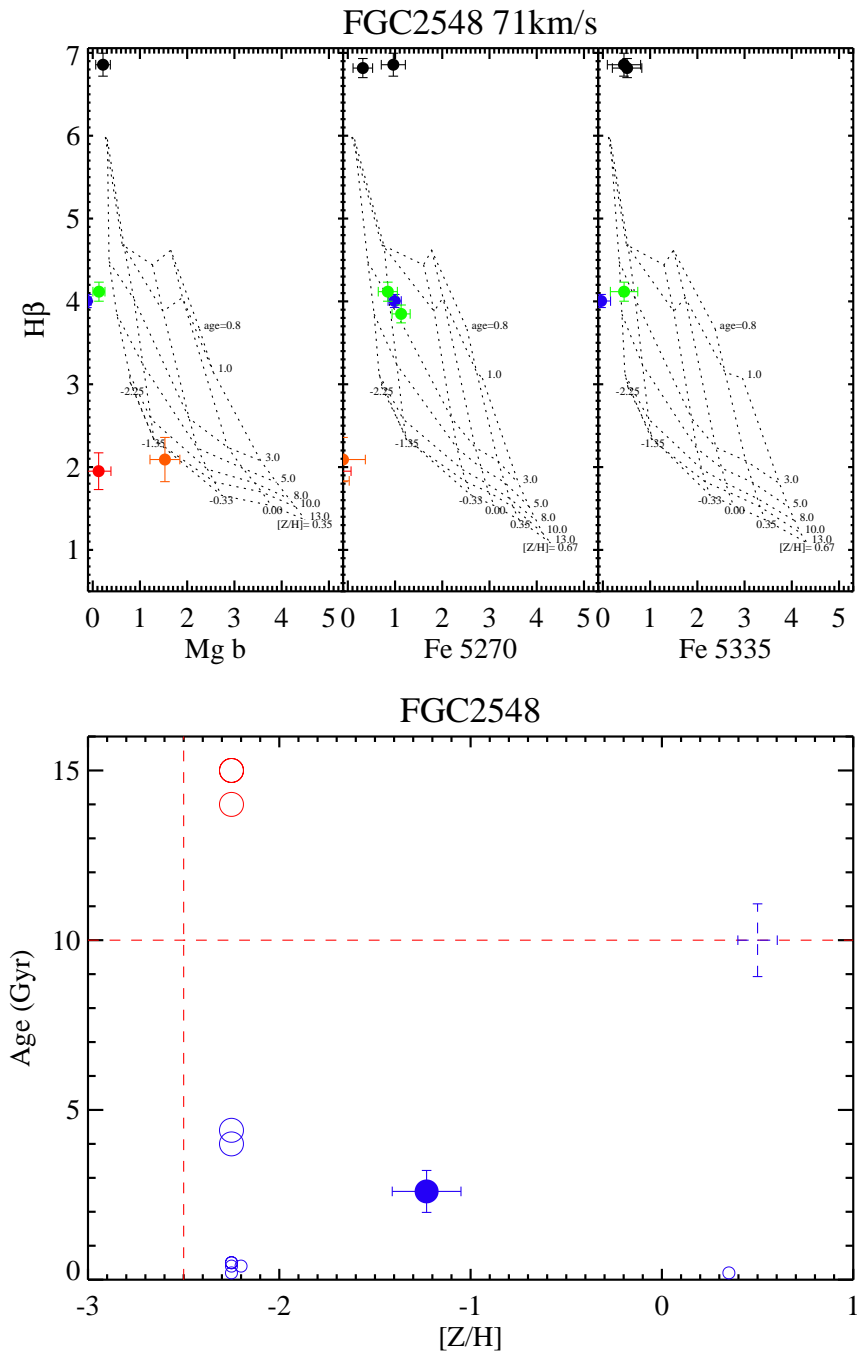


Figure 4.10 Same as Figure 4.7.

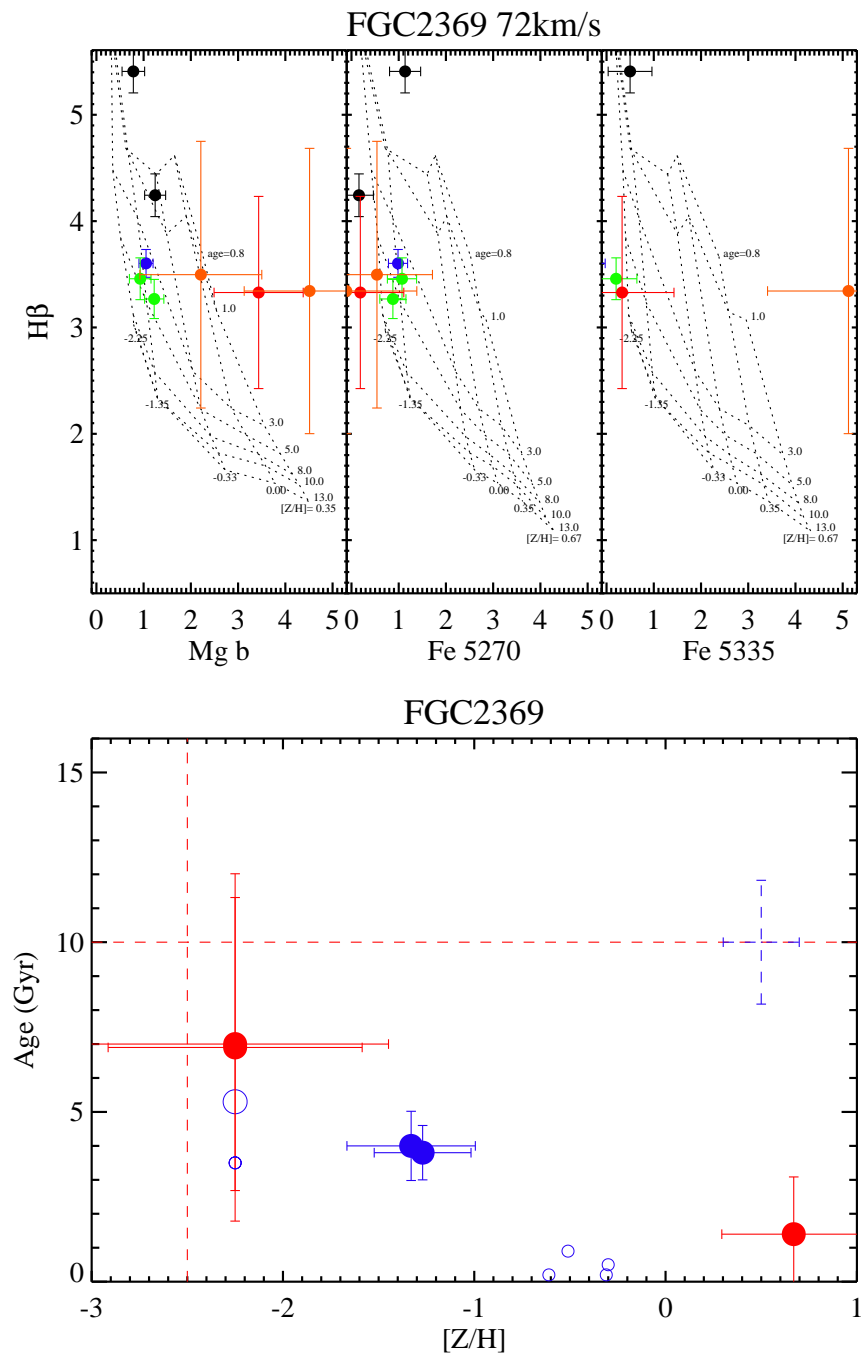


Figure 4.11 Same as Figure 4.7.

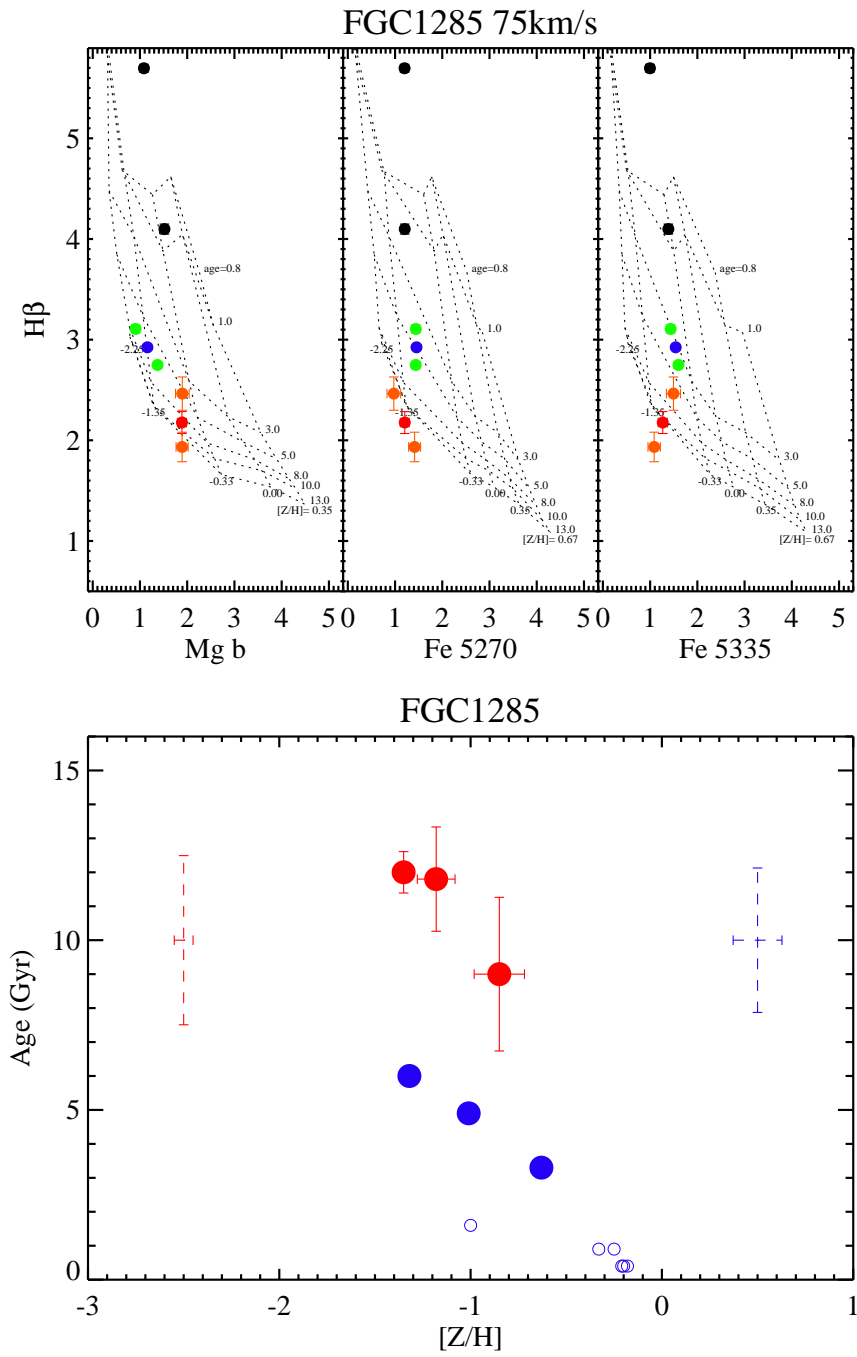


Figure 4.12 Same as Figure 4.7.

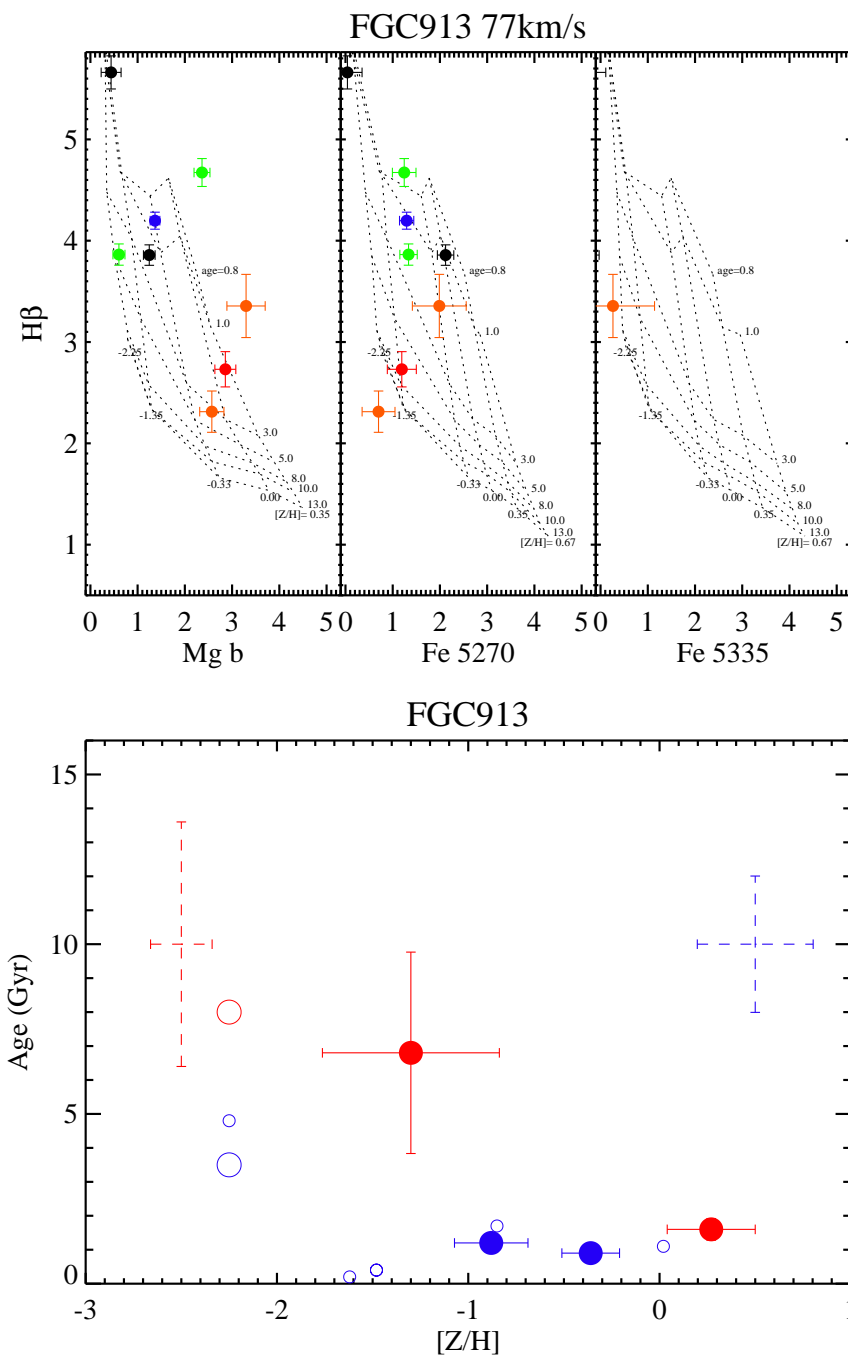


Figure 4.13 Same as Figure 4.7.

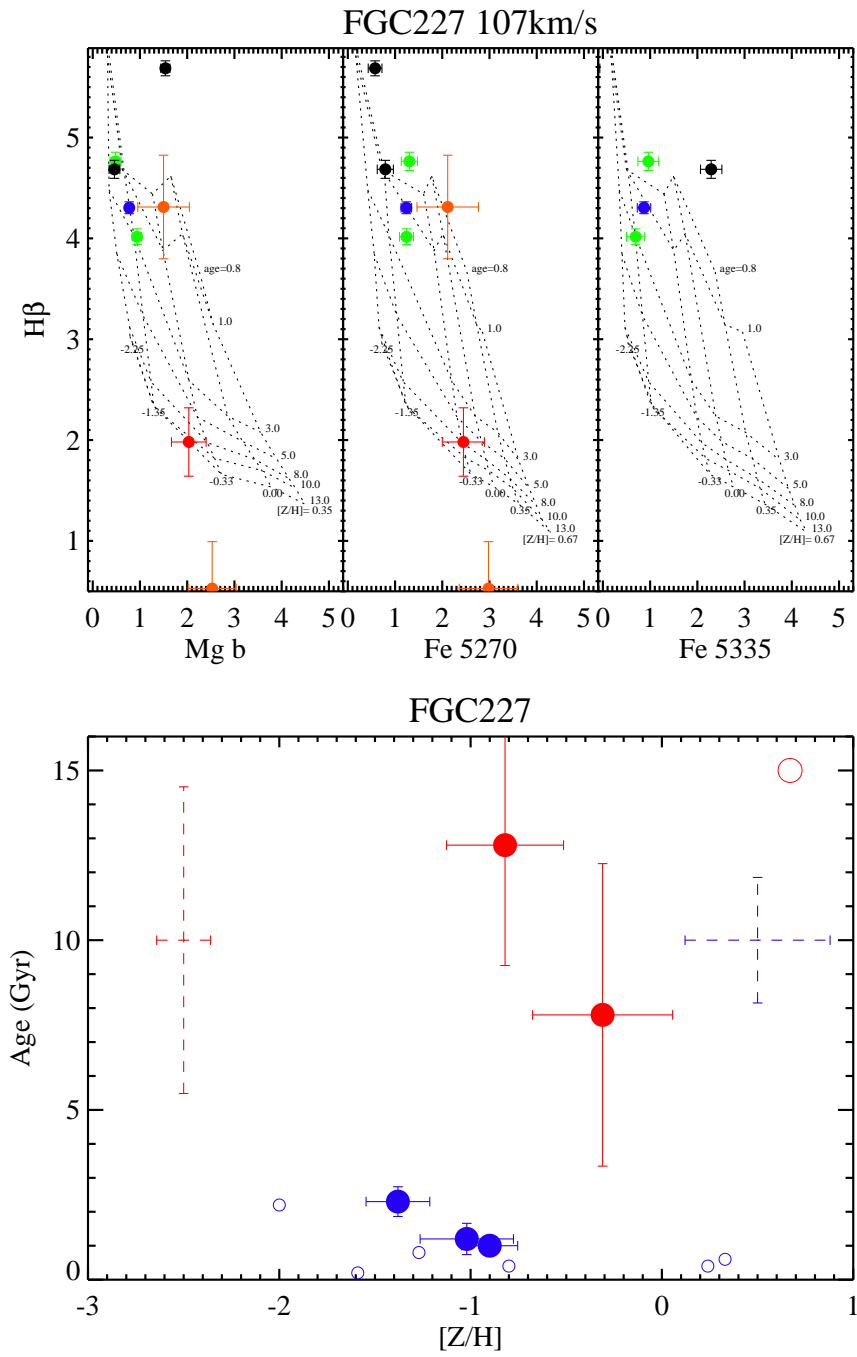


Figure 4.14 Same as Figure 4.7.

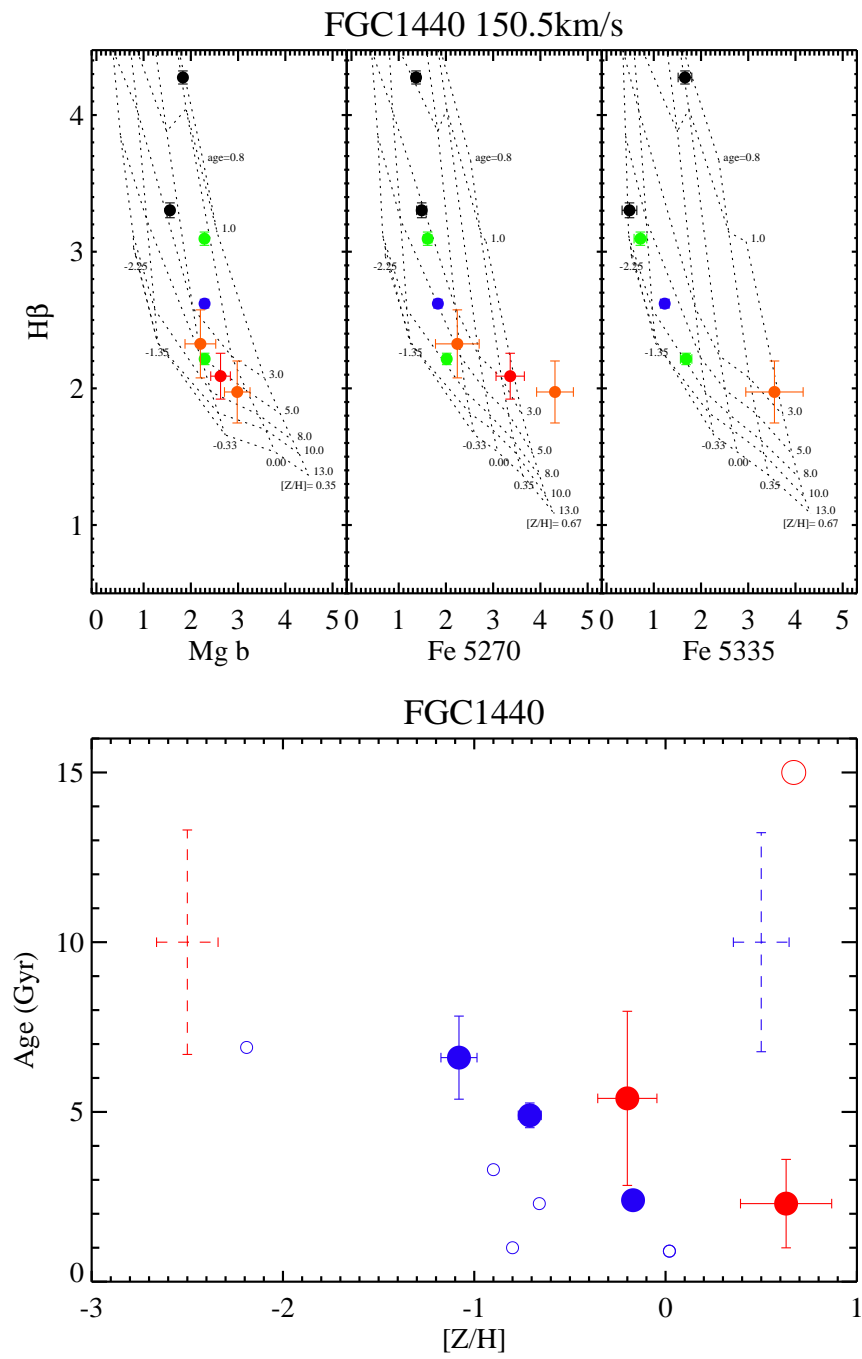


Figure 4.15 Same as Figure 4.7.

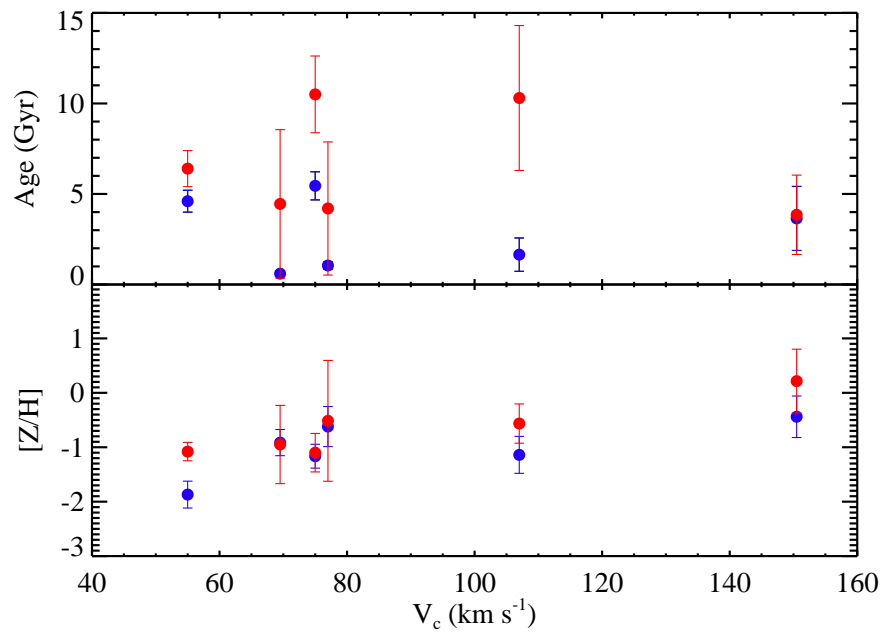


Figure 4.16 Average ages and metallicities as measured by Lick indices $H\beta$, $Mg\ b$, and $Fe\ 5270$. Blue points show midplane (thin disk) observations while red points show offplane (thick disk) observations.

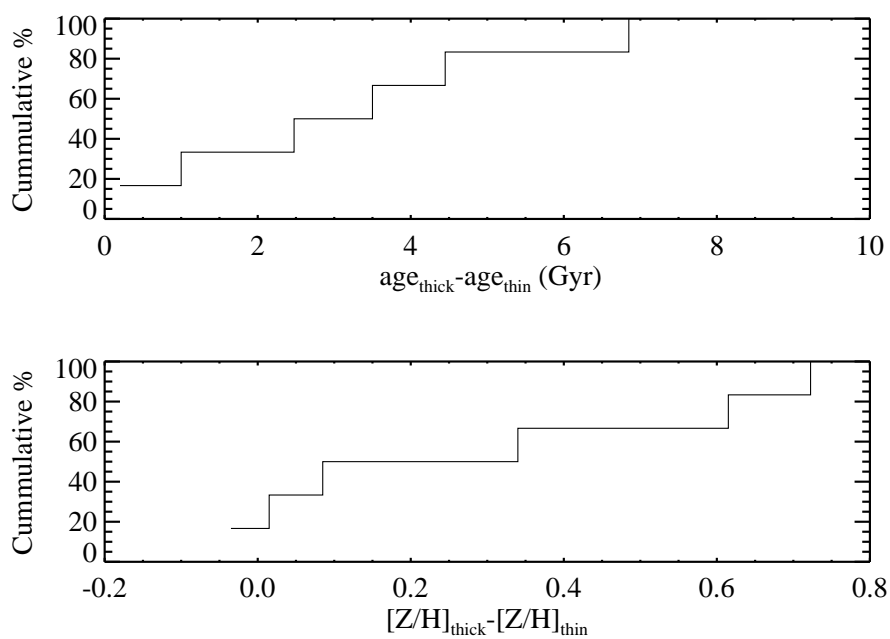


Figure 4.17 Cumulative distribution plots showing the differences between the thin disk and thick disk ages and metallicities. Positive ages mean the thick disk is older while negative metallicity differences mean the thick disk is metal poor in comparison to the thin disk.

a large drop on only one side of the galaxy. On the other hand the Fe 5270 index shows a decreasing metallicity on both sides of the galaxy. Fitting a line to the radial data, we find that the Mg b index has a metallicity gradient of $-0.40 \text{ dex}/h_R$ while the Fe 5270 index reveals a much steeper gradient of $-0.70 \text{ dex}/h_R$. This seems to imply that there is a radially changing level of α -enhancement throughout the galaxy, with the central regions being close to solar composition and the outer regions becoming more α -enhanced, thereby inflating the metallicity measured from Mg b . There is also the possibility that we should adopt a radially varying emission line correction. This seems likely, as FGC 1440 hosts a dustlane which becomes less prominent with radius.

While we cannot draw broad conclusions based on a single galaxy, it is clear we detect stronger radial gradients than have been found in other disk systems. This is even more surprising given that edge-on projection effects should act to smooth any radial population gradients we observe. We discuss these results further in §4.6.5.

4.5.4 Possible Errors

Emission Line Correction

Both the midplane and offplane have prominent emission lines. For the midplane spectra, we applied an average $H\beta$ correction of 4.9 \AA , while the offplane had an average correction of 2.2 \AA . If we did not take reddening or continuum shape into account and naively used just the case B recombination correction for both the midplane and offplane, we would derive slightly younger ages for the midplane. This simple correction would place many of the observations near the upper edges of the model grids, suggesting we were under correcting. If instead we assume an even higher amount of dust extinction for the midplane, several of the thin and thick disks would then have similar SSP ages. However, it would take fairly extreme levels of dust extinction to drive all of the thin disks to have similar ages as the thick disks. The blue broad-band

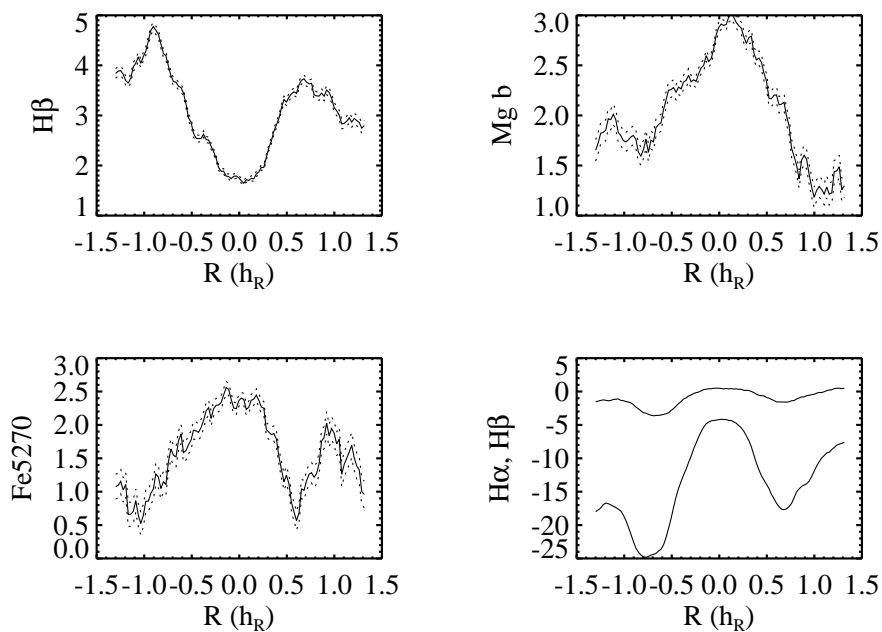


Figure 4.18 Radial gradients of the Lick equivalent-widths measured in FGC 1440. Top left shows the $H\beta$ index after correcting for emission line fill-in, top right shows $Mg\ b$, lower left shows the $Fe5270$ index, and the lower right shows the uncorrected $H\beta$ EW as well as the $H\alpha$ EW. Dotted lines show the uncertainties calculated from the extracted spectra SNR.

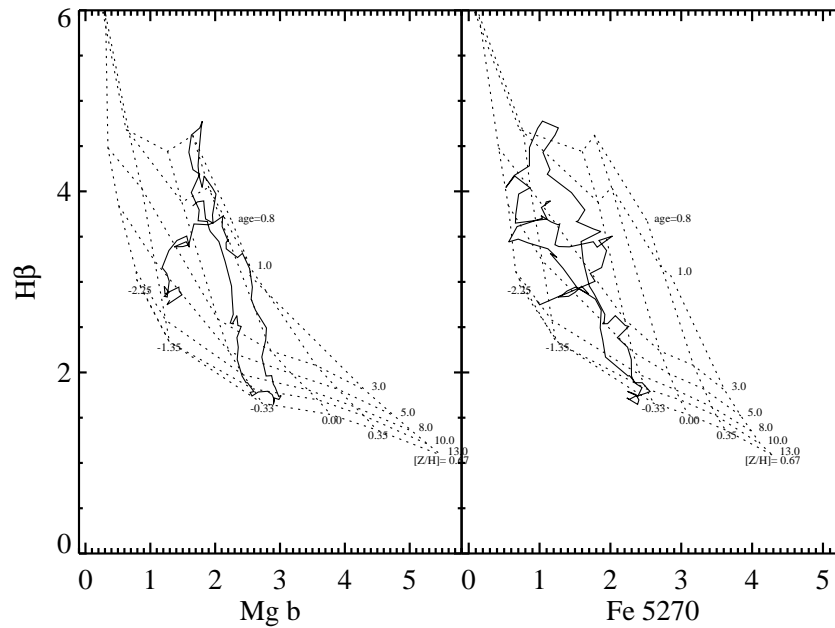


Figure 4.19 The measured Lick indices from the radial extent of FGC 1440's midplane placed on the model grids of Thomas et al. (2003).

colors for these galaxies are inconsistent with such high levels of dust.

Cross Contamination

While we have placed our longslits at regions that should be dominated by the thin or thick components, we expect some thick disk stars to be present in the midplane and vice-versa. Using the photometric fits in Yoachim & Dalcanton (2006b), we find that our midplane observations typically contain $\sim 20\%$ thick disk flux, while the offplane observations have a flux contribution of $\sim 25\%$ from the thin disk. As can be seen in Figure 4.1, we did not have large gaps between our slit positions. Observations made in poor seeing conditions might therefore experience extra cross-contamination as light from the midplane could be smeared into the offplane slit position. This should not be a major problem as we avoided making offplane observations during the worst seeing

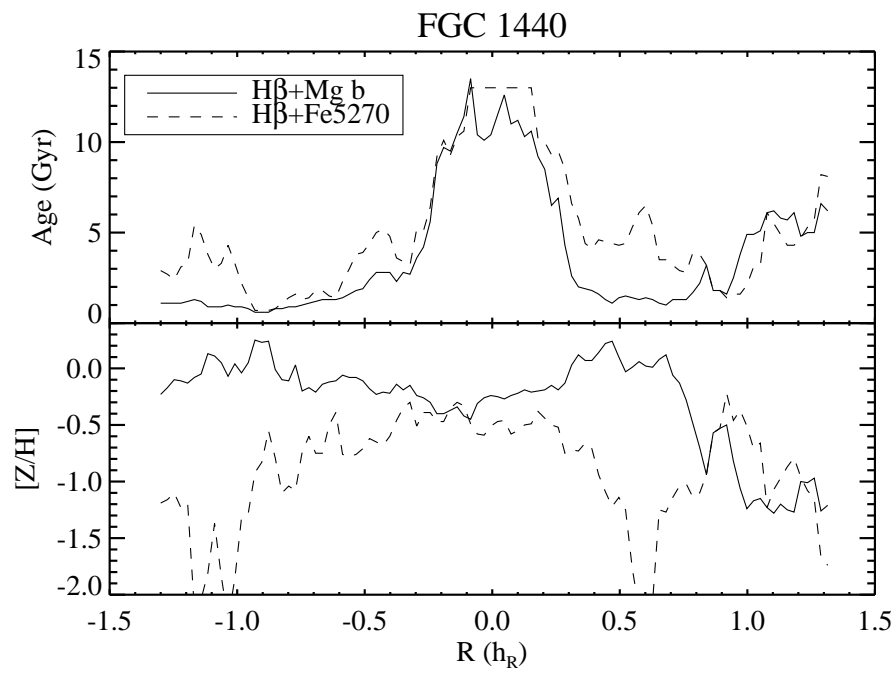


Figure 4.20 The interpolated age and metallicity measured along the midplane of FGC 1440. There is a very strong age gradient present. The $Mg\ b$ index shows a fairly flat metallicity gradient, while the Fe 5270 index shows a radially decreasing metallicity.

conditions, but could slightly increase the amount of expected cross-contamination.

Serra & Trager (2007) study how Lick indices and their derived SSP ages and metallicities are affected when there are multiple stellar populations present. They find that the derived ages are very sensitive to the youngest stars present, while the metallicity measures are predominantly influenced by an older population. Contamination could therefore explain the similar metallicities we measure for the thin and thick disk stars. However, resolved stellar population studies have found small vertical metallicity gradients in low mass galaxies as well (Seth et al., 2005b). If enough thick disk stars contaminate the midplane, our SSP derived metallicities will be slightly biased towards those of the older population, even in the young midplane. Of course, it is also possible that these low mass galaxies have simply not undergone substantial star formation episodes and thus have not chemically enriched the thin disks above the level of the thick disk. Overall, the effects of cross-contamination would lead us to underestimate the true metallicity differences between the thin and thick disks, but to overestimate the flux-weighted age differences.

Complex Stellar Populations

While we are measuring SSP-equivalent ages and metallicities, it is fairly obvious that the midplanes of disk galaxies have undergone multiple epochs of star formation and are not well described by a single age and metallicity. Our ages and metallicities are thus best interpreted as flux-weighted averages across the extracted radial region, particularly for our midplane spectra where we see very steep radial age gradients. Because we are forced to bin our spectra over a large spatial region to reach adequate SNR, we include flux from the younger outer regions of the galaxy. Our midplane ages should probably be interpreted as minimums, as the central region is undoubtedly older than the flux averaged measure we have made.

α -element Enhancement

Many spectroscopic observations of elliptical galaxies and spiral bulges have found stellar populations that have systematic differences between the metallicity calculated from the Mg *b* index compared to the Fe indices. This systematic shift is usually interpreted as being caused by a stellar population that is significantly enhanced with α -elements compared to the spectra which were used in building the Lick model grids. Such an enhancement is expected for stellar populations that form rapidly (< 1 Gyr) and that are primarily enriched by Type II supernovae (Matteucci, 1994). Enhancements in α -elements are often seen in elliptical galaxies (Worthey et al., 1992; Fisher et al., 1996; Thomas et al., 2003), as well as in local MW thick disk stars (Bensby et al., 2005).

The galaxies in our sample are all fairly low mass and therefore also low metallicity. In the low metallicity regime, the signature of α -element enhancement becomes weaker in the Lick indices. Unlike massive elliptical galaxies where the metallicity indicators can show systematic offsets of ~ 0.5 dex for an α -enhanced population, our galaxies are all sub-solar metallicity and thus would show little bias even if they are α -enhanced. If we used model SSP grids with $[\alpha/\text{Fe}]=0.3$, our derived metallicities would change by only ~ 0.1 dex.

We are hesitant to try and use our data to fit the α -element enhancement level. If we forge ahead and do so, we find considerable spread between the metallicities returned, but neither the thin or thick disk have systematically larger metallicities returned from the Mg *b* index, as we would expect if the stars were α -enhanced. However, given the small expected offset and lower SNR than available for elliptical galaxy spectra, we do not consider this a significant result, and include it here only for completeness.

4.6 Discussion

4.6.1 *Are Low Mass Thick Disks Old?*

Measuring accurate ages for thick disk stars has been done in relatively few systems. In the MW, stars that are kinematically identified as thick disk stars typically have ages greater than 8 Gyr (Fuhrmann, 1998; Bensby et al., 2004b). HST studies of resolved stellar populations in nearby galaxies show the offplane regions are dominated by old stars. Seth et al. (2005b) find that in 8 galaxies the offplane RGB stars have ages in the range of 2-6 Gyr. Similarly, Mould (2005) uses the ratio of RGB and AGB stars to find ages of thick disks in a sample of 4 galaxies to be older than 3 Gyr. Our measured thick disk SSP ages fall between 3.8 and 10 Gyr with a median age of 6.4 Gyr, consistent with other studies that show thick disks to be dominated by ancient stars.

4.6.2 *Are Low Mass Thick Disks Metal Poor?*

Many of our thick disks appear to be more metal rich than the embedded thin disks. This is probably just a result of the flux weighted nature of our measurement. The young, metal-poor outer regions dilute the true central ages and metallicities of the thin disks.

Thick disk metallicities have only been measured for a handful of systems. MW thick disk stars typically have metallicities in the range $[\text{Fe}/\text{H}] \sim -0.7$ to -0.2 , with the highest metallicity thick disk stars possibly reaching solar values (Bensby et al., 2006). One difficulty with comparing to the MW thick disk is that the observed properties are of thick disk stars near the solar radius, while we have only been able to measure thick disk properties near the central regions of the galaxies. Fortunately there are signs that the MW thick disk has relatively small age and metallicity gradients (Bensby et al., 2005).

Constraints of thick disk metallicities have also been derived from HST studies

imaging resolved stars. Seth et al. (2005b) used ACS images of 6 nearby edge-on disks to constrain vertical gradients in the stellar populations using the color and distribution of AGB and RGB stars. The older RGB stars have a systematically larger scale height compared to the younger AGB and main sequence stars. They find little to no metallicity gradients in the thick disk stars in their systems, with the metallicities of the thick disks peaked around $[\text{Fe}/\text{H}] \sim -1$. This is slightly more metal poor than the measurements we have for our thick disks. However, the offset is unlikely to be significant, given that the Seth et al. (2005b) study is able to study a cleaner sample of thick disk stars by reaching higher vertical heights which reducing the contamination of thin disk stars. Like the data presented here, Seth et al. (2005b) only studies lower mass systems, limiting the magnitude of any possible metallicity gradient due to the low metallicity of the midplane. Using similar HST observations, Mould (2005) finds that thick disk stars in 4 edge-on galaxies have $[\text{Fe}/\text{H}]$ between -1.0 and -0.78, again very similar to the metallicities we find.

4.6.3 *Are Thick Disks α -enhanced?*

The level of α -enhancement can be a major clue to the formation process of a thick disk. If a stellar population is α -enhanced, it is a sign that it has been enriched mostly over a short time period by Type II SNe, whereas stars with solar composition formed over an extended period and have been enriched by both Type II and Type Ia SNe. Numerous papers have found that MW thick disk stars are enhanced in α -elements compared to thin disk stars at similar total metallicities (e.g., Bensby et al., 2003, 2004a, 2005; Feltzing et al., 2003; Reddy et al., 2006; Tautvaišienė et al., 2001; Mashonkina et al., 2003; Prochaska et al., 2000; Fuhrmann, 1998, 2004). Unfortunately, we do not have the SNR to definitively say if our thick disks are α -enhanced, due to the overall low metallicities of our target galaxies.

4.6.4 *Are Thick Disks “Normal” Stellar Populations?*

Using a sample of >1000 SDSS images of edge-on disk galaxies, Zibetti et al. (2004) examine the faint halo that appears when the images are stacked. This extended halo has anomalous colors, requiring stars that are either metal rich or have a bottom heavy IMF (Zibetti et al., 2004; Zackrisson et al., 2006). We find no such anomalies with the thick disks we observe spectroscopically, as most of them fall on model grids using standard IMFs and metallicities. The few galaxies where we measure Lick indices that are inconsistent with the SSP models can easily be explained as spurious measurements caused by low SNR, and do not require exotic stellar populations to explain them.

4.6.5 *Radial Color Gradients in the Thin Disks*

Bell & de Jong (2000) observed broadband colors for a large sample of galaxies and found that the radial gradients were predominantly caused by age gradients in the stellar populations. They found an average metallicity gradient, but broadband sensitivity to dust makes this a much harder measurement. Their work has been expanded on by MacArthur et al. (2004), who found both metallicity and age gradients are stronger in the inner regions of galaxies, and that galaxies with strong age gradients had smaller metallicity gradients. The Lick indices ability to lift the age-metallicity degeneracy, and relative insensitivity to dust makes it much easier to quantify how much of the radial color gradients in disk galaxies are due to age versus metallicity changes.

In the only study that has explicitly targeted Lick indices in the disk-dominated regions of galaxies, MacArthur (2006) detect age gradients in only 2 of their 8 galaxies, and find strong negative metallicity gradients in 4. The age gradients in MacArthur (2006) are also rather small (-0.5 and -1.3 Gyr/ h_R). Our measurements of FGC 1440 show a much steeper age gradient, with the SSP age dropping by ~ 9 Gyr over one

scale length.

Our finding that the thin disk of FGC 1440 might have stellar populations of near solar composition and be α -enhanced at larger radii is puzzling. Looking at the transition between bulge and disk dominated regions, Moorthy & Holtzman (2006) finds that the central bulges are either solar-composition or α -enhanced, with little to no α -enhancement in the disks. With the presence of old thick disks in all of the galaxies, we would expect the galaxies to have experienced plenty of chemical evolution and enrichment from SNe Ia. Instead, the outer regions of FGC 1440 are α -enhanced, suggesting that the central region of the galaxy has undergone extended chemical enrichment, while the outer regions have not, despite being surrounded by old thick disk stars.

This could be a sign that the thick disk stars in FGC 1440 have been recently accreted, and thus have not contributed to the chemical enrichment the galaxy. Another possibility is that the central region of the galaxy is the only place where the gravitational potential is deep enough to retain SN ejecta, and the outer disk has historically suffered from SN blow-out and failed to retain metal enriched gas. Another possibility is that the metallicity in the outer disk is dominated by enrichment from the latest burst of star-formation which has α -enhanced the region.

4.7 Conclusions

We have spectroscopically confirmed that the thick disks observed in edge-on late type galaxies are old, metal-poor stellar populations, analogous to the thick disk stars seen in the MW and nearby edge-on systems. This is the first time ages and metallicities of thick disks have been measured in unresolved stellar populations. Because all of our targets are fairly low mass, we are unable to detect any significant differences between thin disk and thick disk metallicities. After correcting for emission line contamination, the thin disks in our sample are found to be quite young, with strong radial age gradients.

We fail to detect any significant trend for thick disk stars to be enhanced in α -elements compared to their thin disks. This is a defining characteristic of the MW thick disk. This is most likely a result of our sample being dominated by low-mass and therefore low metallicity galaxies.

For one galaxy in our sample we have measured the radial gradients of the Lick indices in the thin disk and find the large gradients are dominated by changes in the average stellar age with a small contribution from a changing average metallicity.

Chapter 5

CONCLUSION AND FUTURE WORK

5.1 *Observational Properties of Thick Disks*

Along with the work presented in this thesis, there is a growing body of observations of thick disks. Here we summarize the results of observations of thick disks made in this thesis as well as the literature.

5.1.1 Morphological Properties

Chapter 2 reviewed previous photometric studies of thick disks and presented thick disk fits for a large number of edge-on late-type galaxies. We confirmed the results of Dalcanton & Bernstein (2002), finding that thick disks are ubiquitous features of disk galaxies. Thick disks have, by definition, larger scale heights than their embedded thin disks. In Chapter 2, we found that thick disks may also have longer scale lengths than thin disks. Larger scale lengths for thick disks have also been found in S0 galaxies (Pohlen et al., 2004), as well as in the MW thick disk (Juric et al., 2005).

Chapter 2 also showed that in lower-mass galaxies, the thick disk component can actually contain the majority of the stellar mass. This is in stark comparison to the MW where only $\sim 10\%$ of the stellar mass is in the thick disk.

5.1.2 Dynamical Properties

The dynamics of thick disk stars in the MW has revealed a variety of results. Canonically, the thick disk shows a lag of around 20 km s^{-1} relative to the thin disk with no sizable vertical gradient (Soubiran et al., 2003; Vallenari et al., 2006). Larger surveys have revealed thick disk stars that lag $\sim 100 \text{ km s}^{-1}$ and substantial vertical gradients

in the magnitude of the thick disk velocity lag (Chiba & Beers, 2000; Girard et al., 2006). These results have been interpreted in a variety of ways, Girard et al. (2006) builds a kinematic model that predicts thick disk stars far from the midplane should exhibit larger lags, while Gilmore et al. (2002) and Wyse et al. (2006) interpret these stars as being the tidally disrupted remnants of a dwarf galaxy, possibly one that heated MW stars to form the thick disk.

Outside the MW, Chapter 3 is the only other study which has successfully isolated and measured the kinematics of thick disks. In that chapter, we found a surprising variety of thick disk behaviors, with some galaxies looking analogous to the MW, some showing more severe thick disk lags, and one galaxy that was best fit with a counter-rotating thick disk.

5.1.3 Ages and Metallicities

The Milky Way thick disk is dominated by old and metal poor stars (Freeman & Bland-Hawthorn, 2002). There is a possibility that the MW thick disk experienced extended star formation and contains stars up to solar metallicity (Bensby et al., 2004b, 2006). The elemental abundance pattern of thick disk stars reveals they are enhanced in α -elements, suggesting they have experienced a chemical enrichment history independent of the thin disk.

In the galaxies that have been resolved by HST, thick disks again look to be older metal poor populations (Seth et al., 2005b, 2007; Tikhonov et al., 2005; Tikhonov & Galazutdinova, 2005; Mould, 2005). In Chapter 4, we used the Lick index absorption line system to once again confirm that the thick disks seen in edge-on galaxies are old and metal-poor.

5.2 Final Thoughts on Thick Disk Formation

Historically, the properties of thick disk in other systems have not been well constrained, and thick disk formation theories have focused on explaining the MW thick

disk. Recognizing that there is no guarantee that the MW is a typical galaxy with a typical thick disk (Hammer et al., 2007), we now look at how well formation models work for explaining the thick disk properties that have been observed across a range of galaxies.

The simplest formation model would be that the thick disk is simply a heated extension of the thin disk, where the oldest thin disk stars have been gradually kinematically heated into thick disk orbits. There is ample evidence that stars gradually heat as they age by scattering off spiral structure, giant molecular clouds, and dark matter substructure (Villumsen, 1985; Hänninen & Flynn, 2002; Benson et al., 2004; Hayashi & Chiba, 2006). Similar heating is seen in external galaxies as an increase between the main-sequence stellar scale height and AGB star scale height Seth et al. (2005b). However, the known heating mechanisms tend to saturate and should not be able to heat stars all the way to thick disk heights. In addition, heating should be more efficient in higher mass galaxies, which host larger molecular clouds and spiral arms, yet we found in Chapter 2 thick disks are proportionally larger in low mass systems. It therefore seems that both gradual heating and heating via late-time major merger are unsupported as the primary thick disk formation scenario. Another problem with gradual heating is that it fails to explain the longer scale lengths of the thick disks we found in Chapter 2. Disk galaxies often show strong radial age gradients (e.g. Bell & de Jong, 2001) which is interpreted as a sign that galactic disks grow from the inside out and are increasing their thin disk scale lengths with time. If this is true, we should expect a thick disk created from a heated ancient thin disk to have a shorter scale length. Additionally, the thin and thick disks should show a continuous metallicity distributions, unlike what is found in the MW.

Rapid heating of a thin disk through a major merger is also a fairly unsatisfactory method of making a thick disk. Simulations consistently show that major mergers create spheroidal systems. Chapter 2's measurements of very late-type galaxies which have no detectable bulge suggest that the major mergers cannot explain all thick disks.

Direct accretion or forming thick disk stars during mergers seem to be the most viable options for making thick disks. Both of these models rely on the predictions of Λ CDM that all galaxies experience a period of heavy merging and accretion of satellites. The differences between these two models is subtle, there is no clear dividing line between accreting a star forming galaxy and having extended star forming substructure off of the midplane.

Only the direct accretion of stars can explain the counter-rotating thick disk we described in Chapter 3. With only one example of a counter-rotating thick disk, it is not clear that accretion is the dominant formation mode for thick disks. Direct accretion can also explain why thick disks tend to have larger scale lengths than thin disks. If satellite galaxies are disrupted far from the galactic center, they can deposit stars at large radii while the thin disk gradually builds from the inside-out.

While we favor the accretion model, Chapter 4 places tight constraints on the epoch of this accretion. Chapter 4, along with HST studies of resolved galaxies (Seth et al., 2005b; Mould, 2005), show that thick disks are uniformly ancient and metal poor. This suggests that if thick disk stars are accreted, the accretion events happened very early as any young recently acquired stellar population would be easily detected.

Of course there is the possibility that the true origin of the thick disk involves some combination of the above scenarios. Details emerging from the MW thick disk studies suggests thick disk stars can come from a variety of sources, with Wyse et al. (2006) describing some stars as merger debris and others as heated ancient thin disk stars. The thick disks which have appeared in N-body simulations also point to a combination of sources for thick disk stars, with some simulations showing thick disks built predominantly through accretion (Abadi et al., 2003b), and others showing thick disks as the remnants of stars that formed off the midplane (Brook et al., 2004).

5.3 Future Work

5.3.1 Radial Gradients of Stellar Populations

As part of the observations for Chapter 4, we found we are able to measure radial gradients in the Lick indices in edge-on galaxies. Very few studies have tried to use the Lick indices in disk systems. One major obstacle is the faint surface brightnesses of disks compared to ellipticals coupled with the fact that high signal to noise is required to measure absorption features. By observing edge-on systems, projection effects greatly enhance the surface brightnesses that are observed.

Our early results show the radial gradients in the stellar populations are very similar to the gradients observed in galaxies with bulges (Moorthy & Holtzman, 2006). This raises the possibility that either the stellar mass in some bulges is just a disk that has been shaped by secular evolution, or there are some intervening physical processes that make inner disks and bulges match in age and metallicity.

In addition, the Ca II features we observed in Chapter 3 can be used as a metallicity indicator (Cenarro et al., 2001; Vazdekis et al., 2003), which we can use as to independently compare with the measurements from Lick indices.

5.3.2 Behavior of Extra-planer Ionized Gas

In Chapter 3, we found that the offplane ionized gas kinematics matched the midplane. This result is quite different from a number of studies which have found extra-planer gas to be lagging in rotation compared to the midplane (Heald et al., 2006b,a, 2007; Fraternali & Binney, 2006; Barbieri et al., 2005). A more robust extraction of the high signal-to-noise gas emission lines could reveal more details about the dynamics of ionized gas off the midplane and further illuminate the popular fountain models that have been used to explain the existence of ionized gas far from the midplane.

5.3.3 Stellar Kinematics at Low Surface Brightness Levels

In Chapter 3, we developed a new technique for extracting stellar kinematics from low signal-to-noise spectra that is contaminated with skyline residuals. By taking spectra of the CaII triplet in the near-IR, we were able to utilize gray-time and did not require excellent seeing conditions, thereby taking advantage of low-demand telescope time. With the new generation of integral field unit spectrographs on 8-meter class telescopes, we can now try to push our techniques beyond long-slit observations and generate full data cubes.

BIBLIOGRAPHY

- Abadi, M. G., Navarro, J. F., Steinmetz, M., & Eke, V. R. 2003a, *ApJ*, 591, 499
— . 2003b, *ApJ*, 597, 21
- Abe, F. et al. 1999, *AJ*, 118, 261
- Aguerri, J. A. L., Balcells, M., & Peletier, R. F. 2001, *A&A*, 367, 428
- Agustsson, I., & Brainerd, T. G. 2007, *ArXiv e-prints*, 704
- Annibali, F., Bressan, A., Rampazzo, R., & Zeilinger, W. W. 2006, *A&A*, 445, 79
- Annibali, F., Bressan, A., Rampazzo, R., Zeilinger, W. W., & Danese, L. 2007, *A&A*, 463, 455
- Aparicio, A., Dalcanton, J. J., Gallart, C., & Martinez-Delgado, D. 1997, *AJ*, 114, 1447
- Aparicio, A., Tikhonov, N., & Karachentsev, I. 2000, *AJ*, 119, 177
- Ardi, E., Tsuchiya, T., & Burkert, A. 2003, *ApJ*, 596, 204
- Baes, M. et al. 2003, *MNRAS*, 343, 1081
- Bahcall, J. N., & Kyllafis, N. D. 1985, *ApJ*, 288, 252
- Bahcall, J. N., & Soneira, R. M. 1980, *ApJS*, 44, 73
- Bailin, J., Power, C., Norberg, P., Zaritsky, D., & Gibson, B. K. 2007
- Banerjee, A., & Jog, C. J. 2007
- Barbanis, B., & Woltjer, L. 1967, *ApJ*, 150, 461
- Barbieri, C. V., Fraternali, F., Oosterloo, T., Bertin, G., Boomsma, R., & Sancisi, R. 2005, *A&A*, 439, 947
- Barker, M. K., Sarajedini, A., Geisler, D., Harding, P., & Schommer, R. 2006
- Barnes, III, T. G., Fernley, J. A., Frueh, M. L., Navas, J. G., Moffett, T. J., & Skillen, I. 1997, *PASP*, 109, 645

- Barris, B. J., Tonry, J. L., Novicki, M. C., & Wood-Vasey, W. M. 2005, *AJ*, 130, 2272
- Barth, A. J., Ho, L. C., & Sargent, W. L. W. 2002, *AJ*, 124, 2607
- Barton, I. J., & Thompson, L. A. 1997, *AJ*, 114, 655
- Beauchamp, D., & Hardy, E. 1997, *AJ*, 113, 1666
- Begum, A., Chengalur, J. N., & Karachentsev, I. D. 2005, *A&A*, 433, L1
- Bekki, K., & Chiba, M. 2001, *ApJ*, 558, 666
- Bell, E. F., Baugh, C. M., Cole, S., Frenk, C. S., & Lacey, C. G. 2003a, *MNRAS*, 343, 367
- Bell, E. F., & de Jong, R. S. 2000, *MNRAS*, 312, 497
- . 2001, *ApJ*, 550, 212
- Bell, E. F., McIntosh, D. H., Katz, N., & Weinberg, M. D. 2003b, *ApJS*, 149, 289
- Bell, E. F. et al. 2007, *ArXiv e-prints*, 706
- Benedict, G. F., et al. 2006
- Bensby, T., Feltzing, S., & Lundström, I. 2003, *A&A*, 410, 527
- . 2004a, *A&A*, 415, 155
- . 2004b, *A&A*, 421, 969
- Bensby, T., Feltzing, S., Lundström, I., & Ilyin, I. 2005, *A&A*, 433, 185
- Bensby, T., Zenn, A. R., Oey, M. S., & Feltzing, S. 2006
- Benson, A. J., Lacey, C. G., Frenk, C. S., Baugh, C. M., & Cole, S. 2004, *MNRAS*, 351, 1215
- Berdnikov, L. N. 1997, *VizieR Online Data Catalog*, 2217, 0
- Berdnikov, L. N., & Turner, D. G. 1995, *Pis ma Astronomicheskii Zhurnal*, 21, 803
- . 2001, *ApJS*, 137, 209
- Bergmann, M. P., Jørgensen, I., & Hill, G. J. 2003, *AJ*, 125, 116
- Bessell, M. S. 1990, *PASP*, 102, 1181

- Bianchi, S. 2007, ArXiv e-prints, 705
- Bilir, S., Karaali, S., Ak, S., Yaz, E., & Hamzaoglu, E. 2006
- Binggeli, B., & Popescu, C. C. 1995, A&A, 298, 63
- Binney, J., & Lacey, C. 1988, MNRAS, 230, 597
- Binney, J., & Merrifield, M. 1998, Galactic astronomy (Galactic astronomy / James Binney and Michael Merrifield. Princeton, NJ : Princeton University Press, 1998. (Princeton series in astrophysics) QB857 .B522 1998 (\$35.00))
- Binney, J., & Tremaine, S. 1987, Galactic dynamics (Princeton, NJ, Princeton University Press, 1987, 747 p.)
- Birnboim, Y., & Dekel, A. 2003, MNRAS, 345, 349
- Bizyaev, D., & Mitronova, S. 2002, A&A, 389, 795
- Bland-Hawthorn, J., & Freeman, K. C. 2004, Publications of the Astronomical Society of Australia, 21, 110
- . 2006, Memorie della Societa Astronomica Italiana, 77, 1095
- Blanton, M. R. et al. 2003, ApJ, 594, 186
- Bochanski, J. e. a. ????
- Bolton, A. S., Burles, S., Koopmans, L. V. E., Treu, T., & Moustakas, L. A. 2006, ApJ, 638, 703
- Bosma, A., Byun, Y., Freeman, K. C., & Athanassoula, E. 1992, ApJL, 400, L21
- Bottema, R. 1988, A&A, 197, 105
- . 1989, A&A, 221, 236
- Bottema, R., & Gerritsen, J. P. E. 1997, MNRAS, 290, 585
- Bottema, R., van der Kruit, P. C., & Valentijn, E. A. 1991, A&A, 247, 357
- Brainerd, T. G. 2005, ApJL, 628, L101
- Brewer, M., & Carney, B. W. 2004, Publications of the Astronomical Society of Australia, 21, 134
- Brewer, M.-M., & Carney, B. W. 2006, AJ, 131, 431

- Brook, C., Richard, S., Kawata, D., Martel, H., & Gibson, B. K. 2006a
- Brook, C., Richard, S., Kawata, D., Martel, H., & Gibson, B. K. 2007a, *ApJ*, 658, 60
- Brook, C. B., Gibson, B. K., Martel, H., & Kawata, D. 2005, *astro-ph/0503273*
- Brook, C. B., Kawata, D., Gibson, B. K., & Flynn, C. 2003, *ApJL*, 585, L125
- Brook, C. B., Kawata, D., Gibson, B. K., & Freeman, K. C. 2004, *ApJ*, 612, 894
- Brook, C. B., Kawata, D., Martel, H., Gibson, B. K., & Bailin, J. 2006b, *ApJ*, 639, 126
- Brook, C. B., Kawata, D., Scannapieco, E., Martel, H., & Gibson, B. K. 2007b, *ApJ*, 661, 10
- Brooks, A. M., et al. 2006
- Bruzual, G., & Charlot, S. 2003, *MNRAS*, 344, 1000
- Bullock, J. S., & Johnston, K. V. 2005, *ApJ*, 635, 931
- Bullock, J. S., Kravtsov, A. V., & Weinberg, D. H. 2000, *ApJ*, 539, 517
- . 2001, *ApJ*, 548, 33
- Burkert, A., Truran, J. W., & Hensler, G. 1992, *ApJ*, 391, 651
- Burstein, D. 1979, *ApJ*, 234, 829
- Burstein, D., Faber, S. M., Gaskell, C. M., & Krumm, N. 1984, *ApJ*, 287, 586
- Buser, R., Rong, J., & Karaali, S. 1999, *A&A*, 348, 98
- Caimmi, R. 2000, *Astronomische Nachrichten*, 321, 323
- Caldwell, N., Rose, J. A., & Concannon, K. D. 2003, *AJ*, 125, 2891
- Calzetti, D. 2001, *PASP*, 113, 1449
- Cappellari, M., & Emsellem, E. 2004, *PASP*, 116, 138
- Carlberg, R. G. 1987, *ApJ*, 322, 59
- Carney, B. W., Latham, D. W., & Laird, J. B. 1989, *AJ*, 97, 423
- Carollo, D. et al. 2007, *ArXiv e-prints*, 706

- Cecil, G., & Rose, J. A. 2007, ArXiv e-prints, 706
- Cenarro, A. J., Cardiel, N., Gorgas, J., Peletier, R. F., Vazdekis, A., & Prada, F. 2001, MNRAS, 326, 959
- Cescutti, G., Matteucci, F., Francois, P., & Chiappini, C. 2007, A&A, 462, 943
- Chen, B. et al. 2001, ApJ, 553, 184
- Chernin, A. D. et al. 2007, ArXiv e-prints, 706
- Chiappini, C., Matteucci, F., & Gratton, R. 1997, ApJ, 477, 765
- Chiba, M., & Beers, T. C. 2000, AJ, 119, 2843
- Cohen, J. G., Blakeslee, J. P., & Côté, P. 2003, ApJ, 592, 866
- Conselice, C. J. 2006, MNRAS, 373, 1389
- Corbin, M. R., Vacca, W. D., Cid Fernandes, R., Hibbard, J. E., Somerville, R. S., & Windhorst, R. A. 2006, ApJ, 651, 861
- Coulson, I. M., & Caldwell, J. A. R. 1985, South African Astronomical Observatory Circular, 9, 5
- Courteau, S. 1997, AJ, 114, 2402
- Dalcanton, J. J. 2006a, ArXiv Astrophysics e-prints
- . 2006b, private comm.
- Dalcanton, J. J., & Bernstein, R. A. 2000a, in ASP Conf. Ser. 197: Dynamics of Galaxies: from the Early Universe to the Present, ed. F. Combes, G. A. Mamon, & V. Charmandaris, 161–+
- Dalcanton, J. J., & Bernstein, R. A. 2000b, AJ, 120, 203
- . 2002, AJ, 124, 1328
- Dalcanton, J. J., & Shectman, S. A. 1996, ApJL, 465, L9+
- Dalcanton, J. J., Spergel, D. N., & Summers, F. J. 1997, ApJ, 482, 659
- Dalcanton, J. J., Yoachim, P., & Bernstein, R. A. 2004, ApJ, 608, 189
- de Grijs, R., & Peletier, R. F. 1997, A&A, 320, L21
- de Grijs, R., Peletier, R. F., & van der Kruit, P. C. 1997, A&A, 327, 966

- de Grijs, R., & van der Kruit, P. C. 1996, *A&AS*, 117, 19
- de Jong, R. S. 1996a, *A&AS*, 118, 557
- . 1996b, *A&A*, 313, 377
- Dehnen, W., & Binney, J. J. 1998, *MNRAS*, 298, 387
- Dekel, A., & Birnboim, Y. 2004, *astro-ph/0412300*
- Dekel, A., & Silk, J. 1986, *ApJ*, 303, 39
- Dekel, A., & Woo, J. 2003, *MNRAS*, 344, 1131
- Denicoló, G., Terlevich, R., & Terlevich, E. 2002, *MNRAS*, 330, 69
- Denicoló, G., Terlevich, R., Terlevich, E., Forbes, D. A., Terlevich, A., & Carrasco, L. 2005, *MNRAS*, 356, 1440
- Donato, F., Gentile, G., & Salucci, P. 2004, *MNRAS*, 353, L17
- Dove, J. B., & Thronson, H. A. 1993, *ApJ*, 411, 632
- Drozdovsky, I., et al. 2007
- Eggen, O. J., Lynden-Bell, D., & Sandage, A. R. 1962, *ApJ*, 136, 748
- Eisenstein, D. J. et al. 2003, *ApJ*, 585, 694
- Elmegreen, B. G., & Elmegreen, D. M. 2005, *ApJ*, 627, 632
- . 2006, *ApJ*, 650, 644
- Erb, D. K., Shapley, A. E., Pettini, M., Steidel, C. C., Reddy, N. A., & Adelberger, K. L. 2006, *ApJ*, 644, 813
- Erb, D. K., Steidel, C. C., Shapley, A. E., Pettini, M., & Adelberger, K. L. 2004, *ApJ*, 612, 122
- Faber, S. M., Friel, E. D., Burstein, D., & Gaskell, C. M. 1985, *ApJS*, 57, 711
- Falcón-Barroso, J. et al. 2006, *MNRAS*, 369, 529
- Falcón-Barroso, J., Peletier, R. F., Vazdekis, A., & Balcells, M. 2003, *ApJL*, 588, L17
- Fall, S. M., & Efstathiou, G. 1980, *MNRAS*, 193, 189
- Feltzing, S., Bensby, T., Gesse, S., & Lundström, I. 2004, in *Origin and Evolution of*

the Elements

- Feltzing, S., Bensby, T., & Lundström, I. 2003, *A&A*, 397, L1
- Ferguson, A. M. N., Irwin, M. J., Ibata, R. A., Lewis, G. F., & Tanvir, N. R. 2002, *AJ*, 124, 1452
- Ferrara, A., & Tolstoy, E. 2000, *MNRAS*, 313, 291
- Fisher, D., Franx, M., & Illingworth, G. 1996, *ApJ*, 459, 110
- Font, A. S., Navarro, J. F., Stadel, J., & Quinn, T. 2001, *ApJL*, 563, L1
- Fraternali, F., Binney, J., Oosterloo, T., & Sancisi, R. 2007, *ArXiv Astrophysics e-prints*
- Fraternali, F., & Binney, J. J. 2006, *MNRAS*, 366, 449
- Freeman, K., & Bland-Hawthorn, J. 2002, *ARA&A*, 40, 487
- Freeman, K. C. 1970, *ApJ*, 160, 811
- Fry, A. M., Morrison, H. L., Harding, P., & Boroson, T. A. 1999, *AJ*, 118, 1209
- Fuhrmann, K. 1998, *A&A*, 338, 161
- . 2004, *Astronomische Nachrichten*, 325, 3
- Fukugita, M., Ichikawa, T., Gunn, J. E., Doi, M., Shimasaku, K., & Schneider, D. P. 1996, *AJ*, 111, 1748
- Fukugita, M. et al. 2007, *ArXiv e-prints*, 704
- Galilei, G. 1632
- Ganda, K., Falcón-Barroso, J., Peletier, R. F., Cappellari, M., Emsellem, E., McDermid, R. M., de Zeeuw, P. T., & Carollo, C. M. 2006, *MNRAS*, 367, 46
- Ganda, K. et al. 2007, *ArXiv e-prints*, 706
- Garnett, D. R. 2002, *ApJ*, 581, 1019
- Geha, M., Blanton, M. R., Masjedi, M., & West, A. A. 2006, *ApJ*, 653, 240
- Geha, M., Guhathakurta, P., & van der Marel, R. P. 2005, *AJ*, 129, 2617
- Gieren, W. 1981, *ApJS*, 47, 315

- Gilmore, G., & Reid, N. 1983, MNRAS, 202, 1025
- Gilmore, G., & Wyse, R. F. G. 1986, Nature, 322, 806
- Gilmore, G., Wyse, R. F. G., & Kuijken, K. 1989, ARA&A, 27, 555
- Gilmore, G., Wyse, R. F. G., & Norris, J. E. 2002, ApJL, 574, L39
- Giovanelli, R., Haynes, M. P., Salzer, J. J., Wegner, G., da Costa, L. N., & Freudling, W. 1995, AJ, 110, 1059
- Girard, T. M., Korchagin, V. I., Casetti-Dinescu, D. I., van Altena, W. F., López, C. E., & Monet, D. G. 2006, AJ, 132, 1768
- Glazebrook, K., & Bland-Hawthorn, J. 2001, PASP, 113, 197
- Gnedin, N. Y. 2000, ApJ, 542, 535
- Goessl, C. A. et al. 2006
- González, J. J. 1993, Ph.D. Thesis
- Governato, F. et al. 2004, ApJ, 607, 688
- Governato, F., Willman, B., Mayer, L., Brooks, A., Stinson, G., Valenzuela, O., Wadsley, J., & Quinn, T. 2007, MNRAS, 374, 1479
- Gratton, R. G., Carretta, E., Desidera, S., Lucatello, S., Mazzei, P., & Barbieri, M. 2003, A&A, 406, 131
- Gratton, R. G., Carretta, E., Matteucci, F., & Sneden, C. 2000, A&A, 358, 671
- Grebel, E. K., & Gallagher, J. S. 2004, ApJL, 610, L89
- Guhathakurta, P., et al. 2005, astro-ph/0502366
- Hammer, F., Puech, M., Chemin, L., Flores, H., & Lehnert, M. 2007, ArXiv Astrophysics e-prints
- Hänninen, J., & Flynn, C. 2002, MNRAS, 337, 731
- Hayashi, H., & Chiba, M. 2006
- Heald, G. H., Rand, R. J., Benjamin, R. A., & Bershadsky, M. A. 2006a, ApJ, 647, 1018
- . 2007, ArXiv Astrophysics e-prints

- Heald, G. H., Rand, R. J., Benjamin, R. A., Collins, J. A., & Bland-Hawthorn, J. 2006b, *ApJ*, 636, 181
- Helmi, A., Navarro, J. F., Meza, A., Steinmetz, M., & Eke, V. R. 2003, *ApJL*, 592, L25
- Henden, A. A. 1996, *AJ*, 111, 902
- Hidalgo, S. L., Aparicio, A., & Martínez-Delgado, D. 2003, *Ap&SS*, 284, 595
- Hodge, P. W., & Hitchcock, J. L. 1966, *PASP*, 78, 79
- Holmberg, E. 1969, *Arkiv for Astronomi*, 5, 305
- Howk, J. C., & Savage, B. D. 1999, *AJ*, 117, 2077
- Hunter, D. A., & Elmegreen, B. G. 2004, *AJ*, 128, 2170
- Ibata, R., Chapman, S., Ferguson, A. M. N., Irwin, M., Lewis, G., & McConnachie, A. 2004, *MNRAS*, 351, 117
- Ibata, R., Chapman, S., Ferguson, A. M. N., Lewis, G., Irwin, M., & Tanvir, N. 2005, *ApJ*, 634, 287
- Ibata, R., Martin, N. F., Irwin, M., Chapman, S., Ferguson, A. M. N., Lewis, G. F., & McConnachie, A. W. 2007, *ArXiv e-prints*, 704
- Ivezic, Z. 2007, in prep.
- Juric, M. et al. 2005, *ArXiv Astrophysics e-prints*
- Kalirai, J. S., Guhathakurta, P., Gilbert, K. M., Reitzel, D. B., Majewski, S. R., Rich, R. M., & Cooper, M. C. 2006, *ApJ*, 641, 268
- Kamphuis, P., et al. 2007
- Kang, X., van den Bosch, F. C., Yang, X., Mao, S., Mo, H. J., Li, C., & Jing, Y. P. 2007, *ArXiv Astrophysics e-prints*
- Karaali, S., Bilir, S., & Hamzaoğlu, E. 2004, *MNRAS*, 355, 307
- Karachentsev, I. D., Karachentseva, V. E., Kudrya, Y. N., Makarov, D. I., & Parnovsky, S. L. 2000a, *Bull. Special Astrophys. Obs.*, 50, 5
- Karachentsev, I. D., Karachentseva, V. E., Kudrya, Y. N., Sharina, M. E., & Parnovsky, S. L. 2000b, *VizieR Online Data Catalog*, 7219, 0

- Karachentsev, I. D., Karachentseva, V. E., & Parnovskij, S. L. 1993, *Astronomische Nachrichten*, 314, 97
- Kauffmann, G. et al. 2003a, *MNRAS*, 341, 33
- . 2003b, *MNRAS*, 341, 54
- Kautsch, S. J., Grebel, E. K., Barazza, F. D., & Gallagher, III, J. S. 2006, *A&A*, 445, 765
- Kelson, D. D. 2003, *PASP*, 115, 688
- Kelson, D. D. et al. 1996, *ApJ*, 463, 26
- Kelson, D. D., Illingworth, G. D., van Dokkum, P. G., & Franx, M. 2000, *ApJ*, 531, 159
- Kelson, D. D., Zabludoff, A. I., Williams, K. A., Trager, S. C., Mulchaey, J. S., & Bolte, M. 2002, *ApJ*, 576, 720
- Keres, D., Katz, N., Weinberg, D. H., & Dave, R. 2004, *astro-ph/0407095*
- Kereš, D., Katz, N., Weinberg, D. H., & Davé, R. 2005, *MNRAS*, 363, 2
- Kewley, L. J., & Dopita, M. A. 2002, *ApJS*, 142, 35
- Koeppen, J., Weidner, C., & Kroupa, P. 2006
- Kregel, M., & van der Kruit, P. C. 2004, *MNRAS*, 355, 143
- . 2005, *MNRAS*, 358, 481
- Kregel, M., van der Kruit, P. C., & de Grijs, R. 2002, *MNRAS*, 334, 646
- Kregel, M., van der Kruit, P. C., & Freeman, K. C. 2005, *MNRAS*, 358, 503
- Kroupa, P. 2002, *MNRAS*, 330, 707
- Kruger, J., & Dunning, D. 1999, *Journal of Personality and Social Psychology*, 77, No. 6, 1121
- Kudrya, Y. N., Karachentsev, I. D., Karachentseva, V. E., & Parnovskii, S. L. 1994, *Astronomy Letters*, 20, 8
- Kuhlen, M., Diemand, J., & Madau, P. 2007, *ArXiv e-prints*, 704
- Kylafis, N. D., & Bahcall, J. N. 1987, *ApJ*, 317, 637

- Lacey, C. G. 1991, in *Dynamics of Disc Galaxies*, 257–+
- Lamport, L. 1994, *LATEX. A document preparation system. User's Guide and Reference Manual* (Reading, Mass.: Addison-Wesley, —c1994, 2nd ed.)
- Larsen, J. A., & Humphreys, R. M. 2003, *AJ*, 125, 1958
- Larson, R. B., Tinsley, B. M., & Caldwell, C. N. 1980, *ApJ*, 237, 692
- Lee, H.-c., & Worthey, G. 2005, *ApJS*, 160, 176
- Leonard, D. C., Kanbur, S. M., Ngeow, C. C., & Tanvir, N. R. 2003, *ApJ*, 594, 247
- López-Corredoira, M., Cabrera-Lavers, A., Garzón, F., & Hammersley, P. L. 2002, *A&A*, 394, 883
- Mac Low, M., & Ferrara, A. 1999, *ApJ*, 513, 142
- MacArthur, L. A. 2005, *ApJ*, 623, 795
- . 2006, Ph.D. Thesis
- MacArthur, L. A., Courteau, S., Bell, E., & Holtzman, J. A. 2004, *ApJS*, 152, 175
- MacArthur, L. A., Courteau, S., & Holtzman, J. A. 2003, *ApJ*, 582, 689
- MacArthur, L. A., Gonzalez, J., & Courteau, S. 2007, *ArXiv Astrophysics e-prints*
- Magrini, L., Vilchez, J. M., Mampaso, A., Corradi, R. L. M., & Leisy, P. 2007, *ArXiv e-prints*, 705
- Majewski, S. R. 1993, *ARA&A*, 31, 575
- Márquez, I., Masegosa, J., Moles, M., Varela, J., Bettoni, D., & Galletta, G. 2002, *A&A*, 393, 389
- Martin, N. F., Ibata, R. A., Bellazzini, M., Irwin, M. J., Lewis, G. F., & Dehnen, W. 2004, *MNRAS*, 348, 12
- Mashonkina, L., Gehren, T., Travaglio, C., & Borkova, T. 2003, *A&A*, 397, 275
- Mateo, M. L. 1998, *ARA&A*, 36, 435
- Matteucci, F. 1994, *A&A*, 288, 57
- Matteucci, F., & Francois, P. 1989, *MNRAS*, 239, 885
- Matthews, L. D. 2000, *AJ*, 120, 1764

- Matthews, L. D., Gallagher, J. S., & van Driel, W. 1999, *AJ*, 118, 2751
- Matthews, L. D., & Wood, K. 2001, *ApJ*, 548, 150
- Mayer, L., & Moore, B. 2004, *MNRAS*, 354, 477
- McConnachie, A. W., & Irwin, M. J. 2006, *MNRAS*, 365, 902
- McGaugh, S. S. 2005, *ApJ*, 632, 859
- McGaugh, S. S., Schombert, J. M., Bothun, G. D., & de Blok, W. J. G. 2000, *ApJL*, 533, L99
- Mendes de Oliveira, C., Coelho, P., González, J. J., & Barbuy, B. 2005, *AJ*, 130, 55
- Miceli, A. et al. 2007, *ArXiv e-prints*, 706
- Minniti, D., & Zijlstra, A. A. 1996, *ApJL*, 467, L13+
- Minniti, D., Zijlstra, A. A., & Alonso, M. V. 1999, *AJ*, 117, 881
- Mishenina, T. V., Soubiran, C., Kovtyukh, V. V., & Korotin, S. A. 2004, *A&A*, 418, 551
- Mo, H. J., Mao, S., & White, S. D. M. 1998, *MNRAS*, 295, 319
- Moffett, T. J., & Barnes, III, T. G. 1984, *ApJS*, 55, 389
- Moffett, T. J., Gieren, W. P., Barnes, III, T. G., & Gomez, M. 1998, *ApJS*, 117, 135
- Molla, M., Cantin, S., Robert, C., Pellerin, A., & Hardy, E. 2006
- Mollá, M., & Hardy, E. 2002, *AJ*, 123, 3055
- Mollá, M., Hardy, E., & Beauchamp, D. 1999, *ApJ*, 513, 695
- Moorthy, B. K., & Holtzman, J. A. 2006, *MNRAS*, 371, 583
- Morrison, H. L., Boroson, T. A., & Harding, P. 1994, *AJ*, 108, 1191
- Morrison, H. L., Miller, E. D., Harding, P., Stinebring, D. R., & Boroson, T. A. 1997, *AJ*, 113, 2061
- Mould, J. 2005, *AJ*, 129, 698
- Nakamura, O., Fukugita, M., Yasuda, N., Loveday, J., Brinkmann, J., Schneider, D. P., Shimasaku, K., & SubbaRao, M. 2003, *AJ*, 125, 1682

- Navarro, J. F., Helmi, A., & Freeman, K. C. 2004, *ApJL*, 601, L43
- Neeser, M. J., Sackett, P. D., De Marchi, G., & Paresce, F. 2002, *A&A*, 383, 472
- Newberg, H. J. et al. 2002, *ApJ*, 569, 245
- Newton, I., Du Chatelet, M., De Breteuil, G., & Le Tonnelier, E. 1756
- Ngeow, C.-C., Kanbur, S. M., Nikolaev, S., Tanvir, N. R., & Hendry, M. A. 2003, *ApJ*, 586, 959
- Nissen, P. E. 1995, in *IAU Symp. 164: Stellar Populations*, 109–+
- Nissen, P. E., Chen, Y., Asplund, M., & Max, P. 2003, *Elemental Abundances in Old Stars and Damped Lyman- α Systems*, 25th meeting of the IAU, Joint Discussion 15, 22 July 2003, Sydney, Australia, 15
- Nissen, P. E., & Schuster, W. J. 1997, *A&A*, 326, 751
- Norris, J. E. 1999, *Ap&SS*, 265, 213
- Norris, J. E., & Ryan, S. G. 1991, *ApJ*, 380, 403
- Ochsenbein, F., Bauer, P., & Marcout, J. 2000, *A&AS*, 143, 23
- Ojha, D. K. 2001, *MNRAS*, 322, 426
- Oosterloo, T., Fraternali, F., & Sancisi, R. 2007
- Osterbrock, D. E. 1989
- Osterbrock, D. E., Fulbright, J. P., & Bida, T. A. 1997, *PASP*, 109, 614
- Osterbrock, D. E., Fulbright, J. P., Martel, A. R., Keane, M. J., Trager, S. C., & Basri, G. 1996, *PASP*, 108, 277
- Pagel, B. E. J., & Tautvaisiene, G. 1995, *MNRAS*, 276, 505
- Parker, J. E., Humphreys, R. M., & Beers, T. C. 2004, *AJ*, 127, 1567
- Peletier, R. F. et al. 2007, *ArXiv e-prints*, 704
- Peletier, R. F. et al. 2007, *New Astronomy Review*, 51, 29
- Peletier, R. F., et al. 2006
- Peñarrubia, J., McConnachie, A., & Babul, A. 2006, *ApJL*, 650, L33

- Percival, W. J., Cole, S., Eisenstein, D. J., Nichol, R. C., Peacock, J. A., Pope, A. C., & Szalay, A. S. 2007, ArXiv e-prints, 705
- Perez, I., Sanchez-Blazquez, P., & Zurita, A. 2006
- Pizzella, A., Corsini, E. M., Vega Beltrán, J. C., & Bertola, F. 2004, *A&A*, 424, 447
- Pohlen, M., Balcells, M., Lütticke, R., & Dettmar, R.-J. 2004, *A&A*, 422, 465
- Pohlen, M., Dettmar, R.-J., & Lütticke, R. 2000, *A&A*, 357, L1
- Pohlen, M., Dettmar, R.-J., Lütticke, R., & Aronica, G. 2002, *A&A*, 392, 807
- Pohlen, M., & Trujillo, I. 2006, *A&A*, 454, 759
- Pohlen, M., Zaroubi, S., Peletier, R. F., & Dettmar, R. J. 2007
- Prantzos, N., & Boissier, S. 2000, *MNRAS*, 313, 338
- Press, W. H., Teukolsky, S. A., Vetterling, W. T., & Flannery, B. P. 1992, *Numerical recipes in C. The art of scientific computing* (Cambridge: University Press, —c1992, 2nd ed.)
- Prochaska, J. X., Naumov, S. O., Carney, B. W., McWilliam, A., & Wolfe, A. M. 2000, *AJ*, 120, 2513
- Prochaska, J. X., & Wolfe, A. M. 1998, *ApJ*, 507, 113
- Proctor, R. N., & Sansom, A. E. 2002, *MNRAS*, 333, 517
- Proctor, R. N., Sansom, A. E., & Reid, I. N. 2000, *MNRAS*, 311, 37
- Prugniel, P., Maubon, G., & Simien, F. 2001, *A&A*, 366, 68
- Puzia, T. H., Kissler-Patig, M., Thomas, D., Maraston, C., Saglia, R. P., Bender, R., Goudfrooij, P., & Hempel, M. 2005, *A&A*, 439, 997
- Quinn, P. J., & Goodman, J. 1986, *ApJ*, 309, 472
- Quinn, P. J., Hernquist, L., & Fullagar, D. P. 1993, *ApJ*, 403, 74
- Ramírez, I., Allende Prieto, C., & Lambert, D. L. 2007, *A&A*, 465, 271
- Rampazzo, R., Annibali, F., Bressan, A., Longhetti, M., Padoan, F., & Zeilinger, W. W. 2005, *A&A*, 433, 497
- Reddy, B. E., Lambert, D. L., & Allende Prieto, C. 2006, *MNRAS*, 367, 1329

- Reddy, B. E., Tomkin, J., Lambert, D. L., & Allende Prieto, C. 2003, MNRAS, 340, 304
- Reid, N. 1998, AJ, 115, 204
- Reid, N., & Majewski, S. R. 1993, ApJ, 409, 635
- Rix, H., & White, S. D. M. 1992, MNRAS, 254, 389
- Robertson, B., Bullock, J. S., Cox, T. J., Di Matteo, T., Hernquist, L., Springel, V., & Yoshida, N. 2006, ApJ, 645, 986
- Robin, A. C., Haywood, M., Creze, M., Ojha, D. K., & Bienayme, O. 1996, A&A, 305, 125
- Robin, A. C., Reyl e, C., Derri re, S., & Picaud, S. 2003, A&A, 409, 523
- Rose, J. A., Arimoto, N., Caldwell, N., Schiavon, R. P., Vazdekis, A., & Yamada, Y. 2005, AJ, 129, 712
- Ryder, S. D., Fenner, Y., & Gibson, B. K. 2005, MNRAS, 358, 1337
- Saha, A., Thim, F., Tammann, G. A., Reindl, B., & Sandage, A. 2006, ApJS, 165, 108
- Sakai, S. et al. 2000, ApJ, 529, 698
- Saleh, L., Beers, T. C., & Mathews, G. J. 2004, ApJ, submitted (astro-ph/0407159)
- S nchez-Bl zquez, P., Forbes, D. A., Strader, J., Brodie, J., & Proctor, R. 2007, MNRAS, 377, 759
- S nchez-Bl zquez, P., Gorgas, J., & Cardiel, N. 2006, A&A, 457, 823
- S nchez-Bl zquez, P., Gorgas, J., Cardiel, N., & Gonz lez, J. J. 2006a, A&A, 457, 787
- . 2006b, A&A, 457, 809
- Sandage, A., & Tammann, G. A. 2006, ARA&A, 44, 93
- Sarajedini, A., & Van Duyne, J. 2001, AJ, 122, 2444
- Sarzi, M. et al. 2006, MNRAS, 366, 1151
- Schiavon, R. P. 2006, ArXiv Astrophysics e-prints

- Schwarzkopf, U., & Dettmar, R.-J. 2000a, *A&AS*, 144, 85
- . 2000b, *A&A*, 361, 451
- Seabroke, G. M., & Gilmore, G. 0700
- Searle, L., & Zinn, R. 1978, *ApJ*, 225, 357
- Sebo, K. M. et al. 2002a, *VizieR Online Data Catalog*, 214, 20071
- . 2002b, *ApJS*, 142, 71
- Sellwood, J. A., & Carlberg, R. G. 1984, *ApJ*, 282, 61
- Serra, P., & Trager, S. C. 2007, *MNRAS*, 374, 769
- Sesar, B. et al. 2007, *ArXiv e-prints*, 704
- Seth, A., De Jong, R., Dalcanton, J., & the GHOSTS team. 2007, *ArXiv Astrophysics e-prints*
- Seth, A. C., Dalcanton, J. J., & de Jong, R. S. 2005a, *AJ*, 129, 1331
- . 2005b, *AJ*, 130, 1574
- Shaw, M. A., & Gilmore, G. 1989, *MNRAS*, 237, 903
- . 1990, *MNRAS*, 242, 59
- Siegel, M. H., Majewski, S. R., Reid, I. N., & Thompson, I. B. 2002, *ApJ*, 578, 151
- Simkin, S. M. 1974, *A&A*, 31, 129
- Simon, J. D., Bolatto, A. D., Leroy, A., Blitz, L., & Gates, E. L. 2005, *ApJ*, 621, 757
- Sirianni, M. et al. 2005, *PASP*, 117, 1049
- Skrutskie, M. F. et al. 2006, *AJ*, 131, 1163
- Smith, R. J., Hudson, M. J., Lucey, J. R., Nelan, J. E., & Wegner, G. A. 2006, *MNRAS*, 369, 1419
- Smolčić, V. et al. 2004, *ApJL*, 615, L141
- Sotnikova, N. Y., & Rodionov, S. A. 2006, *Astronomy Letters*, 32, 649
- Soubiran, C., Bienaymé, O., & Siebert, A. 2003, *A&A*, 398, 141

- Sparke, L. S., & Gallagher, III, J. S. 2000, Galaxies in the universe : an introduction (Galaxies in the Universe, by Linda S. Sparke and John S. Gallagher, III, pp. 416. ISBN 0521592410. Cambridge, UK: Cambridge University Press, September 2000.)
- Spergel, D. N. et al. 2003, ApJS, 148, 175
- Spitzer, L. J. 1942, ApJ, 95, 329
- Spitzer, L. J., & Schwarzschild, M. 1951, ApJ, 114, 385
- Springel, V., & Hernquist, L. 2005, ApJL, 622, L9
- Statler, T. 1995, AJ, 109, 1371
- Statler, T. S. 1988, ApJ, 331, 71
- Staveley-Smith, L., Davies, R. D., & Kinman, T. D. 1992, MNRAS, 258, 334
- Stinson, G., Seth, A., Katz, N., Wadsley, J., Governato, F., & Quinn, T. 2006, MNRAS, 373, 1074
- Strickland, D. K., Heckman, T. M., Colbert, E. J. M., Hoopes, C. G., & Weaver, K. A. 2004, ApJ, 606, 829
- Sung, E., Han, C., Ryden, B. S., Patterson, R. J., Chun, M., Kim, H., Lee, W., & Kim, D. 1998, ApJ, 505, 199
- Swaters, R. A., & Balcells, M. 2002, A&A, 390, 863
- Swaters, R. A., van Albada, T. S., van der Hulst, J. M., & Sancisi, R. 2002, A&A, 390, 829
- Tantalo, R., Chiosi, C., & Bressan, A. 1998, A&A, 333, 419
- Tanvir, N. R., Hendry, M. A., Watkins, A., Kanbur, S. M., Berdnikov, L. N., & Ngeow, C. C. 2005, MNRAS, 363, 749
- Tautvaišienė, G., Edvardsson, B., Tuominen, I., & Ilyin, I. 2001, A&A, 380, 578
- Taylor, J. 1997, Introduction to Error Analysis, the Study of Uncertainties in Physical Measurements, 2nd Edition (Published by University Science Books, 648 Broadway, Suite 902, New York, NY 10012, 1997.)
- Thomas, D., Maraston, C., & Bender, R. 2003, MNRAS, 339, 897
- Tikhonov, N. A., & Galazutdinova, O. A. 2005, Astrophysics, 48, 221

- Tikhonov, N. A., Galazutdinova, O. A., & Drozdovsky, I. O. 2005, *A&A*, 431, 127
- Tojeiro, R., Heavens, A. F., Jimenez, R., & Panter, B. 2007, *ArXiv e-prints*, 704
- Tonry, J., & Davis, M. 1979, *AJ*, 84, 1511
- Toth, G., & Ostriker, J. P. 1992, *ApJ*, 389, 5
- Trager, S. C., Faber, S. M., Worthey, G., & González, J. J. 2000a, *AJ*, 120, 165
- . 2000b, *AJ*, 119, 1645
- Trager, S. C., Worthey, G., Faber, S. M., Burstein, D., & Gonzalez, J. J. 1998, *ApJS*, 116, 1
- Tremonti, C. A. et al. 2004, *ApJ*, 613, 898
- Tsikoudi, V. 1979, *ApJ*, 234, 842
- Tully, R. B., Pierce, M. J., Huang, J., Saunders, W., Verheijen, M. A. W., & Witchalls, P. L. 1998, *AJ*, 115, 2264
- Udalski, A., Soszynski, I., Szymanski, M., Kubiak, M., Pietrzynski, G., Wozniak, P., & Zebrun, K. 1999a, *Acta Astronomica*, 49, 223
- . 1999b, *Acta Astronomica*, 49, 437
- Vallenari, A., Pasetto, S., Bertelli, G., Chiosi, C., Spagna, A., & Lattanzi, M. 2006, *A&A*, 451, 125
- Valotto, C., & Giovanelli, R. 2004, *AJ*, 128, 115
- van den Bosch, F. C. 2002, *MNRAS*, 332, 456
- van der Kruit, P. C. 1984a, *A&A*, 140, 470
- . 1984b, *A&A*, 140, 470
- . 1988, *A&A*, 192, 117
- van der Kruit, P. C., Jiménez-Vicente, J., Kregel, M., & Freeman, K. C. 2001, *A&A*, 379, 374
- van der Kruit, P. C., & Searle, L. 1981a, *A&A*, 95, 116
- . 1981b, *A&A*, 95, 105
- . 1982, *A&A*, 110, 61

- van Dokkum, P. G., Peletier, R. F., de Grijs, R., & Balcells, M. 1994, *A&A*, 286, 415
- van Zee, L., Salzer, J. J., Haynes, M. P., O'Donoghue, A. A., & Balonek, T. J. 1998, *AJ*, 116, 2805
- Vansevicius, V. et al. 2004, *ApJL*, 611, L93
- Vazdekis, A., & Arimoto, N. 1999, *ApJ*, 525, 144
- Vazdekis, A., Casuso, E., Peletier, R. F., & Beckman, J. E. 1996, *ApJS*, 106, 307
- Vazdekis, A., Cenarro, A. J., Gorgas, J., Cardiel, N., & Peletier, R. F. 2003, *MNRAS*, 340, 1317
- Vazdekis, A., Trujillo, I., & Yamada, Y. 2004, *ApJL*, 601, L33
- Velazquez, H., & White, S. D. M. 1999, *MNRAS*, 304, 254
- Verde, L., Oh, S. P., & Jimenez, R. 2002, *MNRAS*, 336, 541
- Verheijen, M. A. W. 2001, *ApJ*, 563, 694
- Villumsen, J. V. 1985, *ApJ*, 290, 75
- Wainscoat, R. J., Freeman, K. C., & Hyland, A. R. 1989, *ApJ*, 337, 163
- Walker, I. R., Mihos, J. C., & Hernquist, L. 1996, *ApJ*, 460, 121
- Weiner, B. J., Williams, T. B., van Gorkom, J. H., & Sellwood, J. A. 2001, *ApJ*, 546, 916
- Westfall, K. B., Bershady, M. A., Verheijen, M. A. W., Andersen, D. R., & Swaters, R. A. 2005, *ArXiv Astrophysics e-prints*
- Wolfe, A. M., & Prochaska, J. X. 1998, *ApJL*, 494, L15+
- Worthey, G. 1994, *ApJS*, 95, 107
- Worthey, G., Faber, S. M., & Gonzalez, J. J. 1992, *ApJ*, 398, 69
- Worthey, G., Faber, S. M., Gonzalez, J. J., & Burstein, D. 1994, *ApJS*, 94, 687
- Worthey, G., & Ottaviani, D. L. 1997, *ApJS*, 111, 377
- Wu, H. et al. 2002, *AJ*, 123, 1364
- Wyse, R. F. G., Gilmore, G., Norris, J. E., Wilkinson, M. I., Kleyana, J. T., Koch, A., Evans, N. W., & Grebel, E. K. 2006, *ApJL*, 639, L13

- Xilouris, E. M., Byun, Y. I., Kylafis, N. D., Paleologou, E. V., & Papamastorakis, J. 1999, *A&A*, 344, 868
- Xilouris, E. M., Kylafis, N. D., Papamastorakis, J., Paleologou, E. V., & Haerendel, G. 1997, *A&A*, 325, 135
- Yahil, A., Tammann, G. A., & Sandage, A. 1977, *ApJ*, 217, 903
- Yang, X., van den Bosch, F. C., Mo, H. J., Mao, S., Kang, X., Weinmann, S. M., Guo, Y., & Jing, Y. P. 2006, *MNRAS*, 369, 1293
- Yanny, B. et al. 2003, *ApJ*, 588, 824
- Yoachim, P., & Dalcanton, J. 2006a, IAU poster
- Yoachim, P., & Dalcanton, J. J. 2005, *ApJ*, 624, 701
- . 2006b, *AJ*, 131, 226
- . 2007
- York, D. G. et al. 2000, *AJ*, 120, 1579
- Zackrisson, E., Bergvall, N., Östlin, G., Micheva, G., & Leksell, M. 2006, *ApJ*, 650, 812
- Zaritsky, D., Kennicutt, Jr., R. C., & Huchra, J. P. 1994, *ApJ*, 420, 87
- Zaritsky, D., Smith, R., Frenk, C. S., & White, S. D. M. 1997, *ApJL*, 478, L53+
- Zentner, A. R., Kravtsov, A. V., Gnedin, O. Y., & Klypin, A. A. 2005, *ApJ*, 629, 219
- Zhao, D. H., Jing, Y. P., Mo, H. J., & Börner, G. 2003, *ApJL*, 597, L9
- Zheng, Z. et al. 1999, *AJ*, 117, 2757
- Zibetti, S., & Ferguson, A. M. N. 2004, *MNRAS*, 352, L6
- Zibetti, S., White, S. D. M., & Brinkmann, J. 2004, *MNRAS*, 347, 556
- Ziegler, B. L., & Bender, R. 1997, *MNRAS*, 291, 527
- Zwaan, M. A., Briggs, F. H., Sprayberry, D., & Sorar, E. 1997, *ApJ*, 490, 173

Appendix A

MY PERSONAL OBJECTION TO ESTABLISHED GRAMMAR CONVENTIONS

There is a growing debate surrounding how the word “data” should be used in scientific publications. Traditionalists maintain that “data” is the plural form of “datum”, and should therefore take a plural verb. These people do not seem to realize that they are speaking English and not Latin. It has actually been several centuries since a significant astronomical study was published in Latin (e.g., Newton et al., 1756). The issue is summarized by the Oxford Dictionary website:

Strictly speaking, data is the plural of datum, and should be used with a plural verb (like facts). However, there has been a growing tendency to use it as an equivalent to the uncountable noun information, followed by a singular verb. This is now regarded as generally acceptable in American use, and in the context of information technology. The traditional usage is still preferable, at least in Britain, but it may soon become a lost cause.¹

An example of how “data” is considered singular in common parlance is well illustrated in the popular² television program *Star Trek: The Next Generation* which features a character named Data. English naming conventions tend to ascribe singular nouns for an individual’s name or nickname. For example, a strong individual might be given the nickname “Bull”, or someone who is particularly rude might be referred to as a “jerk”. Plural monikers are reserved for groups. By using Data as a name

¹<http://www.askoxford.com/asktheexperts/faq/aboutgrammar/data?view=uk>

²popular among astronomers at least

for a character that does not suffer from multiple-personality disorder, the singular nature of the word is clearly implied.

Unfortunately, many scientific journals insist on using the archaic form of “data” as plural. For example, the *Astrophysical Journal* lists as their eleventh instruction for authors, “The word ‘data’ is plural and takes a plural verb.”³

Galilei (1632) established that it is preferable to write in a style that is accessible to the largest possible audience. Despite many having the noble goal of making their scientific writing more accessible, recent years have seen an explosion in the use of TLAs⁴ and other jargon. By treating “data” as a singular noun, we have an opportunity to move closer to common language and better widespread understanding. An example of how I would prefer to use the word data is illustrated in Figure A.1.

I hereby appeal to the general scientific community to start treating “data” as a singular noun. By working together, we can eradicate an unnecessary difference between scientific discourse and popular language and sound less snooty⁵.

³<http://www.journals.uchicago.edu/ApJ/instruct.html>

⁴Three Letter Acronym

⁵i.e., British

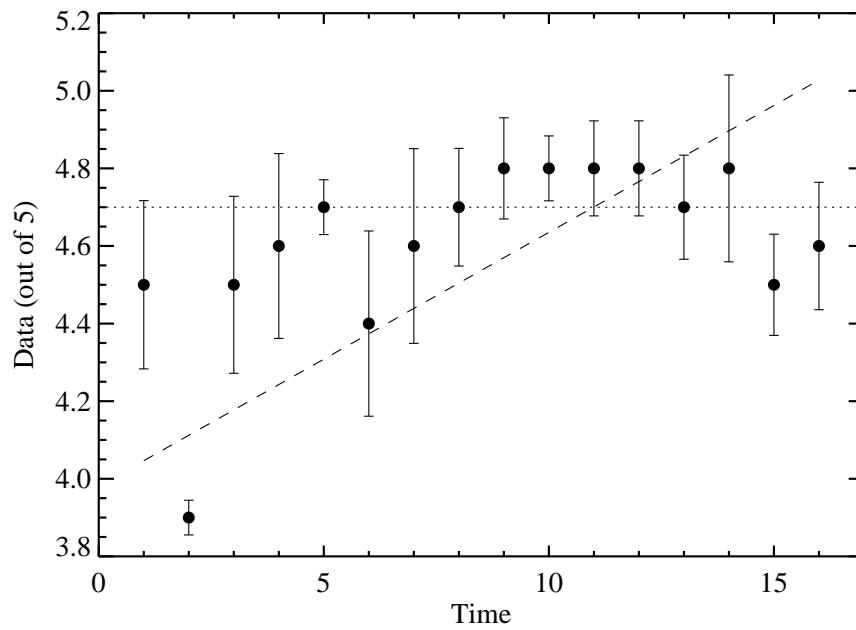


Figure A.1 This data shows no significant trend with time, even if a best-fit line is added to aid the eye (dashed line).

VITA

Peter Yoachim was born on February 24, 1978 and grew up in the suburbs⁶ of Olympia, Washington. After graduating from Capital High School in 1996, Peter attended the the University of California at Berkeley. While taking a freshman seminar course on Cosmology, Peter had an epiphany that one can major in Astronomy simply because it's really cool. Peter returned to Washington in 2001 to attend graduate school in the Astronomy Department at the University of Washington where he worked with Julianne Dalcanton on observational properties of thick disks in external galaxies. Peter defended his Ph.D. in July 2007 and will begin a postdoc at the University of Texas, Austin in the fall of 2007.

Peter likes cheese.

⁶“Suburbia-where they cut down the trees and name the streets after them”